Advancing Zinc-Ion Batteries: Holistic Solutions for Cathode, Anode, and Electrolyte Optimisation

Zixuan Li

Trinity College

University of Oxford

A thesis submitted for the degree of

Doctor of Philosophy

Trinity 2025

Acknowledgements

First, I would like to express my deepest gratitude to my supervisors, Dr. Alex W. Robertson and Sir Prof. Peter G. Bruce, for their support and invaluable guidance throughout my DPhil studies.

To Alex, I cannot thank you enough for being the best supervisor I could have ever asked for. You are incredibly smart, kind, and supportive. For the past four years, you travelled from Warwick to Oxford every single week to meet with me, a remarkable display of dedication and responsibility that I deeply admire. If I am ever fortunate enough to become an independent PI one day, my greatest aspiration will be to mentor my students with the same care and commitment that you have shown me.

I am also profoundly grateful to Peter for providing a truly world-class research environment. Being part of the PGB group has been one of the most rewarding experiences of my PhD journey. The group is filled with cutting-edge science that has both fascinated and inspired me. I have learned from the very best, which has broadened my perspective and helped me develop new insights into the field. I could not have asked for a more fulfilling PhD experience and my satisfaction with this journey is truly 100 out of 100.

I would like to sincerely thank the Jardine Scholarship for its continuous support over the past four years. It has given me the opportunity to study at the University of Oxford, which is not only a prestigious place but also an expensive one, and I am truly grateful for the financial support that eased this burden and allowed me to focus on my studies. It has also been a real pleasure to meet other Jardine Scholars and to be part of such a supportive and inspiring community. I really appreciate all the help and encouragement from the Jardine Foundation, and I hope to contribute positively to society in the future.

Special thanks to Dr. Rob House for his valuable insights into my cathode project. Thanks to YC Wong and Ashok Menon for the collaboration we had. I would also like to thank the group members for their support and friendship. Thanks to Dr. Yi Yuan and Dr. Shengda Pu for being fantastic teammates. Thanks to Dr. Sofia De Sousa Coutinho, Dr. Xueyan Hou and Murray Sanderson being such amazing office neighbors. Thanks for Lechen Yang, Dr. Mingzhi Cai, Dr. Bingkun Hu, Dr. Shengming Zhang, Jiabin Li Wang, Yuanhui Zhu for sharing so many enjoyable lunch breaks together. Thanks for other lovely group members Dr. Tammy Nimmo, Dr. Jun Chen, Dr. Longlong Wang, Nicole Mitchell, Bartholomew Payne, Dr Max Jenkins and Dr. Mikkel Juelsholt for the great times and all the fun we shared. Special thanks to Chen Shen, Hewen Chen, and Shenghuan Ding for being such loyal and supportive friends.

There were difficult moments along the way, and many people helped me get through them. I am deeply grateful to Sofia, who is truly one of the kindest and most supportive people I have ever met and who helped me enormously. I would also like to thank Dr. Adrian Taylor and Alex for listening to my concerns and offering so much help and guidance. My thanks also

go to the departmental staff and my colleagues in the group for their support. Being a genuinely caring and supportive person takes real effort and commitment, and I cannot fully express how much I appreciate those who were willing to help and understand during challenging times. Their kindness has inspired me, and I hope to be someone who can offer the same support to others in the future and be there when people need a helping hand.

Huge thanks go to my partner, Rui Qi, for his endless love and support throughout this roller-coaster journey. I have learned so much from him, and I am grateful to destiny for bringing us both to Oxford and even into the same research group.

I am also deeply thankful to my parents for their constant encouragement and belief in me.

Finally, I would like to thank myself for persevering through challenges and remaining persistent. This journey has shaped me not only as a scientist but also as a person. I am committed to continuing to grow, to stay curious, and to become someone who approaches both science and life with integrity and kindness.

Abstract

Zinc-ion batteries (ZIBs) have emerged as promising energy storage systems owing to compatibility of zinc anodes with aqueous electrolytes. While aqueous electrolytes provide advantages in safety, they also introduce critical challenges at both electrodes. At the zinc anode, parasitic side reactions and dendritic growth compromise reversibility, while Mn-based cathodes suffer from Mn dissolution, limiting cycle life. Together, these interfacial instabilities hinder the practical deployment of ZIBs in large-scale applications.

This thesis develops an understanding of degradation mechanism and proposes strategies to overcome them. Firstly, the zinc anode–electrolyte interface is investigated. While high current densities can promote planar Zn growth, they are incompatible with cathode operation. To resolve this, an approach using uniaxial mechanical pressure is introduced, enabling stable zinc plating/stripping under practical current densities.

Secondly, the focus shifts to the MnO_2 cathode–electrolyte interface. Using operando analysis, it is shown that the primary charge storage mechanism proceeds via reversible Mn dissolution and redeposition. Furthermore, the role of Mn^{2+} additives is found to act as a soluble redox reservoir, supplying additional active material during charging. These findings highlight the strong coupling between battery electrochemical performance and electrolyte composition.

Thirdly, recognising that many challenges are inherent to aqueous environments, zinc-metal-free cell architectures are explored. A new zinc-containing disordered rocksalt (DRX) cathode, $ZnMnO_2$, is developed to pair with a zinc-free current collector. This anode free cell demonstrated promising electrochemical performance, offering advantages such as extended shelf life and higher energy density.

Finally, to further mitigate side reactions, non-aqueous ZIBs are explored. To unlock efficient Zn^{2+} diffusion in DRX cathodes under non-aqueous conditions, cation vacancies are engineered by delithiating Li-based DRX precursors, leading to improved Zn^{2+} transport and enhanced battery performance.

These insights provide guiding principles for the rational design of next-generation ZIBs with improved stability and performance.

Contents

List of Abbreviations

List of Publication

Table of Contents

List of Abbreviations

EVs	Electric Vehicles
LIBs	Lithium-Ion Batteries
EC	Ethylene Carbonate
DMC	Dimethyl Carbonate
PE	Polyethylene
PP	Polypropylene
OCV	Open-Circuit Voltage
NMC811	$LiNi_{0.8}Mn_{0.1}Co_{0.1}O_2$
LFP	$LiFePO_4$
ZIBs	Zinc-Ion Batteries
TM	Transition Metal
HER	Hydrogen Evolution Reaction
CE	Coulombic Efficiency
ZHS	Zinc Hydroxide Sulphate
ZHT	Zinc Hydroxide Triflate
ZHTSI	Zinc Hydroxide Triflimide
ZHO	Zinc Hydroxide
XCT	X-ray Computed Tomography
HCP	Hexagonal Close-Packed
MOFs	Metal–Organic Frameworks
ALD	Atomic Layer Deposition
FCC	Face Centered Cubic
3D	Three-Dimensional
PEI	Polyethyleneimine
PEG	Polyethylene Glycol
DMC	Dimethyl Carbonate
EG	Ethylene Glycol
Et_2O	Diethyl Ether
DMSO	Dimethyl Sulfoxide
AN	Acetonitrile
DME	Dimethoxyethane
PBAs	Prussian Blue Analogues
EDX	Energy-dispersive X-ray Spectroscopy
NMR	Nuclear Magnetic Resonance
XAS	X-ray Absorption Spectroscopy
XRF	X-ray Fluorescence
OER	Oxygen Evolution Reaction
IPFY	Inverse Partial Fluorescence Yield
SEI	Solid Electrolyte Interphase
PTFE	Polytetrafluoroethylene
SEM	Scanning Electron Microscopy
SE	Secondary Electrons
TEM	Transmission Electron Microscopy
HRTEM	High-Resolution TEM
SAED	Selected Area Electron Diffraction
XRD	X-ray Diffraction
XPDF	X-ray Pair Distribution Function
sXAS	soft XAS
CCE	Cumulative Coulombic Efficiency
RTC	Relative Texture Coefficient
OM	Optical Microscopy
DI	Deionised
PXRD	Powder X-ray Diffraction
UV-Vis	Ultraviolet-Visible
DRX	Cation-Disordered Rocksalt
CV	Cyclic Voltammetry
LCF	Linear Combination Fitting
SRO	Short-Range Ordering
DFT	Density Functional Theory
NEB	Nudged Elastic Band
HAADF	High-Angle Annular Dark-Field

ICP-OES	Inductively Coupled Plasma Optical Emission Spectroscopy
XANES	X-ray Absorption Near Edge Structure
GITT	Galvanostatic Intermittent Titration Technique
STEM	Scanning Transmission Electron Microscopy
EXAFS	Extended X-ray Absorption Fine Structure
ICP-MS	Inductively Coupled Plasma Mass Spectrometry

List of Publications

[1] **Z. Li**, Y. Yuan, SD. Pu, R. Qi, S. Ding, R. Qin, A. Kareer, PG. Bruce, AW. Robertson. Achieving Planar Zn Electroplating in Aqueous Zinc Batteries with Cathode-Compatible Current Densities by Cycling under Pressure. *Adv. Mater.* **2024**, 36 (32), 2401576.

[2] SD. Pu, † B. Hu, † **Z. Li**, † Y. Yuan, C. Gong, Z. Ning, C. Chau, SJ. Marrow, X. Gao, PG. Bruce, AW. Robertson. Decoupling, Quantifying, and Restoring Aging-Induced Zn-Anode Losses in Rechargeable Aqueous Zinc Batteries. *Joule*, **2023**, 7(2), 366-379.

[3] **Z. Li**, AW. Robertson. Electrolyte Engineering Strategies for Regulation of the Zn Metal Anode in Aqueous Zn-Ion Batteries. *Battery Energy*, **2023**, 2(1), 20220029

[4] Y. Yuan, **Z. Li**, R. Deng, SD. Pu, M. Walker, PG. Bruce, AW. Robertson. Identifying the role of Zn self-dissolution in the anode corrosion process in Zn-ion batteries. *Energy Environ. Sci.* **2025**, 18(11):5610-21.

[5] R. Deng, Y. Yuan, **Z. Li**, AW. Robertson, F. Wu, A liquid-infiltrated Al_2O_3 framework electrolyte enables aqueous zinc batteries. *Chem. Commun.* **2024**, 60 (97), 14423-14426

[6] Y. Yuan, SD. Pu, MA. Pérez-Osorio, **Z. Li**, S. Zhang, S. Yang, B. Liu, C. Gong, AS. Menon, LF. Piper, X.Gao, PG. Bruce, AW. Robertson. Diagnosing the electrostatic shielding mechanism for dendrite suppression in aqueous zinc batteries. *Adv. Mater.* **2024**, 36(9), 2307708.

[7] **Z. Li,** R. Qi, Y. Yuan, L. Yang, L. Song, AS. Menon, LFJ. Piper, D. Wermeille, P. Thompson, RA. House, PG. Bruce, AW. Robertson. Cation-Disordered Rocksalt Cathode for Anode-Free Zinc-Ion Batteries. *Energy Environ. Sci.* accepted.

[8] **Z. Li**, K. Sowa, T. Kołodziej, Y. Yuan, H. Chen, L. Song, P. Wróbel, D. Wermeille, P. Thompson, P. Korecki, PG. Bruce, AW. Robertson. Diagnosing the True Role of Mn Additives in Aqueous Zn/MnO_2 Batteries. Manuscript submitted.

1

1 Introduction

1.1 The Broader Context of Battery Technologies

The accelerating threat of global warming, largely driven by anthropogenic CO_2 emissions, demands urgent and sustained action. Achieving net-zero carbon emissions has become a global imperative to mitigate climate change and reduce the environmental footprint of human activity. Among all sectors, transportation stands out as a major contributor to greenhouse gas emissions, making its decarbonisation a critical component of the broader transition to sustainable energy systems. Over the past decade, the widespread deployment of electric vehicles (EVs) has emerged as a viable and rapidly evolving solution to this challenge. At the centre of EV technology is the lithium-ion battery, a high-performance electrochemical energy storage system that is progressively replacing internal combustion engines as the dominant power source in modern vehicles.[1,2]

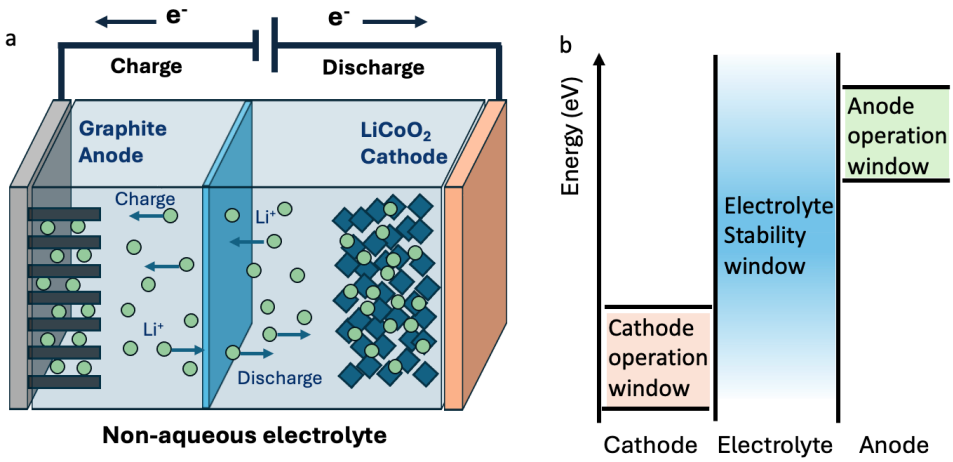

Figure 1.1 (a) Schematic illustration of a Li-ion battery comprising a graphite anode and a $LiCoO_2$ cathode operating in a Li-based non-aqueous electrolyte, driven by an external circuit. (b) Electrochemical stability window of the electrolyte, showing the relative energy levels of the cathode, anode, and electrolyte under open-circuit conditions.

Lithium-ion batteries (LIBs), as the dominant energy storage technology in modern electrochemical systems, typically employ a simple configuration: a graphite anode, a lithium cobalt oxide ($LiCoO_2$) cathode, and a non-aqueous electrolyte.[3] These devices operate via

reversible redox reactions that convert chemical energy into electrical energy through the coupled transport of lithium ions and electrons, as illustrated in Figure 1.1a.

During the charging process, oxidation occurs at the $LiCoO_2$ cathode, releasing lithium ions and electrons according to the reaction:

$$LiCoO_2 \rightarrow Li_{1-x}CoO_2 + xLi^+ + xe^-$$

The liberated electrons flow through an external circuit, while the lithium ions simultaneously migrate from cathode through the electrolyte toward the anode. At the graphite anode, reduction takes place as lithium ions are intercalated into the carbon matrix:

$$xC_6 + xLi^+ + xe^- \rightarrow xLiC_6$$

Due to the reversible nature of the electrochemical reactions, the discharge process proceeds in the opposite direction of charging. During discharge, lithium ions deintercalate from the graphite anode and migrate through the electrolyte toward the cathode, where they are reinserted into the $LiCoO_2$ structure, accompanied by the flow of electrons through the external circuit to deliver usable electrical energy.

The electrolyte plays a critical role in this charging/discharging process. It must enable rapid Li^+ ion transport while maintaining electrochemical stability across the full operating voltage range of the cell. Typically, the electrolyte is a non-aqueous liquid, composed of a mixture of organic carbonate solvents such as ethylene carbonate (EC) and dimethyl carbonate (DMC), containing a dissolved lithium salt, most commonly lithium hexafluorophosphate ($LiPF_6$).[4] This composition ensures high ionic conductivity, typically in the range of 10^{-3} to 10^{-2} S cm^{-1}, while maintaining a wide electrochemical stability window (up to ~4.5 V vs. Li^+/Li).[5] To prevent internal short circuits and allow selective ionic transport, a microporous polymer separator which is often made from polyethylene (PE) or polypropylene (PP), is used to physically isolate the electrodes.[6] Soaked in electrolyte, this separator permits

lithium-ion migration through its interconnected pores, with solvation–desolvation dynamics governing the movement of Li^+ and enabling efficient ionic conduction during operation.

To evaluate battery performance, one of the most critical parameters is energy density, which quantifies the amount of energy a battery can deliver per unit mass. It is typically expressed in watt-hours per kilogram (Wh kg^{-1}). This parameter is fundamentally determined by both the cell voltage (V) and the specific capacity (mAh g^{-1}) of the electrode materials.

Battery voltage (V) arises from the difference in chemical potential between the anode and cathode materials, as illustrated in Figure 1.1b. For safe and stable operation, the electrolyte's electrochemical stability window must encompass the redox potentials of both the anode and the cathode to prevent undesired side reactions. The equilibrium voltage of the cell, corresponding to the open-circuit voltage (OCV) can be quantitatively described by the Nernst equation, which relates the cell voltage to the Gibbs free energy change of the electrochemical reaction and the activities of the involved species.[7] The Nernst equation is expressed as:

$$E_{cell} = E^{o}_{cell} - \frac{RT}{zF} lnQ_r$$

where $E^{\circ}cell$ is the standard equilibrium voltage, R the ideal gas constant, T the temperature, z the charge of the ion, and F the Faraday constant. Specifically, the reaction quotient Q_r, defined by the ratio of the activities of the reduced and oxidised species, captures the effect of concentration variations on cell voltage.[7]

On cathode side reaction:

$$Q_r^{cathode} = \frac{a_{Li^+}^{x} \cdot a_{Li_{1-x}CoO_2}}{a_{Li_{1-x}CoO_2}}$$

While on anode side reaction:

$$Q_r^{anode} = \frac{a_{LiC_6}^x}{a_{Li+}^x \cdot a_C^x}$$

where a represents the real-time molar concentration of each species involved in the reaction (mol L^{-1}).[8] This relationship demonstrates that battery voltage is influenced not only by the intrinsic chemical potentials of the electrode materials but also by the dynamic electrochemical environment within the cell.[8]

Another important parameter influencing energy density is the capacity (mAh g^{-1}) of the battery, which determines the total amount of electric charge that can be stored or released during operation. The theoretical specific capacity Q_f of an electrode material[9] can be estimated using the following equation:

$$Q_f = \frac{n \cdot F}{M}$$

Here, *n* is the number of electrons transferred per formula unit during the electrochemical reaction, *F* is Faraday's constant (96,485 C mol^{-1}), and *M* is the molar mass of the active material (g mol^{-1}). This relationship offers key design strategies for enhancing capacity: (i) selecting redox-active materials with a lower molar mass (*M*) increases the number of moles per gram, and (ii) employing materials that support multi-electron transfer reactions (n>1) allows for greater charge storage per formula unit.

In real-world applications, limitations often stem from the both the intrinsic properties and electrochemical behaviour of electrode materials during extended cycling. Graphite anodes, which dominate commercial lithium-ion batteries, are constrained by a relatively low specific capacity of 372 mAh g^{-1}.[10] Lithium metal anodes, by contrast, offer a much higher theoretical capacity (3,860 mAh g^{-1}), making them attractive for next-generation systems such as lithium-sulfur (Li-S) and lithium-oxygen (Li-O_2) batteries.[11] However, their practical application is hindered by issues such as uncontrolled dendritic Li growth, which can penetrate

the separator, leading to internal short circuits and potential safety risks, including thermal runaway.[12] On the cathode side, nickel-rich layered oxides (e.g., NMC811, $LiNi_{0.8}Mn_{0.1}Co_{0.1}O_2$) achieve high volumetric energy densities (>700 Wh L^{-1}) but suffer from structural degradation and interfacial instability at high operating voltages (~4.3 V vs. Li^+/Li).[13] In contrast, lithium iron phosphate ($LiFePO_4$, LFP) cathodes provide excellent thermal and structural stability, offering superior safety and cycle life.[14] Although LFP operates at a lower voltage (~3.2 V vs. Li^+/Li) compared to NMC (~3.8 V), its robustness and cost-effectiveness combined with efficient cell engineering techniques such as dense electrode stacking, can result in competitive pack-level energy densities. Moreover, the abundance and low cost of iron relative to critical metals like cobalt and nickel make LFP a highly sustainable option. Thus, advancing high-energy-density battery technologies through both materials innovation and system-level design optimisation remains a central objective for the future of energy storage.

1.2 Overview of Zinc Ion Batteries (ZIBs)

Multivalent-ion batteries have attracted increasing attention as a promising complement to Li-ion technology, offering the prospect of sustainable and cost-effective energy storage beyond lithium. Abundant and earth-rich metals such as zinc (Zn), magnesium (Mg), calcium (Ca), and aluminium (Al) offer attractive prospects for next-generation rechargeable batteries. Unlike monovalent ions such as Li^+, multivalent metal cations (e.g., Zn^{2+}, Mg^{2+}, Ca^{2+}, Al^{3+}) are capable of transferring two or more electrons per ion, theoretically enabling significantly higher specific capacities and energy densities.[15] However, as described by the Nernst equation, the cell voltage in multivalent-ion systems tends to decrease with increasing charge number (z), due to the inverse dependence of voltage on the number of electrons transferred, which may limit their overall energy output.

Among multivalent candidates, Zn stands out due to its favourable electrochemical properties and material abundance. It offers a high theoretical specific capacity of 820 mAh g^{-1} and an exceptionally high volumetric capacity of 5,851 mAh cm^{-3}, outperforming many other multivalent metals such as Mg (3,833 mAh cm^{-3}), Ca (2,073 mAh cm^{-3}).[15]

Similar to Li-ion batteries, Zn-ion batteries are composed of a Zn anode, a cathode, and an electrolyte. Owing to Zn's relatively low standard reduction potential (-0.76 V vs. the standard hydrogen electrode, SHE), Zn metal anodes are compatible not only with organic electrolytes but also with aqueous electrolytes, without significant side reaction. In contrast, other multivalent metal anodes such as Mg, Ca, and Al tend to undergo severe parasitic reactions with water, forming electrochemically inert byproducts that passivate the electrode surface and compromise battery performance, make them incompatible with aqueous electrolyte. Zn, by contrast, allows for more efficient and reversible electrochemical cycling in aqueous environment.

Aqueous zinc-ion batteries (ZIBs) have attracted considerable attention due to the unique advantages provided by aqueous electrolytes. These includes:

- Cost and safety: Water is inexpensive, abundant, and environmentally benign. Unlike flammable organic solvents, it is non-volatile and non-toxic, making aqueous ZIBs inherently safer, particularly attractive for applications in wearable electronics.
- Superior ionic conductivity: Aqueous electrolytes exhibit much higher ionic conductivity (typically 10^{-2} to 6×10^{-2} S cm^{-1}) than their organic counterparts (10^{-3} to 10^{-2} S cm^{-1}). This facilitates faster Zn^{2+} ion transport and enhances rate capability and power performance.

- Enhanced reaction kinetics: The presence of water significantly reduces interfacial resistance at the electrode–electrolyte interface, accelerating redox reactions and improving charge transfer kinetics, which translates to improved battery efficiency.
- Improved salt solubility: Water's high dielectric constant allows it to dissolve zinc salts (e.g., $Zn(CF_3SO_3)_2$) at high concentrations (~3 M), compared to <0.5 M in typical organic solvents like acetonitrile. This promotes a high concentration of mobile Zn^{2+} ions, essential for maintaining capacity over long cycles.
- Simplified manufacturing: Aqueous ZIBs can be fabricated in ambient conditions without the need for dry-room environments or stringent moisture control, reducing manufacturing cost and complexity. This makes them competitive with moisture and air sensitive systems.

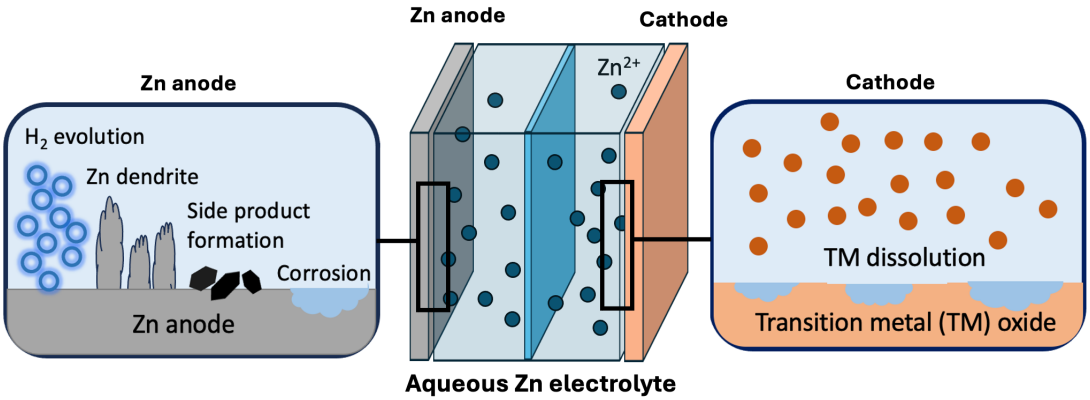

Figure 1.2 Schematic of an aqueous Zn-ion battery, comprising a Zn metal anode and a transition metal oxide cathode, both of which suffer from interfacial degradation induced by the aqueous electrolyte. At the anode–electrolyte interface, key issues include hydrogen evolution, dendrite formation, by-product accumulation, and Zn corrosion. At the cathode–electrolyte interface, transition metal (TM) dissolution is a primary degradation pathway.

These advantages stem from using water as the electrolyte solvent. However, water can be a double-edged sword. While it brings cost, safety, and ionic conductivity benefits, its inherent reactivity can also introduce significant challenges, particularly at the electrode–

electrolyte interfaces, as illustrated in Figure 1.2. At the Zn anode–electrolyte interface, side reactions frequently occur due to the mildly acidic nature of typical aqueous electrolytes (pH ~3–5).[16] These conditions promote Zn corrosion, hydrogen gas evolution, and formation of insoluble byproducts. On the cathode side, transition-metal-based materials such as manganese-, vanadium-, cobalt-based oxides, and Prussian blue analogues are often prone to transition metal (TM) dissolution in aqueous environments,[17] which might lead to gradual capacity fading over repeated cycles.

Meanwhile, nonaqueous ZIBs have been also attracting growing interest for their ability to overcome several intrinsic limitations of aqueous systems. By employing organic solvents with wider electrochemical stability windows, nonaqueous ZIBs can operate at higher voltages, potentially exceeding 3 V, which significantly enhances energy density. In addition, they generally exhibit fewer parasitic side reactions and improved interfacial stability, particularly at the electrode–electrolyte interfaces.[18] However, these benefits come with trade-offs: organic electrolytes increase cost and introduce safety concerns due to their flammability. As a result, both aqueous and nonaqueous ZIBs offer distinct advantages and face unique challenges, driving continued research efforts into both systems.

Many research efforts have focused on improving either the anode or the cathode independently. However, because a Zn-ion battery is a closed, interdependent electrochemical system, reactions at one electrode can influence and even exacerbate degradation processes at the other. Therefore, a holistic design approach that simultaneously addresses the optimisation of the anode, cathode, and electrolyte is essential for the development of high-performance, stable, and long-lasting ZIBs.

Given that the first three results chapters of this thesis are focused on aqueous ZIBs, the following sections will examine in detail the key failure mechanisms and interfacial

challenges associated with both zinc anodes and cathode materials specifically in aqueous electrolyte environments.

1.3 Challenges at the Zinc Anode

1.3.1 Issues at the Anode–Electrolyte Interface

In aqueous ZIBs, the Zn anode is prone to a variety of interfacial degradation phenomena arising from both spontaneous chemical reactions and electrochemical processes. These interfacial issues significantly compromise battery efficiency, cycle stability, and overall lifespan.

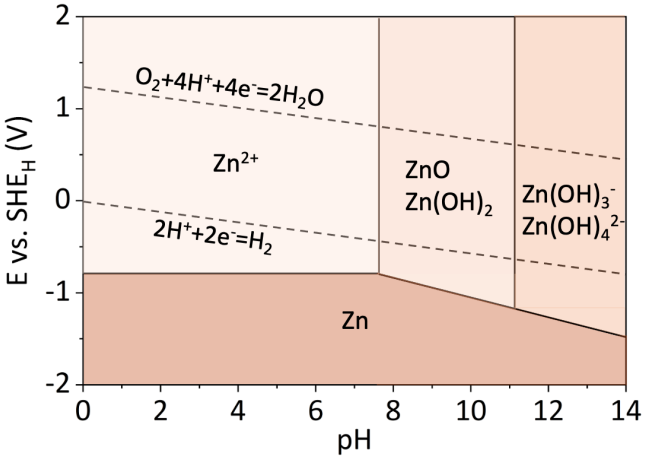

Figure 1.3 The Pourbaix diagram of Zn in aqueous solution.

Zinc Corrosion

Upon contact with an aqueous electrolyte, particularly one with a mildly acidic pH (≈ 3-5), the zinc anode undergoes spontaneous corrosion. As illustrated in Figure 1.3, the Zn–electrolyte interface resides within a thermodynamically unstable regime, where zinc metal readily oxidises to Zn^{2+}, while protons (H^+) from the electrolyte are reduced to hydrogen gas.

This behaviour stems from the fact that the standard reduction potential of the Zn/Zn^{2+} couple is lower than that of H^+/H_2 across the entire pH spectrum. As a result, zinc corrosion is thermodynamically favoured in aqueous environments. The reaction proceeds as follows:

$$Zn(s) \rightarrow Zn^{2+}(aq) + 2e^-$$

This corrosion process leads to the loss of active zinc, reducing the battery's accessible capacity. Furthermore, it promotes the formation of insulating byproducts and increases interfacial resistance, both of which deteriorate electrochemical performance over time.

Hydrogen Evolution Reaction (HER)

The hydrogen evolution reaction occurs concurrently with zinc corrosion and further contributes to the degradation of the anode–electrolyte interface. The HER can be represented by the following reaction:

$$2H^+ + 2e^- \rightarrow H_2(g)$$

HER presents several critical challenges in aqueous ZIBs. In sealed battery systems, the generation of hydrogen gas can lead to gas accumulation, which impairs contact between the electrolyte and electrode, thereby increasing interfacial resistance and reducing the coulombic efficiency (CE). Moreover, Additionally, Zn dendrite formation, which is often induced by non-uniform deposition, could further increase the Zn surface area, accelerating both HER and corrosion.

Formation of Side Byproducts

During the HER, protons (H^+) are consumed, resulting in a localised increase in pH near the zinc anode surface. This elevated pH promotes the generation of hydroxide ions (OH^-), which can subsequently react with Zn^{2+} and other electrolyte anions to form electrochemically inactive byproducts. These side products accumulate at the anode–electrolyte interface and significantly impair battery performance. For example, Cai et al. reported the formation of

$Zn_4(OH)_6SO_4 \cdot xH_2O$ in electrolytes based on $ZnSO_4$, supported by X-ray diffraction (XRD) analysis.[19] The generalised reaction is:

$$4Zn^{2+} + 6OH^- + SO_4^{2-} + xH_2O \rightarrow Zn_4(OH)_6SO_4 \cdot xH_2O$$

This composition of interfacial parasitic side products depends heavily on the specific aqueous electrolyte salt used. In a $ZnSO_4$ electrolyte, the byproduct is zinc hydroxide sulfate ($Zn_4(OH)_6SO_4 \cdot xH_2O$, ZHS); in a zinc triflate ($Zn(OTf)_2$) electrolyte, the product is zinc hydroxide triflate (ZHT); and in a $Zn(C_2F_6NS_2O_4)_2$ electrolyte, it is zinc hydroxide triflimide (ZHTSI). These byproducts typically exhibit loosely packed, plate-like morphologies that lack a continuous conforming film across the surface. As a result, they fail to prevent continuous electrolyte access to the Zn surface, allowing side reactions to persist. Moreover, their presence disrupts uniform Zn^{2+} ion flux, promoting nonuniform deposition and dendrite formation. This cascade of degradation mechanisms leads to a low CE for Zn plating/stripping and contributes to premature battery failure.

The aforementioned Zn corrosion, hydrogen evolution, and related parasitic byproduct formation are spontaneous chemical processes that occur even when a ZIB is in an idle state. As a result, the Zn anode is susceptible to substantial capacity loss during calendar aging. Recent studies (Figure 1.4) have shown that even a 24-hour resting period can result in significant degradation, with capacity losses exceeding 70% in some cases.[20]

This degradation becomes more pronounced with longer resting times, higher anode mass loading, and lower charging rates, all of which reduce the reversibility of Zn plating/stripping and shorten the overall shelf life of the cell. While part of the irreversible capacity loss is attributed to the formation of corrosion products such as ZHS and zinc hydroxide (ZHO), a substantial portion (over 40% in some cases) is linked to the formation of so-called “screened Zn.”[20]

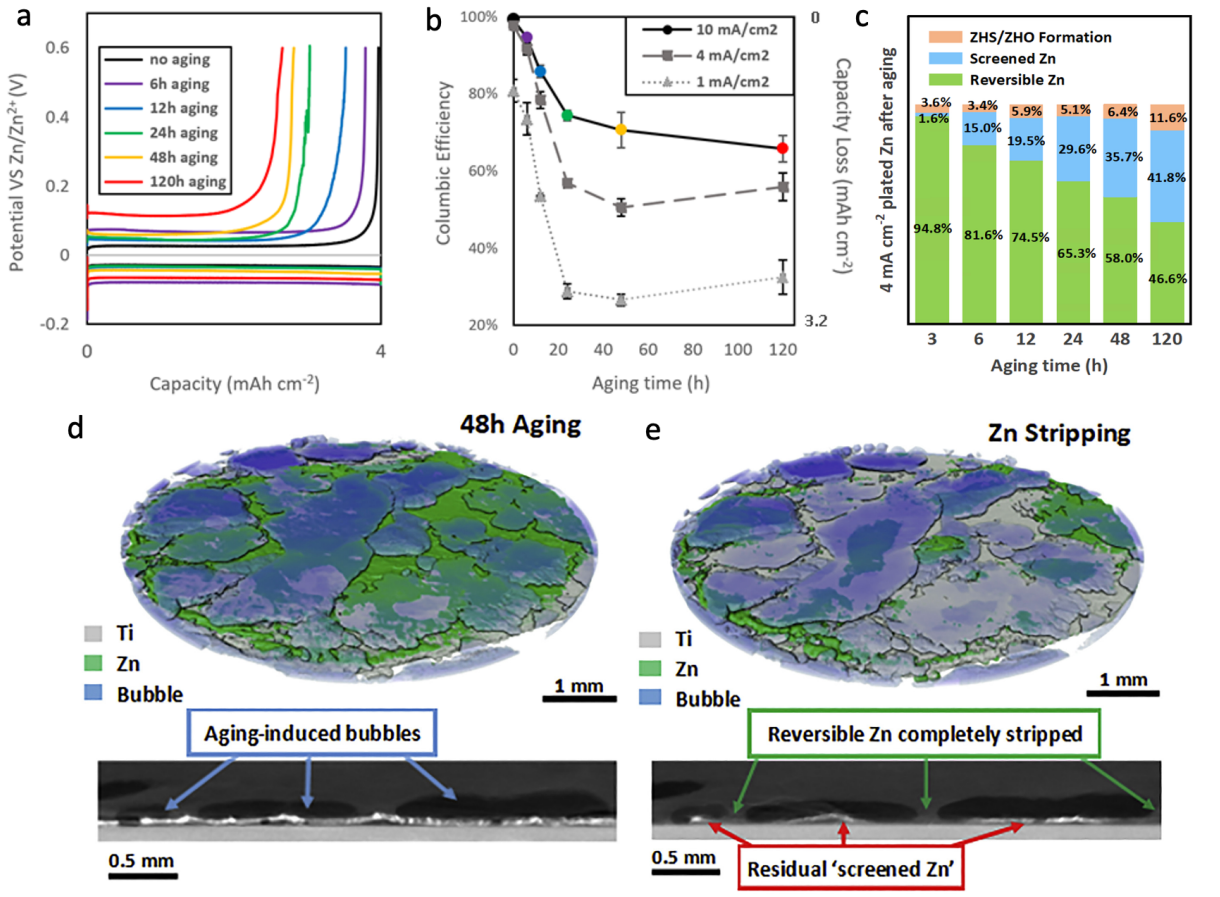

Figure 1.4 (a) Representative charge–discharge curves of Zn/2 M $ZnSO_4$/Ti cells after different aging times, used to evaluate Zn anode loss.[20] (b) Post-aging CE and capacity loss as a function of aging duration under three current densities: 1, 4, and 10 mA cm^{-2}. Notably, cells cycled at 1 mA cm^{-2} exhibit the greatest capacity loss, attributed to mossy Zn deposition that increases surface area and accelerates parasitic reactions with the aqueous electrolyte. In contrast, dense Zn deposition at 10 mA cm^{-2} results in less degradation during aging.[20] (c) Quantitative Zn usage after aging (at 4 mA cm^{-2}), distinguishing between fully reversible Zn, screened Zn, and Zn irreversibly consumed in by-products such as ZHS or ZHO.[20] (d) In situ XCT showing 3D renderings and cross-sectional images of aged Zn anodes, where hydrogen gas bubbles are observed to accumulate on active Zn surfaces.[20] (e) XCT showing these bubbles physically isolate portions of the Zn, preventing their electrochemical participation and resulting in screened Zn that cannot be stripped during discharge.[20]

In situ X-ray computed tomography (XCT) analyses have revealed that gas bubbles accumulate at the Zn anode–electrolyte interface during aging periods (Figure 1.4d,e).[20] These gas physically isolate zinc surface from the electrolyte, rendering those regions electrochemically inaccessible during subsequent stripping which leads to “screened Zn”. This

phenomenon highlights the severity of uncontrolled Zn–electrolyte interactions, which can severely degrade battery performance even in the absence of cycling, posing a significant barrier to achieving long shelf life in practical aqueous ZIB systems.

Dendrite Formation

An ideal zinc anode surface should be flat, dense, and morphologically uniform to ensure high CE and stable long-term cycling. However, in practical systems, non-uniform Zn deposition is frequently observed, primarily due to heterogeneities in electric field. During the initial stages of deposition, Zn^{2+} ions tend to nucleate at structural imperfections such as grain boundaries, dislocations, and surface impurities. These defects serve as preferential nucleation sites, where subsequent Zn deposition becomes localised, forming protrusions or "tips" with intensified local electric fields.[21] These regions further promote Zn accumulation, leading to the growth of dendritic structures.

Zinc dendrites pose multiple threats to the performance, safety, and longevity of ZIBs. Mechanically, they can penetrate the separator, causing internal short circuits and catastrophic cell failure. This issue is especially critical in Zn-based systems because zinc has a significantly higher Young's modulus (~108 GPa) compared to lithium (~7.8 GPa),[22] making Zn dendrites more rigid. As a result, they are more likely to physically puncture separators, rendering dendrite suppression a greater challenge in ZIBs.

Meanwhile, the breakage of zinc dendrites can lead to the formation of electrically isolated "dead Zn", which no longer participates in electrochemical reactions, thereby contributing to irreversible capacity loss. Furthermore, the increased surface area of dendritic deposits accelerates parasitic side reactions, such as corrosion and HER, further degrading battery efficiency and lifespan.

1.3.2 Current Strategies

Anode Engineering Approaches

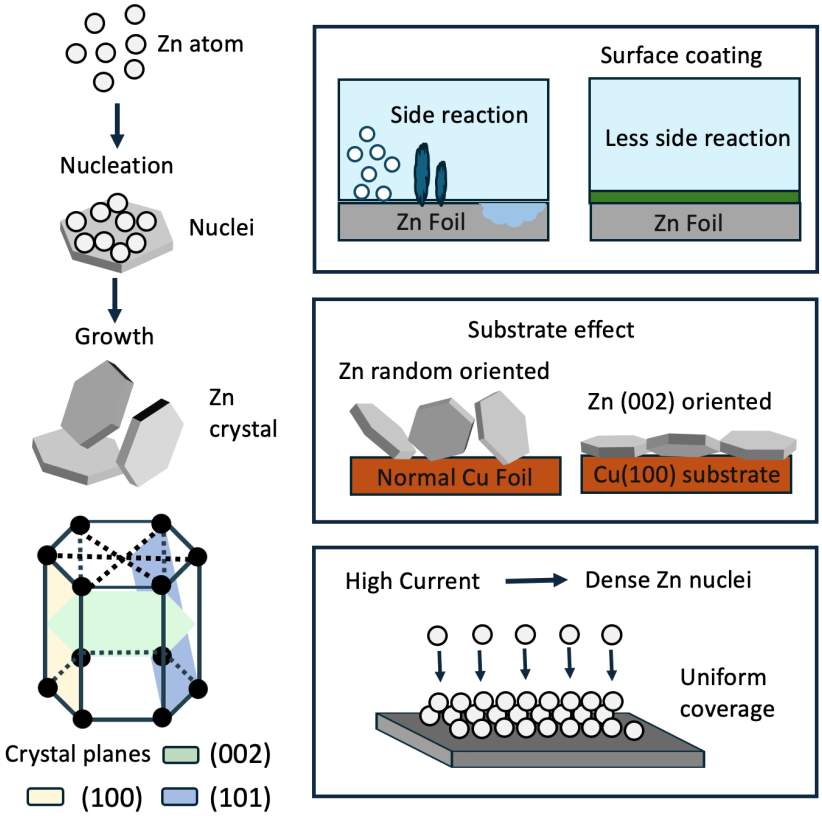

Figure 1.5 Schematic illustration of the Zn deposition process, highlighting the progression from initial nucleation to Zn crystal growth. Various strategies to regulate Zn anode behaviour are depicted, including: (i) introducing artificial interphase layers to stabilise the Zn–electrolyte interface, (ii) manipulating the crystallographic orientation of the hexagonal close-packed Zn to guide uniform deposition, and (iii) applying high current densities to promote uniform nuclei formation.

The undesired side reactions between the zinc anode and aqueous electrolyte primarily originate from their direct physical contact, which facilitates zinc corrosion, hydrogen evolution, and the accumulation of insulating by-products. To mitigate these interfacial issues, a promising approach involves introducing a protective barrier layer between the electrolyte and the Zn surface, thereby preventing direct exposure of Zn anode to the corrosive aqueous environment, as illustrated in Figure 1.5.

A wide range of artificial interfacial layers have been explored to passivate the Zn surface while maintaining ion transport.[23] These include inorganic materials such as nano-$CaCO_3$,[24] TiO_2,[25] ZrO_2,[26] metal–organic frameworks (MOFs),[27] and kaolin,[28] as well as organic coatings like poly(vinylidene fluoride-trifluoroethylene) [P(VDF-TrFE)][29] and polyoxyethylene (40) nonylphenyl ether.[30] Such layers are designed to be chemically stable, ionically conductive, and mechanically robust to effectively suppress parasitic reactions without hindering electrochemical performance.

For instance, Zhao et al. reported that an ultrathin TiO_2 layer, deposited via atomic layer deposition on the Zn anode, served as an effective artificial interfacial coating.[25] This TiO_2 layer significantly suppressed Zn corrosion, reduced gas evolution, and minimised the formation of corrosion by-products. More importantly, it enhanced the CE of Zn plating/stripping processes. As a result, a TiO_2-coated Zn anode, when paired with a MnO_2 cathode, enabled a full ZIB to achieve 1,000 stable cycles with 85% capacity retention at a current density of 3 mA cm^{-2}, marking a substantial improvement in both cycle life and electrochemical stability.[25]

Meanwhile, the choice of current collector or substrate can significantly influence the crystallographic orientation of Zn deposition, thereby promoting uniform Zn plating and effectively mitigating dendrite formation.[31] Zinc crystallises in a hexagonal close packed (HCP) structure with the space group $P6_3/mmc$, and during electrodeposition, the dominant crystal facets observed are typically the (100), (002), and (101) planes, as illustrated in Figure 1.5. Among these, the (002) plane possesses the highest atomic packing density and the lowest surface energy, making it the most thermodynamically stable surface. It is generally accepted that promoting preferential growth along the Zn (002) orientation facilitates the formation of a uniform Zn deposition layer.

To exploit and control the facet-dependent growth behaviour of Zn, Zeng et al. engineered a modified Zn anode interface using a zincophilic face centred cubic (fcc) Cu(100) substrate, which promotes preferential Zn deposition along the (002) plane.[32] The lattice compatibility between Cu(100) and Zn(002) enables epitaxial growth, guiding the formation of a planar and densely packed Zn layer (Figure 1.5). This controlled orientation inherently resists dendritic growth and suppresses unwanted interfacial side reactions, contributing to improved interfacial stability. As a result, Zn@Cu(100) anodes exhibit superior electrochemical performance in both symmetric cells and half-cell configurations, demonstrating enhanced cycling stability and CE compared to conventional Zn anodes.[32]

In addition to artificial interfacial layer modification, the development of three-dimensional (3D) anode architectures has emerged as a promising strategy for suppressing Zn dendrite growth.[33,34] Increasing the surface area reduces the local Zn^{2+} ion flux, thereby mitigating dendritic formation and promoting more uniform Zn plating. To be effective, 3D Zn anodes must exhibit zincophilicity, chemical and mechanical stability, and electrolyte compatibility. A wide range of conductive porous substrates have been investigated to fulfil these criteria, including porous copper,[35] copper foam,[36] 3D porous titanium,[37] stainless steel mesh,[38] MOF-derived frameworks,[39] Zn foam,[40] MXene,[41] graphene,[42] carbon cloth,[43] and carbon fiber.[44] These materials offer both high surface area and favourable Zn deposition characteristics, making them ideal scaffolds for dendrite-suppressive architectures.

While artificial interlayers and substrate engineering offer effective, albeit often complex, approaches for suppressing zinc dendrites, a simpler and more accessible strategy, adjusting the operating current density,[45,46] has shown remarkable promise. Counterintuitively, increasing the current density has been reported to significantly enhance Zn plating/stripping efficiency, in some cases approaching nearly 100%, while also improving cycle life and

promoting uniform Zn deposition. This observation challenges conventional assumption, which traditionally associates high current densities with accelerated dendrite formation due to rapid ion depletion near the electrode–electrolyte interface and the emergence of steep concentration gradients. However, in aqueous electrolytes, the high ionic conductivity and rapid ion mobility allow for efficient electrolyte replenishment, effectively mitigating mass transport limitations. As a result, even at relatively high current densities, for example, 20 mA cm^{-2}, Zn deposition remains uniform, and dendritic growth is substantially suppressed.[47]

This phenomenon is further supported by classical nucleation theory, which suggests that high current densities increase the nucleation rate, leading to the formation of more numerous, smaller nuclei that favour dense and planar Zn growth (Figure 1.5). This uniform deposition morphology contributes to improved surface uniformity and suppresses the formation of protrusive dendrites, ultimately enhancing the reversibility and stability of Zn plating/stripping over cycles.

Electrolyte Engineering Approaches

Electrolyte engineering, particularly through the incorporation of additives, has emerged as a powerful strategy to regulate Zn electrodeposition and mitigate undesirable side reactions at the Zn–electrolyte interface. Additives can influence the Zn^{2+} solvation structure, modulate interfacial energy, and suppress dendrite formation, thereby enhancing the overall electrochemical performance and longevity of ZIBs.

A wide variety of inorganic additives have been investigated for their ability to control Zn deposition morphology and interfacial chemistry. These include Na_2SO_4,[48] LiCl,[49] $LiClO_4$,[50,51] boric acid,[52,53] $Ce_2(SO_4)_3$,[54] $La_2(SO_4)_3$,[55] K_2SnO_3,[56] lithium magnesium silicate (LMS, $(MgLi)_3Si_4O_{10}(OH)_2{\cdot}4H_2O$),[57] $NiSO_4$,[58] $CuSO_4$,[58] and $PbSO_4$.[59] These compounds can function as

electrostatic shields, modifiers of Zn crystal orientation, or nucleation promoters, depending on their chemical nature.

In parallel, numerous organic additives have also been explored. Solid organic additives include cationic surfactants such as dodecyltrimethylammonium chloride[60] and benzyltrimethylammonium chloride,[60] anionic surfactants like sodium dodecyl sulfate (SDS)[61] and sodium dodecylbenzene sulfonate,[62] and polymeric additives such as polyethyleneimine (PEI)[63] and polyethylene glycol (PEG).[64] Liquid organic additives, on the other hand, are typically polar solvents that alter Zn^{2+} solvation and deposition kinetics. Common examples include DMC,[65] ethylene glycol (EG),[66] diethyl ether (Et_2O),[67] dimethyl sulfoxide (DMSO),[68] and acetonitrile (AN).[69] These solvents help restructure the solvation shell around Zn^{2+} ions and inhibit 2D diffusion of Zn^{2+} ions, thus enabling smoother deposition and reducing side reaction pathways.

One of the primary mechanisms by which electrolyte additives improve Zn deposition behaviour is through the formation of an electrostatic shield at the electrode interface. As illustrated in Figure 1.6, Zn tends to deposit preferentially at surface protrusions due to the local enhancement of the electric field, a phenomenon known as the “tip effect”. To counter this, positively charged cationic additives with lower reduction potentials than Zn^{2+} can be introduced into the electrolyte. These cations are not electrochemically reduced under Zn plating conditions but instead accumulate at the protrusions, forming a localised electrostatic shield. This positively charged barrier repels incoming Zn^{2+} ions and suppresses further deposition at protrusion regions, promoting more uniform and planar Zn growth. For example, Wan et al. demonstrated that the addition of Na_2SO_4 to $ZnSO_4$ electrolyte effectively suppressed dendrite formation.[48] Na^+ ions, having a lower reduction potential than Zn^{2+},

selectively aggregated on Zn protrusions, forming a shield that inhibited localised Zn nucleation and dendrite growth.

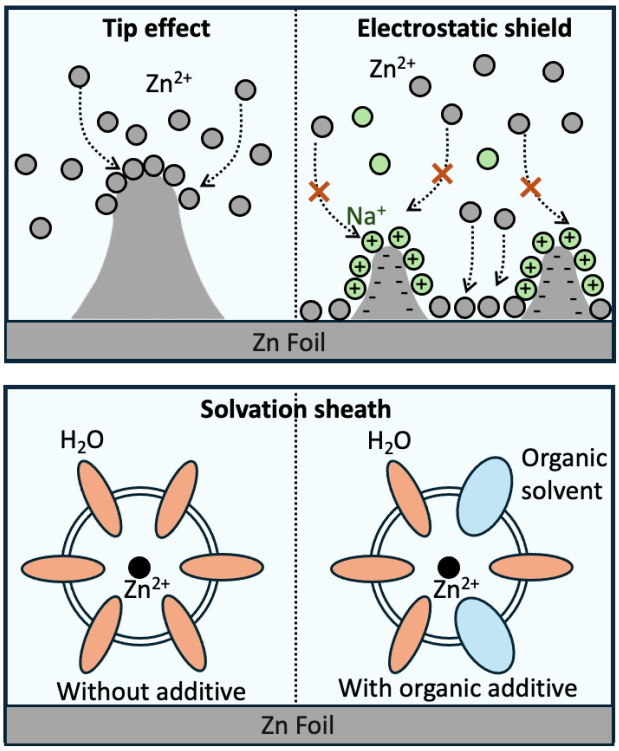

Figure 1.6 Schematic illustration of electrolyte additive strategies to regulate the Zn anode–aqueous electrolyte interface. These approaches include: (i) electrostatic shielding by introducing cations with lower reduction potentials than Zn^{2+} (e.g., Na^{+}) to suppress dendritic Zn growth; and (ii) solvation structure modulation by incorporating organic additives that alter the Zn^{2+} solvation sheath, thereby enhancing interfacial stability and suppressing side reactions.

Another important additive function involves regulating the solvation structure of Zn^{2+}, as also depicted in Figure 1.6. In mildly acidic aqueous electrolytes, Zn^{2+} predominantly exists in the form of $Zn(H_2O)_6^{2+}$, characterised by strong Zn–H_2O coordination. The introduction of organic molecules with higher Gutmann donor numbers than water can partially displace water from the primary solvation shell, weakening Zn–H_2O interactions. This adjustment reduces the participation of water in interfacial electrochemical reactions during cycling and lowers the population of free water in the bulk electrolyte, thereby mitigating spontaneous side reactions such as hydrogen evolution and Zn corrosion.

For instance, Hou et al. incorporated AN into $ZnSO_4$ electrolytes, enabling symmetric Zn cells to cycle stably for over 650 hours at 2 mA cm^{-2} with an areal capacity of 2 mAh cm^{-2}.[70] Molecular dynamics simulations confirmed that AN partially replaced water in the solvation sheath, forming mixed-ligand complexes such as $Zn(H_2O)_5(AN)_1^{2+}$, $Zn(H_2O)_4(AN)_2^{2+}$, and $Zn(H_2O)_3(AN)_3^{2+}$. This solvation shell restructuring improved Zn plating/stripping kinetics, suppressed dendrite formation, and yielded smoother deposit morphologies. Similar effects have been observed with other organic additives such as glucose,[71] dimethoxyethane (DME),[72] and DMC,[65] all of which contribute to regulate solvation sheath.

Beyond additive-based approaches, electrolyte concentration plays a pivotal role in regulating Zn deposition behaviour. In super-concentrated electrolytes, the scarcity of free water molecules and the high ratio of salt to solvent lead to the formation of highly coordinated ionic structures, including extensive ion pairing between cations and anions and anion clustering within the Zn^{2+} solvation shell. These solvation environments reduce the activity of water near the electrode surface, thereby suppressing water-induced parasitic reactions, expanding the electrochemical stability window, and facilitating the formation of dense, anion-derived interphases that help stabilise zinc deposition. A particularly promising example of this strategy is the use of "water-in-salt" electrolytes, such as 1 M $Zn(TFSI)_2$ + 20 M LiTFSI.[73] At these high salt concentrations, $TFSI^-$ anions progressively displace water molecules in the Zn^{2+} solvation sheath, ultimately leading to the formation of fully $TFSI^-$-coordinated Zn^{2+} complexes.[73] This transformation effectively removes free water from the coordination environment, inhibits hydrogen evolution and Zn corrosion, and promotes uniform, dendrite-free Zn plating with the reduced formation of insulating byproducts.

1.3.3 Limitations of Current Approaches

As previously discussed, ZIBs operate as sealed and interdependent electrochemical systems. This interconnectivity means that modifications to a single component, such as the anode or electrolyte, can significantly influence the behaviour and performance of other components, particularly the cathode. However, many current optimisation strategies treat components in isolation, often overlooking cell-level interactions, which introduces key limitations when evaluating full-cell performance.

On the anode side, strategies such as surface coatings and substrate engineering have demonstrated considerable promise in stabilising Zn plating/stripping and mitigating dendritic growth. These approaches are largely specific to the anode and generally do not interfere directly with cathode operation.

However, the use of elevated current densities (e.g., >20 mA cm^{-2}), although effective in promoting uniform Zn deposition, can be incompatible with the cathode's electrochemical limitations. In aqueous ZIBs, cathode performance is often hindered by sluggish interfacial kinetics, which constrain their ability to operate efficiently at high rates. This limitation arises from a combination of factors, including the low electronic conductivity of many cathode materials, the strong electrostatic repulsion experienced by divalent Zn^{2+} ions that impedes their diffusion into the cathode lattice, and the energy barrier associated with Zn^{2+} desolvation. As a result, most cathodes exhibit suboptimal performance under high current densities, with stable and efficient operation typically observed only at moderate or low cycling rates (e.g., below 5 mA cm^{-2}). This mismatch between optimal conditions for the anode and cathode underscores the importance of adopting holistic, cell-level design strategies.

On the electrolyte side, several optimisation strategies, though effective for stabilising the Zn anode, can unintentionally compromise cathode performance, especially when full-cell interactions are not carefully considered. The key challenges can be summarised as follows:

Active cation interference: The introduction of inorganic additives such as LiCl, Na_2SO_4, and $CuSO_4$ introduces foreign cations (e.g., Li^+, Na^+, Cu^{2+}) into the electrolyte, which may participate in redox reactions at the cathode. Notably, monovalent cations like Li^+ and Na^+ have lower charge densities and experience weaker electrostatic repulsion than Zn^{2+}, making them more likely to intercalate into cathode host structures. These competing intercalation processes introduce ambiguity in capacity attribution, making it difficult to isolate the electrochemical contribution of Zn^{2+}. This complicates the evaluation of cathode performance and may lead to overestimated or misleading results in full-cell studies.

Narrow electrochemical stability window: Additives such as LiCl and $LiNO_3$ introduce anions (e.g., Cl^-, NO_3^-) with limited oxidative stability. While these anions are stable at the low potentials associated with Zn plating/stripping (<0.2 V vs. Zn^{2+}/Zn), they are prone to oxidative decomposition at higher voltages (~1.3 V vs. Zn^{2+}/Zn).[74,75] This presents a significant challenge when pairing the electrolyte with high-voltage cathodes, such as Mn-based oxides and Prussian blue analogues (PBAs) cathodes, which typically operate up to ~1.9 V vs. Zn^{2+}/Zn. In such cases, the instability of these anions at elevated potentials constrains the usable voltage window, limiting energy density and overall cell performance.

Suppression of free water molecules: Many electrolyte engineering strategies aim to stabilise the Zn anode by reducing the activity of free water through solvation structure regulation by introducing organic additives or increasing salt concentration. While this is beneficial for inhibiting hydrogen evolution and Zn corrosion, it may hinder cathode kinetics. For example, Mn-based oxide cathodes that operate via a dissolution–deposition mechanism

require sufficient water and protons to facilitate redox reactions.[76] In vanadium-based cathodes that function via Zn^{2+} intercalation/deintercalation, reduced water activity imposes a higher desolvation energy barrier for Zn^{2+} ions, slowing ion transport and leading to sluggish electrochemical kinetics and diminished capacity.[77]

pH shifts induced by electrolyte additives: Electrolyte additives can also alter the bulk or local pH of the system through hydrolysis. When salts dissolve in aqueous media, their cations or anions may hydrolyse, releasing either H^+ or OH^-. For example, K_2SnO_3 increases pH by generating OH^-, while salts such as $In_2(SO_4)_3$, $Ce_2(SO_4)_3$, and $La_2(SO_4)_3$ lower pH by releasing protons. These pH variations are especially critical for Mn-based oxide cathodes, where redox reactions depend heavily on proton availability. Shifts in pH can alter the redox potentials for both MnO_2 dissolution and Mn^{2+} oxidation, directly impacting reaction kinetics, voltage profiles, and cycle stability.

These insights underscore the importance of a holistic electrolyte design approach. Electrolyte composition must be co-optimised with both the Zn anode and the cathode to achieve balanced, stable, and high-performance ZIBs. Ignoring these interdependencies can lead to short-term gains at the expense of long-term degradation and poor full-cell compatibility.

1.4 Challenges at the Mn-Based Cathode

1.4.1 Intrinsic Mn-Based Cathode Material Challenges

The cathode materials employed in aqueous ZIBs encompass a diverse range of compounds, including manganese-based oxides, vanadium-based oxides, PBAs, as well as emerging materials such as layered sulphides and organic redox-active compounds.[78,79] Among these candidates, manganese-based oxides have been the most extensively

investigated, owing to their natural abundance, low cost, and non-toxicity. These characteristics align well with the overarching goals of aqueous ZIBs development, which prioritise affordability, material sustainability, and scalable production. In this thesis, Mn is the principal TM component of all the cathode materials studied.

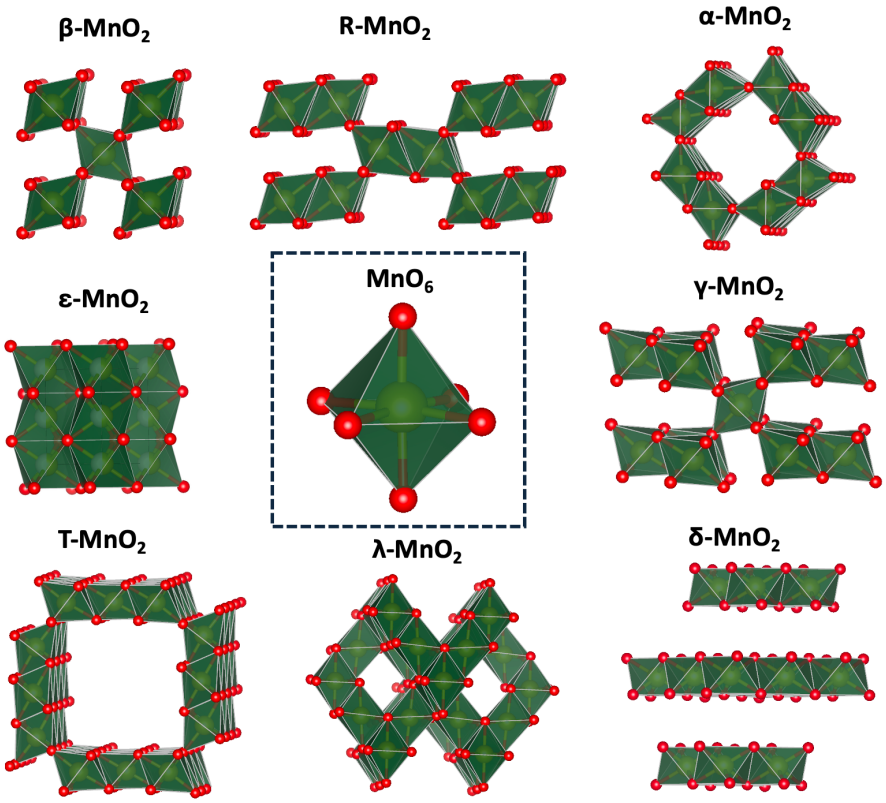

Figure 1.7 Common polymorphs of MnO_2, including α-, β-, γ-, R-, δ-, T-, ε- and λ-MnO_2, each constructed from the fundamental MnO_6 building unit.

Common manganese-based oxide cathodes in ZIBs include MnO_2, Mn_2O_3, Mn_3O_4, MnO, and $ZnMn_2O_4$. Among these, manganese dioxide (MnO_2) stands out as a particularly promising candidate, owing to its abundance, low toxicity, and high theoretical capacity up to 616 mAh g^{-1} if the full Mn^{4+}/Mn^{2+} redox couple is accessed during cycling. Structurally, MnO_2 consists of MnO_6 octahedra connected via edge- or corner-sharing, resulting in a wide variety of polymorphic forms. As shown in Figure 1.7, these include tunnel-type structures (α-, β-, R-, γ-, and T-MnO_2), layered structures (δ-MnO_2), and spinel-type frameworks (λ-MnO_2). While each polymorph possesses distinct crystal symmetry and ion transport characteristics, they all

share a common MnO_6 octahedral backbone and can undergo interconversion under electrochemical or chemical stimuli, enabling flexible redox behaviour during cycling.

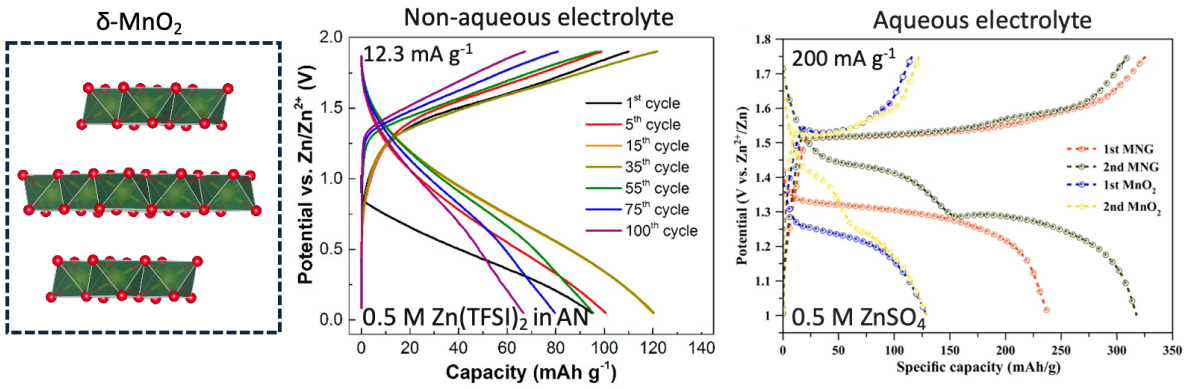

Figure 1.8 Comparison of galvanostatic charge–discharge profiles for Zn/δ-MnO_2 cells in non-aqueous and aqueous electrolytes.[80,81] The two systems exhibit distinct redox potentials and curve shapes, highlighting fundamentally different energy storage mechanisms in different electrolyte.

The electrochemical performance of MnO_2 varies significantly depending on the electrolyte environment. As shown in Figure 1.8, Zn/δ-MnO_2 cells using a nonaqueous electrolyte (0.5 M $Zn(TFSI)_2$ in acetonitrile)[80] deliver a discharge capacity of ~123 mAh g^{-1} at a low current density of 12.3 mA g^{-1} and display a smooth, featureless voltage profile during discharge, indicative of a solid-solution-type mechanism. It has been well established that Zn^{2+} intercalation/deintercalation is the dominant charge storage mechanism in nonaqueous electrolytes,[80] typically described by the reversible reaction:

$$MnO_2 + xZn^{2+} + 2xe^- \rightleftharpoons Zn_xMnO_2$$

The observed discharge capacity of 123 mAh g^{-1} cathode corresponds to a transfer of only 0.4 electrons per Mn center, which lead to $Zn_{0.2}MnO_2$ at full discharge. This falls significantly short of the theoretical maximum of 2 electrons per Mn center achievable if the full Mn^{4+}/Mn^{2+} redox couple were utilised. This severe limitation arises primarily from the fundamental challenge of inserting the doubly charged Zn^{2+} ion into the MnO_2 host structure. The high charge density of Zn^{2+} creates intense electrostatic repulsion forces within the crystal

lattice. For cathode materials where Zn^{2+} intercalation/deintercalation is the sole charge storage mechanism, mitigating electrostatic repulsion and facilitating Zn^{2+} transport are critical steps toward improving electrochemical performance.

In contrast, when operated in an aqueous electrolyte (0.5 M $ZnSO_4$), Zn/δ-MnO_2 cells show two distinct discharge plateaus at approximately 1.3 V and 1.2 V, as well as two well-defined charge plateaus.[81] At a much higher current density of 200 mA g^{-1}, these aqueous ZIBs deliver an impressive discharge capacity of ~320 mAh g^{-1}, with an average discharge voltage of ~1.3 V which substantially higher than the 0.6–0.7 V observed in nonaqueous systems. These differences highlight the distinct charge storage mechanisms operative in non-aqueous and aqueous electrolytes. And in aqueous electrolytes, the underlying mechanism remains the subject of ongoing debate. Early studies proposed that charge storage primarily arose from the intercalation of Zn^{2+} ions into the tunnel, layered, or spinel frameworks of MnO_2, similar to behaviour observed in nonaqueous systems.[82]

More recent investigations, however, have uncovered reversible side reactions that complicate this narrative. During discharge in aqueous systems, a layered zinc hydroxide phase (e.g., ZHS) is often observed, suggesting a co-insertion mechanism involving both Zn^{2+} and H^+ ions.[83] Specifically, the intercalation of H^+ into MnO_2 increases the local pH at the cathode–electrolyte interface, thereby inducing the precipitation of layered zinc hydroxide complexes. The formation of side products is highly dependent on the specific aqueous electrolyte used, just as it is on the anode side. For example, in $ZnSO_4$ electrolyte, it forms ZHS; in zinc triflate $Zn(OTf)_2$ electrolyte, it forms ZHT; and in $Zn(C_2F_6NS_2O_4)_2$ electrolyte, it forms ZHTSI.

During the charging process, protons released from the cathode lattice increase the local pH, which in turn promotes the dissolution of zinc hydroxide complexes. These observations suggest a dual-ion charge storage mechanism, in which both Zn^{2+} and H^+ ions are

reversibly inserted and extracted, accompanied by ZHS precipitation and dissolution reactions. The overall electrochemical processes can be summarised as follows:

$$MnO_2 + xZn^{2+} + 2xe^- \rightleftharpoons Zn_xMnO_2$$

$$MnO_2 + yH^+ + ye^- \rightleftharpoons H_yMnO_2$$

$$4Zn^{2+} + SO_4^{2-} + 6OH^- + nH_2O \rightleftharpoons Zn_4(OH)_6(SO_4)\cdot nH_2O$$

It is important to recognise that, although many studies claim a co-insertion mechanism involving both Zn^{2+} and H^+ in MnO_2 cathodes, few have successfully decoupled their individual contributions to the overall energy storage process. This difficulty arises from the fact that Zn^{2+} insertion and H^+ insertion often occur simultaneously, and are inherently challenging to distinguish using conventional characterisation techniques.

For instance, in the discharged state, the formation of zinc hydroxide-based byproducts introduces numerous diffraction peaks, complicating the identification of discharge products via XRD. In addition, energy-dispersive X-ray spectroscopy (EDX) cannot detect hydrogen, and residual Zn^{2+} from the electrolyte often adheres to particle surfaces, obscuring the actual extent of Zn incorporation and further confounding analysis.

One proposed strategy to isolate the role of Zn^{2+} is to operate the MnO_2 cathode in a non-aqueous electrolyte, where only Zn^{2+} intercalation/deintercalation can occur. Conversely, isolating the role of H^+ requires a proton-only electrolyte. However, strongly acidic electrolytes such as 1 M H_2SO_4, although containing only H^+ and no Zn^{2+}, often lead to substantial Mn dissolution, compromising the structural stability of the cathode and limiting their practical utility for mechanistic studies. To address this, some researchers have proposed using deuterium oxide (D_2O) as the electrolyte solvent, allowing the role of protons to be probed more selectively. By analysing the discharged samples using nuclear magnetic resonance

(NMR) spectroscopy, the incorporation of deuterons ($^2H^+$) into the MnO_2 structure can be quantitatively assessed, offering insight into the extent of H^+ involvement during cycling.

Nevertheless, due to the intertwined electrochemical behaviour of Zn^{2+} and H^+, their sensitivity to the local chemical environment, and the limitations of current characterisation techniques, it remains extremely difficult to unambiguously separate or quantify their individual contributions to the overall performance of Mn-based cathodes in aqueous ZIBs.

With growing research efforts, emerging evidence like ex situ X-ray absorption spectroscopy (XAS) have raised critical challenges to the widely accepted Zn^{2+} and H^+ co-insertion mechanism as the dominant energy storage process in MnO_2-based cathodes.[84] This skepticism stems from observations indicating that the valence state change of Mn during electrochemical cycling is too small to account for the high measured capacities. Given that the redox activity of Mn is central to energy storage, whether the inserted cation is Zn^{2+} or H^+, a substantial shift in Mn oxidation state would be expected to accompany significant capacity.

However, X-ray absorption near edge structure (XANES) results consistently show that the average Mn valence shifts by less than 0.2 electron per Mn centre between the charged and discharged states, which suggests limited Zn^{2+} or H^+ insertion.[84] This is inconsistent with commonly observed discharge capacities of approximately 300 mAh g^{-1}, which would require the transfer of nearly 1 electron per Mn.[84] Such a discrepancy suggests that cation intercalation/deintercalation alone cannot account for the observed electrochemical behaviour.

Instead, a new mechanism involving the dissolution and subsequent redeposition of Mn has been proposed. In this model, MnO_2 is reduced and dissolves as Mn^{2+} ions in the electrolyte during discharge. Upon charging, these Mn^{2+} ions are oxidised and re-deposited onto the cathode surface as MnO_2. During discharge, the consumption of H^+ elevates the local

pH at the cathode–electrolyte interface, promoting the formation of Zn hydroxide phase like ZHS. These byproducts dissolve back into the electrolyte during the charging process.

The overall redox processes can be summarised as:

$$MnO_2 + 4H^+ + 2e^- \rightleftharpoons Mn^{2+}(aq) + 2H_2O$$

$$4Zn^{2+} + SO_4^{2-} + 6OH^- + nH_2O \rightleftharpoons 3Zn(OH)_2{\cdot}ZnSO_4{\cdot}nH_2O$$

A growing recognition has emerged that while Zn^{2+} and H^+ intercalation/deintercalation contribute partially to the capacity of aqueous Zn/MnO_2 batteries, the predominant charge storage mechanism involves the reversible dissolution of Mn^{2+} from the cathode during discharge and its subsequent re-deposition (typically as MnO_2) during charge. This dissolution/deposition pathway is now strongly supported by a combination of operando and ex situ experimental evidence:

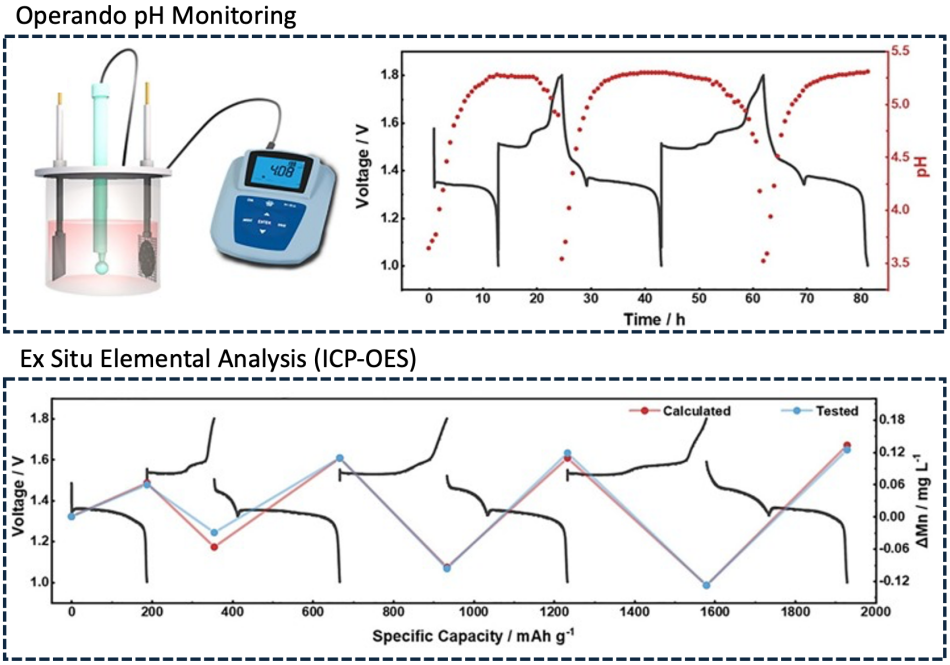

Figure 1.9 Experimental evidence supporting the MnO_2 dissolution–redeposition mechanism in Zn/MnO_2 cells in 2 M $ZnSO_4$ electrolyte.[85] In situ pH monitoring reveals dynamic pH fluctuations during cycling, indicating proton-coupled Mn redox reactions.[85] Ex situ inductively coupled plasma optical emission spectroscopy (ICP-OES) analysis quantifies the Mn content in the electrolyte over time, confirming Mn dissolution during discharge and redeposition during charge.[85]

Operando pH monitoring: Direct measurement of the electrolyte pH evolution (Figure 1.9)[85] during cycling reveals a significant increase during discharge, consistent with the consumption of protons (H^+) in the dissolution reaction $MnO_2 + 4H^+ + 2e^- \rightarrow Mn^{2+} + 2H_2O$. This localised pH shift within the cathode microenvironment promotes the precipitation of ZHS. Crucially, the process demonstrates reversibility, as the pH returns nearly to its initial value during charging, aligning with the re-oxidation and deposition of Mn species.

Ex-situ elemental analysis: Quantitative analysis of Mn concentrations within the electrolyte-soaked separator via inductively coupled plasma optical emission spectrometry (ICP-OES) provides direct evidence of Mn dissolution and deposition (Figure 1.9).[85] Measurements confirm a substantial increase in dissolved Mn^{2+} concentration within the bulk electrolyte during discharge, corresponding directly to the discharge depth. This dynamic fluctuation of Mn concentration in the electrolyte providing direct chemical evidence of Mn species shuttling between the solid phase and the electrolyte.

Together, these techniques provide compelling evidence that the dissolution of Mn^{2+} into the electrolyte and its re-deposition constitute the dominant capacity-delivering process in aqueous Zn/MnO_2 systems.

However, the charge storage mechanism has been reported to vary with specific Mn-based oxide phase employed. Some studies have proposed different mechanisms depending on the specific manganese oxide phase including Mn_2O_3, $ZnMn_2O_4$, MnO, and Mn_3O_4. For example, Mn_2O_3 is reported to support Zn^{2+} intercalation.[87] For $ZnMn_2O_4$, both Zn^{2+} intercalation and a dissolution–deposition mechanism has been proposed.[88,89] MnO is reported to involve H^+ and Zn^{2+} co-insertion.[90]

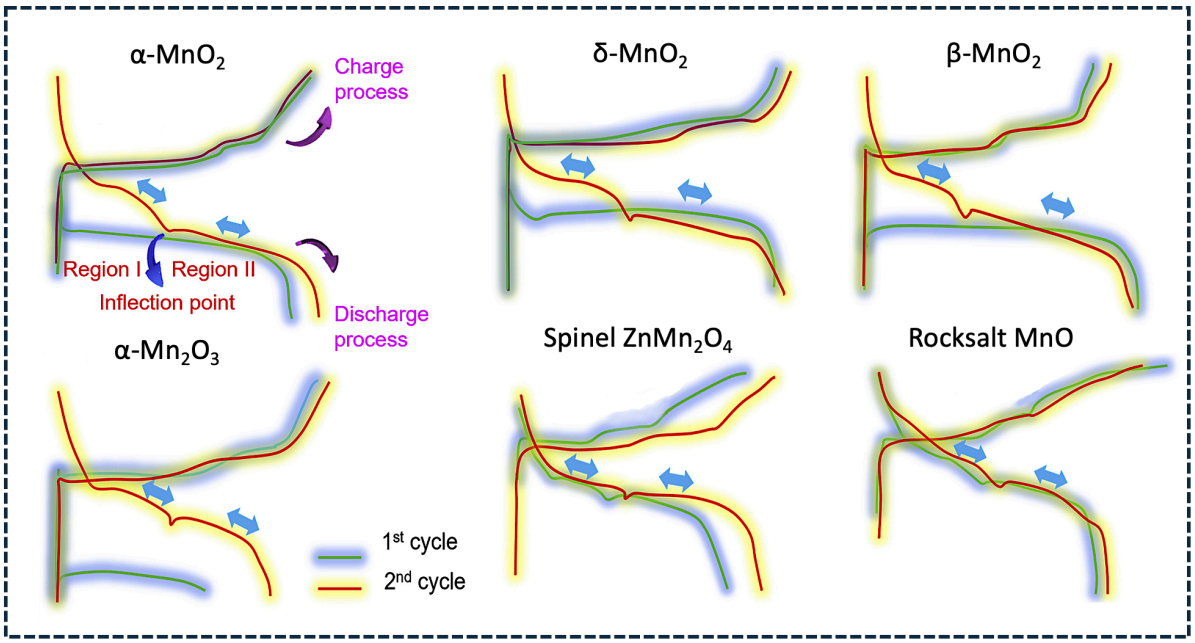

Figure 1.10 Charge–discharge profiles of various manganese-based cathodes, including α-MnO_2, δ-MnO_2, β-MnO_2, α-Mn_2O_3, spinel $ZnMn_2O_4$, and rock-salt MnO. demonstrating strikingly similar electrochemical behaviour in the second cycle despite their differing crystallographic structures and reported charge storage mechanisms. This similarity suggests a potentially common underlying reaction pathway, such as the Mn dissolution–redeposition mechanism.[86]

Despite these mechanistic differences, the galvanostatic charge–discharge profiles at second cycle of various Mn-based oxides display only subtle variations, as shown in Figure 1.10. These minor differences in electrochemical behaviour raise questions about the sharply divergent mechanisms reported in the literature. It is increasingly likely that most Mn-based cathodes exhibit a combination of Zn^{2+}/H^{+} intercalation and Mn dissolution/re-deposition, with the relative contribution of each pathway governed by the material's crystal structure and composition. Specifically, the extent of intercalation is influenced by the structural openness and ion mobility within the oxide framework, while the propensity for dissolution depends on surface chemistry and structure stability.

The frequent proposal of a single dominant mechanism in some reports may stem from incomplete or insufficient characterisation. For example, techniques such as XRD, XANES,

and NMR are essential for verifying ion intercalation into the crystal lattice. In parallel, methods like ICP-OES and X-ray fluorescence (XRF) are necessary to detect and quantify Mn dissolution and redeposition processes. Without such comprehensive and complementary analyses, interpretations of the charge storage mechanism risk being oversimplified or potentially misleading.

Importantly, the primary charge storage process in many Zn/Mn-based oxide systems appears to involve conversion chemistry, in which the cathode material undergoes substantial phase transformations and volumetric changes during cycling. While this mechanism supports high specific capacity, it also induces significant mechanical stress and strain, which can lead to structural degradation, loss of electrical contact with the current collector, and reduced cycle life. Thus, despite the abundance, low cost, and environmental advantages of Mn-based oxides, these mechanical and interfacial challenges remain key obstacles to their commercial deployment in high-performance aqueous ZIBs.

1.4.2 Issues at the Cathode–Electrolyte Interface

Mn-based cathodes are highly prone to dissolution in electrolyte environments, a well-known issue even in conventional Li-ion batteries employing nonaqueous electrolytes. This problem becomes more pronounced in aqueous electrolytes, which are typically more protic and chemically reactive, thereby accelerating the degradation of Mn-based materials.

There are three primary scenarios that can lead to Mn dissolution from Mn-based cathode materials. First, it occurs during battery operation, where Mn dissolution is primarily attributed to the instability of Mn^{3+} under electrochemical cycling conditions. This dissolution is closely tied to the intrinsic energy storage mechanism. According to several studies, Mn in MnO_2 is reduced to Mn^{3+} during the discharge process. It is widely acknowledged that Mn^{3+}, due to its electronic structure, is prone to Jahn–Teller distortion, which results in its

disproportionation via the reaction: $2Mn^{3+} \rightarrow Mn^{2+} + Mn^{4+}$. This disproportionation reaction releases Mn^{2+} into the electrolyte, contributing to active material loss.

The Jahn–Teller distortion is especially pronounced in Mn^{3+} due to the electronic configuration of the MnO_6 octahedral units that form the basis of Mn-based oxides,[91] as shown in Figure 1.11. In these structures, Mn ions are coordinated by six oxygen atoms, forming MnO_6 octahedra that are interconnected via corner or edge sharing. The Mn^{4+} ion, with a $3d^3$ configuration, has its electrons occupy the lower-energy triply degenerate t_{2g} orbitals, forming a stable octahedral geometry. However, upon reduction to Mn^{3+} ($3d^4$), the additional electron enters one of the higher-energy doubly degenerate e_g orbitals, typically the dz^2 orbital. This uneven occupancy of the e_g orbitals (dz^2 vs. dx^2-y^2) leads to an asymmetric electron distribution, causing a distortion of the MnO_6 octahedron from ideal octahedral, typically through axial elongation or compression.[92] The resulting structural instability promotes the disproportionation of Mn^{3+} and exacerbates Mn dissolution into the electrolyte.

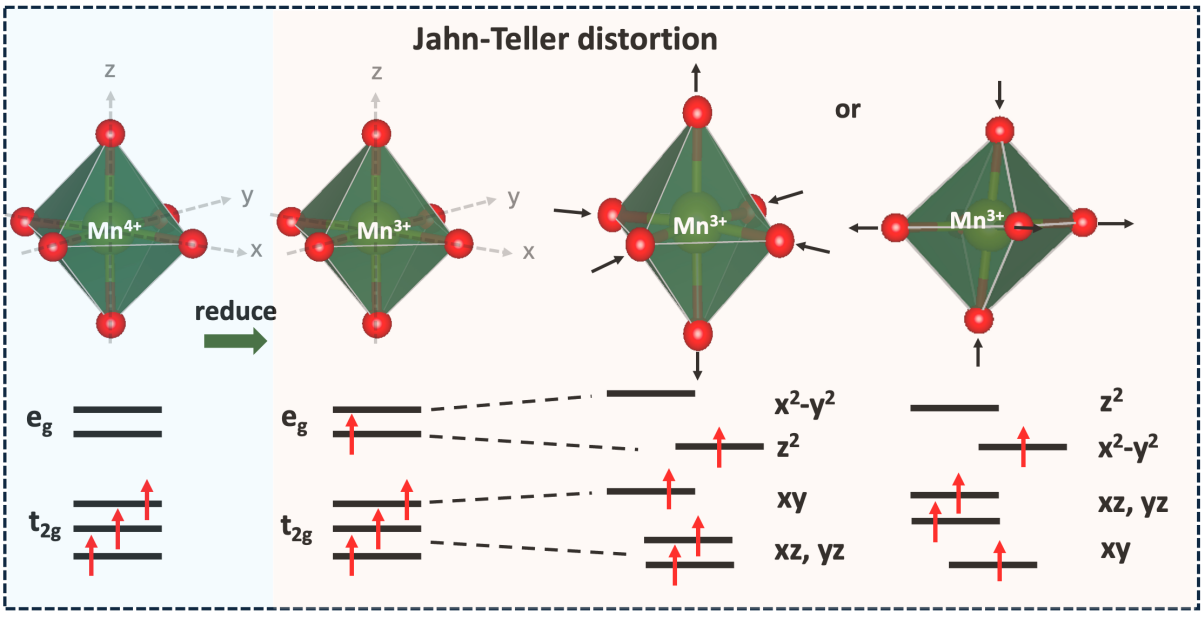

Figure 1.11 Schematic illustration of the Jahn–Teller distortion associated with Mn^{3+} in a MnO_6 octahedron. The distortion arises due to the electronic configuration of high-spin Mn^{3+} (d^4), leading to elongation or compression along one axis of the octahedron and resulting in local structural asymmetry within Mn-based oxides.

Second, Mn dissolution can also occur prior to battery operation, simply upon contact between the cathode material and the aqueous electrolyte. Several studies have demonstrated that Mn-based cathode materials are susceptible to chemical dissolution in mildly acidic aqueous electrolytes. For instance, Hunter reported that spinel $LiMn_2O_4$ undergoes Mn dissolution when treated with aqueous acid, resulting in the chemical delithiation of $LiMn_2O_4$ and its transformation into nearly pure λ-MnO_2.[93] Further investigations have examined the dissolution behaviour of various Mn oxides including MnO_2, Mn_2O_3, Mn_3O_4, and MnO by immersing them in 3 M $ZnSO_4$ electrolyte (pH ≈ 3.88) for 8 hours.[94] The results revealed no significant dissolution for MnO_2, Mn_2O_3, and Mn_3O_4; however, MnO exhibited substantial dissolution, with 28.2% of Mn leached into the electrolyte.[94] Interestingly, Mn dissolution is not always detrimental. In the case of MnO, its spontaneous dissolution in $ZnSO_4$ electrolyte has been linked to performance activation.[94] The dissolved Mn^{2+} ions participate in Zn–Mn hybrid redox reactions and facilitate the ZHS-assisted deposition/dissolution mechanism. Moreover, a positive correlation was observed between the battery's capacity and the rest time of MnO in the electrolyte, suggesting that controlled Mn dissolution plays a crucial role in activating electrochemical performance.

Third, a critical degradation pathway in Zn–MnO_2 battery systems arises from cathode dissolution under overcharging conditions, particularly at elevated voltages exceeding 1.7 V vs Zn^{2+}/Zn. This phenomenon has been elucidated by Bischoff et al.,[95] who demonstrated that, although the bulk electrolyte pH remains relatively stable, the local microenvironment at the cathode–electrolyte interface experiences severe acidification during overcharge. This localised acidification is driven by the electrochemically induced oxygen evolution reaction (OER) that occurs at the cathode surface when the potential surpasses 1.7 V:

$$6H_2O \rightarrow O_2 + 4H_3O^+ + 4e^- \quad (E^o = +1.23 \text{ V vs SHE})$$

The OER effectively acts as a proton pump, generating hydronium ions (H_3O^+) at a rate that outpaces their diffusion into the bulk electrolyte. As a result, the local pH at the cathode surface can decrease by as much as 2 pH units, corresponding to a 100-fold increase in H_3O^+ concentration. Crucially, this acidic microenvironment persists even after overcharging ceases. At a C/3 rate (with 1C defined as 150 mAh g^{-1}), it takes approximately 30 minutes for the local pH to return to baseline levels.[95] During this extended recovery window, the combined factors of elevated operational voltage and localised drop in pH force the system into a thermodynamic regime where Mn species are highly soluble. This creates a prolonged period where cathode material dissolution is thermodynamically favoured and kinetically accessible.

1.4.3 Current Strategies and Their Limitation

In the literature, Mn dissolution is often regarded as a major contributor to capacity fading in Mn-based cathodes due to the associated loss of active material. Consequently, various strategies have been proposed to suppress this dissolution.

Cathode Engineering Approaches

On the cathode side, both elemental doping and surface modification strategies have been actively investigated. For example, Ni^{2+} doping into Mn_2O_3,[96] Mo^{5+} into MnO_2,[97] and Co^{2+} into Mn_3O_4[98] have been reported to effectively suppress Mn dissolution. The underlying rationale is twofold:(i) Transition metal doping enhances the electronic conductivity of Mn-based oxides, thereby improving charge transfer kinetics; and (ii) Dopants act as structural stabilisers, reinforcing the Mn–O framework and mitigating Jahn–Teller distortion, which supress Mn dissolution under electrochemical cycling. In addition to doping, surface coatings have been widely adopted as an effective strategy to reduce Mn dissolution by acting as physical barriers at the cathode–electrolyte interface. Materials such as $Mn_3(PO_4)_2$,[99]

carbonaceous layers,[100] and conductive polymers like poly(3,4-ethylenedioxythiophene) (PEDOT)[101] have been employed to coat Mn-based cathode surfaces.

However, there remains a critical lack of direct evidence demonstrating that Mn dissolution is inherently detrimental to battery performance. Without conclusive proof that Mn dissolution directly correlates with capacity fading, efforts aimed solely at suppressing dissolution may be misguided. As discussed before, three scenarios could lead to Mn dissolution:

The first is operation-induced Mn dissolution, which may be intrinsically linked to the Mn dissolution–deposition mechanism, now recognised by many studies as a dominant contributor to charge storage in Mn-based cathode systems. Some researchers attribute Mn dissolution to the Jahn–Teller distortion of Mn^{3+} formed during discharge.[102] However, there is limited evidence supporting significant formation of Mn^{3+} via cation intercalation (e.g., H^+ or Zn^{2+}), as the intercalation capacity is typically small. If only a minor fraction of Mn^{4+} is reduced to Mn^{3+}, the disproportionation reaction ($2Mn^{3+} \rightarrow Mn^{2+} + Mn^{4+}$) would not be pronounced and unlikely to account for the extent of Mn dissolution observed. Instead, it is plausible that Mn^{4+} undergoes direct reduction and dissolution to Mn^{2+} without passing through a Mn^{3+} intermediate. In this context, Mn dissolution is not necessarily a parasitic side reaction but may be an integral component of the reversible energy storage mechanism.

The second mechanism is chemical (spontaneous) dissolution. In certain manganese oxides, such as MnO, dissolution can occur even in the absence of an applied current when exposed to mildly acidic aqueous electrolytes (e.g., $ZnSO_4$). Interestingly, this spontaneous dissolution has been reported to activate electrochemical performance, indicating that, under specific conditions, Mn dissolution may not signify material degradation but rather serve as an essential part of the charge storage mechanism.

The third scenario involves overcharging-induced Mn dissolution, which is generally undesirable. Overcharging is typically accompanied by the OER at the cathode, an irreversible process that leads to structural degradation and capacity fading. To mitigate this, cells must be operated within a carefully controlled voltage window. Specifically, limiting the upper cutoff voltage is critical to avoid triggering OER and the associated Mn loss.

If researchers assert that Mn dissolution is detrimental and should be suppressed, then it is imperative to rigorously demonstrate that the observed energy storage arises exclusively from cation intercalation, whether by H^+ or Zn^{2+}, with no contribution from dissolution-deposition processes. However, many studies fall short of this standard. In most cases, the evidence provided relies heavily on ex situ XRD to detect lattice parameter changes, an approach that, while useful for phase identification, cannot quantitatively resolve the capacity contributions from different charge storage mechanisms. More definitive analysis is needed. For instance, ICP-OES conducted at multiple states of charge, is essential for quantifying Mn dissolution. Furthermore, XANES or inverse partial fluorescence yield (IPFY) spectroscopy should be employed to accurately track changes in Mn valence states. These techniques are necessary to directly correlate redox activity with electrochemical capacity and to verify whether Zn^{2+} or H^+ intercalation alone can account for the observed charge storage.

Electrolyte Engineering Approaches

To mitigate manganese dissolution, researchers have introduced soluble Mn^{2+} additive directly into the electrolyte.[103] This strategy primarily targets the suppression of the Mn^{3+} disproportionation reaction, by utilising excess Mn^{2+} shifts the disproportionation away from the formation of soluble Mn^{2+} products (according to this reaction: $2Mn^{3+} \rightarrow Mn^{2+} + Mn^{4+}$).[86] Empirically, numerous studies have demonstrated that the inclusion of Mn^{2+} salts (e.g., $MnSO_4$)

leads to improved capacity retention and enhanced cycling stability in Mn-based cathodes. [89,104-106]

However, this approach introduces a significant complication, as several studies have reported that the added Mn^{2+} is electrochemically active. During the charging process, Mn^{2+} ions present in the electrolyte can undergo direct electrochemical oxidation at the cathode surface, leading to the re-deposition of Mn oxide (often as MnO_2). This re-deposited MnO_2 is electrochemically active and contributes to the measured capacity in subsequent cycles.

This dual role of Mn^{2+}, as reported to be both a stabilising agent and an active redox participant, introduces fundamental ambiguity in interpreting electrochemical performance. In particular, it becomes difficult to disentangle the intrinsic capacity of the Mn-based cathode from the extrinsic contribution of the Mn^{2+} additive. As a result, performance comparisons across studies that utilise Mn^{2+}-containing electrolytes may be misleading, unless this contribution is carefully isolated and quantified.

As emphasised earlier, without conclusive evidence that Mn dissolution is intrinsically detrimental, or a definitive understanding of the dominant charge storage mechanism in Mn-based systems, efforts to suppress Mn dissolution may be misdirected. Given that Mn^{2+} itself can be redox-active under typical operating conditions, its role in the overall charge storage process warrants deeper mechanistic investigation. In particular, elucidating how Mn^{2+} participates in oxidation and deposition reactions during cycling is crucial for the rational design of future Mn-based cathodes and electrolyte formulations.

1.5 The Role of Electrolytes in ZIBs

1.5.1 Aqueous Electrolytes

Aqueous electrolytes are a central component in ZIBs, offering advantages such as high ionic conductivity, low cost, environmental safety, and ease of processing. Common Zn salts used include $ZnSO_4$, $Zn(ClO_4)_2$, $Zn(Ac)_2$, $Zn(OTf)_2$, and $ZnBr_2$. Regardless of the specific salt, the aqueous solution typically exhibits a mildly acidic character due to the strong Lewis acidity of Zn^{2+} ions. At a standard concentration of 1 M, the pH usually falls within the range of 3 to 5.[107] As previously discussed, Zn metal anodes are thermodynamically unstable in such mildly acidic aqueous electrolytes, leading to parasitic reactions including Zn corrosion, HER, and by-product formation. Simultaneously, the mildly acidic environment also promotes the dissolution of transition metals at the cathode, such as Mn,[108] V,[109] Fe,[110] and Cu.[111] As a result, the aqueous electrolyte triggers complex degradation processes at both the anode and cathode interfaces.

Moreover, the electrochemical stability window of aqueous electrolytes is typically limited to below 2.4 V due to water hydrolysis,[112] as shown in Figure 1.12. This narrow voltage window restricts the use of high-voltage cathodes, which are essential for improving the overall energy density of the battery system.

1.5.2 Co-Solvent Electrolytes

Introducing organic co-solvents into aqueous Zn^{2+}-based electrolytes has proven effective in mitigating side reactions at the anode and delaying water-splitting, thereby expanding the electrochemical stability window. Unlike “water-in-salt” systems that require large quantities of salt, co-solvent electrolytes maintain low salt concentrations by partially replacing water with an organic solvent. Generally, if the organic solvent comprises less than

10 vol%, it is classified as an organic additive. When the organic content exceeds 10 vol%, the solvent begins to influence the solvation environment significantly and can be referred to as a co-solvent.

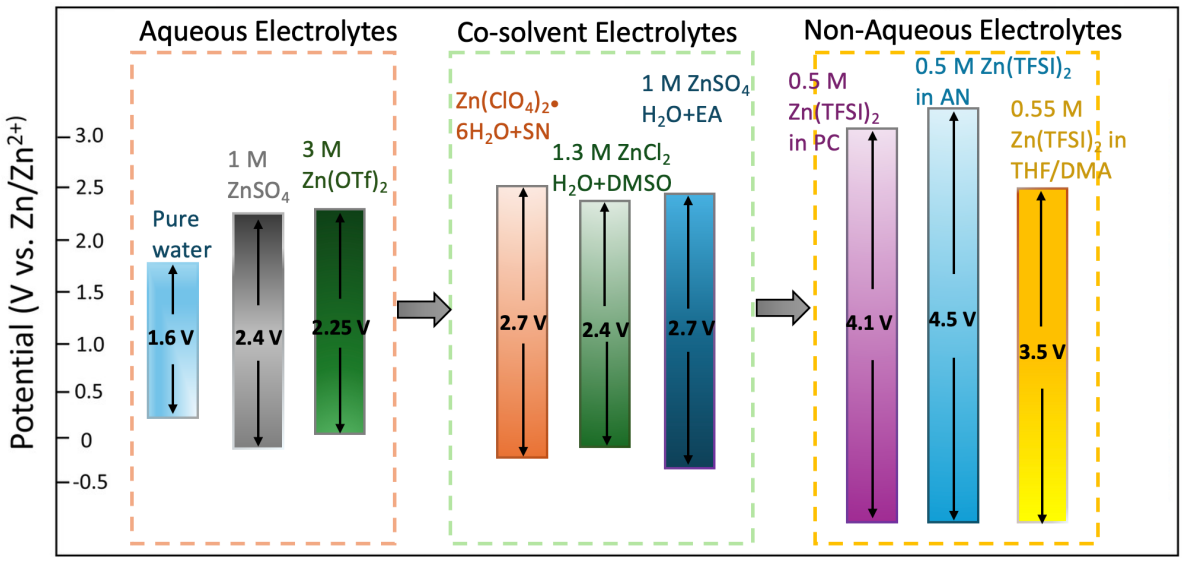

Figure 1.12 Schematic comparison of the electrochemical stability windows of aqueous electrolytes, co-solvent electrolytes, and non-aqueous electrolytes, illustrating the progressive widening of the electrochemical window. This expansion enables higher operating voltages and broader compatibility with various electrode materials. Data adapted from reference.[112-118]

The inclusion of organic co-solvents reduces the activity of H_2O in the Zn^{2+} solvation sheath, which in turn suppresses parasitic reactions and the formation of ZHS originating from H_2O decomposition. Electrolyte-derived species (from both anions and organic solvents) can contribute to the formation of solid electrolyte interphase (SEI). The SEI has been reported to consist of ZnF_2,[119] $ZnCO_3$,[120] $Zn_3(PO_4)_2$,[121] ZnP_2O_6,[121] and various organic species. When the SEI layer is uniform and stable, it plays a key role in shielding the Zn metal from direct contact with the electrolyte, thereby suppressing further side reactions.

Examples of such co-solvent systems include 1 M $Zn(ClO_4)_2$ in H_2O and succinonitrile (SN),[115] and 1.3 m $ZnCl_2$ in H_2O and DMSO.[116] These systems have demonstrated expanded

electrochemical windows of up to 2.7 V, significantly broader than that of conventional aqueous electrolytes (Figure 1.12).

However, reduced water activity can also be a limitation, particularly for tunnel-structured Mn-based oxides like α-, β-, and R-MnO_2, where Zn^{2+} intercalation is limited, and capacity mainly arises from dissolution–deposition mechanisms. Such processes are less compatible with co-solvent electrolytes. In contrast, vanadium-based cathodes, which rely primarily on Zn^{2+} intercalation, are more compatible with co-solvents but may suffer from desolvation penalties that hinder ion transport.

1.5.3 Non-Aqueous Electrolytes

Replacing water entirely with organic solvents yields a non-aqueous electrolyte, which achieves a significantly broader electrochemical stability window (often exceeding 3.5 V, as shown in Figure 1.12),[116,117] enabling the development of high-voltage ZIBs. The complete elimination of water dramatically improves Zn anode performance: it enhances electrochemical reversibility, suppresses HER, eliminates Zn corrosion, and prevents irreversible byproducts formed through water decomposition. Additionally, dendrite growth on Zn anodes is often mitigated in organic electrolytes compared to aqueous systems, though challenges persist.

However, these benefits come with new challenges. A stable and uniform solid SEI must form on the Zn surface, but this is difficult to maintain because Zn undergoes significant volume changes during cycling. Mechanical cracking of the SEI exposes fresh Zn, leading to repeated SEI formation, irreversible capacity loss, and the creation of localised regions that can initiate dendrite growth. In addition, organic electrolytes are generally more expensive and flammable, with lower ionic conductivity than water, raising concerns about safety, cost, and rate performance. Thus, while nonaqueous electrolytes expand the voltage window and

reduce some aqueous-related side reactions, they introduce their own interfacial and transport limitations that must be carefully managed.

Beyond the electrolyte itself, pairing nonaqueous electrolytes with compatible cathode materials presents a significant challenge due to two interrelated issues: First; a large effective solvation shell. In organic electrolytes, solvated Zn^{2+} ions have a much larger effective ionic radius compared to their hydrated counterparts in aqueous systems. This size often exceeds the interlayer spacing of common layered cathode materials, creating a severe desolvation energy barrier during Zn^{2+} insertion. As a result, charge transfer resistance increases, and ion diffusion becomes sluggish. As shown in Figure 1.13, $V_3O_7{\cdot}H_2O$, a vanadium-based oxide, relies solely on Zn^{2+} intercalation and deintercalation for its charge storage mechanism.[77] This is further evidenced by the similar charge-discharge profiles observed in both aqueous and nonaqueous electrolytes, indicating that Zn^{2+} intercalation/deintercalation governs the energy storage process in both electrolytes. However, in the aqueous electrolyte, $V_3O_7{\cdot}H_2O$ demonstrates a significantly higher capacity at high current densities, whereas in the nonaqueous electrolyte, the capacity is notably lower even at low current densities.[77] This disparity highlights the substantial desolvation energy penalty associated with Zn^{2+} ions in nonaqueous electrolytes, which impedes efficient Zn^{2+} intercalation and limits capacity under those conditions.

Second; strong electrostatic interactions: The divalent nature of Zn^{2+} leads to intense electrostatic repulsion within host lattice frameworks. This limits the range of materials that can support fast, reversible Zn^{2+} (de)intercalation. Typically, MnO_2 with layered or spinel structures has the ability to support Zn transport, while tunnel structures are more limited. However, these materials still struggle to fully exploit their redox capacity due to limitations imposed by Zn^{2+} insertion. For instance, in layered δ-MnO_2, the theoretical redox window

spans from Mn^{4+} to Mn^{2+}. Yet in practice, only partial reduction occurs, resulting in a final composition of $Zn_{0.2}MnO_2$ at the end of discharge (as shown in Figure 1.8) corresponding to a redox transition of Mn^{4+} to $Mn^{3.6+}$.[80] This incomplete reduction highlights the difficulty of achieving full Mn^{4+}/Mn^{2+} redox activity due to Zn^{2+} repulsion. Similarly, in γ'-V_2O_5, Zn^{2+} insertion leads to a final composition of $Zn_{0.41}V_2O_5$, involving a limited redox transition of V^{5+} to $V^{4.59+}$ rather than a full V^{5+}/V^{3+} transition.[122] This again underscores how electrostatic repulsion limits deep Zn^{2+} insertion and full redox utilisation.

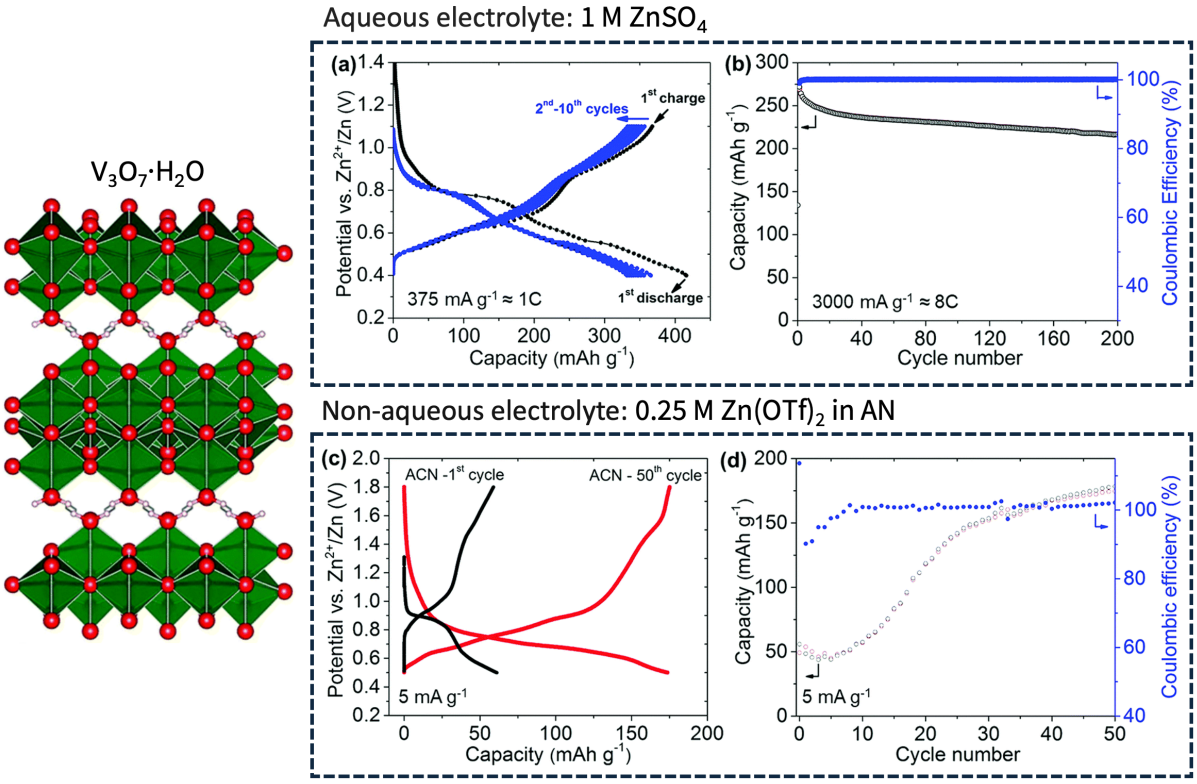

Figure 1.13 Electrochemical zinc storage performance of the $V_3O_7{\cdot}H_2O$ cathode in aqueous (1 M $ZnSO_4/H_2O$) and nonaqueous (0.25 M $Zn(OTf)_2$/acetonitrile) electrolytes.[77] Aqueous electrolyte: (a) Charge-discharge curves at 375 mA g^{-1}; (b) Cycling stability at 3000 mA g^{-1}. Nonaqueous electrolyte: (c) Charge-discharge curves at 5 mA g^{-1}; (d) Cycling stability at 5 mA g^{-1}.[77]

Even in spinel-type MnO_2, partial Zn^{2+} intercalation during discharge results in the formation of $ZnMn_2O_4$ (structurally equivalent to $Zn_{0.5}MnO_2$), utilising only the Mn^{4+}/Mn^{3+} redox couple. The parent spinel MnO_2 possesses a cubic *Fd-3m* structure, but upon Zn^{2+}

incorporation, coupled with the Jahn–Teller distortion of Mn^{3+}, induces a phase transformation to a tetragonal *I4₁/amd* structure $ZnMn_2O_4$. This structural distortion, driven by both Zn^{2+} repulsion and electronic instability, illustrates the difficulty of accommodating Zn^{2+} while accessing the full redox range without compromising structural integrity. Moreover, there are very few viable Zn-containing cathode materials that offer fast kinetics. Although organic electrolytes can mitigate transition metal dissolution, these limitations significantly constrain the development of high-performance cathodes for non-aqueous ZIBs.

1.6 Thesis Objectives and Scope

Over the past decade, ZIBs have garnered significant interest due to the favourable redox potential of zinc and its intrinsic compatibility with aqueous electrolytes. These attributes offer compelling advantages in terms of safety, cost, and environmental sustainability. However, persistent interfacial instabilities, such as parasitic reactions and dendrite formation at the Zn anode, and Mn dissolution and structural degradation at Mn-based cathodes, continue to constrain the cycle life and practical viability of ZIBs. While substantial research has addressed these issues individually, few studies have taken a full-cell level approach. This thesis aims to bridge that gap by offering a holistic, mechanistic understanding of interfacial degradation and proposing coordinated strategies to enhance overall ZIB performance.

The first part of this work investigates the zinc anode–electrolyte interface in aqueous ZIBs. It is established that planar Zn deposition is essential for suppressing side reactions and achieving high reversibility. Although high current densities (>20 mA cm^{-2}) can promote such deposition, these conditions are typically incompatible with cathode operation. To address this challenge, a novel approach was introduced: applying uniaxial mechanical pressure to

induce planar Zn growth. This strategy enables stable anode deposition under cathode-compatible current densities, reinforcing the importance of designing coordinated anode–cathode interactions at the full-cell level.

The second part of this thesis focuses on elucidating the interactions between MnO_2 cathodes and aqueous electrolytes. Using operando techniques to monitor changes in Mn concentration within the electrolyte, it was established that the primary charge storage mechanism proceeds through reversible Mn dissolution and redeposition. In addition, the influence of Mn^{2+} additives on Zn/MnO_2 battery performance was systematically investigated to evaluate their effects on cycling stability and capacity retention. Together, these findings reveal a strong coupling between electrolyte composition and cathode behaviour, underscoring the need to consider cathode–electrolyte interfacial processes in the design and optimisation of the full battery system.

Recognising that many challenges associated with Zn metal originate from the aqueous environment, the third section of this thesis explores an anode-free ZIB architecture. In this configuration, no metallic Zn is present at the start of operation, which helps reduce parasitic side reactions that typically occur between Zn metal and the aqueous electrolyte during storage. To complement this design, Zn-containing cathodes were developed and can release Zn^{2+} ions during the initial charge, thereby providing the Zn source required for subsequent cycling. The resulting anode-free cells demonstrated promising electrochemical performance, highlighting the feasibility of this approach. This strategy simplifies cell construction while also offering the potential for longer shelf life during storage and higher energy density through the elimination of heavy metallic Zn.

In the final part of this thesis, the focus shifts to the development of non-aqueous ZIBs aimed at addressing the intrinsic limitations of aqueous systems. Replacing water with organic

electrolytes significantly broadens the electrochemical stability window, enabling operation at higher voltages and potentially increasing energy density. However, these systems require cathode materials with structural stability and the ability to reversibly intercalate Zn^{2+} ions. To meet this need, new cathode frameworks were developed and evaluated, demonstrating stable cycling, high-voltage operation, and efficient Zn^{2+} transport in non-aqueous environments.

Together, the studies presented in this thesis form a cohesive strategy, from mechanistic understanding to full-cell implementation, for overcoming the interrelated limitations of Zn anodes and Mn-based cathodes in both aqueous and non-aqueous ZIB systems. This work provides new insights and design principles that advance the field toward the practical realisation of next-generation zinc-based energy storage technologies.

1.7 Reference

1 Li, M., Lu, J., Chen, Z. & Amine, K. 30 years of lithium-ion batteries. *Adv. Mater.* **30**, 1800561 (2018).

2 Deng, D. Li-ion batteries: basics, progress, and challenges. *Energy Sci. Eng.* **3**, 385-418 (2015).

3 Etacheri, V., Marom, R., Elazari, R., Salitra, G. & Aurbach, D. Challenges in the development of advanced Li-ion batteries: a review. *Energy Environ. Sci.* **4**, 3243-3262 (2011).

4 Nitta, N., Wu, F., Lee, J. T. & Yushin, G. Li-ion battery materials: present and future. *Mater. Today* **18**, 252-264 (2015).

5 Yang, H. & Wu, N. Ionic conductivity and ion transport mechanisms of solid-state lithium-ion battery electrolytes: A review. *Energy Sci. Eng.* **10**, 1643-1671 (2022).

6 Huang, X. Separator technologies for lithium-ion batteries. *J. Solid State Electrochem.* **15**, 649-662 (2011).

7 Islam, S. R., Park, S.-Y. & Balasingam, B. Circuit parameters extraction algorithm for a lithium-ion battery charging system incorporated with electrochemical impedance spectroscopy. *IEEE Applied Power Electronics Conference and Exposition (APEC).* 3353-3358 (2018).

8 Cengiz, E. C., Rizell, J., Sadd, M., Matic, A. & Mozhzhukhina, N. Reference electrodes in Li-ion and next generation batteries: correct potential assessment, applications and practices. *J. Electrochem. Soc.* **168**, 120539 (2021).

9 Cao, W., Zhang, J. & Li, H. Batteries with high theoretical energy densities. *Energy Storage Mater.* **26**, 46-55 (2020).

10 Zhao, L. *et al.* Revisiting the roles of natural graphite in ongoing lithium-ion batteries. *Adv. Mater.* **34**, 2106704 (2022).
11 Zheng, J. *et al.* Regulating electrodeposition morphology of lithium: towards commercially relevant secondary Li metal batteries. *Chem. Soc. Rev.* **49**, 2701-2750 (2020).
12 Cao, D. *et al.* Lithium dendrite in all-solid-state batteries: growth mechanisms, suppression strategies, and characterizations. *Matter* **3**, 57-94 (2020).
13 Li, T. *et al.* Degradation mechanisms and mitigation strategies of nickel-rich NMC-based lithium-ion batteries. *Electrochem. Energy Rev.* **3**, 43-80 (2020).
14 Chen, S.-P., Lv, D., Chen, J., Zhang, Y.-H. & Shi, F.-N. Review on defects and modification methods of $LiFePO_4$ cathode material for lithium-ion batteries. *Energy Fuels* **36**, 1232-1251 (2022).
15 Wang, L. & Zheng, J. Recent advances in cathode materials of rechargeable aqueous zinc-ion batteries. *Mater. Today Adv.* **7**, 10078 (2020).
16 Wang, D. *et al.* Insight on Organic Molecules in Aqueous Zn-Ion Batteries with an Emphasis on the Zn Anode Regulation. *Adv. Energy Mater.* **12**, 2102707 (2022).
17 Li, G. *et al.* Developing cathode materials for aqueous zinc ion batteries: challenges and practical prospects. *Adv. Funct. Mater.* **34**, 2301291 (2024).
18 Han, S.-D. *et al.* Origin of electrochemical, structural, and transport properties in nonaqueous zinc electrolytes. *ACS Appl. Mater. Interfaces* **8**, 3021-3031 (2016).
19 Cai, Z. *et al.* Chemically resistant Cu–Zn/Zn composite anode for long cycling aqueous batteries. *Energy Storage Mater.* **27**, 205-211 (2020).
20 Pu, S. D. *et al.* Decoupling, quantifying, and restoring aging-induced Zn-anode losses in rechargeable aqueous zinc batteries. *Joule* **7**, 366-379 (2023).
21 Zuo, Y. *et al.* Zinc dendrite growth and inhibition strategies. *Mater. Today Energy* **20**, 100692 (2021).
22 Ledbetter, H. Elastic properties of zinc: A compilation and a review. *J. Phys. Chem. Ref. Data* **6**, 1181-1203 (1977).
23 Zhang, Q., Luan, J., Tang, Y., Ji, X. & Wang, H. Interfacial Design of Dendrite-Free Zinc Anodes for Aqueous Zinc-Ion Batteries. *Angew. Chem. Int. Ed.* **59**, 13180-13191 (2020).
24 Kang, L. *et al.* Nanoporous $CaCO_3$ coatings enabled uniform Zn stripping/plating for long-life zinc rechargeable aqueous batteries. *Adv. Energy Mater.* **8**, 1801090 (2018).
25 Zhao, K. *et al.* Ultrathin Surface Coating Enables Stabilized Zinc Metal Anode. *Adv. Mater. Interfaces* **5**, 1800848 (2018).
26 Liu, Y. *et al.* Ultrathin ZrO_2 coating layer regulates Zn deposition and raises long-life performance of aqueous Zn batteries. *Mater. Today Energy* **28**, 101056 (2022).
27 Yuksel, R., Buyukcakir, O., Seong, W. K. & Ruoff, R. S. Metal-organic framework integrated anodes for aqueous zinc-ion batteries. *Adv. Energy Mater.* **10**, 1904215 (2020).
28 Deng, C. *et al.* A sieve-functional and uniform-porous kaolin layer toward stable zinc metal anode. *Adv. Funct. Mater.* **30**, 2000599 (2020).
29 Wang, Y. *et al.* Controlled deposition of zinc-metal anodes via selectively polarized ferroelectric polymers. *Adv. Mater.* **34**, 2106937 (2022).
30 Deyab, M. Application of nonionic surfactant as a corrosion inhibitor for zinc in alkaline battery solution. *J. Power Sources* **292**, 66-71 (2015).
31 Yang, X. *et al.* Crystallographic manipulation strategies toward reversible Zn anode with orientational deposition. *Adv. Energy Mater.* **14**, 2401293 (2024).

32 Yan, Y. *et al.* Surface-Preferred Crystal Plane Growth Enabled by Underpotential Deposited Monolayer toward Dendrite-Free Zinc Anode. *ACS Nano* **16**, 9150-9162. (2022).
33 Zeng, L. *et al.* 3D printing architecting reservoir-integrated anode for dendrite-free, safe, and durable Zn batteries. *Adv. Energy Mater.* **12**, 2103708 (2022).
34 Guo, N. *et al.* A review on 3D zinc anodes for zinc ion batteries. *Small Methods* **6**, 2200597 (2022).
35 Kang, Z. *et al.* 3D porous copper skeleton supported zinc anode toward high capacity and long cycle life zinc ion batteries. *ACS Sustain. Chem. Eng.* **7**, 3364-3371 (2019).
36 Li, C. *et al.* Spatially homogeneous copper foam as surface dendrite-free host for zinc metal anode. *Chem. Eng. J.* **379**, 122248 (2020).
37 An, Y., Tian, Y., Xiong, S., Feng, J. & Qian, Y. Scalable and controllable synthesis of interface-engineered nanoporous host for dendrite-free and high rate zinc metal batteries. *ACS Nano* **15**, 11828-11842 (2021).
38 Zhao, J. *et al.* High-performance flexible quasi-solid-state zinc-ion batteries with layer-expanded vanadium oxide cathode and zinc/stainless steel mesh composite anode. *Nano Energy* **62**, 94-102 (2019).
39 Li, C. *et al.* A lean-zinc anode battery based on metal–organic framework-derived carbon. *Carbon Energy* **5**, e301 (2023).
40 Fan, X. *et al.* Enabling stable Zn anode via a facile alloying strategy and 3D foam structure. *Adv. Mater. Interfaces* **8**, 2002184 (2021).
41 Ma, G. *et al.* Porous V_2CT_x MXene as a High Stability Zinc Anode Protective Coating. *Nano Lett.* **24**, 14552-14558 (2024).
42 Hu, L. *et al.* Interface engineering with porous graphene as deposition regulator of stable Zn metal anode for long-life Zn-ion capacitor. *J. Colloid Interface Sci.* **631**, 135-146 (2023).
43 Qian, Y., Meng, C., He, J. & Dong, X. A lightweight 3D Zn@ Cu nanosheets@ activated carbon cloth as long-life anode with large capacity for flexible zinc ion batteries. *J. Power Sources* **480**, 228871 (2020).
44 Du, Y., Chi, X., Huang, J., Qiu, Q. & Liu, Y. Long lifespan and high-rate Zn anode boosted by 3D porous structure and conducting network. *J. Power Sources* **479**, 228808 (2020).
45 Zhang, J. *et al.* Nonepitaxial Electrodeposition of (002)-Textured Zn Anode on Textureless Substrates for Dendrite-Free and Hydrogen Evolution-Suppressed Zn Batteries. *Adv. Mater.* **35**, e2300073 (2023).
46 Yuan, W. *et al.* Realizing Textured Zinc Metal Anodes through Regulating Electrodeposition Current for Aqueous Zinc Batteries. *Angew. Chem. Int. Ed.* **62**, e202218386 (2023).
47 Yang, Y., Yang, H., Zhu, R. & Zhou, H. High reversibility at high current: the zinc electrodeposition principle behind the “trick”. *Energy Environ. Sci.* **16**, 2723-2731 (2023).
48 Xu, Y. *et al.* A rechargeable aqueous zinc/sodium manganese oxides battery with robust performance enabled by Na_2SO_4 electrolyte additive. *Energy Storage Mater.* **38**, 299-308 (2021).
49 Song, Y. *et al.* Dual-Functional LiCl Additive for Highly Reversible Zinc Metal Anode. *Adv. Funct. Mater.* **34**, 2410305 (2024).
50 Tian, G. *et al.* Active Water Optimization in Different Electrolyte Systems for Stable Zinc Anodes. *Small* **21**, 2410332 (2025).

51 Olbasa, B. W. *et al.* Highly reversible Zn metal anode stabilized by dense and anion-derived passivation layer obtained from concentrated hybrid aqueous electrolyte. *Adv. Funct. Mater.* **32**, 2103959 (2022).

52 Ou, T. *et al.* Boric acid-induced preferential deposition of (002) plane for highly stable zinc anode. *Appl. Phys. Lett.* **124**, 183903 (2024).

53 Sun, K. E., Hoang, T. K., Doan, T. N. L., Yu, Y. & Chen, P. Highly sustainable zinc anodes for a rechargeable hybrid aqueous battery. *Chem. Eur. J.* **24**, 1667-1673 (2018).

54 Li, Y. *et al.* A progressive nucleation mechanism enables stable zinc stripping–plating behavior. *Energy Environ. Sci.* **14**, 5563-5571 (2021).

55 Zhao, R. *et al.* Lanthanum nitrate as aqueous electrolyte additive for favourable zinc metal electrodeposition. *Nat. Commun.* **13**, 3252 (2022).

56 Xie, M.-j., Guan, J.-j., Meng, X.-m. & Zhao, Y. Effect of K_2SnO_3 in Electrolyte on the Property of Single-Flow Zinc-Nickel Battery. *Int. J. Electrochem. Sci.* **16**, 210645 (2021).

57 Cao, J. *et al.* Regulating solvation structure to stabilize zinc anode by fastening the free water molecules with an inorganic colloidal electrolyte. *Nano Energy* **93**, 106839 (2022).

58 Chang, G. *et al.* Inhibition role of trace metal ion additives on zinc dendrites during plating and striping processes. *Adv. Mater. Interfaces* **6**, 1901358 (2019).

59 Hoang, T. K. *et al.* Sustainable gel electrolyte containing Pb^{2+} as corrosion inhibitor and dendrite suppressor for the zinc anode in the rechargeable hybrid aqueous battery. *Mater. Today Energy* **4**, 34-40 (2017).

60 Guan, K. *et al.* Anti-corrosion for reversible zinc anode via a hydrophobic interface in aqueous zinc batteries. *Adv. Energy Mater.* **12**, 2103557 (2022).

61 Sun, K. E. *et al.* Suppression of dendrite formation and corrosion on zinc anode of secondary aqueous batteries. *ACS Appl. Mater. Interfaces* **9**, 9681-9687 (2017).

62 Hao, J. *et al.* Toward high-performance hybrid Zn-based batteries via deeply understanding their mechanism and using electrolyte additive. *Adv. Funct. Mater.* **29**, 1903605 (2019).

63 Hashemi, A. B., Kasiri, G. & La Mantia, F. The effect of polyethyleneimine as an electrolyte additive on zinc electrodeposition mechanism in aqueous zinc-ion batteries. *Electrochim. Acta* **258**, 703-708 (2017).

64 Zhou, J. *et al.* Highly reversible and stable Zn metal anode under wide temperature conditions enabled by modulating electrolyte chemistry. *Chem. Eng. J.* **442**, 136218 (2022).

65 Dong, Y. *et al.* Non-concentrated aqueous electrolytes with organic solvent additives for stable zinc batteries. *Chem. Sci.* **12**, 5843-5852 (2021).

66 Nguyen Thanh Tran, T., Zhao, M., Geng, S. & Ivey, D. G. Ethylene glycol as an antifreeze additive and corrosion inhibitor for aqueous zinc-ion batteries. *Batteries Supercaps* **5**, e202100420 (2022).

67 Xu, W. *et al.* Diethyl ether as self-healing electrolyte additive enabled long-life rechargeable aqueous zinc ion batteries. *Nano Energy* **62**, 275-281 (2019).

68 Kao-ian, W. *et al.* Highly stable rechargeable zinc-ion battery using dimethyl sulfoxide electrolyte. *Mater. Today Energy* **21**, 100738 (2021).

69 Shi, J. *et al.* Ultrahigh coulombic efficiency and long-life aqueous Zn anodes enabled by electrolyte additive of acetonitrile. *Electrochim. Acta* **358**, 136937 (2020).

70 Hou, Z. *et al.* Tailoring desolvation kinetics enables stable zinc metal anodes. *J. Mater Chem. A* **8**, 19367-19374 (2020).

71 Sun, P. *et al.* Simultaneous regulation on solvation shell and electrode interface for dendrite-free Zn ion batteries achieved by a low-cost glucose additive. *Angew. Chem.* **133**, 18395-18403 (2021).
72 Li, T. C. *et al.* A universal additive strategy to reshape electrolyte solvation structure toward reversible Zn storage. *Adv. Energy Mater.* **12**, 2103231 (2022).
73 Wang, F. *et al.* Highly reversible zinc metal anode for aqueous batteries. *Nat. Mater.* **17**, 543-549 (2018).
74 Zhang, N. *et al.* Cation-deficient spinel $ZnMn_2O_4$ cathode in $Zn(CF_3SO_3)_2$ electrolyte for rechargeable aqueous Zn-ion battery. *J. Am. Chem. Soc.* **138**, 12894-12901 (2016).
75 Kasiri, G., Trócoli, R., Hashemi, A. B. & La Mantia, F. An electrochemical investigation of the aging of copper hexacyanoferrate during the operation in zinc-ion batteries. *Electrochim. Acta* **222**, 74-83 (2016).
76 Guo, X. *et al.* Zn/MnO_2 battery chemistry with dissolution-deposition mechanism. *Mater. Today Energy* **16**, 100396 (2020).
77 Kundu, D. *et al.* Aqueous vs. nonaqueous Zn-ion batteries: consequences of the desolvation penalty at the interface. *Energy Environ. Sci.* **11**, 881-892 (2018).
78 Zhou, Y. *et al.* Oxide-based cathode materials for rechargeable zinc ion batteries: Progresses and challenges. *J. Energy Chem.* **57**, 516-542 (2021).
79 Zhang, M. *et al.* Recent Progress on High-Performance Cathode Materials for Zinc-Ion Batteries. *Small Struct.* **2**, 2000064 (2020).
80 Han, S.-D. *et al.* Mechanism of Zn insertion into nanostructured δ-MnO_2: a nonaqueous rechargeable Zn metal battery. *Chem. Mater.* **29**, 4874-4884 (2017).
81 Khamsanga, S., Pornprasertsuk, R., Yonezawa, T., Mohamad, A. A. & Kheawhom, S. δ-MnO_2 nanoflower/graphite cathode for rechargeable aqueous zinc ion batteries. *Sci. Rep.* **9**, 8441 (2019).
82 Xu, C., Li, B., Du, H. & Kang, F. Energetic zinc ion chemistry: the rechargeable zinc ion battery. *Angew. Chem. Int. Ed.* **51**, 933-935 (2012).
83 Sun, W. *et al.* Zn/MnO_2 battery chemistry with H^+ and Zn^{2+} coinsertion. *J. Am. Chem. Soc.* **139**, 9775-9778 (2017).
84 Wu, D. *et al.* Quantitative temporally and spatially resolved X-ray fluorescence microprobe characterization of the manganese dissolution-deposition mechanism in aqueous Zn/α-MnO_2 batteries. *Energy Environ. Sci.* **13**, 4322-4333 (2020).
85 Li, H. *et al.* Interface regulated MnO_2/Mn^{2+} redox chemistry in aqueous Zn ion batteries. *Chem. Eng. J.* **446**, 137205 (2022).
86 Sambandam, B. *et al.* An analysis of the electrochemical mechanism of manganese oxides in aqueous zinc batteries. *Chem.* **8**, 924-946 (2022).
87 Jiang, B. *et al.* Manganese sesquioxide as cathode material for multivalent zinc ion battery with high capacity and long cycle life. *Electrochim. Acta* **229**, 422-428 (2017).
88 Chen, L., Yang, Z., Qin, H., Zeng, X. & Meng, J. Advanced electrochemical performance of $ZnMn_2O_4$/N-doped graphene hybrid as cathode material for zinc ion battery. *J. Power Sources* **425**, 162-169 (2019).
89 Soundharrajan, V. *et al.* The dominant role of Mn^{2+} additive on the electrochemical reaction in $ZnMn_2O_4$ cathode for aqueous zinc-ion batteries. *Energy Storage Mater.* **28**, 407-417 (2020).
90 Sun, K. *et al.* MOF-derived Zn/Co co-doped MnO/C microspheres as cathode and Ti_3C_2@ Zn as anode for aqueous zinc-ion full battery. *Chem. Eng. J.* **454**, 140394 (2023).

91 Yamada, A., Tanaka, M., Tanaka, K. & Sekai, K. Jahn–Teller instability in spinel Li–Mn–O. *J. Power Sources* **81**, 73-78 (1999).
92 Li, S., Zhang, H., Liu, Y., Wang, L. & He, X. Comprehensive understanding of structure transition in $LiMn_yFe_{1-y}PO_4$ during delithiation/lithiation. *Adv. Funct. Mater.* **34**, 2310057 (2024).
93 Hunter, J. C. Preparation of a new crystal form of manganese dioxide: λ-MnO_2. *J. Solid State Chem.* **39**, 142-147 (1981).
94 Liu, Y. *et al.* Spontaneously dissolved MnO: A better cathode material for rechargeable aqueous zinc-manganese batteries. *Chem. Eng. J.* **473**, 145490 (2023).
95 Bischoff, C. F. *et al.* Revealing the local pH value changes of acidic aqueous zinc ion batteries with a manganese dioxide electrode during cycling. *J. Electrochem. Soc.* **167**, 020545 (2020).
96 Zhang, D. *et al.* Inhibition of manganese dissolution in Mn_2O_3 cathode with controllable Ni^{2+} incorporation for high-performance zinc ion battery. *Adv. Funct. Mater.* **31**, 2009412 (2021).
97 Xia, X. *et al.* Mo doping provokes two electron reaction in MnO_2 with ultrahigh capacity for aqueous zinc ion batteries. *Nano Res.* **16**, 2511-2518 (2023).
98 Ji, J. *et al.* $Co^{2+}/^{3+}/^{4+}$-Regulated electron state of Mn-O for superb aqueous zinc-manganese oxide batteries. *Adv. Energy Mater.* **11**, 2003203 (2021).
99 Zheng, J. *et al.* Compact and insoluble $Mn_3(PO_4)_2$ coating layer confined amorphous MnO_2 as cathode for aqueous zinc ion batteries. *Appl. Surf. Sci.* **635**, 157665 (2023).
100 Islam, S. *et al.* Carbon-coated manganese dioxide nanoparticles and their enhanced electrochemical properties for zinc-ion battery applications. *J. Energy Chem.* **26**, 815-819 (2017).
101 Wang, L. *et al.* Facile in situ synthesis of PEDOT conductor interface at the surface of MnO_2 cathodes for enhanced aqueous zinc-ion batteries. *Surf. Interfaces* **33**, 102222 (2022).
102 Lv, H. *et al.* Disproportionation enabling reversible MnO_2/Mn^{2+} transformation in a mild aqueous Zn-MnO_2 hybrid battery. *Chem. Eng. J.* **430**, 133064 (2022).
103 Pan, H. *et al.* Reversible aqueous zinc/manganese oxide energy storage from conversion reactions. *Nat. Energy* **1**, 16039 (2016).
104 Chamoun, M., Brant, W. R., Tai, C.-W., Karlsson, G. & Noréus, D. Rechargeability of aqueous sulfate Zn/MnO_2 batteries enhanced by accessible Mn^{2+} ions. *Energy Storage Mater.* **15**, 351-360 (2018).
105 Alfaruqi, M. H. *et al.* Structural transformation and electrochemical study of layered MnO_2 in rechargeable aqueous zinc-ion battery. *Electrochim. Acta* **276**, 1-11 (2018).
106 Cui, S., Zhang, D. & Gan, Y. The effect of Mn^{2+} additives on the capacity of aqueous Zn/δ-MnO_2 batteries: Elucidating the Mn^{2+} concentration dependence of the irreversible transformation of δ-MnO_2. *J. Power Sources* **579** (2023).
107 Rajabi, R. *et al.* Insights into chemical and electrochemical interactions between Zn anode and electrolytes in aqueous Zn− ion batteries. *J. Electrochem. Soc.* **169**, 110536 (2022).
108 Kim, S. J. *et al.* Unraveling the dissolution-mediated reaction mechanism of α-MnO_2 cathodes for aqueous Zn-ion batteries. *Small* **16**, 2005406 (2020).
109 Dai, Y. *et al.* Inhibition of vanadium cathodes dissolution in aqueous Zn-ion batteries. *Adv. Mater.* **36**, 2310645 (2024).

110 Wang, Z., Wang, Y., Wang, G., Wu, W. & Zhu, J. Earth-abundant magnetite with carbon coatings as reversible cathodes for stretchable zinc-ion batteries. *J. Energy Chem.* **62**, 552-562 (2021).
111 Yang, X. *et al.* Suppressing Cu-based cathode dissolution in rechargeable aqueous zinc batteries with equilibrium principles. *Appl. Surf. Sci.* **568**, 150948 (2021).
112 Wu, B., Mu, Y., Li, Z., Li, M., Zeng, L. and Zhao, T.. Realizing high-voltage aqueous zinc-ion batteries with expanded electrolyte electrochemical stability window. *Chin. Chem. Lett.* **34**, 107629 (2023).
113 Ni, Q., Kim, B., Wu, C. & Kang, K. Non-electrode components for rechargeable aqueous zinc batteries: Electrolytes, solid-electrolyte-interphase, current collectors, binders, and separators. *Adv. Mater.* **34**, 2108206 (2022).
114 Zhao, Z. *et al.* Long-life and deeply rechargeable aqueous Zn anodes enabled by a multifunctional brightener-inspired interphase. *Energy Environ. Sci.* **12**, 1938-1949 (2019).
115 Yang, W. *et al.* Hydrated eutectic electrolytes with ligand-oriented solvation shells for long-cycling zinc-organic batteries. *Joule* **4**, 1557-1574 (2020).
116 Cao, L. *et al.* Solvation structure design for aqueous Zn metal batteries. *J. Am. Chem. Soc.* **142**, 21404-21409 (2020).
117 Asselin, G. M., Paden, O., Qiu, W., Yang, Z. & Sa, N. A Systematic Electrochemical Investigation of a Dimethylamine Cosolvent-Assisted Nonaqueous Zinc (II) Bis (trifluoromethylsulfonyl) imide Electrolyte. *J. Electrochem. Soc.* **168**, 030516 (2021).
118 Jia, H. *et al.* Hybrid Co-Solvent-Induced High-Entropy Electrolyte: Regulating of Hydrated Zn^{2+} Solvation Structures for Excellent Reversibility and Wide Temperature Adaptability. *Adv. Energy Mater.* **14**, 2304285 (2024).
119 Xie, D. *et al.* ZnF_2-riched inorganic/organic hybrid SEI: in situ-chemical construction and performance-improving mechanism for aqueous zinc-ion batteries. *Angew. Chem. Int. Ed.* **62**, e202216934 (2023).
120 Liu, L. *et al.* Salt anion amphiphilicity-activated electrolyte cosolvent selection strategy toward durable Zn metal anode. *ACS Nano* **17**, 23065-23078 (2023).
121 Liu, S. *et al.* Monolithic phosphate interphase for highly reversible and stable Zn metal anode. *Angew. Chem. Int. Ed.* **62**, e202215600 (2023).
122 Bhatia, A., Xu, J., Pereira-Ramos, J.-P., Rousse, G. & Baddour-Hadjean, R. γ'-V_2O_5 polymorph: a genuine Zn intercalation material for nonaqueous rechargeable batteries. *Chem. Mater.* **34**, 1203-1212 (2021).

2

2 Experimental Techniques

2.1 Synthesis Techniques

2.1.1 Solid-State Synthesis

Solid-state synthesis is the most common synthesis method in inorganic materials chemistry, prized for its ability to produce high-purity, thermodynamically stable oxides and sulphides without the use of solvents. In this method, finely ground precursors, which are typically oxides, carbonates, or nitrates, are mixed in precise stoichiometric ratios and subjected to high temperature calcination (commonly between 500 and 1500 °C). At these temperatures, atomic diffusion across particle interfaces drives nucleation and growth of the target phase.[1] Because diffusion rates depend strongly on particle size, achieving uniform, submicron to nanometer scale powders by mechanical pre-treatment both increases interfacial contact area and introduces defects that accelerate reactivity, allowing phase formation at lower temperatures or in shorter times.

Key synthesis parameters must be carefully balanced. Temperature provides the energy to overcome diffusion barriers, but excessive heat can induce partial melting, exaggerated grain growth, or phase decomposition; intermediate calcination steps and controlled heating rates help ensure complete reaction while minimising kinetic bottlenecks. Likewise, the gas atmosphere dictates oxidation state and stoichiometry: an oxygen rich environment preserves higher valence cations in transition metal oxides, whereas reducing (H_2/Ar) or inert (Ar, N_2) atmospheres are employed to stabilise lower oxidation states or prevent unwanted side reactions with air-sensitive precursors.

2.1.2 Hydrothermal Synthesis

Hydrothermal synthesis is a widely employed solution-phase method for the preparation of crystalline inorganic materials under elevated temperature and pressure

conditions.[2] This technique involves carrying out chemical reactions in water (or occasionally in organic solvents) inside sealed, high-pressure vessels known as autoclaves. The combination of elevated temperature and the autogenous pressure generated from solvent vapour allows reactions to proceed at relatively low temperature compared to traditional solid-state methods. This makes hydrothermal synthesis particularly attractive for the formation of metastable or low-temperature crystalline phases that are otherwise inaccessible under ambient or high-temperature conditions.

The method operates on the principle of enhanced solubility and reactivity of precursors under hydrothermal conditions, which facilitates a dissolution–recrystallisation mechanism. In this process, precursor species dissolve into the solvent at elevated temperature and subsequently nucleate and grow into well-defined crystals, often exhibiting controlled size, shape, and crystallographic orientation.

The outcome of hydrothermal synthesis is highly sensitive to several key parameters. Temperature, typically ranging from 100 °C to 300 °C, plays a crucial role in altering the solubility of reactants and modifying solvent properties. At these temperatures, water exhibits a reduced dielectric constant and enhanced ionic mobility, which significantly impacts reaction dynamics and crystal growth behaviour. Pressure is generated autogenously due to the confined vapour of the solvent and can reach several megapascals. This pressure affects the thermodynamic stability of different phases and influences the kinetics of nucleation and crystal growth. Other critical factors include solvent composition, precursor concentration, reaction duration, and pH, all of which can be tuned to control phase purity, particle morphology, and crystallinity.

2.1.3 Ball-Milling Synthesis

While traditionally ball milling method is employed for particle size reduction and powder mixing, this technique has evolved into a powerful synthetic tool. The process involves confining precursor powders within a robust milling vessel, typically constructed from zirconia or hardened steel, along with grinding balls of matching composition. When subjected to high-speed rotation or vibration, the milling media undergo violent collisions, generating intense localised heat and pressure.

The localised heat and pressure come from collisions between the milling balls, as well as between the balls and the jar wall, which generating instantaneous temperature spikes (reaching several hundred degrees Celsius) and transient pressure pulses.[3] Simultaneously, shear forces and fracturing create fresh and reactive surfaces. This unique combination of effects enables the formation of metastable phases and novel materials that would ordinarily require extreme temperature or pressure conditions in conventional synthesis.

Critical process parameters govern the outcome of ball mill synthesis, with milling duration, rotational velocity, the size of balls, ball-to-powder mass ratio serving as key variables. These factors collectively determine the energy transfer dynamics between the milling balls and powder, influencing the balance of chemical transformation.

2.2 Electrochemical Techniques

2.2.1 Electrode Preparation

Dry electrode preparation was employed in this thesis in place of conventional slurry-based electrode fabrication. Given the inherently low electronic conductivity of transition metal oxide and sulphide cathode materials, a carbon additive (20 wt%) was homogeneously blended with the active material using a mortar and pestle or mechanochemical methods to

ensure uniform dispersion. A polymer binder, typically polytetrafluoroethylene (PTFE), was then introduced at 10wt % to form a fibrous network that binds the active material and carbon particles, providing both mechanical integrity and electrical connectivity.

The resulting dry mixture was subsequently calendered to a thickness of several hundred micrometres. While thick electrodes are advantageous for achieving high areal capacities in practical batteries, it is essential to maintain a certain degree of porosity to ensure sufficient electrolyte penetration and wetting of the electrode particles. Finally, the electrodes were cut to the desired size and weighed for electrochemical testing.

2.2.2 Coin Cell Assembly

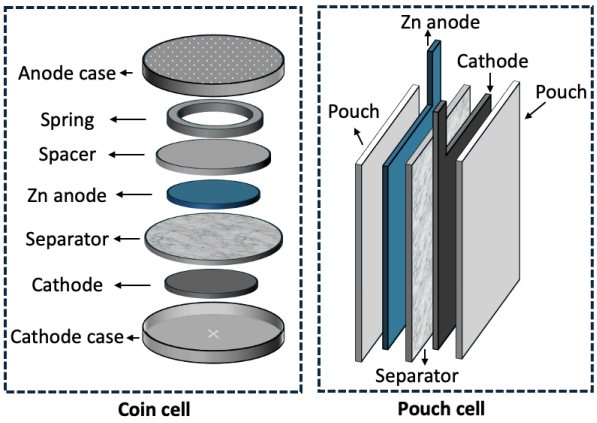

Figure 2.1 Schematic of coin cell and pouch cell configurations.

Coin cell assembly is a standardised laboratory-scale method used to evaluate the electrochemical performance of anodes and cathodes. The CR2032 coin cell format is commonly employed. The assembly process begins with the cathode case as the base component. The stack (Figure 2.1) is constructed by sequentially placing the cathode, followed by two electrolyte-saturated separators (18 mm in diameter), which serve to prevent electrical short circuits while allowing efficient ionic transport. The anode (16 mm in diameter) is then precisely positioned, after which a spacer and spring are added to maintain consistent internal pressure and ensure proper electrical contact throughout the cell's operation. The assembly

is completed with the anode case, which forms the upper enclosure. The components are hermetically sealed under controlled pressure to provide controlled and stable internal environment, preventing unwanted chemical reactions and electrolyte loss. Stable contact between electrodes is achieved through the deformation of the spring, which applies a pressure in the range of approximately 0.1–1 MPa.

In this thesis, various types of coin cells were assembled depending on the electrolyte system. For aqueous electrolytes, assembly was conducted in a standard wet lab. Asymmetric cells such as Zn/aqueous electrolyte/Ti were used to evaluate Zn anode stripping/plating efficiency, while Zn/aqueous electrolyte/cathode cells were assembled to investigate full-cell performance. For non-aqueous electrolytes, assembly was carried out in an inert atmosphere (e.g., an argon-filled glovebox) to avoid contamination from air or moisture.

2.2.3 Pouch Cell Assembly

The assembly process of pouch cells is similar to that of coin cells, with the core components being the anode, electrolyte-soaked separators, and cathode stacked together though without the use of spacers or springs (Figure 2.1). Once assembled, the pouch cell undergoes vacuum sealing. Pouch cells use laminated aluminium-plastic film as the outer casing, resulting in significantly lower stack pressure compared to coin cells. However, external pressure can be applied using adjustable folding clamps. In this thesis, Zn/aqueous electrolyte/Ti pouch cells were assembled and operated under varying stack pressures to investigate the effect of pressure on Zn plating behaviour.

Pouch cells offer higher energy density than conventional cell formats due to their lightweight and compact packaging. Also benefiting from their cost-efficiency and design flexibility, pouch cells represent the most scalable manufacturing approaches in commercial lithium-ion battery production.

2.2.4 Cell Cycling

Galvanostatic cycling is a widely used electrochemical technique for evaluating the performance of battery electrodes, including both anodes and cathodes. As a controlled-current method, it involves applying a fixed current density, typically normalised by electrode mass (mA g^{-1}) or area (mA cm^{-2}) during charge and discharge processes, while continuously monitoring the corresponding voltage response. This method closely simulates real-world battery operation, where devices often function under constant-current conditions, making it highly relevant for both fundamental research and practical applications.

Cycling protocols are generally defined by upper and lower voltage cutoffs to prevent overcharging or overdischarging, both of which can trigger irreversible side reactions and electrolyte decomposition.

Key performance metrics derived from galvanostatic cycling include specific capacity, coulombic efficiency (CE), and voltage hysteresis. Specific capacity (typically expressed in mAh g^{-1} or mAh cm^{-2}) indicates the amount of charge the material can store, while CE, the ratio of discharge to charge capacity or the ratio of charge to discharge capacity, reflects the reversibility of electrochemical reactions. The voltage profile, plotted as potential versus capacity, provides further insights into redox mechanisms, phase transitions, kinetic limitations, and polarisation effects.

Moreover, advanced techniques such as the galvanostatic intermittent titration technique (GITT) can be employed to extract additional thermodynamic and kinetic information, offering a deeper understanding of diffusion processes and material behaviour under operating conditions.

2.3 Imaging Characterisation Techniques

2.3.1 Scanning Electron Microscopy (SEM)

Scanning electron microscopy is a powerful analytical technique for characterising surface morphology with micro- to nanoscale resolution. In this thesis, SEM was employed to investigate Zn anode deposition, where achieving uniform and planar morphology is critical for ensuring stable cycling performance. SEM was also used to examine the particle size and surface features of cathode materials, as these parameters significantly influence Zn^{2+} diffusion kinetics and overall electrochemical behaviour.

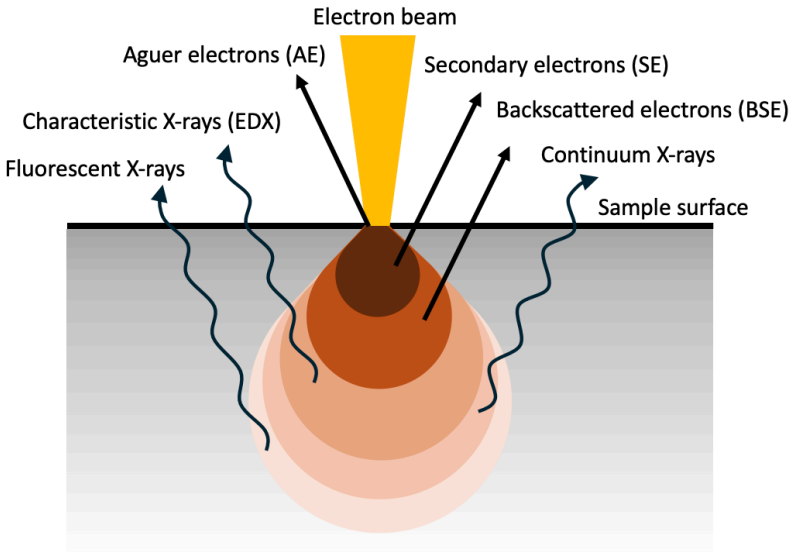

Figure 2.2 Schematic illustration of electron beam interactions with sample material in SEM.

During SEM operation, a focused electron beam raster scans the sample surface. The beam penetrates the sample to a depth of a few microns, before interacting with atoms in the sample. The extent of the interaction volume will depend upon the accelerating voltage of the primary electrons and the density of the sample material. Low-density samples facilitate a tear-drop interaction volume, as shown in Figure 2.2. As the beam interacts with the sample, it generates various signals, most notably secondary electrons, backscattered electrons, and characteristic X-rays.[4] Secondary electrons, emitted when primary electrons dislodge surface-

level electrons, are especially valuable for high-resolution imaging due to their sensitivity to surface topography. Backscattered electrons, which are primary electrons reflected by atomic nuclei, provide compositional contrast based on the atomic number of elements present.

Furthermore, when the electron beam ejects an inner-shell electron from an atom, an electron from a higher energy shell falls into the vacancy, releasing energy in the form of a characteristic X-ray. These X-rays are unique to specific elements and their electronic transitions. With the addition of an EDX detector, SEM can perform elemental analysis, offering both qualitative and quantitative insights into the sample's composition. However, it is important to note that EDX has limited sensitivity for detecting light elements, such as hydrogen. In this thesis, EDX was employed to analyse the elemental distribution on both the Zn anode and the Mn-based cathode.

2.3.2 Scanning Transmission Electron Microscopy (STEM)

Scanning Transmission Electron Microscopy (STEM) offers atomic-scale imaging, enabling precise structural characterisation of materials. Unlike SEM which primarily provides surface morphology information using secondary or backscattered electrons, STEM achieves much higher resolution by transmitting a finely focused electron probe through an ultrathin sample. This configuration allows for the simultaneous acquisition of high-resolution structural and elemental information with exceptional spatial precision.

One of the most widely used imaging modes in STEM is high-angle annular dark-field (HAADF) imaging, which provides atomic-resolution contrast that is highly sensitive to differences in atomic number (Z-contrast). In HAADF-STEM, electrons scattered at high angles are collected by an annular detector, producing images in which heavier elements appear brighter due to their greater scattering power.[5]

To complement HAADF imaging, STEM is often integrated with EDX for spatially resolved elemental mapping. The combined use of HAADF-STEM and STEM-EDX provides a powerful correlative approach to materials characterisation, linking local chemistry with atomic-scale structural features.

For sample preparation, powders are typically dispersed in a volatile solvent such as ethanol or acetonitrile and drop-cast onto a holey carbon-coated Cu TEM grid. Individual particles are suspended over the holes in the grid, allowing the electron beam to probe their protruding edges. As electron transmission is significantly attenuated by thick regions of the sample, meaningful imaging and analysis are generally limited to the thinner edge regions where sufficient beam penetration is possible.

2.3.3 Transmission Electron Microscopy (TEM)

Transmission Electron Microscopy utilises a broad, coherent electron beam to enable high-resolution visualisation of the internal structure of materials at the atomic level. When the electron beam is transmitted through an ultra-thin sample, interactions such as scattering and absorption convey detailed information about the specimen's structure, composition, and other physical properties. These interactions are used to form both real-space images and diffraction patterns.

Image formation in TEM relies on contrast mechanisms to distinguish between different features within a sample.[6] The primary sources of contrast include: 1. Mass-thickness contrast, which arises from variations in atomic number and specimen thickness. Regions with higher mass or greater thickness scatter more electrons, resulting in fewer transmitted electrons and thus darker areas in the image. 2. Diffraction contrast, which is commonly used to visualise crystalline defects such as dislocations, grain boundaries, and stacking faults. This contrast occurs due to variations in electron diffraction between different crystallographic

orientations. 3. Phase contrast, which is essential in high-resolution TEM (HRTEM) for imaging atomic columns and lattice fringes. It originates from the interference between the incident and scattered electron waves, producing intensity variations that reveal atomic-scale features.

Due to the strong interaction between electrons and sample material, TEM requires specimens to be extremely thin, typically less than 100 nanometers, to allow electron transmission. The same sample preparation techniques used for STEM can often be applied to TEM to achieve the necessary thinness and dispersion.

Selected Area Electron Diffraction (SAED)

When a high-energy electron beam passes through a thin specimen, it interacts with the atomic planes of the crystal lattice, producing a diffraction pattern that reveals critical information about the material's phase, crystallographic orientation, lattice symmetry, and defects. Unlike XRD, electron diffraction in TEM offers localised structural information, allowing the analysis of individual nanoparticles and grains. While XRD provides excellent resolution in reciprocal space, its measurements represent an average over a large sample volume, whereas TEM-based electron diffraction can probe structural variations at the nanometer scale within specific regions of interest.

The formation of electron diffraction patterns is governed by Bragg's Law, where constructive interference occurs when the electron beam satisfies specific angle-wavelength conditions relative to the crystal lattice. The resulting diffraction pattern varies depending on the sample structure: sharp spots appear for single crystals, concentric rings for polycrystalline or nanocrystalline materials, and diffuse halos for amorphous phases. By analysing the positions and intensities of these features, researchers can extract detailed structural information such as the Bravais lattice type, space group, lattice parameters, and identify phases through comparison with reference or simulated patterns.

A commonly employed technique in TEM is selected-area electron diffraction (SAED), in which a small aperture is used to isolate a specific region of the sample for diffraction analysis. This allows precise correlation between the real-space microstructure and reciprocal-space information.

In-situ Liquid Cell TEM

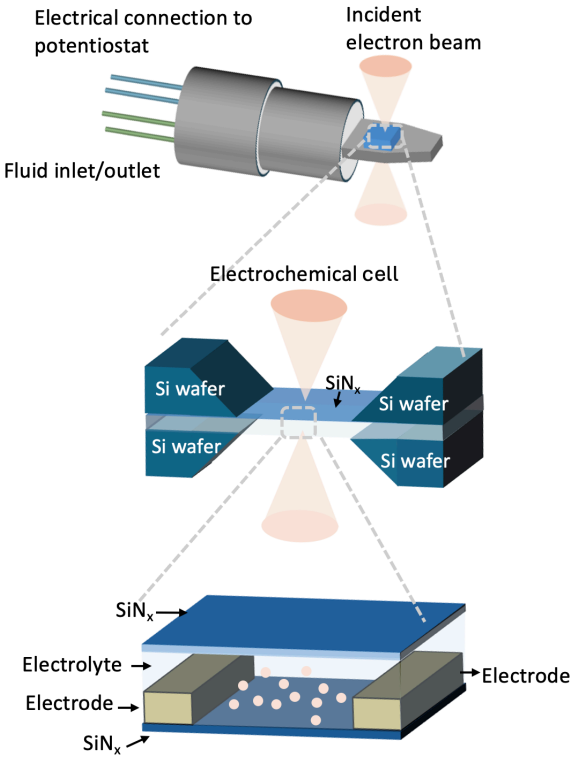

Figure 2.3 Schematic of an in-situ liquid cell TEM setup, including a small fluidic chamber for real-time observation of electrochemical processes under liquid conditions.

In situ liquid cell transmission electron microscopy (TEM) is enabled through a sealed liquid environment, where silicon nitride (SiN_x) membranes confine the liquid electrolyte, preventing its leakage into the TEM vacuum while still permitting electron transmission for imaging.[7] As shown in Figure 2.3, a typical liquid cell consists of two silicon chips: a smaller bottom chip and a larger top chip. The bottom chip is equipped with spacers with varying heights that control the thickness of the liquid layer, facilitate fluid flow, and provide space for

electrochemical reactions. Both chips feature a central, ultrathin SiN_x membrane that is electron-transparent, allowing beam transmission for high-resolution imaging.

The imaging resolution in liquid-cell TEM is largely determined by the total thickness of the liquid cell, which comprises the SiN_x membrane thickness and the thickness of the confined liquid layer. Resolution improves with decreasing total thickness and increasing electron beam dose rate. However, thinner liquid layers, while beneficial for resolution, reduce ion mobility and limit the observable volume. In this thesis, the total liquid cell thickness was typically between 500 nm and 1 μm, offering a balance between ionic diffusion, particle observation, and imaging clarity.

Although higher beam dose rates enhance resolution, they can introduce significant beam-induced damage, especially in liquid environments. Inelastic interactions between the accelerated electrons and the liquid can lead to radiolysis, thermal effects, and knock-on damage. Among these, radiolysis is the most critical in aqueous systems, as it leads to chemical decomposition, local pH changes, and gas bubble formation, which can distort the experiment. Therefore, beam dose optimisation tests were performed prior to imaging to determine the minimum dose necessary for adequate resolution while minimising damage.

2.4 Structure Characterisation Techniques

2.4.1 X-ray Diffraction (XRD)

Powder X-ray diffraction is a powerful technique for identifying the long-range atomic arrangement in crystalline materials that exhibit structural symmetry. It is widely used to determine phase composition in multi-phase samples and to quantify phase fractions in crystalline mixtures. Additionally, XRD can provide information about atomic site occupancies within the crystal structure.

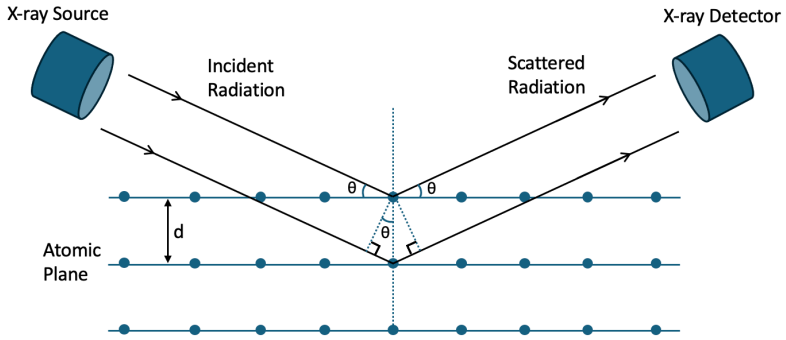

Figure 2.4 Schematic illustration demonstrating Bragg's Law and the conditions for constructive interference of X-rays scattered by atomic planes.

Diffraction arises from the interaction between incident X-ray radiation and the periodic arrangement of atoms in a crystal. When the X-ray beam enters a crystalline material, it is scattered by the electrons surrounding the atoms. Due to the highly ordered nature of the crystal lattice, these scattered waves can interfere constructively, producing measurable diffraction peaks.

As shown in Figure 2.4, this constructive interference occurs when the difference in path length between waves scattered from successive atomic planes equals an integer multiple of the X-ray wavelength. This condition is described by Bragg's Law:

$$n\lambda = 2d \sin \theta$$

where n is the order of reflection, λ is the X-ray wavelength, d is the interplanar spacing, and θ is the angle of incidence.

Each set of atomic planes in the crystal is indexed by a set of integers (h, k, l), known as Miller indices, which represent the reciprocal intercepts of the plane with the crystallographic axes (a, b, and c). The resulting diffraction pattern serves as a fingerprint for the crystalline structure, enabling phase identification, lattice parameter determination, and structural refinement.

The number and positions of peaks in a powder XRD pattern are determined by the crystal's space group and unit cell parameters, which together define the interplanar spacings (d_{hkl}) for different lattice planes. In contrast, the absolute intensity (I_{hkl}) of each diffraction peak is governed by the atomic arrangement within those planes, as described by the structure factor. The structure factor is calculated using the atomic scattering factors of all atoms in the unit cell. Additionally, peak broadening can result from several factors, including limited crystallite size (described by the Scherrer effect), thermal vibrations, and microstrain within the crystal lattice.

In typical laboratory XRD instruments, X-rays are produced by bombarding a metal target (commonly copper, but also molybdenum or silver) with high-energy electrons. This interaction produces X-rays at discrete wavelengths characteristic of the target metal. The most commonly used radiation in lab-based diffractometers is Cu $K\alpha_1$ (λ = 1.541 Å), which provides strong and well-defined diffraction. To isolate this primary wavelength, monochromation is required. A nickel filter is often used to suppress the unwanted Cu $K\beta$ radiation, while a germanium monochromator can further refine the beam by removing Cu $K\alpha_2$ components, improving resolution and peak shape.

Refinement of XRD

The Rietveld refinement method is a powerful computational technique used in XRD to extract detailed structural and microstructural information from powder diffraction data. Rietveld refinement fits the entire experimental diffraction pattern using a theoretical model that accounts for both structural parameters (e.g., lattice constants, atomic positions, site occupancies, and thermal displacement factors) and instrumental effects (e.g., peak shape, background, and zero-point error). The refinement process employs a least-squares minimisation approach to iteratively adjust these parameters until the calculated pattern

closely matches the observed data, quantified by reliability factors such as R_p, R_{wp}, and χ^2. This method enables precise determination of phase composition, even in multiphase samples, through quantitative phase analysis, while also providing insights into crystallite size, microstrain, and preferred orientation. In this thesis, Rietveld refinement of XRD data was performed using the GSAS-II software package.

2.4.2 X-ray Pair Distribution Function (XPDF)

X-ray pair distribution function analysis is derived from total scattering data. When high-energy X-rays interact with a material, they scatter from electron clouds through both elastic and inelastic processes. The total scattering signal includes contributions from both. This elastic component consists of Bragg scattering, which arises from periodic lattice planes, and diffuse scattering, which originates from local deviations from perfect crystallinity. By utilising the total scattering signal, XPDF enables the investigation of structural features at local length scales that extend beyond the traditional crystallographic unit cell.

The transformation from reciprocal-space total scattering data to real-space structural information involves a mathematical procedure.[8] The total scattering structure function, S(Q), is first extracted from the data. A Fourier transform of this function, using a sine kernel Q[S(Q)−1], yields the pair distribution function, G(r). This real-space function provides a measure of the probability of finding pairs of atoms separated by a distance r. The positions of peaks in G(r) correspond to specific interatomic distances and reflect bond lengths and unit cell geometry. The areas under these peaks are proportional to coordination numbers and atomic occupancies, while the peak widths reflect thermal vibrations. The damping of the signal with increasing r indicates the degree of static disorder within the material. This real-space representation allows for intuitive interpretation of local structural motifs, particularly

in materials with disorder, nanoscale features, or amorphous character, which are often inaccessible to conventional diffraction techniques.

2.5 Spectroscopy Techniques

2.5.1 Soft X-ray Absorption Spectroscopy (sXAS)

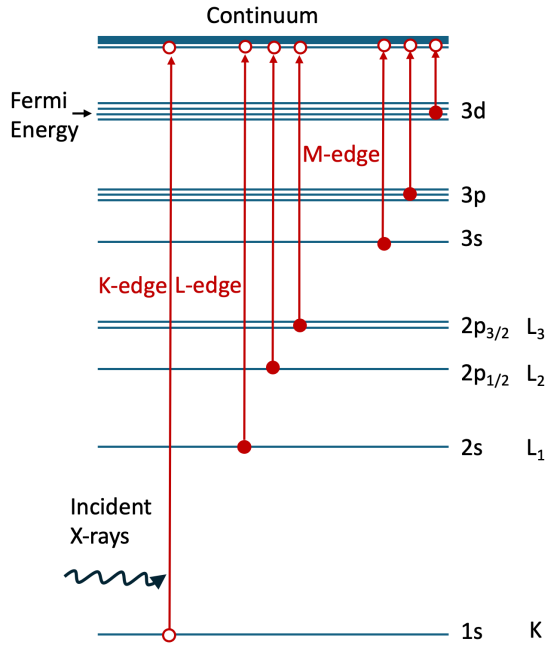

Figure 2.5 Schematic illustration of core electron excitation from the K, L, and M edges in 3d TMs as observed in XAS.

X-ray absorption spectroscopy is a powerful technique for probing the electronic structure and local coordination environment of materials by measuring the excitation of core electrons to unoccupied states.[9] The technique is based on the absorption of high-energy photons by atoms in a material, which promotes electronic transitions from filled to empty orbitals. These transitions are governed by selection rules that allow excitations only between adjacent electron shells. As shown in Figure 2.5, the absorption edges are labelled K, L, M, etc., according to the principal quantum number of the core electron being excited. Transition metal L-edges typically require low-energy (soft) X-rays in the range of 500–1000 eV, while K-edges demand higher-energy (hard) X-rays between 5–10 keV.

In this thesis, soft XAS (sXAS) at the Mn L-edge was employed. Among the available detection modes, fluorescence yield (FY) detection, which monitors emitted photons following core excitation, offers bulk-sensitive information but is prone to self-absorption effects that can distort spectral line shapes. To overcome this limitation, inverse partial fluorescence yield (IPFY) has been developed as an advanced detection approach. IPFY measurements at the Mn L-edge often use the oxygen K-edge emission as a detection channel to mitigate the severe self-absorption that affects conventional FY. When soft X-rays excite the Mn 2p core level, the relaxation process can induce secondary excitations of oxygen 1s electrons in Mn–O systems. The resulting O Kα photons (~525 eV) have significantly lower energy than the Mn L-edge features (~640–660 eV), allowing them to escape the sample without substantial reabsorption by Mn atoms. This IPFY method preserves the intrinsic line shape of the Mn L-edge spectrum, enabling more accurate analysis of spectral features, such as the L_3/L_2 branching ratio and pre-edge structure.

The penetration depth of incident X-rays is strongly influenced by their energy. Soft X-rays, with relatively low photon energies, exhibit limited penetration into matter and are thus typically employed in reflection geometry combined with fluorescence detection. Within the sample, the X-ray intensity attenuates exponentially with depth according to the Beer–Lambert law, governed by the attenuation coefficient (μ), which itself depends sensitively on the photon energy and the material's composition. As a result, the effective probe depth in soft X-ray absorption spectroscopy varies with incident energy—an important consideration for depth-dependent studies and the interpretation of signals in systems with chemical or structural gradients.

2.5.2 X-ray Absorption Near Edge Structure (XANES)

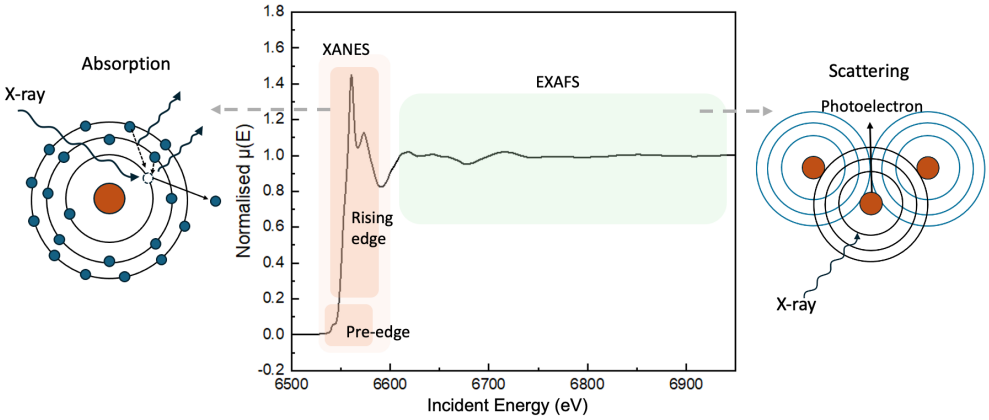

Figure 2.6 Different spectral regions in Mn K-edge XAS, including XANES and EXAFS.

X-ray absorption near edge structure spectroscopy serves as a powerful analytical tool for probing the electronic structure and local coordination environment of specific elements within materials.[9] This technique is particularly valuable for metal K-edge analysis, typically employing hard X-rays in the 5-10 keV energy range to examine the near-edge region. As illustrated in Figure 2.6, the XANES spectrum contains three important regions: pre-edge, main edge and beyond edge. The pre-edge region, located just below the main absorption edge, reveals subtle transitions that are exquisitely sensitive to local symmetry distortions and orbital hybridisation effects, particularly in transition metal oxides where metal 3d-oxygen 2p mixing occurs. The main edge position shows systematic shifts of 1-3 eV per oxidation state change, serving as a reliable indicator of valence state. Beyond the edge, the post-edge region transitions into the extended X-ray absorption fine structure (EXAFS) regime where scattering phenomena dominate.

In standard transmission mode XANES measurements, the absorption spectrum is derived from the logarithmic ratio of incident to transmitted beam intensities ($\ln(I_0/I_t)$). However, for samples with dilute element concentrations, fluorescence detection is preferred,

where the absorption profile is constructed from the fluorescence yield (I_f/I_0) to maintain adequate signal-to-noise.

2.5.3 Extended X-ray Absorption Fine Structure (EXAFS)

Extended X-ray absorption fine structure is a powerful spectroscopic technique that provides detailed insight into the local atomic structure surrounding a specific element within a material. In a typical XAS experiment, the absorption spectrum beyond the edge often displays a series of oscillations (Figure 2.6). These oscillations arise from interactions between photoelectrons and neighbouring atoms and contain rich structural information about the local environment of the absorbing atom.[10]

When the incident X-ray energy exceeds the absorption edge, core electrons are ejected into the continuum, and they escaped atom as photoelectrons. These photoelectrons propagate outward and are partially scattered by nearby atoms. The interference between the outgoing and backscattered photoelectron waves modulates the X-ray absorption coefficient, producing the characteristic EXAFS oscillations.[9] These modulations encode quantitative information about interatomic distances, coordination numbers, and structural disorder.

The EXAFS signal is typically described by the χ(k) function, where k is the photoelectron wave vector. To enhance features at higher energies, a k-weighting (e.g., $k^2\chi(k)$ or $k^3\chi(k)$) is applied. Fourier transformation of the weighted χ(k) function yields a radial distribution function that reveals the distances to neighbouring atoms. Each peak in the resulting spectrum corresponds to a specific coordination shell, with peak positions indicating bond lengths and peak intensities reflecting coordination numbers and thermal or static disorder.

2.6 Elemental Analysis Technique

2.6.1 Inductively Coupled Plasma (ICP) – Optical Emission Spectroscopy (OES)/ Mass Spectrometry (MS)

Inductively coupled plasma–optical emission spectroscopy (ICP-OES) is a highly sensitive analytical technique used for the quantitative determination of elemental composition in a sample. The technique operates by introducing the sample into a high-temperature argon plasma (typically 6,000–10,000 K), where the constituents are atomised and excited, leading to the emission of element-specific optical signals.

The analytical process involves three main steps: sample introduction, plasma excitation, and spectral detection. Liquid samples are nebulised into a fine aerosol and transported into the plasma torch. The intense thermal energy of the plasma vaporises, atomises, and ionises the elements present. As the excited atoms and ions return to lower energy states, they emit photons at characteristic wavelengths corresponding to their unique electronic transitions. These emissions are detected using a photomultiplier tube or a charge-coupled device (CCD), which records the intensity of light at selected wavelengths. The measured intensities are compared against those of calibration standards of known concentrations, allowing for the construction of calibration curves to determine the elemental concentrations in the sample.

Accurate analysis requires careful sample preparation. Solid materials, such as cathodes or separators, must be digested in strong acids (e.g., aqua regia or concentrated nitric acid) to convert them into a homogeneous solution. This solution is then diluted to ensure the elemental concentrations fall within the optimal detection range of the instrument, which normally lies below 1 ppm. As ICP-OES is a destructive technique, it can only be performed ex situ.

While ICP-OES offers reliable multi-element detection with reasonable sensitivity and throughput, inductively coupled plasma–mass spectrometry (ICP-MS) is often used when even higher sensitivity and lower detection limits are required. Like ICP-OES, ICP-MS uses an argon plasma to atomise and ionise the sample. However, instead of measuring emitted light, ICP-MS detects and quantifies ions based on their mass-to-charge ratio using a mass analyser, typically a quadrupole or time-of-flight detector.

2.6.2 X-ray Fluorescence (XRF)

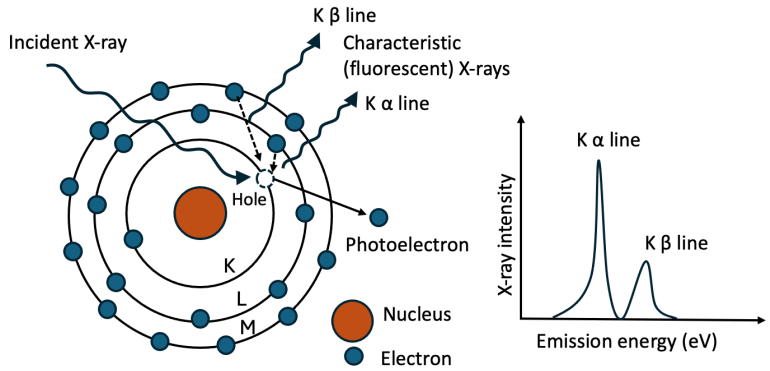

Figure 2.7 Schematic of X-ray excitation and the generation of characteristic fluorescent X-ray emission, illustrating the fundamental process of XRF analysis.

X-ray fluorescence spectroscopy is a non-destructive analytical technique used to determine the elemental composition of materials by detecting the characteristic secondary (fluorescent) X-rays emitted from a sample when it is irradiated with high-energy X-rays.[11] As shown in Figure 2.7, the fundamental principle involves the interaction of the incident radiation with the inner-shell electrons of atoms in the sample. When the primary X-ray beam strikes the material, it can eject core electrons (typically from the K shells) via the photoelectric effect, creating vacancies in the atom's inner orbitals. These vacancies are unstable, and electrons from higher energy levels (typically from the L, M shells) transition downward to fill them, releasing fluorescent X-rays whose energies are specific to the element and the electronic transition involved (e.g., Kα, Kβ lines).

The emitted X-rays are detected and analysed using an energy-dispersive (ED-XRF) spectrometer. In ED-XRF, a semiconductor detector measures the energy of the emitted photons, producing a spectrum in which the peak positions identify the elements present, and the peak intensities correspond to their relative concentrations. Recent advancements, such as micro-XRF, have enabled spatially resolved elemental mapping with micron-scale precision, greatly broadening the technique's applicability. Owing to its non-destructive nature, XRF is particularly well-suited for in situ analysis of elemental distribution in battery systems, providing critical insight into dynamic processes without compromising sample integrity.

2.7 Reference

1 Stein, A., Keller, S. W. & Mallouk, T. E. Turning down the heat: design and mechanism in solid-state synthesis. *Science* **259**, 1558-1564 (1993).

2 Morey, G. W. Hydrothermal synthesis. *J. Am. Ceram. Soc.* **36**, 279-285 (1953).

3 Driscoll, L. L. *et al.* Under pressure: offering fundamental insight into structural changes on ball milling battery materials. *Energy Environ. Sci.* **16**, 5196-5209 (2023).

4 Mohammed, A. & Abdullah, A. Scanning electron microscopy (SEM): A review. *Proceedings of the 2018 international conference on hydraulics and pneumatics—HERVEX,* ISSN 1454 - 8003 (2018).

5 Pennycook, S. J. & Nellist, P. D. *Scanning transmission electron microscopy: imaging and analysis*. (Springer Science & Business Media, 2011).

6 Wang, Z. L. New developments in transmission electron microscopy for nanotechnology. *Adv. Mater.* **15**, 1497-1514 (2003).

7 Pu, S., Gong, C. & Robertson, A. W. Liquid cell transmission electron microscopy and its applications. *R. Soc. Open Sci.* **7**, 191204 (2020).

8 Billinge, S. J. The rise of the X-ray atomic pair distribution function method: a series of fortunate events. *Philos. Trans. R. Soc. A* **377**, 20180413 (2019).

9 Iglesias-Juez, A., Chiarello, G. L., Patience, G. S. & Guerrero-Pérez, M. O. Experimental methods in chemical engineering: X-ray absorption spectroscopy—XAS, XANES, EXAFS. *Can. J. Chem. Eng.* **100**, 3-22 (2022).

10 Henderson, G. S., De Groot, F. M. & Moulton, B. J. X-ray absorption near-edge structure (XANES) spectroscopy. *Rev. Mineral. Geochem.* **78**, 75-138 (2014).

11 Acquafredda, P. XRF technique. *Phys. Sci. Rev.* **4**, 20180171 (2019).

3

3 Regulating Zinc Anode Behaviour in Aqueous ZIBs at Cathode-Compatible Current Densities

3.1 Introduction

Operating at high current densities (typically 20–200 mA cm^{-2}) has emerged as an effective strategy to enhance the plating/stripping efficiency of Zn anodes without requiring modifications to the electrolyte or electrode composition. High current operation induces a large nucleation overpotential, which promotes widespread nucleation events across the current collector. The resulting dense distribution of nucleation sites leads to the formation of a macroscopically uniform zinc layer with improved surface coverage. While this approach effectively mitigates dendrite formation and anode degradation, it poses a significant challenge when viewed from a full-cell perspective. Most cathodes used in aqueous ZIBs cannot sustain such high current densities due to limitations in ion transport, electronic conductivity, and interfacial kinetics.

To illustrate this high rate limitation for AZB cathodes, here we highlight some of the best performing cathodes in the current literature: (i) *Manganese-based oxides.* An α-MnO_2 nanorod cathode exhibited discharge capacities of 353 mAh g^{-1} at an areal current density of 0.0512 mA cm^{-2} (16 mA g^{-1}),[1] while mesoporous γ-MnO_2 has been reported to deliver a high discharge capacity of 285 mAh g^{-1} at an equivalent areal current rate of 0.05 mA cm^{-2}.[2] (ii) *Vanadium-based oxides*. V_2O_5 nanofibers have been shown to demonstrate a remarkable discharge capacity of 319 mAh g^{-1}, but at a low areal current density of 0.04 mA cm^{-2} (20 mA g^{-1}).[3] (iii) *Prussian blue analogues*. Zinc hexacyanoferrate, ZnHCF, has been shown to deliver a capacity of 65.4 mAh g^{-1} at 0.48 mA cm^{-2} (60 mA g^{-1}).[4] (iv) *Organic materials*. The conductive polymer polyaniline (PANI) supported on Ni foam has been found to reach up to 183.28 mAh g^{-1} capacity at a rate of 2.5 mA cm^{-2}.[5]

These examples illustrate that the current densities at which the four main cathode candidates operate are orders of magnitude lower than the high current densities

(>20 mA cm^{-2}) that have been proposed for stable anode deposition. Therefore, simply increasing the current density at the anode is unlikely to lead to overall performance gain when paired with current ZIB cathode materials in a full cell. While this could be solved by the development of new cathode materials, the divalent character of Zn^{2+} means designing new cathodes with speedier kinetics will be inherently challenging. It is therefore worthwhile to explore alternative approaches that enable uniform and dense Zn deposition under cathode compatible current densities, facilitating stable full-cell cycling without compromising overall energy storage performance.

This chapter proposed the application of pressure to improve the reliability of Zn plating and stripping processes under low to moderate current densities of 1 and 10 mA cm^{-2}. The pressure-induced force confinement in the z-direction restricts the orientation and growth of plated Zn, ultimately resulting in dense and uniform coverage that resembles that achieved by high current density plating. The influence of pressure on deposition mechanisms is examined by analysing changes in microstructure and macroscopic surface coverage. These results are correlated with the performance benefits typically associated with high-rate plating, demonstrating that pressure-assisted deposition provides a viable strategy for achieving stable cycling under current densities compatible with practical cathode operation.

As this work has been published in Advanced Materials, there is some overlap between the content of this chapter and the published manuscript. This chapter is reproduced from Ref. 6 with permission from the rights holder, Wiley.

3.2 Experimental Methods

Materials Preparation:

Synthesis of MnO_2 was achieved by taking $KMnO_4$ (98%, Alfa Aesar) and $Mn(CH_3COO)_2{\cdot}4H_2O$ (99%, Sigma-Aldrich) with a stoichiometric ratio of $KMnO_4$:$Mn(CH_3COO)_2{\cdot}4H_2O$ = 2:3 and were ground together in a mortar with a pestle. The mixture was then placed in a furnace and held at 100 °C for 12 h. After the reaction, the resulting black powder was rinsed by distilled water to remove residual unreacted salt, and dried at 70 °C for 12 h.

Electrochemistry:

Zn/Ti pouch cell tests: Zn/Ti cells were prepared to compare electrochemical performance with and without externally applied pressure across different current densities. Zn foil (0.25 mm and rolled to 0.18 mm thick, Sigma Aldrich) was cut to 5 mm × 5 mm squares and Ti foil (0.15 mm thick, Sigma Aldrich) was cut to 7 mm × 7 mm squares. The Zn/Ti pouch cells were assembled using prepared Zn foil and Ti foil with a glass fiber separator (10 mm × 10 mm, Whatman) soaked into 1 M $ZnSO_4$ (Sigma Aldrich). The cells were cycled under no external pressure and under various applied pressures of 1.2, 5.6 or 8.4 MPa. The external pressure was applied to the pouch cell via spring clamps. A piezoelectric load cell (OMEGA) was used to determine the clamping force of each spring clamp. Unless stated otherwise, cells were cycled with a fixed capacity of 1 mAh cm^{-2}, and the charging/discharging process was operated under constant current densities of 1, 10, 30, 60, 120 mA cm^{-2}. The cut off voltage for stripping was set at 0.6 V vs. Zn/Zn^{2+}.

Full-cell pouch cell assembly: Pouch cells were assembled using a Zn anode (0.18 mm thick foil), glass fiber separator, and 80 µL of 1 M $ZnSO_4$ electrolyte, with cathodes prepared from MnO_2, and V_2O_5 (98%, Sigma-Aldrich). For all cathodes, the active material, Super P carbon, and PTFE binder were mixed in a mass ratio of 7:2:1 and rolled onto Ti foil. The MnO_2 cathodes were fabricated with a film thickness of 50 µm, resulting in a loading of

approximately 3.6 mg cm^{-2}. The V_2O_5 cathodes were prepared with a film thickness of ~100 µm, resulting in loadings of 8.16 mg cm^{-2}. After assembly, external pressures of 0, 1.2, or 5.6 MPa were applied to the cells using calibrated spring clamps. Galvanostatic charging and discharging were performed at a current density of 1 A g^{-1}, and all electrochemical measurements were conducted at room temperature using a Biologic VMP3 potentiostat.

In-situ Characterisation:

In situ liquid cell TEM: A Protochips Poseidon 510 TEM holder was utilised for in situ liquid cell study. This holder facilitates real-time electrochemical observations within a thin electrolyte layer (1 M $ZnSO_4$) enclosed between two Si-SiN chips. The electrolyte was constantly flowed through the holder during the experiment with a flow rate of 120 µL h^{-1}, which is managed by a syringe pump. The chips featured three Pt electrodes (working, counter and reference electrodes) patterned onto them. The galvanostatic study was carried out between working and counter Pt electrodes using a Gamry Reference 600 potentiostat with current densities of 10 or 120 mA cm^{-2}. The driven current density is determined by dividing the total current applied by the exposed surface area of the Pt electrode, which is measured through SEM images. Notably, due to the small size of the electrode, this calculated current density might be amplified, and the actual current density could be lower due to any potential electrode roughness and porosity contributing to its effective area. The TEM imaging was executed using a JEOL 3000 TEM operating at 200 kV, utilising a 50 µm condenser aperture and a spot size of 2. Beam current calibration was achieved via a Faraday cup with 20 pA measured under this condition, corresponding to a low dose rate of 0.04 electrons $Å^{-2}$ s^{-1}. To minimise beam-induced damage, the total imaging time was confined to 30-60 s, and the beam was blanked during electrolyte replenishment. The recorded in situ liquid cell TEM videos and images were subsequently analysed using ImageJ software.

In situ optical microscopy: The in situ optical microscopy setup for Zn plating imaging was custom-built in-house. One side of a Ti foil was covered with tape, leaving the other side exposed for observing the Zn plating process. The experimental cell configuration involves a transparent cuvette housing a Ti foil as the working electrode (with the exposed side for optical microscopy), a Zn foil as the counter electrode, and a 1 M $ZnSO_4$ electrolyte solution. The galvanostatic test was conducted on a Gamry Reference 600 potentiostat with current densities of 10, 120 mA cm^{-2} with a capacity of 1 mAh cm^{-2}. Videos were recorded on the digital camera-included optical microscope (GXML 3030, GT Vision).

Ex-situ Characterisation:

Electroplated Zn on Zn foil and Ti foil cycled under different current densities (1, 10, 30, 60, 120 mA cm^{-2} with a capacity of 1 mAh cm^{-2}) without or with additional applied pressure (1.2, 5.6, 8.4 MPa) was recovered from pouch cells following cycling. The samples were rinsed with deionised (DI) water and ethanol, then dried at 50 °C for 12 h. The application of pressure made removing the glass fiber separator challenging, resulting in residual glass fibers remaining on the electroplated Zn recovered from cells cycled under pressure. This was more pronounced for cells cycled under higher pressure. The samples were then characterised using a Carl Zeiss Merlin SEM. XRD data were collected using a Cu source Rigaku 3 kW diffractometer.

Indentation Measurement:

Nanoindentation testing was used to determine the elastic modulus and hardness of electroplated Zn with and without applied pressure using an MTS nanoindenter XP with a diamond Berkovich tip calibrated against fused silica. Elastic modulus and hardness were calculated using the Oliver-Pharr method. 100 indentations were performed at different locations on each sample to obtain statistically significant results due to the uneven surface roughness. The tests are based on the method of ‘G-Series Hardness and Modulus via Cycles

Load Control'. The maximum load was controlled at 50 mN for each test. The loading/unloading speed was 3.33 mN s^{-1}. A 60-second holding was conducted at maximum load to investigate the creep behaviour.

Calculation of Relative Texture Coefficients (RTC):

$$\mathrm{RTC}_{(hkl)} = \frac{I_{(hkl)}/I_{0(hkl)}}{\sum I_{(hkl)}/I_{0(hkl)}} \times 100\%$$

where $I_{(hkl)}$ is the measured intensity of a plane (*hkl*), and $I_{0(hkl)}$ is the intensity of the plane (*hkl*) from the original sample, which is Zn foil in this case. It shows the main preferred orientations of Zn crystal.

3.3 Results and Discussion

3.3.1 Electrochemical Performance

To unravel the impact of external pressure on the Zn plating and stripping process, the electrochemical performance of asymmetric cells operated without and with different externally applied pressures were assessed. The asymmetric cell used Ti as the working electrode, Zn as the counter electrode, and 1 M $ZnSO_4$ as the electrolyte with glass fiber separators (Figure 3.1a). A Ti substrate was chosen for its anti-corrosion properties against the electrolyte (unlike stainless steel)[7] and its inability to form an alloy with Zn (unlike copper).[8] To compare the effects of pressure, a pouch cell was employed instead of a coin cell. Coin cells have intrinsic pressures ranging from 0.1 to 2 MPa between their electrodes due to the exertion of the deformed spring.[9-11] The inconsistent nature of the intrinsic pressure resulting from varying degrees of spring deformation may lead to inter-cell variability, yet the effect of this pressure is often overlooked since the stacking pressure is inherent to the coin cell's design. Pouch cells allow for the direct application of external pressure, providing more precise control over the experimental conditions, whereas the internal spring of a coin cell

prevents the selection of a specific pressure due to the inconsistent spring deformation. In this experiment, uniaxial pressure was applied to the pouch cell using spring clamps, with the applied pressure measured by a load cell sensor.

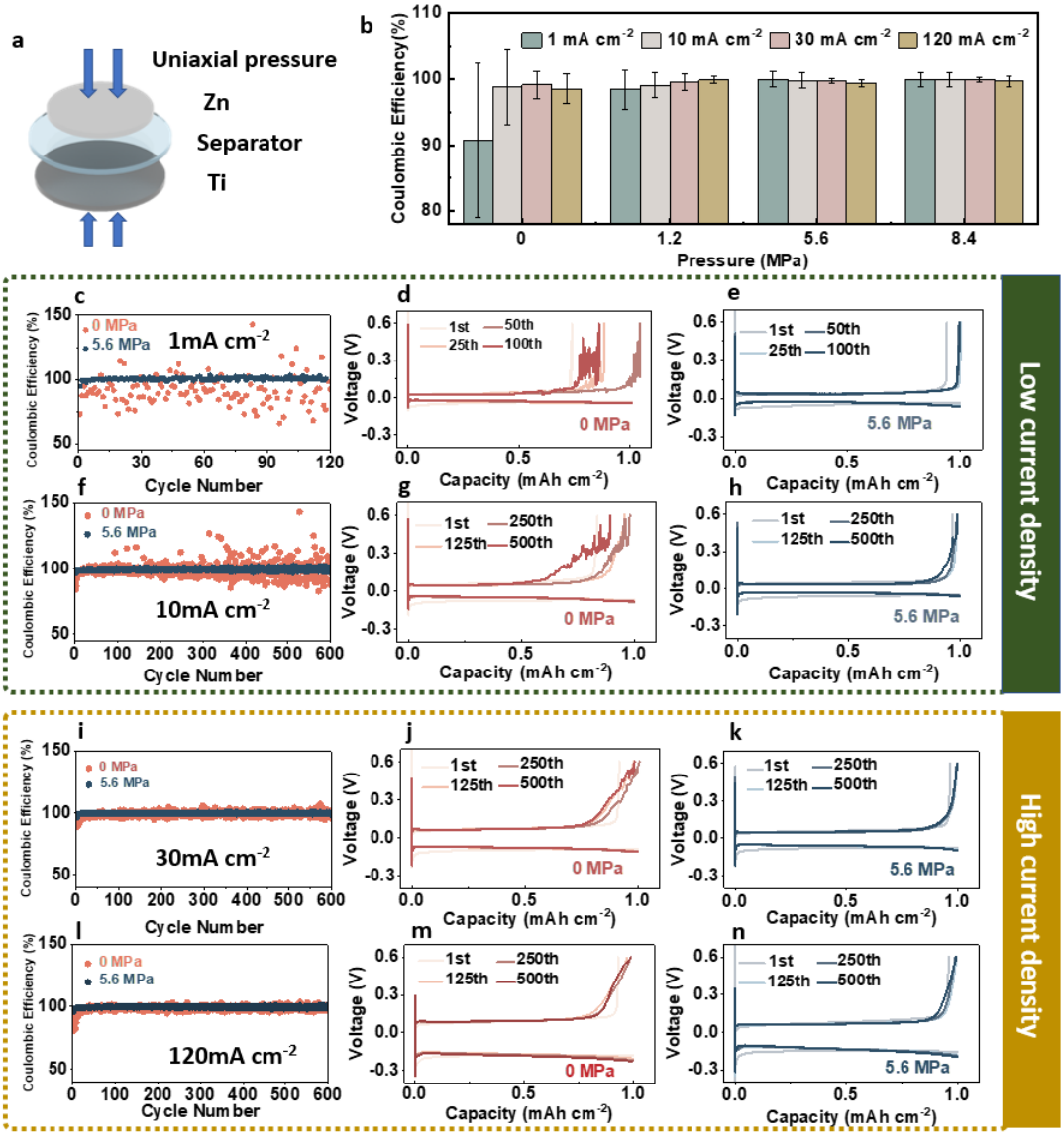

Figure 3.1 (a) Schematic of the asymmetrical cell which features a Zn/Ti configuration. (b) CE of the Zn/Ti cell under varied pressure of 0, 1.2, 5.6, 8.4 MPa. CE plotted against cycle number, along with the corresponding charging/discharging curves, under varying current densities: (c, d, e) 1 mA cm^{-2}, (f, g, h) 10 mA cm^{-2}, (i, j, k) 30 mA cm^{-2}, and (l, m, n) 120 mA cm^{-2} for both applied pressure of 5.6 MPa and no applied pressure conditions. All voltages are vs. Zn^{2+}/Zn.

The Zn plating and stripping performance was examined at applied uniaxial pressure of 0, 1.2, 5.6, 8.4 MPa, spanning a rate range of 1 to 120 mA cm^{-2} while maintaining a fixed

capacity of 1 mAh cm^{-2}. As shown in Figure 3.1b, increased pressure not only improves the CE, but also significantly reduced the inter-cycle variation in CE for all current densities. In the absence of applied pressure, the CE is low and exhibits significant fluctuations. The CE becomes notably more stable when the applied pressure was increased to 5.6 MPa, with a further increase of the pressure to 8.4 MPa appearing to offer minimal additional performance benefit. For the rest of this study, unless specified otherwise, an applied pressure of 5.6 MPa is used to investigate the influence of pressure on Zn plating and stripping performance.

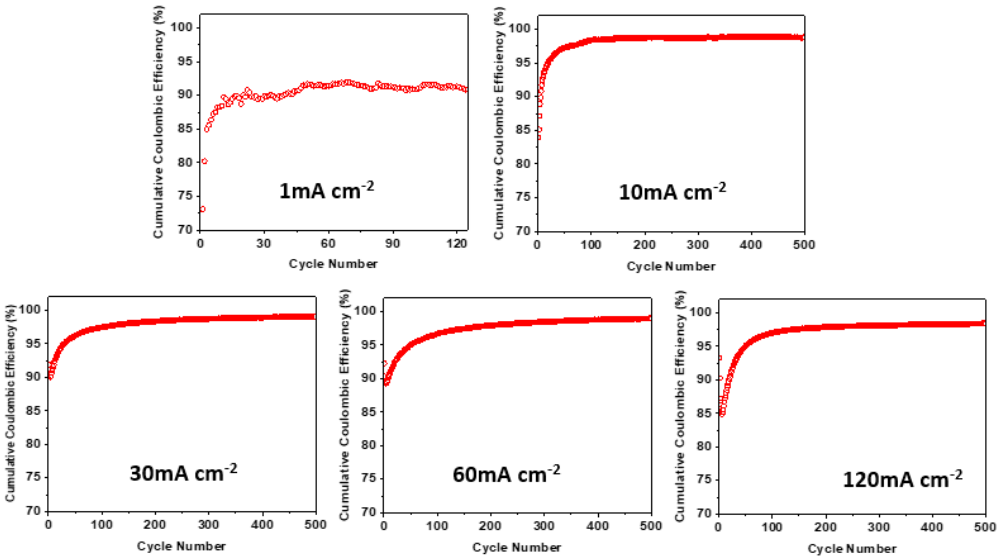

Figure 3.2 Cumulative coulombic efficiency versus cycle number data for Zn/Ti pouch cells tested without pressure under various current densities.

As shown in Figure 3.1c-n, the CE between cycles exhibited wide variation, especially with cells cycled at low current density, which is indicative of the cell losing and subsequently regenerating capacity from one cycle to the next.[12] This is due to the formation and subsequent reconnection of dead Zn, a phenomenon that has been proposed in Li metal batteries.[11,13] During the stripping process, fragments of Zn break off from the current collector, forming electrically isolated "dead" Zn. As this dead Zn is not stripped it lowers the CE. However, dead Zn has the potential to reconnect and recover in subsequent cycles, resulting

in an apparent increase in the stripping capacity and, consequently, an elevated cycle-to-cycle CE that can even exceed 100%. The lack of an electrically insulating interphase layer forming around dead Zn should make this effect significantly more common in aqueous ZIBs compared to other metal anode chemistries. The cumulative coulombic efficiency (CCE) was calculated to confirm no anomalous capacity was gained overall (Figure 3.2). The CCE considers the rolling sum of stripping capacities over all cycles relative to the sum of plating capacities over all cycles, and confirms that our observed stochastic high CEs are due to partial capacity recovery. Thus, stable CE cycling, that is a CE that does not vary from cycle to cycle, can be considered a signature of good plating and stripping performance with minimal dead Zn detachment. When there is no pressure applied to the cell, high current density leads to improved and stable CE.

From the data of Zn/Ti cells cycled under an applied pressure of 5.6 MPa (Figure 3.1c-n), it was found that subjecting the cycled cell to applied pressure significantly lowered the growth overpotential, with detailed values presented in Figure 3.4. This reduction in growth overpotential signifies that the application of pressure reduces the driving force required for Zn growth, making the growth in the deposition process more favourable. A marked difference was found in the extent of pressure-induced CE improvement at different current densities. At low current densities (1 and 10 mA cm^{-2}), the application of pressure significantly enhances the stripping efficiency and largely removed the inter-cycle CE variation. However, this improvement with pressure becomes less pronounced at higher current densities (30, 60, 120 mA cm^{-2}).

Table 3.1 The fluctuation of the CE measured as the average of CE values and standard deviation between cycles 0 and 120 for 1 mA m^{-2} and between 0 and 600 for 10, 30, 120 mA cm^{-2} (a) without pressure and with an applied pressure of (b) 1.2 MPa ,(c) 5.6MPa and (d) 8.4 MPa.

(a) Without pressure

Current density (mA cm^{-2})	Average CE (%)	Standard deviation of CE (%)
1	91.28	11.57
10	98.82	5.71
30	99.12	2.07
120	98.53	2.24

(b) With pressure of 1.2 MPa

Current density (mA cm^{-2})	Average CE (%)	Standard deviation of CE (%)
1	98.45	2.96
10	99.09	1.95
30	99.54	1.24
120	99.87	0.51

(c) With pressure of 5.4 MPa

Current density (mA cm^{-2})	Average CE (%)	Standard deviation of CE (%)
1	96.90	1.13
10	99.80	1.14
30	99.78	0.39
120	99.38	0.59

(a) With pressure of 8.6 MPa

Current density (mA cm^{-2})	Average CE (%)	Standard deviation of CE (%)
1	99.99	1.38
10	99.99	1.10
30	99.91	0.42
120	99.67	0.85

At a low current density of 1 mA cm^{-2}, the addition of pressure resulted in a significant enhancement and stability in stripping efficiency. The average CE stabilised at 96.90% with standard deviation of 1.13% when operated under pressure of 5.6 MPa. In contrast, without pressure the CE exhibited fluctuations, with an average of 91.28% and a larger standard deviation of 11.57% (as outlined in Table 3.1). The charging and discharging curves (Figure 3.1d) demonstrated that without pressure, the stripping curve exhibited irregularities and waves, indicating poor contact and the occurrence of severe side reactions. However, the

application of pressure resulted in smoother curves and reduced growth overpotential (Figure 3.1e).

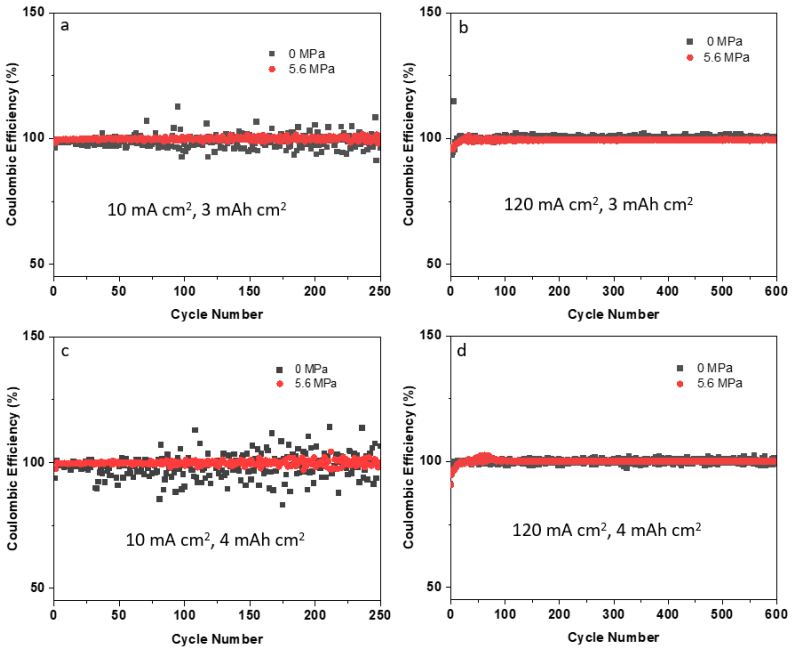

Figure 3.3 CE of the Zn/Ti cell at (a) 10 mA cm^{-2}, 3mAh cm^{-2}, (b) 120 mA cm^{-2}, 3 mAh cm^{-2}, (c) 10 mA cm^{-2}, 4 mAh cm^{-2}, (d) 120 mA cm^{-2}, 4 mAh cm^{-2} for both applied pressure of 5.6 MPa and no applied pressure conditions.

At a moderate current density of 10 mA cm^{-2}, the cells subjected to applied pressure also showed an improvement and stabilisation in CE (Figure 3.1f). However, as the current density increased to 30 mA cm^{-2} (Figure 3.1i), the impact of pressure was less, with the addition of pressure only slightly increasing the average CE from 99.12 to 99.78%, and standard deviation from 2.07 to 0.39%, compared with the no-pressure case. At an extremely high current density of 120 mA cm^{-2}, slight enhancements in CE were also observed with the application of pressure, indicating that stability of Zn deposition had already been largely achieved without the need for added pressure under these high-rate conditions (>30 mA cm^{-2}). Moreover, to validate the universality of these findings, the electrochemical performance was also assessed at higher capacities of 3 and 4 mAh cm^{-2} (Figure 3.3).

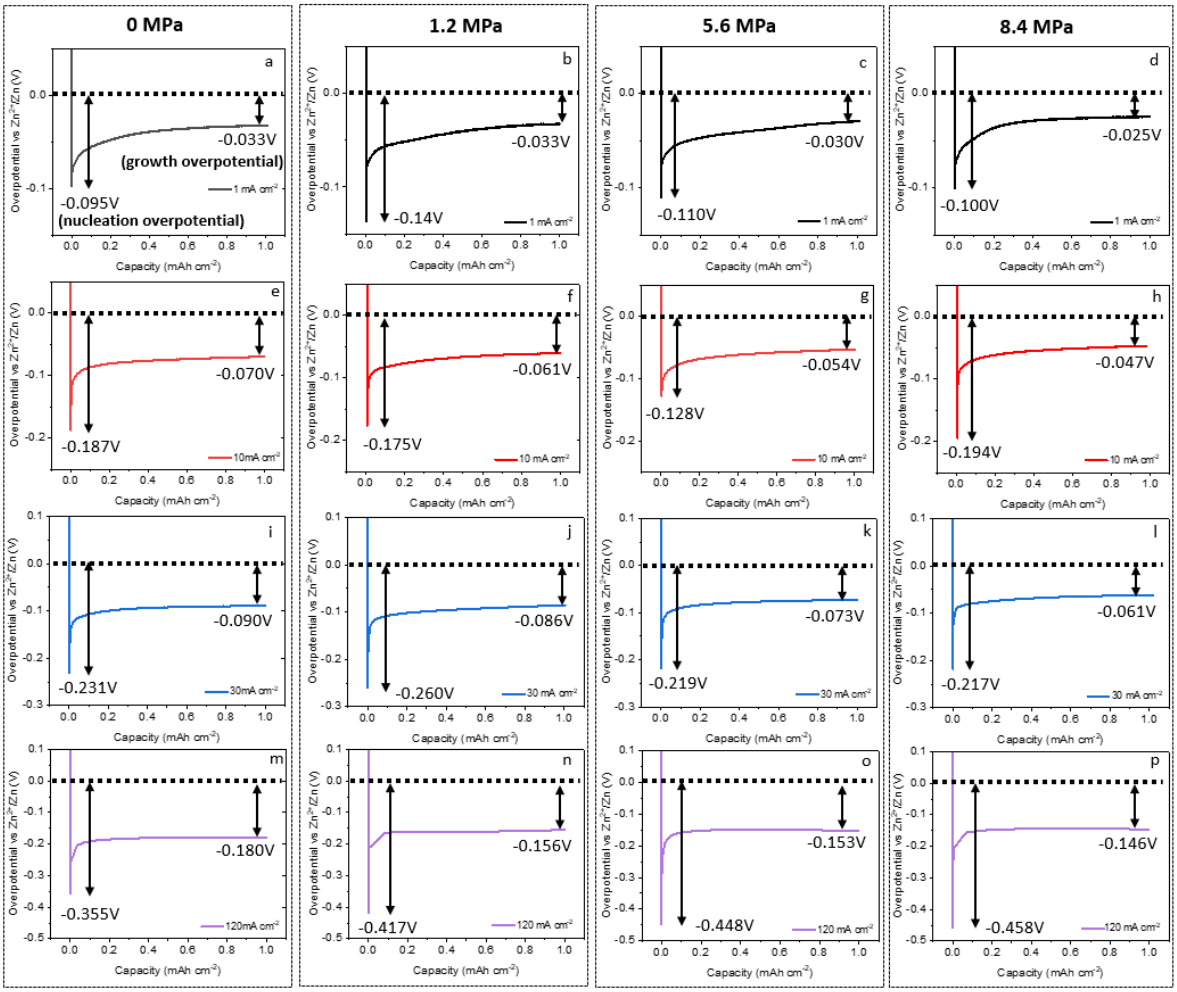

Figure 3.4 Voltage curves of Zn plating process at 1, 10, 30 and 120 mA cm^{-2} (a,e,i,m) without pressure and with pressure of (b,f,j,n) 1.2 MPa, (c,g,k,o) 5.6 MPa and (d,h,l,p) 8.4 MPa.

During the Zn plating process, the voltage profile typically exhibits two distinct overpotentials. As shown in Figure 3.4a, the voltage initially rises sharply as Zn^{2+} ions begin to reduce on the Zn metal surface. When the voltage reaches its peak, nucleation occurs, this point corresponds to the nucleation overpotential. Following nucleation, the voltage drops as the system transitions to the growth phase, which requires less driving force than initial nucleus formation. The subsequent plateau represents the growth overpotential, where Zn deposition proceeds more steadily. In later sections, this voltage profile will be frequently referenced to analyse and interpret the Zn deposition mechanism.

3.3.2 Microstructure Change

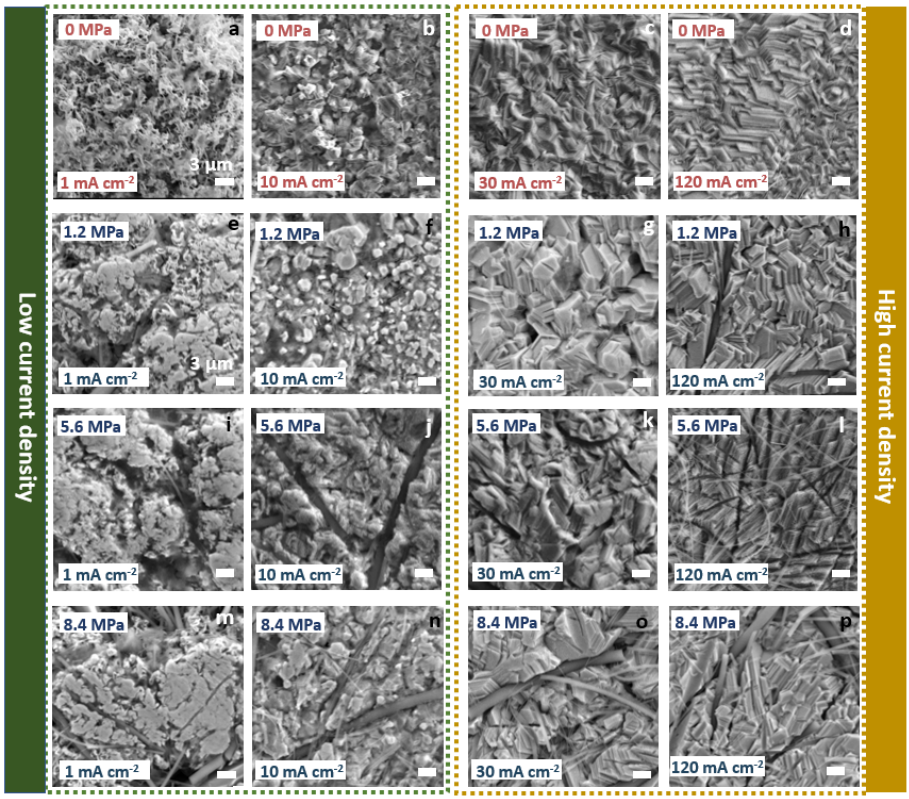

Figure 3.5 SEM images of Zn deposits on Zn foil under different plating conditions. (a–d) Without applied pressure at current densities of (a) 1 mA cm^{-2}, (b) 10 mA cm^{-2}, (c) 30 mA cm^{-2}, and (d) 120 mA cm^{-2}. (e–h) With applied pressure of 1.2 MPa at (e) 1 mA cm^{-2}, (f) 10 mA cm^{-2}, (g) 30 mA cm^{-2}, and (h) 120 mA cm^{-2}. (i–l) With applied pressure of 5.6 MPa at (i) 1 mA cm^{-2}, (j) 10 mA cm^{-2}, (k) 30 mA cm^{-2}, and (l) 120 mA cm^{-2}. (m–p) With applied pressure of 8.4 MPa at (m) 1 mA cm^{-2}, (n) 10 mA cm^{-2}, (o) 30 mA cm^{-2}, and (p) 120 mA cm^{-2}.

Post-deposition characterisation was undertaken to elucidate the mechanism by which pressure improved performance for low cycling rates. Zn foil was selected as the substrate for these measurements instead of Ti foil, as Zn deposits tend to peel away from Ti foil during cell disassembly after cycling under pressure, whereas they remain well-adhered to the Zn foil. Our characterisation demonstrates that pressure has a significant impact on the Zn deposition, encompassing alterations in the microstructure and deposition coverage.

SEM (Figure 3.5a-d) reveals significant transformations to the microstructure of the Zn deposit across different plating current densities under no applied pressure. At a low current

density of 1 mA cm^{-2}, the microstructure exhibits a highly porous mossy-like morphology that deviates from the expected HCP structure of Zn crystal. This mossy-like morphology, which normally forms under a low driving force (that is a low current density or low nucleation overpotential, as shown in Figure 3.4), has been attributed to "spiral" growth of crystalline Zn.[14] As the current density increases to 10 mA cm^{-2}, the Zn deposit undergoes a transition to a more well-defined crystalline morphology composed of particulate crystallites. The overall shape of Zn flakes conforms to the HCP structure, but the arrangement of Zn flakes appears to be random. However, when the current density reaches 30 mA cm^{-2}, the microstructure begins to present a densely packed Zn hexagonal morphology, which becomes even more pronounced as the current density is increased to 120 mA cm^{-2}.

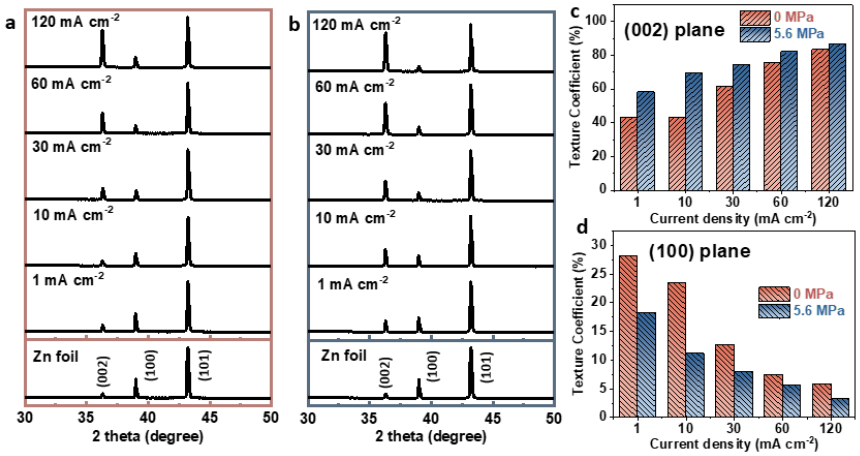

Figure 3.6 XRD of Zn electrodeposition of varying current densities when plating (a) without applied pressure and (b) with applied pressure of 5.6 MPa. The intensity of XRD is normalised using its maximum value. Comparison of texture coefficient of (c) Zn (002) plane and (d) Zn (100) plane of Zn deposit calculated from (a-b). The capacity of Zn deposition was fixed at 1 mAh cm^{-2} for all cells.

The morphology of plated Zn deposits formed under various pressures and at different current densities was investigated (Figure 3.5e-p). The application of pressure made removing the glass fiber separator challenging, resulting in the residual glass fiber seen in the images. Plating at a low current density (1 mA cm^{-2}) under pressure yields a Zn deposit with a denser

morphology and fewer voids. At a current density of 10 mA cm^{-2} the morphology of the Zn deposit undergoes significant flattening under pressure compared to the no applied pressure counterpart. However, at high current densities such as 30 and 120 mA cm^{-2}, the morphology of the deposited Zn is already densely packed without the need for additional pressure. Consequently, when Zn deposition takes place under pressure at high current densities, the morphology remains relatively unaffected, displaying only minor changes.

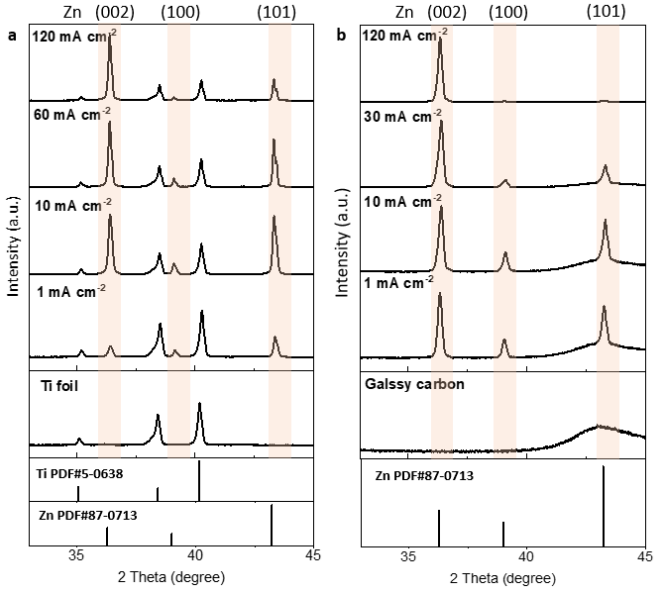

Figure 3.7 XRD of Zn electrodeposition of varying current densities when plating without applied pressure on (a) Ti foil and (b) glassy carbon.

The texture behaviour of the Zn deposited under varying current densities without applied pressure was studied using XRD, as shown in Figure 3.6a. The results demonstrate that as the depositing current density increases, the Zn deposit favours orienting in the (002) direction. This finding is consistent with recent work that attributed the (002) orientation preference to the high response nucleation overpotential during deposition at high current densities (Figure 3.4).[15,16] The high nucleation overpotential provides additional deposition energy, weakening the substrate effect and promoting the growth of non-epitaxial (002) Zn.[16] The influence of other substrates – Ti and glassy carbon – on the observed texturing behaviour

of the Zn deposit was also investigated. Regardless of the substrate used, the same trend was observed (Figure 3.7).

Based on the XRD result of plated Zn with and without applied pressure (Figure 3.6a-b), the RTC of Zn (002) and Zn (100) planes were calculated (Figure 3.6c-d), which provide insights into the preferred orientation of the plated Zn. The results demonstrate that the application of pressure leads to a preference for the (002) plane and a reduced favourability of the (100) plane in the plated Zn. Due to the anisotropic nature of the Zn crystal, different Zn planes correspond to different angles between the crystal and the substrate. Specifically, the (002) plane represents an angle of 0-30 degrees between the Zn crystal and the substrate, while the (100) plane represents an angle of 70-90 degrees.[17] RTC indicates that, while deposited under pressure, the plated Zn exhibits a stronger preference for growth along the basal plane, resulting in a flatter anode surface. These findings are consistent with the SEM images. Interestingly, the extent of the influence of applied pressure in encouraging orientation changes depends on the plated current density. At low current densities of 1 and 10 mA cm^{-2}, the RTC of Zn (002) increases by approximately 15% when depositing under pressure. In contrast, at high current densities of 30, 60, and 120 mA cm^{-2}, the increase in RTC of Zn (002) is less significant. RTC of the Zn (100) plane further confirms that the orientation changes are more pronounced at lower current densities compared to higher current densities.

Zinc exhibits pronounced elastic anisotropy, where its stiffness varies significantly with crystallographic orientation.[18] Consequently, when applying mechanical pressure during electrodeposition, individual grains of differing orientations will experience different elastic strains. Under a given applied stress, grains aligned along elastically stiffer directions store lower elastic strain energy, whereas grains oriented along elastically softer directions store more.[19] As the system evolves toward lower-energy states, this anisotropic distribution of

strain energy provides a thermodynamic driving force for texture evolution.[20] In this study, the application of external pressure favours grain orientations that minimise the total elastic strain energy. Consequently, under uniaxial pressure, grains with energetically unfavourable orientations, such as those associated with the (100) plane, are suppressed, while the low-strain-energy (002) orientation becomes increasingly dominant in the resulting microstructure.

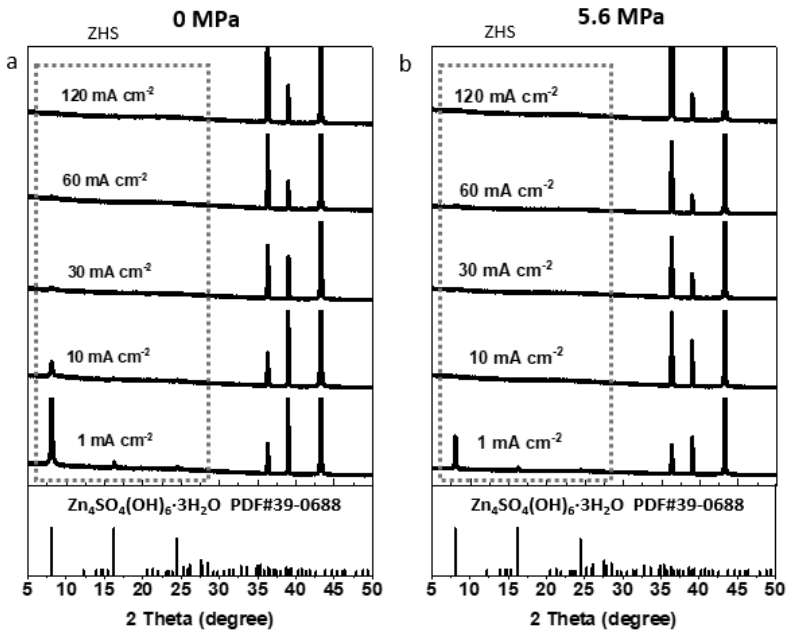

Figure 3.8 XRD of Zn electrodeposition of varying current densities when plating (a) without pressure and (b) with pressure of 5.6 MPa.

As shown in Figure 3.8, XRD also confirmed the formation of side product ZHS. The application of pressure was found to mitigate the formation of ZHS to some extent during Zn electrodeposition, as supported by the observation of reduced intensity of side product peaks in the XRD analysis. This is due to the influence of pressure on the microstructure and crystallographic orientation of the Zn deposit, which in turn affects its corrosion rate. Under pressure, the compacted microstructure has reduced contact surface area with the electrolyte, reducing the area available for side reactions. Additionally, different crystal planes of Zn exhibit varying resistance to corrosion by the electrolyte. The Zn (002) plane, which has low surface energy and high atomic density, inhibits Zn corrosion.[21] After applying pressure, the

Zn electrodeposition across different current densities becomes more oriented along the (002) plane. Both the pressure-induced microstructure and orientation modification contribute to the mitigation of side reactions.

Based on the results discussed above, it is evident that pressure plays a constructive role in enhancing plating and stripping efficiency. This effect is particularly pronounced at low plating current densities (1 and 10 mA cm^{-2}), and becomes less significant as current densities rise to 30 mA cm^{-2}. Our SEM images suggest this phenomenon is closely tied to the microstructure changes in Zn deposition, with cycling conditions linked to apparently denser morphologies yielding far less variation in CE. This is true regardless of the morphology being achieved by plating under pressure, or plating under high current density. This large variation in CE can be attributed to re-attaching of detached dead Zn, with the sparser and more tortuous plated morphologies more susceptible to this. However, SEM images of samples only provide a limited and inherently qualitative understanding of the integrity of an electroplated anode. To build a more complete understanding of how Zn deposition structure influences CE variation, the micro-scale mechanical properties of Zn deposition formed under different plating current density were investigated, allowing us to quantitatively ascertain which deposition morphologies were more or less susceptible to mechanical deformity.

3.3.3 Mechanical Properties of Electroplated Zn

The mechanical properties of electroplated Zn deposits were measured by nanoindentation with a Berkovich diamond tip, calibrated against fused silica. The experiments were conducted on Zn deposits prepared without pressure, and multiple indentations were performed at different locations on each sample to obtain statistically significant results. The indentation was performed to a maximum load of 50 mN with a hold time of 60 s at the peak load.

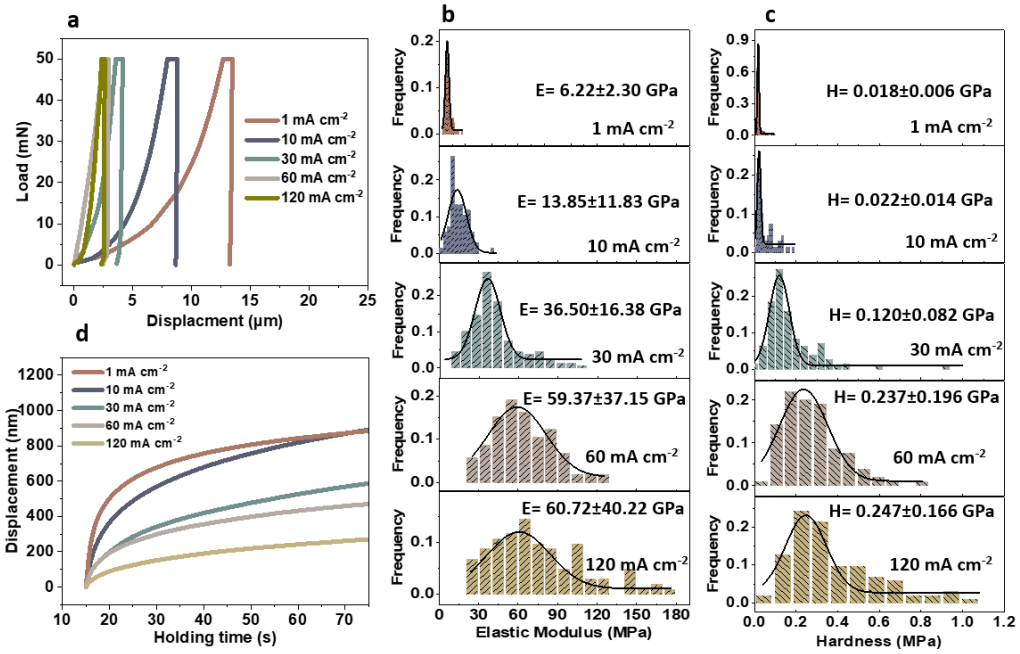

Figure 3.9 (a) The typical load displacement of Zn deposited at different current densities without external pressure. Distribution histogram of (b) elastic modulus and (c) the hardness of Zn deposit electrode. (d) The relations of creep depth with time during the holding time of 60 s. The fixed capacity of Zn sample preparation is 10 mAh cm^{-2}.

The fluctuation in the load-displacement curve can be attributed to the inherent heterogeneity of deposition microstructure. From these data, typical load-displacement curves (Figure 3.9a) were selected based on the expectation value of indentation depth using a Gaussian distribution. The loading and unloading curves indicate that during the loading process, the displacement increases and continues to increase during the holding time. Subsequently, upon unloading, the material demonstrates elastic recovery by several nanometres, signifying the dominance of plastic deformation over elastic deformation.[22,23] Notably, an upward trend can be observed in the maximum displacement depth as the plating current density is heightened. This correlation implies a connection between the plating current density and the observed mechanical response of the plated Zn.

The elastic modulus (*E*) and hardness (*H*) of the Zn deposit were determined using the Oliver-Pharr method,[24] and their distribution was described by fitting Gaussian functions

(Figure 3.9b-c). The results reveal that both the elastic modulus and hardness of the Zn deposit increase with higher plating current densities. Specifically, when deposited at low current densities like 1 and 10 mA cm^{-2}, the Zn deposit exhibits relatively lower modulus and hardness, which can be attributed to the compliance of the porous microstructure. However, at higher current densities, the Zn deposit demonstrates higher modulus and hardness due to the denser microstructure it acquires.

Figure 3.9d shows the indentation displacement of different samples during the maximum load holding time of 60 s, which indicates the creep behaviour of the plated Zn. It was found that the creep distance of the plated Zn decreases with increasing plating current density. This trend is related to the porosity of the Zn deposit, and similar results have been reported in other materials.[25-27] The presence of pores in a material can act as stress concentrators, accelerating the movement of dislocations and the diffusion of atoms, ultimately leading to an increase in the creep compliance.[22,25] Consequently, the high porosity characteristic of the deposited Zn at 1 mA cm^{-2} leads to heightened localised stress and increased creep deformation. Conversely, the low porosity of the deposited Zn at 120 mA cm^{-2} signifies reduced stress concentration and, therefore, diminished creep deformation.

As shown in Figure 3.10, under the applied pressure of 1.2 MPa, both elastic modulus and hardness of deposited Zn are enhanced compared to non-pressure samples across all current densities, indicating dense deposition. However, when the applied pressure reaches 5.4 MPa, there is an excessive amount of glass fiber residue on the deposited Zn (as shown in Figure 3.5), making it difficult to conduct nanoindentation tests.

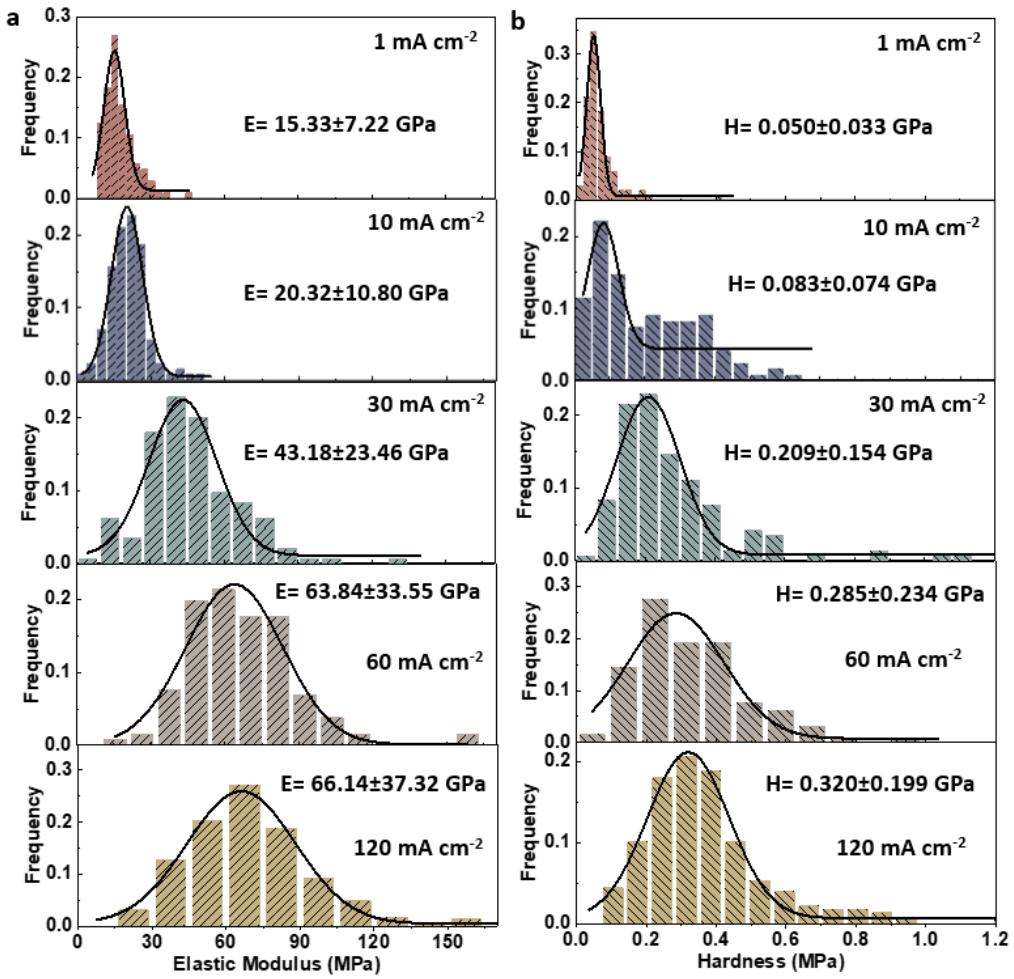

Figure 3.10 Distribution histogram of (a) elastic modulus and (b) the hardness of deposited Zn under applied pressure of 1.2 MPa.

The indentation tests comprehensively diagnose the mechanical properties of Zn plated under various current densities, and show these properties correlate with the distinct microstructures formed under the different current densities. The porous mossy features of Zn plated at low current densities render it susceptible to being squashed under pressure due to its low modulus and hardness. Conversely, the denser morphology of plated Zn at high current densities makes it more resistant to deformation, as evidenced by its elevated modulus and hardness. This explains how there are pronounced pressure-induced microstructural changes in Zn electroplated at low current densities, while minimal pressure effect is seen at high current densities.

3.3.4 Deposition Coverage Change

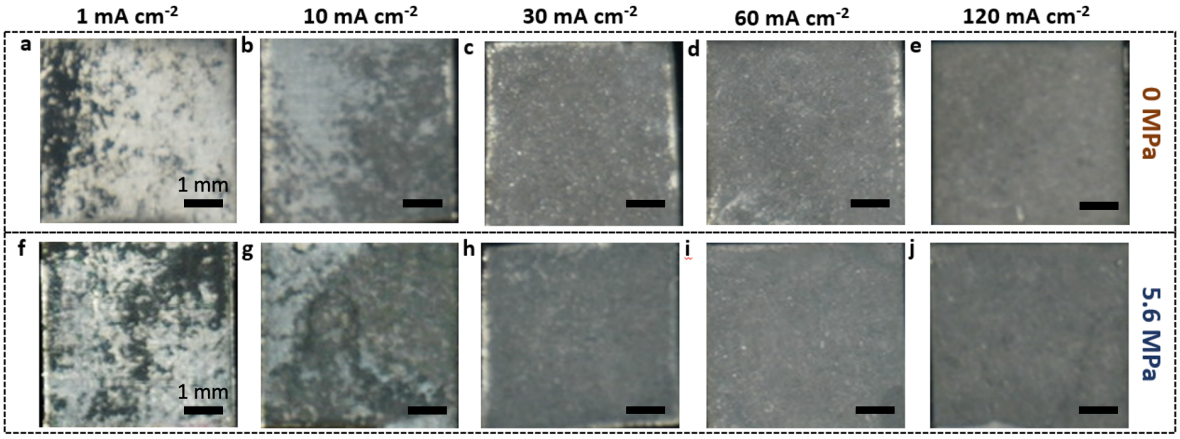

Figure 3.11 Photos of Zn electrodeposition on Zn foil at current densities of (a,f) 1, (b,g) 10, (c,h) 30, (d,i) 60, (e,j) 120 mA cm^{-2} under 0 MPa and 5.6 MPa. The darker area is electroplated Zn and the shining area is underlying Zn foil substrate.

In addition to the observed variations in microstructure influenced by current densities and applied pressure, there are distinct differences in macroscopic deposition coverage, as illustrated by the photographs of Zn foil in Figure 3.11. At low current densities of 1 and 10 mA cm^{-2}, Zn deposition appears sparse and unevenly distributed on the Zn foil. In contrast, at higher current densities ranging from 30 to 120 mA cm^{-2}, Zn deposition is more uniform, completely covering and concealing the underlying Zn foil. Notably, the application of pressure is seen to enhance this coverage. The extent that the current collector is covered following plating is an important macroscopic property, as it reflects the plating quality and is necessary to achieve optimal capacity and stripping efficiency. The analysis first focuses on how current density affects the macroscopic coverage of the current collector, then examines how this effect compares to the influence of applied pressure in achieving similar coverage.

In order to study the effect of current density on macroscopic coverage, in situ microscopy was conducted since due to its ability to capture the initial nucleation which are crucial in shaping the final morphology and coverage of zinc deposition. In situ

electrochemical liquid-cell TEM, allowed us to directly visualise these initial nucleation processes at the sub-microscale.[28] Electroplating from 1 M $ZnSO_4$ electrolyte on to a Pt working electrode was performed at 10 mA cm^{-2} (Figure 3.12a), and revealed a strong preference for nucleation along the electrode edges, as confirmed by the intensity profile taken across the electrode (Figure 3.12b). The coverage uniformity of Zn electrodeposition at high plating current density of 120 mA cm^{-2} (Figure 3.12c) showed nucleation sites were activated across both the edge and surface regions of the working electrode, with a consistent decrease in intensity across the whole electrode confirming this (Figure 3.12d).

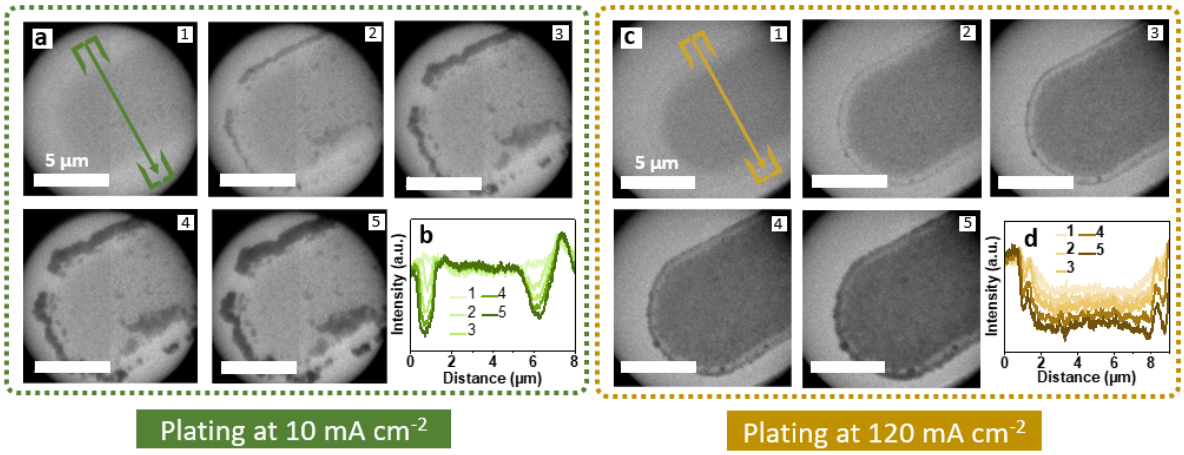

Figure 3.12 Liquid-cell TEM imaging of Zn electroplated on a Pt working electrode. (a) Galvanostatic Zn plating at 10 mA cm^{-2}. Annotation in panel 1 shows where box-averaged intensity profiles were acquired from each panel. (b) Intensity profiles extracted from the indicated area across panels 1 to 5 in Figure 3.12a. (c) Galvanostatic Zn plating at 120 mA cm^{-2}. (d) Intensity profiles extracted from panels 1 to 5 in Figure 3.12c. The circular border in the TEM images is from the TEM condenser aperture

At low current densities, the supplied extra nucleation energy is relatively small, leading to nuclei preferentially forming at locations where the energy conditions are most favourable.[29] In this case, the electrode's edges represent energetically-favourable sites due to the uneven distribution of the electric field.[30] This phenomenon is associated with the lower nucleation overpotential at low current densities. As plating current densities increase, the nucleation overpotential also rises (Figure 3.4), facilitating the formation of more nucleation

sites.[29,31-34] These many nucleation sites, not just limited to energetically preferred edge/defect locations, allow for high electroplated coverage across a whole electrode at high current densities.

In situ optical microscopy (OM) provides a much larger field of view for observing Zn deposition on Ti foil electrodes (Figure 3.13), complementing the higher-resolution observations from liquid-cell TEM. At high current densities, OM reveals a more uniform distribution of nucleation sites, resulting in a more homogeneous and continuous deposition layer.

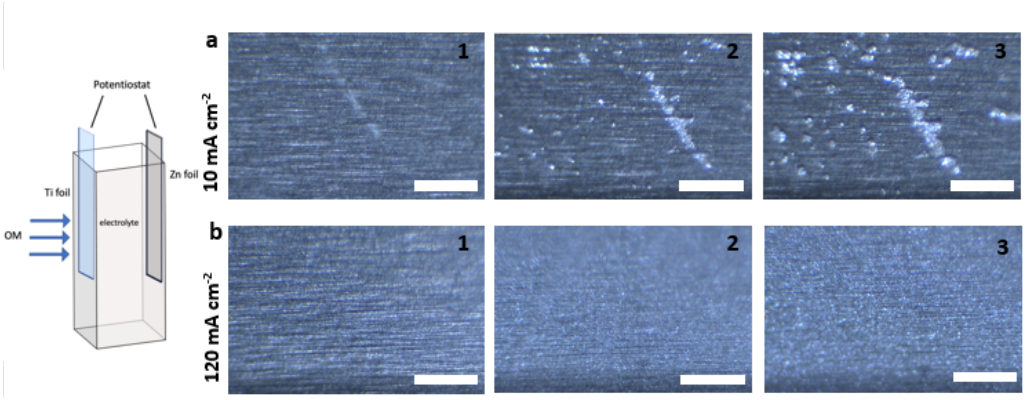

Figure 3.13 The in situ optical microscopy images of Zn electrodeposition in 1 M $ZnSO_4$ at a current density of (a) 10 mA cm^{-2} and (b) 120 mA cm^{-2} with a fixed capacity of 1 mAh cm^{-2}. The scale bar is 400 µm.

Electroplating under applied pressure, instead of at a high rate, was also found to improve electrode coverage, as shown in Figure 3.10. This is further supported by SEM of Zn electrodeposition plated at 10 and 120 mA cm^{-2} with and without pressure (Figure 3.14). Uneven Zn deposition at 10 mA cm^{-2} was largely removed by cycling under pressure (Figure 3.14b,d), offering an analogous result to cycling under a high 120 mA cm^{-2} current density (Figure 3.14g). This shows that the favourable coverage performance found when electroplating under high current densities may also be achieved at modest rates, as long as external pressure is applied to the cell. However, from the voltage profiles in Figure 3.4, the nucleation overpotential does not consistently increase with the application of pressure to

the cell, as it does with current density. This suggests that the mechanism that leads to good electrode coverage due to pressure application is distinct to the high nucleation rate found by plating at high current rates. Therefore, the improvement in coverage instead is due to pressure-induced changes to the growth stage of electrodeposition, rather than nucleation.

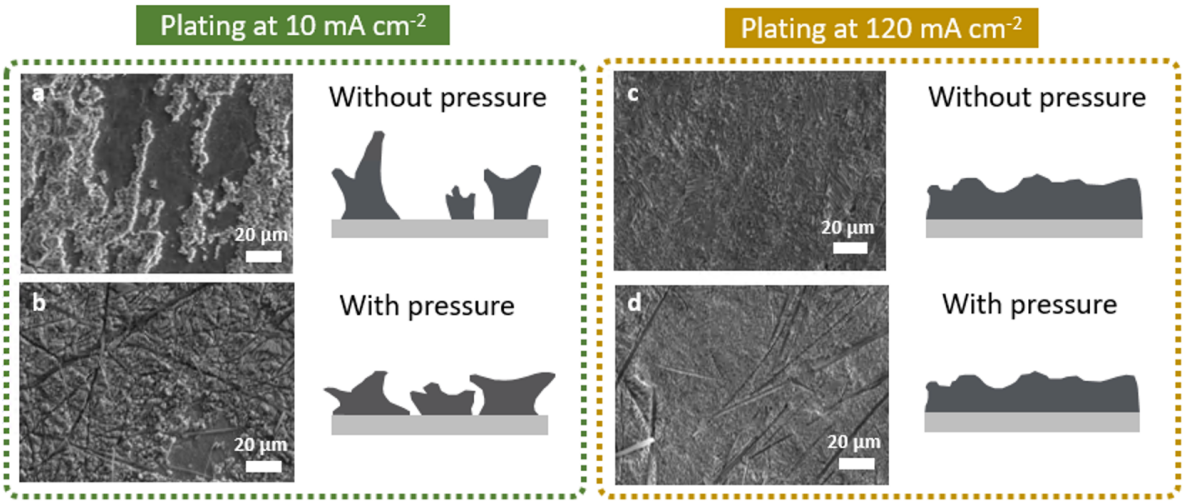

Figure 3.14 SEM image and schematic of Zn electrodeposition on Zn foil in pouch cell when deposited (a) without applied pressure at 10 mA cm^{-2}, (b) with applied pressure of 5.6 MPa at 10 mA cm^{-2}, (c) without applied pressure at 120 mA cm^{-2}, and (d) with applied pressure of 5.6 MPa at 120 mA cm^{-2}. The capacity of Zn deposited was fixed at 1 mAh cm^{-2}.

The differences in Zn coverage uniformity observed with and without applied pressure are attributed to similar effects found in previous Li and Na metal anode studies,[10,35,36] where the application of pressure changes the post-nucleation growth stage of the deposition. Without additional external pressure, Zn deposition grows freely in the vertical direction, perpendicular to the anode surface (Figure 3.14e, schematic). However, under external pressure, further deposited Zn tends to grow laterally along with the anode (Figure 3.14f), forcing coalescence of what would otherwise be spread out initial nucleation sites.[37,38] This behaviour is due to the additional force experienced by the dendrite as it comes up against the separator in a squeezed cell, causing further deposition along this interface to be energetically unfavourable due to increasing the compressive stress component of the

deposition's Gibbs free energy.[39] Zhang *et al*. used a mechano-electrochemical phase field model to reproduce metal deposition under various pressures, and found that there is maximum hydrostatic pressure at the tip of dendrite, which largely inhibits tip growth and promotes the lateral growth.[38] Further deposition occurs along the lateral interfaces, leading to improved surface coverage. This is reinforced by our mechanical measurements, which show that the electroplated structures deposited under low current rates are pliant and susceptible to be compressed over the electrode surface.

3.3.5 Full Cell Study

To demonstrate the practical utility of applying an external pressure, a standard full cell aqueous ZIBs configuration was assembled to show the effect of pressure on the performance of a Zn anode paired with a MnO_2 cathode. When comparing the performance of the full cell under different pressure conditions, it was observed that all three cells exhibited similar initial discharge capacities of approximately 74 mAh g^{-1} (Figure 3.15a-c). However, after undergoing 100 cycles, the cell without applied pressure experienced a severe capacity decline, retaining only 23.6% of its initial capacity. In contrast, the cell subjected to 1.2 MPa of applied pressure showed improved capacity retention of 59.2%, and the cell cycled under 5.6 MPa of pressure demonstrated remarkable performance, retaining an impressive 99.3% of its initial capacity (Figure 3.15d).

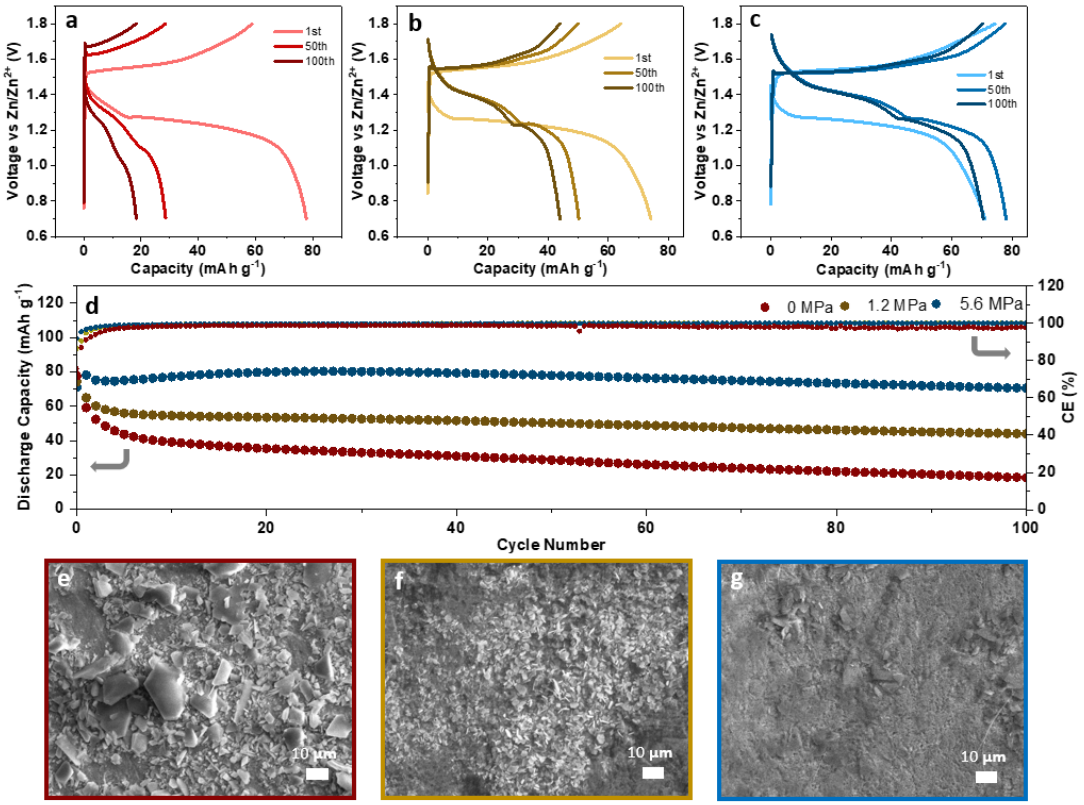

Figure 3.15 The charging/discharging curve of a Zn/MnO_2 pouch cell with loading mass of 3.6 mg cm^{-2} in 1 M $ZnSO_4$ electrolyte cycled at 3.6 mA cm^{-2} (1 A g^{-1}) (a) without external pressure, (b) with 1.2 MPa pressure, and (c) with 5.6 MPa pressure. (d) The cycling performance of a Zn/MnO_2 pouch cell under different pressures. (e-g) SEM images of the Zn anode after cycling 100 times (e) without external pressure, (f) with 1.2 MPa applied pressure, and (g) with 5.6 MPa applied pressure.

To further investigate the influence of pressure on the Zn anode, the Zn/MnO_2 full cell was disassembled, and the status of the Zn anode was examined using SEM. The SEM images in Figure 3.15e revealed that in the absence of pressure, there were noticeable clusters of large Zn flakes present on the surface of the anode. However, when pressure was applied, the Zn anode appears to have a flatter and compacted surface (Figure 3.15f-g), which is consistent with prior half-cell anode studies.

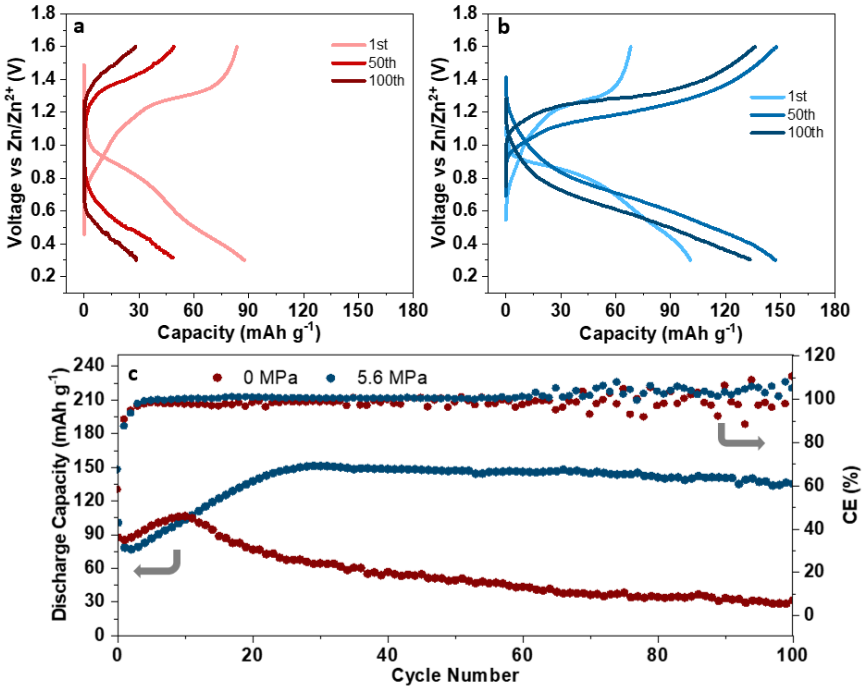

Figure 3.16 The charging/discharging curve of a Zn/V_2O_5 pouch cell with loading mass of 8.16 mg cm^{-2} with 1 M $ZnSO_4$ electrolyte cycled at 8.16 mA cm^{-2} (1 A g^{-1}) (a) without external pressure, (b) with 5.6 MPa pressure. (d) The cycling performance of a Zn/V_2O_5 pouch cell under different applied pressures.

To verify the compatibility of cell pressurisation across different full cell types, full cells with other cathode materials V_2O_5 was also studied. As shown in Figure 3.16, the cells subjected to externally applied pressure exhibited better capacity retention compared to those without applied pressure. The initial increase in capacity may be attributed to structural changes within the cathode. According to previous studies,[40] during the initial cycling process, the insertion of water molecules and H^+ ions activates V_2O_5, transforming it into a hydrated phase, $V_2O_5 \cdot nH_2O$. This hydrated phase serves as the host material for subsequent cycling. The expanded interlayer spacing in $V_2O_5 \cdot nH_2O$ compared to pristine V_2O_5 facilitates Zn insertion and enhances structural stability. Further confirmation of this transformation could be obtained through ex situ XRD analysis.

Overall, these results highlight the significant impact of pressure on the performance and stability of ZIB full cell. The application of pressure plays a crucial role in maintaining the

structural stability of the Zn anode, potentially mitigating the formation of detrimental Zn flakes and improving overall cell performance.

3.4 Conclusion

Electroplating Zn metal anodes under externally applied pressure enables durable repeatable cycling under cathode-compatible areal current densities of between 1 and 10 mA cm^{-2}. This is due to the pressure-induced morphology changes of the deposited structures, resulting in a Zn microstructure that is more robust to metal detachment during stripping. This limits anode degradation from both dead Zn formation and corrosion losses. Mechanical microstructure measurements show that Zn electroplated under cathode-compatible areal current densities is more pliant to compression-induced deformation, hence the significant improvement in cycling performances found when electroplating under pressure with these lower rates. These pliant electrodeposited Zn structures also permit well anode coverage when plated under pressure, comparable to plating under high rates, due to the restriction of zinc growth outward from the electrode and instead confining it to the electrode plane. These findings are reflected in drastically improved full-cell cycling performances when they are operated under applied pressure. While applying pressure in the practical application presents challenges, lessons learned from solid-state batteries, which require external pressure to enhance cell cyclability, suggest that it may be feasible to implement pressure by packing cells in large stacks within appropriate metallic cases.

3.5 Reference

1 Alfaruqi, M. H. *et al.* Enhanced reversible divalent zinc storage in a structurally stable α-MnO_2 nanorod electrode. *J. Power Sources* **288**, 320-327 (2015).

2 Alfaruqi, M. H. *et al.* Electrochemically Induced Structural Transformation in a γ-MnO_2 Cathode of a High Capacity Zinc-Ion Battery System. *Chem. Mater.* **27**, 3609-3620 (2015).

3 Chen, X., Wang, L., Li, H., Cheng, F. & Chen, J. Porous V_2O_5 nanofibers as cathode materials for rechargeable aqueous zinc-ion batteries. *J. Energy Chem.* **38**, 20-25 (2019).
4 Zhang, L., Chen, L., Zhou, X. & Liu, Z. Towards high-voltage aqueous metal-ion batteries beyond 1.5 V: the zinc/zinc hexacyanoferrate system. *Adv. Energy Mater.* **5**, 1400930 (2015).
5 Xia, Y., Zhu, D., Si, S., Li, D. & Wu, S. Nickel foam-supported polyaniline cathode prepared with electrophoresis for improvement of rechargeable Zn battery performance. *J. Power Sources* **283**, 125-131 (2015).
6 Li, Z. *et al.* Achieving Planar Zn Electroplating in Aqueous Zinc Batteries with Cathode-Compatible Current Densities by Cycling under Pressure. *Adv. Mater.* **36**, 2401576 (2024).
7 Wu, G. *et al.* The pitfalls of using stainless steel (SS) coin cells in aqueous zinc battery research. *Energy Environ. Sci.* **16**, 4320-4325 (2023).
8 Liu, B. *et al.* Novel 3D nanoporous Zn–Cu alloy as long-life anode toward high-voltage double electrolyte aqueous zinc-ion batteries. *Small* **16**, 2001323 (2020).
9 Liu, H.-W. *et al.* A Comparative Study of Polycrystal/Single-Crystal $LiNi_{0.8}Co_{0.1}Mn_{0.1}O_2$ in All-Solid-State Li-Ion Batteries with Halide-Based Electrolyte under Low Stacking Pressure. *Energy Technol.* **11**, 2201439 (2023).
10 Jiao, W. *et al.* Critical Role of Pressure for Chemo-Mechanical-Induced Stability of Sodium Metal Battery Anodes. *ACS Energy Lett.* **8**, 2711-2717 (2023).
11 Harrison, K. L. *et al.* Effects of Applied Interfacial Pressure on Li-Metal Cycling Performance and Morphology in 4 M LiFSI in DME. *ACS Appl. Mater. Interfaces* **13**, 31668-31679 (2021).
12 Mohammadi, A. *et al.* Assessing Coulombic Efficiency in Lithium Metal Anodes. *Chem. Mater.* **35**, 2381-2393 (2023).
13 Harrison, K. L. *et al.* Cryogenic electron microscopy reveals that applied pressure promotes short circuits in Li batteries. *iScience* **24**, 103394 (2021).
14 Yi, Z. *et al.* Decoding the Mechanisms of Reversibility Loss in Rechargeable Zinc-Air Batteries. *Nano Lett.* **23**, 7642-7649 (2023).
15 Zhang, J. *et al.* Nonepitaxial Electrodeposition of (002)-Textured Zn Anode on Textureless Substrates for Dendrite-Free and Hydrogen Evolution-Suppressed Zn Batteries. *Adv. Mater.* **35**, e2300073 (2023).
16 Yuan, W. *et al.* Realizing Textured Zinc Metal Anodes through Regulating Electrodeposition Current for Aqueous Zinc Batteries. *Angew. Chem. Int. Ed.* **62**, e202218386 (2023).
17 Guo, S. *et al.* Fundamentals and perspectives of electrolyte additives for aqueous zinc-ion batteries. *Energy Storage Mater.* **34**, 545-562 (2021).
18 Nagy, K. S. & Siegel, D. J. Anisotropic elastic properties of battery anodes. *J. Electrochem. Soc.* **167**, 110550 (2020).
19 Seibert, P., & Susmel, L., Berto, F., Kästner, M. Razavi, N. Applicability of strain energy density criterion for fracture prediction of notched PLA specimens produced via fused deposition modeling. *Eng. Fract. Mech.* **258**, 108103 (2021).
20 Wen, Y. et al. Stacking Pressure Modulated Deposition and Dissolution of Zinc Anode. *Small* **21**, 2501242 (2025).
21 Zhou, M. *et al.* Surface-Preferred Crystal Plane for a Stable and Reversible Zinc Anode. *Adv. Mater.* **33**, e2100187 (2021).

22 Wang, Y., Dang, D., Xiao, X. & Cheng, Y.-T. Structure and mechanical properties of electroplated mossy lithium: Effects of current density and electrolyte. *Energy Storage Mater.* **26**, 276-282 (2020).
23 Wang, Y., Dang, D., Wang, M., Xiao, X. & Cheng, Y.-T. Mechanical behavior of electroplated mossy lithium at room temperature studied by flat punch indentation. *Appl. Phys. Lett.* **115**, 043903 (2019).
24 Oliver, W. C. & Pharr, G. M. An improved technique for determining hardness and elastic modulus using load and displacement sensing indentation experiments. *J. Mater. Res.* **7**, 1564-1583 (2011).
25 Krstic, V. & Erickson, W. Effect of porosity and stress concentration associated with pores on elastic creep by crack growth in brittle solids. *J. Mater. Sci.* **23**, 4097-4102 (1988).
26 Kováčik, J. Correlation between Young's modulus and porosity in porous materials. *J. Mater. Sci. Lett.* **18**, 1007-1010 (1999).
27 Biener, M. M. *et al.* ALD functionalized nanoporous gold: thermal stability, mechanical properties, and catalytic activity. *Nano Lett.* **11**, 3085-3090 (2011).
28 Yuan, Y., Pu, S. D., Gao, X. & Robertson, A. W. The application of in situ liquid cell TEM in advanced battery research. *Energy Mater.* **3**, 300032 (2023).
29 Hou, Z., Gao, Y., Zhou, R. & Zhang, B. Unraveling the Rate-Dependent Stability of Metal Anodes and Its Implication in Designing Cycling Protocol. *Adv. Funct. Mater.* **32**, 2107584 (2021).
30 Mehdi, B. L. *et al.* Observation and quantification of nanoscale processes in lithium batteries by operando electrochemical (S)TEM. *Nano Lett.* **15**, 2168-2173 (2015).
31 Zhang, Z., Zhou, X. & Liu, Z. Optimization of lithium nucleation by current density toward dendrite-free Li metal anode. *J. Alloys Compd.* **893**, 162389 (2022).
32 Pei, A., Zheng, G., Shi, F., Li, Y. & Cui, Y. Nanoscale Nucleation and Growth of Electrodeposited Lithium Metal. *Nano Lett.* **17**, 1132-1139 (2017).
33 Liu, H. *et al.* Understanding and Controlling the Nucleation and Growth of Zn Electrodeposits for Aqueous Zinc-Ion Batteries. *ACS Appl. Mater. Interfaces* **13**, 32930-32936 (2021).
34 Biswal, P., Stalin, S., Kludze, A., Choudhury, S. & Archer, L. A. Nucleation and Early Stage Growth of Li Electrodeposits. *Nano Lett.* **19**, 8191-8200 (2019).
35 Sun, J. *et al.* Lithium deposition mechanism on Si and Cu substrates in the carbonate electrolyte. *Energy Environ. Sci.* **15**, 5284-5299 (2022).
36 Kazyak, E. *et al.* Understanding the electro-chemo-mechanics of Li plating in anode-free solid-state batteries with operando 3D microscopy. *Matter* **5**, 3912-3934 (2022).
37 Fang, C. *et al.* Pressure-tailored lithium deposition and dissolution in lithium metal batteries. *Nat. Energy* **6**, 987-994 (2021).
38 Shen, X., Zhang, R., Shi, P., Chen, X. & Zhang, Q. How Does External Pressure Shape Li Dendrites in Li Metal Batteries? *Adv. Energy Mater.* **11**, 2003416 (2021).
39 He, Y. *et al.* Origin of lithium whisker formation and growth under stress. *Nat. Nanotechnol.* **14**, 1042-1047 (2019).
40 Li, R., Zhang, H., Zheng, Q. & Li, X. Porous V_2O_5 yolk–shell microspheres for zinc ion battery cathodes: activation responsible for enhanced capacity and rate performance. *J. Mater. Chem. A* **8**, 5186-5193 (2020).

4

4 Understanding the Role of Mn Electrolyte Additives in Aqueous Zn/MnO_2 Batteries

4.1 Introduction

Many studies have claimed that introducing Mn^{2+} additives into the electrolyte can suppress MnO_2 degradation. The intent is to shift the disproportionation equilibrium ($2Mn^{3+} \rightarrow Mn^{2+} + Mn^{4+}$) and suppress further Mn dissolution by stabilising Mn^{2+}.[1] This strategy has become widespread in the field, with numerous reports demonstrating substantial improvements in cycling performance from including Mn electrolyte additive.[2-5] However, emerging evidence challenges this interpretation. Recent operando and ex situ studies suggest that Mn^{2+} can actively participate in the charge storage process.[5] This duality renders the role of Mn^{2+} ambiguous, and raises critical questions about the nature of MnO_2 dissolution: Is it inherently detrimental, or is it an essential component of the redox cycle? If both solid-phase MnO_2 and Mn^{2+} additive contribute to capacity, how can their individual contributions be decoupled and quantified? Does the Mn^{2+} electrolyte additive genuinely suppress cathode dissolution or does it merely compensate for it, acting as a Mn reservoir? These unresolved questions are central to how MnO_2-based AZIBs are designed, evaluated, and interpreted.

In this chapter, the electrochemical role of Mn^{2+} additives in Zn/MnO_2 batteries was systematically investigated based on electrochemical profiling and characterisation method with operando XRF mapping.

By decoupling capacity contributions, it is found that Mn^{2+} additives have no effect during the initial discharge. However, during the first charge, Mn^{2+} significantly contributes to capacity. Over long-term cycling, Mn^{2+} additives improve cycling stability, but not by suppressing Mn dissolution. Instead, the Mn^{2+} additives act as a soluble redox reservoir, supplying additional active material during charging. For instance, in a typical CR2032 cell with 140 µL of electrolyte, 0.1 M and 0.4 M Mn^{2+} additive correspond to ~1.23 mg and ~4.92 mg of MnO_2-equivalent active material, respectively. This artificially inflates coulombic efficiency

and masks the irreversible losses originating from the MnO_2 cathode, giving the false impression of long-term cycling stability. However, the additive does not address the cathode's irreversible degradation.

Our results identify capacity fading persists regardless of Mn^{2+} additive inclusion, arising from two fundamental degradation mechanisms: incomplete MnO_2 dissolution during discharge, and incomplete Mn^{2+} redeposition during charge. These inefficiencies result in the partial utilization of both the solid-state MnO_2 cathode and the soluble Mn^{2+} additive active material, limiting the full electrochemical potential of the system.

4.2 Experimental Methods

Materials Preparation:

Synthesis of Alpha Phase MnO_2:

Alpha-phase MnO_2 was synthesised using the hydrothermal method. Solution A was prepared by dissolving 0.486 g $KMnO_4$ (98%, Alfa Aesar) in 60 mL of DI water and magnetically stirring for 30 minutes. Solution B was prepared by dissolving 1.135 g $Mn(CH_3COO)_2{\cdot}4H_2O$ (99%, Sigma-Aldrich) in 20 mL of DI water and stirring for 30 minutes. Solution B was added to Solution A and stirred for 60 minutes. The resulting mixture was then transferred to a 100 mL Teflon autoclave and heated at 120 °C for 12 h. After the reaction was complete, the powder was rinsed with DI water and vacuum dried at 70 °C for 12 h.

Synthesis of Delta Phase MnO_2:

Delta-phase MnO_2 was synthesised using the hydrothermal method. Solution A was prepared by dissolving 1.98 g $KMnO_4$ (98%, Alfa Aesar) in 40 mL of DI water and magnetically stirring for 30 minutes. Solution B was prepared by dissolving 0.336 g $MnSO_4{\cdot}H_2O$ (99%, Sigma-Aldrich) in 40 mL of DI water and stirring for 30 minutes. Solution B was added to Solution A

and stirred for 60 minutes. The resulting mixture was then transferred to a 100 mL Teflon autoclave and heated at 160 °C for 24 h. After the reaction was complete, the powder was rinsed with DI water and vacuum dried at 70 °C for 12 h.

Electrochemistry:

The free-standing MnO_2 cathode film was prepared by thoroughly mixing MnO_2, acetylene black carbon (99.9+%, Thermo Scientific Chemicals), and PTFE in a mass ratio of 7:2:1 using a pestle and mortar. The resulting mixture was mechanically rolled into a film approximately 0.1 mm thick. For the operando XRF cells, MnO_2 film samples were cut into 0.5 × 0.5 mm^2 pieces, each weighing about 2.3 mg. In the operando XRF experiments, all cathode films were prepared with a consistent mass of 2.3 mg to ensure comparability between samples. In the operando cell, a Zn metal anode was used, with an electrolyte volume of 50 µL and two layers of separators (0.6 × 0.6 mm^2) incorporated. For coin cells, CR2032 were assembled using an anode, MnO_2 film (5-10 mg), and two layers of glass fiber separators (22 mg each) soaked in 140 µL of electrolyte. Three electrolyte compositions were investigated: 1 M $Zn(CF_3SO_3)_2$, 1 M $Zn(CF_3SO_3)_2$ with 0.1 M $Mn(CF_3SO_3)_2$, and 1 M $Zn(CF_3SO_3)_2$ with 0.4 M $Mn(CF_3SO_3)_2$. Zinc trifluoromethanesulfonate ($Zn(CF_3SO_3)_2$, 98%, Sigma-Aldrich) and manganese trifluoromethanesulfonate ($Mn(CF_3SO_3)_2$, 95%, Sigma-Aldrich) were used as received. All electrochemical tests were performed at room temperature using a Maccor Series 4000 battery tester.

In-situ Characterisation:

An MTI operando cell was employed to monitor Mn and Zn species in real time during electrochemical cycling. The cell configuration consisted of a Zn anode, an α-MnO_2 cathode, and an electrolyte soaked into two stacked separators. Due to the compact design, the separators were sized at 6 mm × 6 mm, and the total electrolyte volume was limited to 50 µL.

As a result of this reduced electrolyte volume, the electrochemical performance of the operando cell differs from that of a conventional coin cell. Three electrolyte formulations were investigated in this setup: 1 M $Zn(CF_3SO_3)_2$, 1 M $Zn(CF_3SO_3)_2$ + 0.1 M $Mn(CF_3SO_3)_2$, and 1 M $Zn(CF_3SO_3)_2$ + 0.4 M $Mn(CF_3SO_3)_2$. A Kapton film was applied to the top of the cell to ensure X-ray transparency.

Operando micro-XRF (μ-XRF) mapping was carried out at the PolyX beamline1 at SOLARIS National Synchrotron Radiation Centre. A monochromatic X-ray beam from the 1.3 T bending magnet was generated using a Si<111> water cooled double crystal monochromator. The beam was focused to a 5 μm spot using ellipsoidal monocapillary optics (Sigray) with a 20 nm-thick Pt inner coating and a 20 mm working distance. Samples were mounted on a motorised translation stage system to perform 2D raster scans with 15μm scan step. X-ray fluorescence spectra were acquired using two Hitachi Vortex EM360 silicon drift detectors (ML3.3 extreme, 25 μm Be windows, 0.5 mm Si sensor thickness, 100 mm^2 active area), each coupled to an XGlab Dante digital pulse processor. The detectors were positioned in a backscatter geometry (45° from the sample surface), with the incident beam oriented normal to the sample. 2D elemental maps were collected in continuous scan mode for horizontal motion and point-by-point for vertical motion. Count rates within the selected energy regions of interest were normalised by the detectors' live time and the incident beam intensity, measured using an ionisation chamber. Data from the two detectors were summed with appropriate scaling, accounting for their relative sensitivity to Mn and Zn signals.

Micro-XAS data at PolyX beamline were collected from the separator during cell operation after each XRF mapping was taken using focusing monocapillary optics (Sigray) with 5μm focal spot. All electrochemical measurements were performed at room temperature using a Gamry potentiostat.

Ex-situ Characterisation:

The ex-situ characterisation was conducted on MnO_2 film or powder samples after charging/discharging to specific states of charge and disassembly from coin cells. The cathode film or powder was thoroughly rinsed several times with DI water to remove any residual electrolyte, followed by vacuum drying at 70 °C.

Powder X-ray diffraction (PXRD) was performed using a Rigaku Miniflex diffractometer with Cu Kα1 radiation. The PXRD data were analysed using the Rietveld refinement method with GSAS-II software.

SEM images were obtained using a Carl Zeiss Merlin field emission scanning electron microscope. HRTEM was carried out using a JEOL JEM-2100 operating at 200 kV.

Hard XAS was conducted at beamline BM28 XMaS of the ESRF (European Synchrotron Radiation Facility) synchrotron source. In BM28, XAS measurements were performed in transmission yield. The beamline optics consists of an LN_2 cooled Si <111> monochromator, as the primary optical element, followed by toroidal mirror focusing the beam onto the sample. Oken ion chambers were used to record both the “I0” and “It” absorption spectra.

For ICP-OES analysis of the electrolyte, the separator closest to the anode side was collected, while the separator near the cathode side was discarded due to residual cathode material. The separator was soaked in concentrated nitric acid for 3 days, then diluted with 2% nitric acid prior to ICP-OES analysis. The sample preparation was carried out by me, while the measurements were performed by Dr. Lijiang Song at the university of Warwick.

4.3 Results and Discussion

4.3.1 Electrochemical Performance

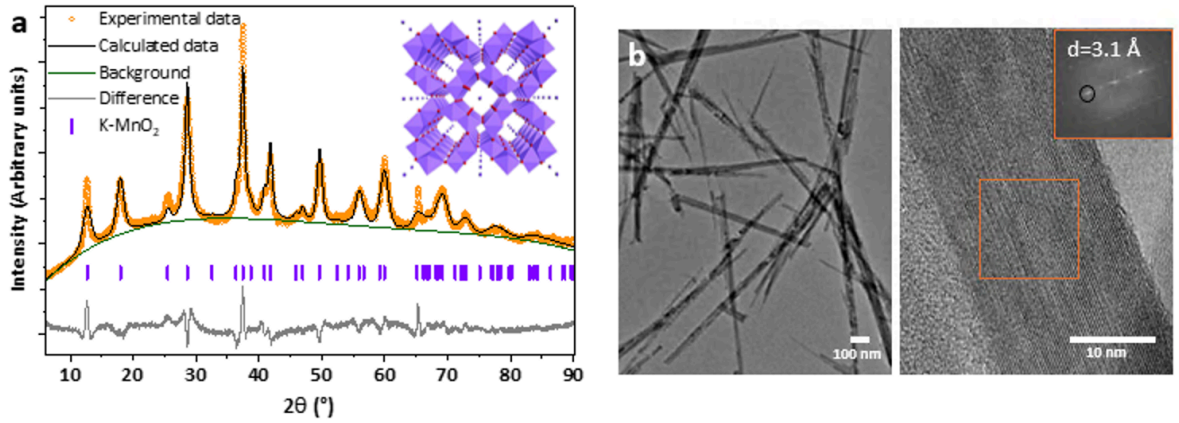

Figure 4.1 (a) Rietveld refinement of the XRD pattern of α-MnO_2, showing a tunnel structure with K^+ ions and refined using the I4/m space group. (b) HRTEM images of α-MnO_2 nanorods.

To investigate and decouple the relative roles of Mn^{2+} electrolyte additive and the MnO_2 cathode, the α-MnO_2 cathode was studied in aqueous ZIBs. The α-MnO_2 polymorph was selected due to its relatively high capacity and extensive prior study, making it a compelling starting point. α-MnO_2 was synthesised via a hydrothermal method using $KMnO_4$ and $Mn(CH_3COO)_2$ as precursors. This synthesis route inherently introduces residual K^+ ions into the tunnel structure of α-MnO_2, as confirmed by Rietveld refinement of the XRD pattern with the I4/m space group (Figure 4.1a). HRTEM images reveal that the synthesised α-MnO_2 exhibits a nanorod morphology, with rod lengths of several micrometers and widths of approximately 10 nanometers (Figure 4.1b). The high magnification HRTEM (Figure 4.1b) shows a lattice spacing of 3.1 Å, which correlates with the (130) plane diffraction data.

To directly monitor Mn spatial dynamics in electrolyte during electrochemical cycling and to resolve the respective contributions of Mn^{2+} additives and the MnO_2 cathode, it is essential to monitor Mn content in the electrolyte in real time during battery operation. Conventional techniques, such as ICP-OES and ultraviolet-visible (UV-Vis) spectroscopy, have

some limitations. ICP-OES requires disassembling the cell and destroying the separator, making it incompatible with operando measurements. Operando UV-Vis spectroscopy experiments would typically require a significant electrolyte volume (~ml) to reliably measure concentrations, skewing the electrolyte to electrode ratio well beyond that found in a practical cell.[6,7] In this work, operando XRF spectroscopy is employed to enable real-time, element-specific quantification of Mn directly within the electrolyte during cycling. Our operando cell closely replicates the structure of a coin cell, enabling tracking of Mn content in a representative setup.

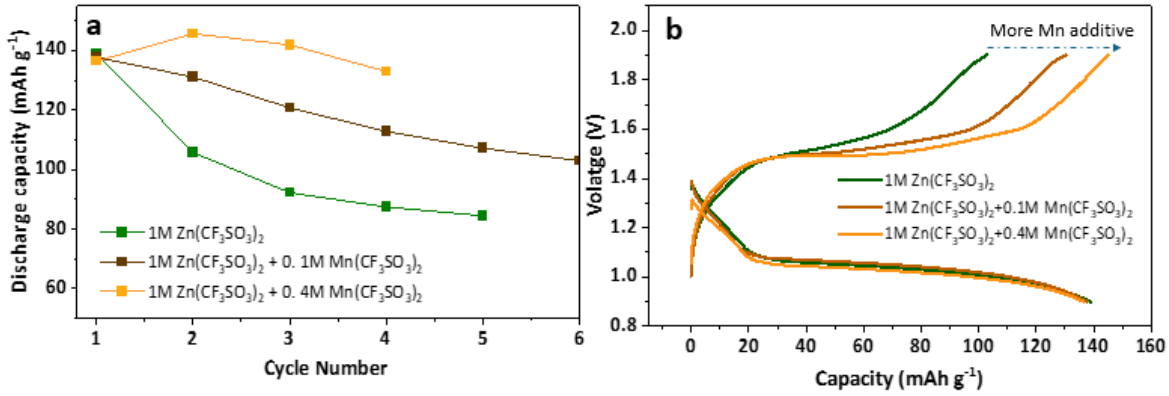

Figure 4.2 (a) Cycling performance (discharge capacity) of operando electrochemical cells with α-MnO_2 cathodes in three different electrolytes: 1 M $Zn(CF_3SO_3)_2$, 1 M $Zn(CF_3SO_3)_2$ + 0.1 M $Mn(CF_3SO_3)_2$, and 1 M $Zn(CF_3SO_3)_2$ + 0.4 M $Mn(CF_3SO_3)_2$. (b) First-cycle voltage profiles of α-MnO_2 cathodes in the three electrolytes. The cells are operated at a current density of 100 mA g^{-1}.

The cycling performance of this operando electrochemical cell used for XRF is shown in Figure 4.2a. α-MnO_2 cathodes were tested in three electrolytes: a baseline of 1 M $Zn(CF_3SO_3)_2$, and two modified electrolytes containing Mn^{2+} additives at concentrations of 0.1 M and 0.4 M, respectively. As expected, increased Mn^{2+} additive concentrations lead to improved cycling performance, a commonly observed phenomenon in aqueous Zn/MnO_2 cells.[2-5] This improvement is often attributed by the literature to the added Mn^{2+} suppressing Mn dissolution from the cathode, thereby enhancing stability.[8]

However, our electrochemical curve of the first cycle challenges this conventional interpretation (Figure 4.2b). Across all three electrolyte conditions, the initial discharge capacities are nearly identical, suggesting that Mn^{2+} additives do not significantly alter the discharge process. However, the first charge capacities increase markedly with higher Mn^{2+} additive concentrations. This divergence in charge capacity indicates that Mn^{2+} additives may play an active electrochemical role during charging. Similar first cycle charge and discharge behavior resulting from including Mn additive has been reported in the literature.[9-12] These observations suggest that the enhanced cycling performance may stem from a distinct mechanism involving Mn^{2+}, which will be further explored through operando XRF analysis in Figure 4.6 to elucidate the dynamics of Mn dissolution and deposition.

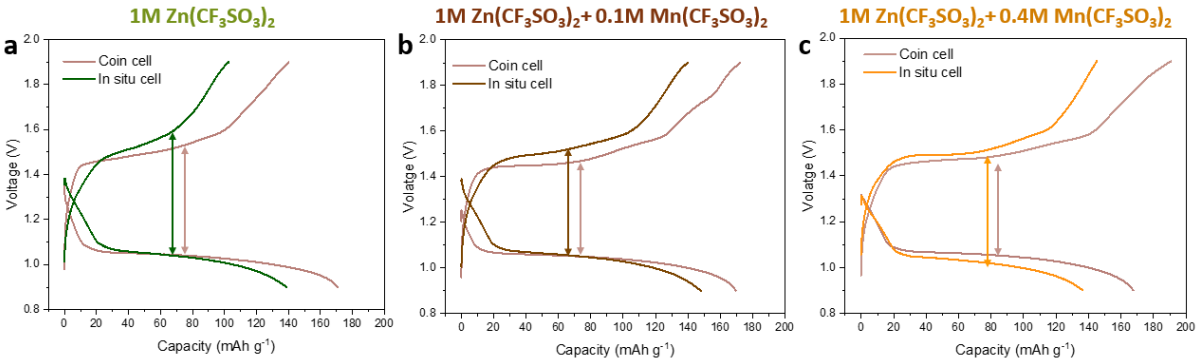

Figure 4.3 Comparison of the first-cycle performance of α-MnO_2 in coin cells and operando cells at a current density of 100 mA g^{-1} in the following electrolytes: (a) 1 M $Zn(CF_3SO_3)_2$, (b) 1 M $Zn(CF_3SO_3)_2$ + 0.1 M $Mn(CF_3SO_3)_2$, and (c) 1 M $Zn(CF_3SO_3)_2$ + 0.4 M $Mn(CF_3SO_3)_2$.

To validate that the electrochemical behaviour observed in the operando cell is representative of coin cell performance, a direct comparison between the two configurations is presented in Figure 4.3 and 4.4. The difference in electrochemical performance between the coin cell and operando cell primarily arise from differences in stack pressure and electrolyte volume. Coin cells benefit from higher stack pressure, resulting in reduced polarisation, as shown in Figure 4.3. Additionally, discharge capacity is strongly linked to the MnO_2 dissolution process, which is pH-dependent. The larger electrolyte volume in the coin

cell provides more protons at the same concentration, allowing more MnO_2 to dissolve before reaching pH equilibrium, thereby yielding a higher discharge capacity.

However, when comparing the first-cycle load curves and long-term cycling performance of the coin and operando cells, the trends align well, which is shown in Figure 4.4. All three electrolyte conditions exhibit similar first-cycle discharge capacities, and the 0.4 M Mn^{2+} additive leads to a higher charge capacity in both configurations. These consistent trends confirm that our operando cell is representative and suitable for investigating the fundamental role of Mn^{2+} additives in aqueous Zn/MnO_2 batteries.

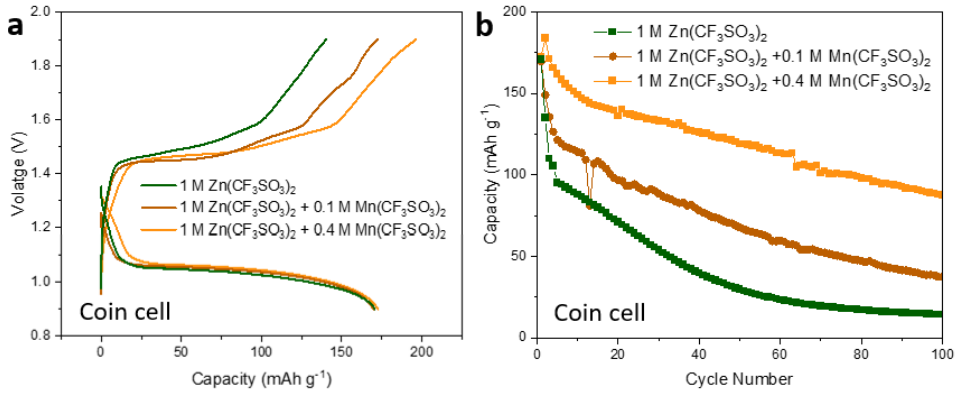

Figure 4.4 (a) First-cycle voltage profiles of α-MnO_2 cathodes in coin cells using different electrolytes. (b) Cycling performance (discharge capacity) of coin cells with α-MnO_2 cathodes in three electrolytes: 1 M $Zn(CF_3SO_3)_2$, 1 M $Zn(CF_3SO_3)_2$ + 0.1 M $Mn(CF_3SO_3)_2$, and 1 M $Zn(CF_3SO_3)_2$ + 0.4 M $Mn(CF_3SO_3)_2$. All cells were cycled at a current density of 100 mA g^{-1}.

4.3.2 Mn Dynamics at First Cycle

To diagnose the role of Mn^{2+} additives, operando microprobe XRF mapping was employed to monitor the spatial and temporal variations of Mn and Zn concentrations, focusing particularly on the first cycle. XRF operates by detecting characteristic fluorescence X-rays emitted by the sample when irradiated with a primary X-ray beam. The beam size used was 5 µm, allowing high spatial resolution mapping of Mn and Zn distribution within the separator. With a penetration depth in the micrometer range,[13] XRF is well-suited for

capturing representative changes in elemental concentrations within the separator. The beamline setup is shown in Figure 4.5a. Figure 4.5b-c presents a schematic of the transverse-type cell design, which features an exposed anode-electrolyte-cathode cross-section to enable direct probing of the electrolyte region. The average Mn and Zn concentrations were derived from the XRF maps across the electrolyte cross-section between anode and cathode. The lateral line feature visible across the middle of the operando XRF maps is a result of the two-layer separator (Figure 4.5b).

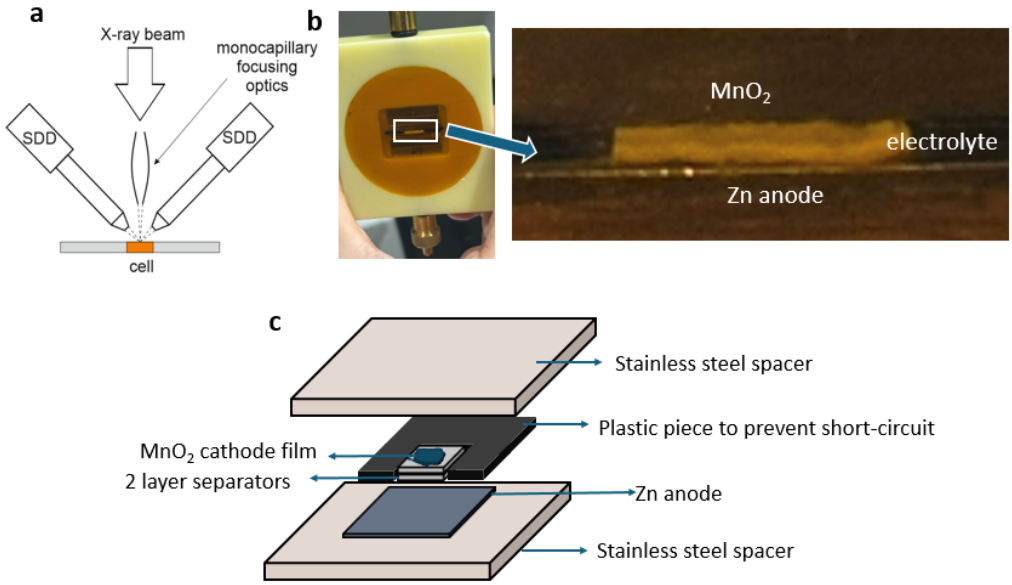

Figure 4.5 (a) Schematic of the beamline setup for the operando cell. (b) Photograph of the operando cell, with an inset showing the two-layered separators, which contribute to the distorted line observed in XRF mapping results. (c) Detailed schematic illustrating the assembly of the operando cell.

In the baseline 1 M $Zn(CF_3SO_3)_2$ electrolyte, α-MnO_2 undergoes dissolution during the first discharge, leading to a noticeable increase in Mn^{2+} concentration within the electrolyte (Figure 4.6a). Initially, the Mn^{2+} concentration was negligible, but during the first discharge, it increased to approximately 0.1 M. Given an electrolyte volume of 50 µL, the mass of MnO_2 dissolved into the electrolyte during the first discharge to yield this concentration increase would be 0.44 mg. Considering the initial MnO_2 mass was 2.3 mg, this dissolution represents

approximately 18.9 wt% of the initial material. Assuming the entire discharge capacity (137 mAh g^{-1}) originates from the MnO_2/Mn^{2+} redox dissolution reaction, which has a theoretical capacity of 618 mAh g^{-1}, the theoretical dissolved MnO_2 fraction would be approximately 22.2 wt%. The discrepancy between the theoretical dissolution (22.2 wt%) and the experimentally observed value (18.9 wt%) suggests that additional charge storage mechanisms, such as Zn^{2+} intercalation, also contribute to the overall capacity. This will be further confirmed in Figure 4.10. Nevertheless, the majority of the discharge capacity, around 85%, can be attributed to the MnO_2 dissolution process. This dissolution is reversible, as Mn^{2+} concentration decreases during charging due to redeposition of Mn. However, a residual Mn concentration of ~0.04 M remains even at the end of charging, suggesting incomplete redeposition, which contributes to the low coulombic efficiency (charge capacity/discharge capacity) observed during the first cycle in the baseline electrolyte.

For the electrolyte with a moderate Mn additive concentration of 0.1 M $Mn(CF_3SO_3)_2$ (Figure 4.6b), it is found that the Mn concentration trends closely resemble those observed in the baseline electrolyte. During the first discharge, the Mn concentration change remains approximately 0.1 M, indicating that the presence of Mn additive does not alter the Mn dissolution extent. However, after the first charge, the Mn concentration exhibits significant reversibility, attributed to the involvement of the pre-added Mn^{2+} in the oxidative deposition process.

To clarify this behaviour, a higher Mn additive concentration of 0.4 M was also studied (Figure 4.6c). Consistent with previous observations, the amount of MnO_2 dissolved during the first discharge remains unchanged. Interestingly, after the first charge, the Mn concentration decreases to 0.33 M, even lower than the initial pristine value of 0.36 M. This net consumption of Mn^{2+} directly explains the observed first-cycle coulombic efficiency

exceeding 100%. The excess Mn^{2+} present in the initial electrolyte contributes additional charge capacity via electrodeposition ($Mn^{2+} \rightarrow MnO_2$) during charging. Although coulombic efficiencies above 100% during the first cycle are frequently reported in aqueous Zn/MnO_2 batteries with Mn additive in the electrolyte,[2,5,14,15] the underlying mechanisms have not been extensively studied. The operando XRF mapping provides direct evidence and insight into this process.

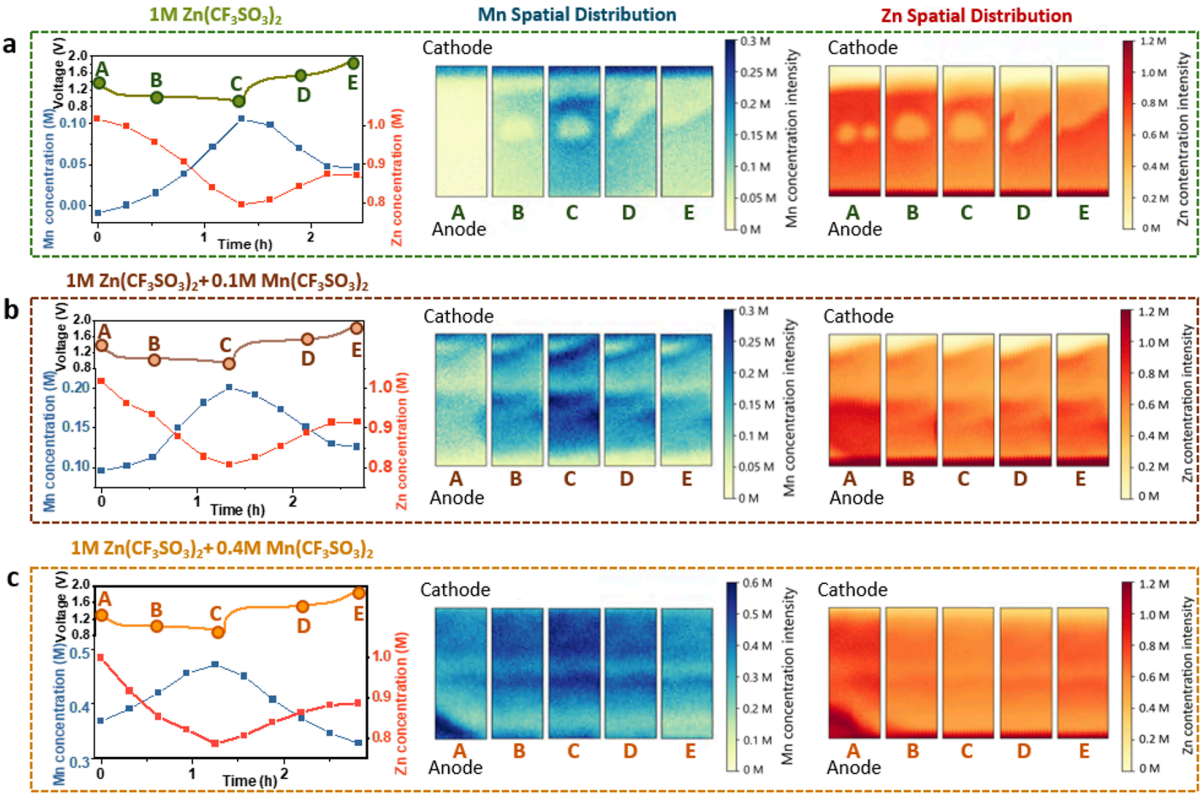

Figure 4.6 (a–c) First-cycle electrochemical performance of α-MnO_2 in different electrolytes, with corresponding average Mn and Zn concentrations across the electrolyte cross-section derived from XRF mapping. Operando XRF maps show Mn K-edge (blue) and Zn K-edge (red) distributions at key states of charge, labelled as A, B, C, D, E in the load curve. Electrolyte compositions: (a) 1 M $Zn(CF_3SO_3)_2$, (b) 1 M $Zn(CF_3SO_3)_2$ + 0.1 M $Mn(CF_3SO_3)_2$, (c) 1 M $Zn(CF_3SO_3)_2$ + 0.4 M $Mn(CF_3SO_3)_2$. The Mn and Zn concentrations were calibrated using reference solutions. The mapped area of the separator in the operando measurement is approximately 400 × 160 µm.

By combining the operando XRF with the electrochemical data, the respective contributions of Mn^{2+} additives and the MnO_2 cathode during both discharge and charge

processes were decoupled. This finding shows that across all electrolytes, regardless of whether Mn^{2+} additives are present or their concentration, the extent of MnO_2 dissolution during discharge remains unchanged. This indicates that Mn^{2+} additives do not suppress MnO_2 dissolution, directly challenging the traditional assumption that Mn^{2+} inhibit cathode dissolution to enhance cycling stability.

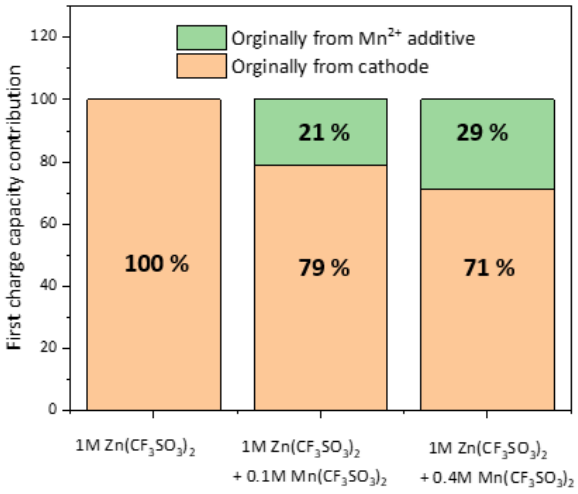

Figure 4.7 Histogram showing the contributions to α-MnO_2 charge capacity at first cycle from the electrolyte and the cathode in different electrolytes, calculated from the electrochemical curves in Figure 4.2b.

The key to the improvement in cycling performance upon Mn^{2+} addition actually lies in the first charging process. In the baseline electrolyte without Mn^{2+} additives, the charge capacity is entirely attributed to the cathode, via reoxidation of dissolved Mn^{2+} (originally from the cathode) and Zn^{2+} deintercalation from the solid MnO_2. However, when Mn^{2+} additives are present (at 0.1 M or 0.4 M), an additional charge capacity manifests that can be attributed to the electrochemical oxidation of the additive Mn^{2+}. Quantitatively, at 0.1 M Mn^{2+}, 21% of the charge capacity originates from the additive, while 79% is from the cathode. At 0.4 M Mn^{2+}, the additive accounts for 29%, and the cathode for 71%. These results are summarised in the histogram shown in Figure 4.7. The new deposited MnO_2 from Mn^{2+} addition then participates in the subsequent discharge, contributing to a higher capacity in the second cycle, artificially

improving capacity retention. Operando XRF mapping directly reveals that this enhanced performance upon Mn^{2+} addition results from the increased soluble Mn active material rather than suppression of Mn dissolution.

In addition to tracking Mn redox behavior, the operando setup also enables simultaneous monitoring of Zn concentration dynamics (Figure 4.6a-c), revealing an interesting trend: the Zn concentration decreases during the first discharge. Although Zn dissolution at the anode generates Zn^{2+} during discharge, a competing process at the cathode dominates. Specifically, MnO_2 dissolution consumes protons, increasing the local pH and promoting the precipitation of zinc hydroxide triflate $Zn_x(CF_3SO_3)_y(OH)_{2x-y}{\cdot}nH_2O$ (ZHT), as confirmed later in Figure 4.12. As a result, ZHT precipitation at the cathode consumes Zn^{2+} more rapidly than it is generated at the anode, leading to a net decrease in Zn^{2+} concentration. During charging, Mn^{2+} redeposition at the cathode releases protons. This acidic shift drives ZHT dissolution (as confirmed in Figure 4.12), releasing Zn^{2+} back into the electrolyte. This causes Zn^{2+} levels to rise again. However, Zn^{2+} does not fully return to its initial concentration by the end of the cycle, likely due to some irreversible ZHT precipitation at the anode.

This dynamic fluctuation of Zn^{2+} concentration observed via operando XRF highlights a critical limitation in commonly used normalisation strategies for measuring electrolyte concentration changes. Studies typically rely on Mn/Zn intensity ratios for normalisation, often derived from ICP-OES to assess Mn concentration changes in the electrolyte.[8,16,17] However, the operando XRF results show that this approach is not appropriate, as the Zn^{2+} concentration in aqueous electrolytes is not constant; it fluctuates due to reactions at both the anode and cathode side (see reaction scheme below).

At the cathode:

$$MnO_2 + 4H^+ + 2e^- \rightleftharpoons Mn^{2+}(aq) + 2H_2O$$

$$xZn^{2+} + yCF_3SO_3^{2-} + (2x\text{-}y)OH^- + nH_2O \rightleftharpoons Zn_x(CF_3SO_3)_y(OH)_{2x\text{-}y}\cdot nH_2O$$

At the anode:

$$Zn(s) \rightleftharpoons Zn^{2+}(aq) + 2e^-$$

$$xZn^{2+} + yCF_3SO_3^{2-} + (2x\text{-}y)OH^- + nH_2O \rightarrow Zn_x(CF_3SO_3)_y(OH)_{2x\text{-}y}\cdot nH_2O$$

To illustrate the importance of this dependence, XRF data was plotted in two ways (Figure 4.8): one based on absolute Mn concentration, and the other using the Mn/Zn ratio. Although both methods show a broadly reversible trend, the numerical values differ significantly, underscoring the potential inaccuracies introduced by relying on relative ratios for quantification.

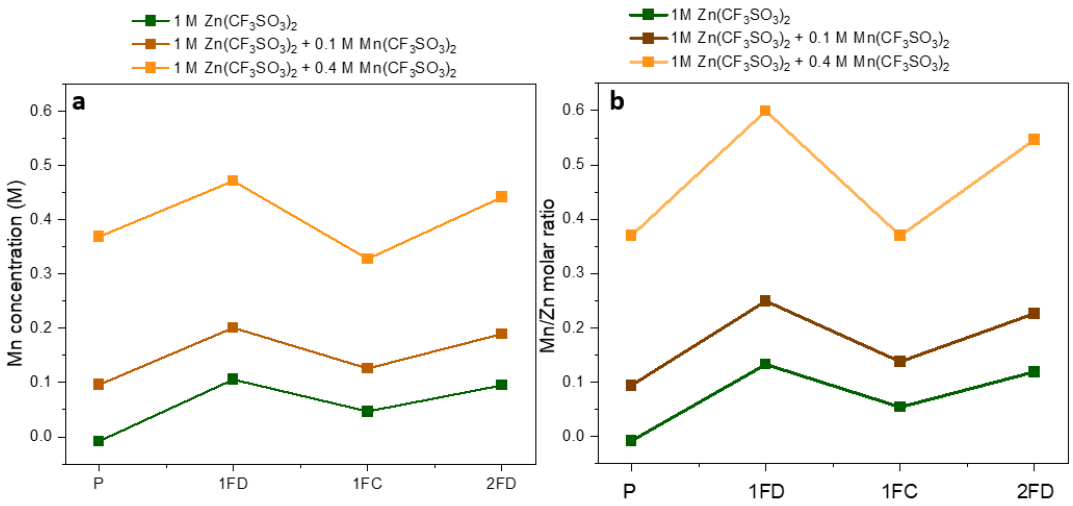

Figure 4.8 (a) Absolute Mn concentration and (b) relative Mn/Zn ratio in the electrolyte at different states of charge for cells containing 1 M $Zn(CF_3SO_3)_2$, 1 M $Zn(CF_3SO_3)_2$ + 0.1 M $Mn(CF_3SO_3)_2$, and 1 M $Zn(CF_3SO_3)_2$ + 0.4 M $Mn(CF_3SO_3)_2$. All data are based on operando XRF results from the operando cell.

Taking advantage of the beamline configuration, it also allows us to confirm the valence state of Mn in the electrolyte. Some studies have suggested that Mn^{3+} (aq) exists as a transient species in solution before disproportionating into Mn^{2+} (aq) and MnO_2.[18,19] Using the operando setup, micro X-ray absorption spectroscopy (μXAS) at the Mn K-edge (Figure 4.9) was performed on the electrolyte after each XRF mapping scan to detect any transient Mn

species. These measurements confirmed that Mn in the bulk electrolyte remains in the +2 oxidation state throughout the cycling process.

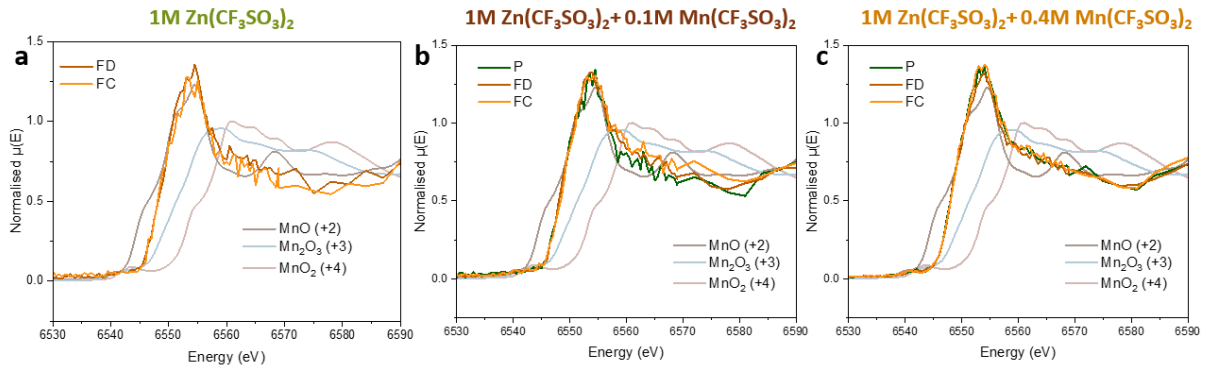

Figure 4.9 Micro-XAS spectra at the Mn K-edge collected from the electrolyte at different states of charge—pristine (P), full discharge (FD), and full charge (FC)—for cells using (a) 1 M $Zn(CF_3SO_3)_2$, (b) 1 M $Zn(CF_3SO_3)_2$ + 0.1 M $Mn(CF_3SO_3)_2$, and (c) 1 M $Zn(CF_3SO_3)_2$ + 0.4 M $Mn(CF_3SO_3)_2$.

4.3.3 Spectroscopic and Structural Characterisation

To further confirm that the majority of the capacity originates from the Mn dissolution/redeposition process, with minimal contribution from Zn^{2+} intercalation/deintercalation, ex situ XANES spectroscopy at the Mn K-edge was performed (Figure 4.10a,c,e). Regardless of the presence or absence of Mn additives, only a slight reduction in Mn valence was observed during discharge, corresponding to limited Zn^{2+} intercalation. Based on the XRF results discussed earlier (Figure 4.6), approximately 85% of the discharge capacity originates from Mn dissolution, with the remaining ~15% attributable to Zn^{2+} intercalation. During the charging process, the Mn valence did not return to its pristine state, suggesting an even smaller contribution from Zn^{2+} deintercalation to the charge capacity. To further isolate the contribution of Zn^{2+} intercalation/deintercalation, α-MnO_2 was cycled in a pure organic electrolyte, where the dissolution–deposition mechanism is largely suppressed. Interestingly, the Mn K-edge XANES spectra (Figure 4.11) displayed spectral shifts comparable to those in aqueous systems. This indicates that even in the absence of significant Mn

dissolution, the redox activity associated with Zn^{2+} intercalation/deintercalation remains limited.

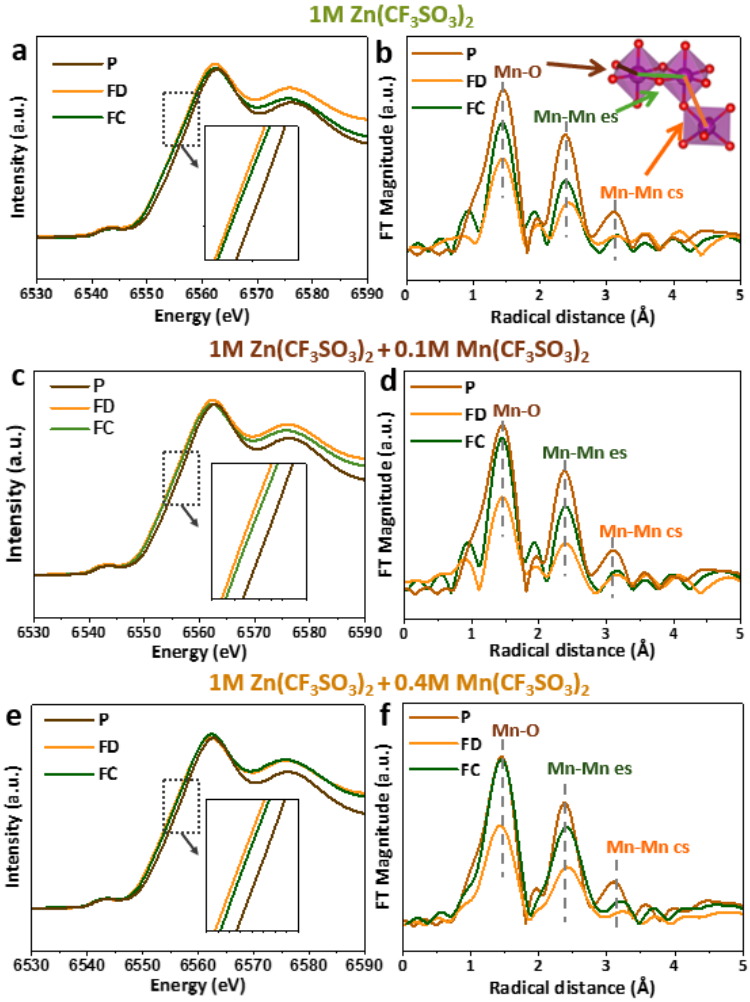

Figure 4.10 Mn K-edge XANES and EXAFS of α-MnO_2 cathodes at P, first-cycle FD, and first-cycle FC states in different electrolytes: (a, b) 1 M $Zn(CF_3SO_3)_2$, (c, d) 1 M $Zn(CF_3SO_3)_2$ + 0.1 M $Mn(CF_3SO_3)_2$ and (e, f) 1 M $Zn(CF_3SO_3)_2$ + 0.4 M $Mn(CF_3SO_3)_2$. Panels (a), (c), and (e) show the Mn K-edge XANES, while panels (b), (d), and (f) display the corresponding EXAFS spectra. "Mn-Mn es" means the Mn–Mn distances in edge-sharing octahedra and "Mn-Mn cs" means the Mn–Mn distances in corner-sharing octahedra.

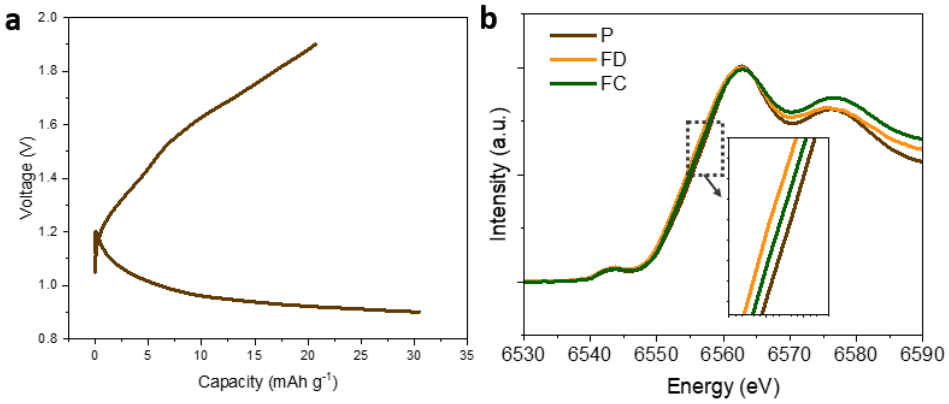

Figure 4.11 (a) The first cycle load curve of of α-MnO_2 in organic electrolyte 1 M $Zn(CF_3SO_3)_2$ in acetonitrile. (b) Mn K-edge XANES of α-MnO_2 cathodes at P, first-cycle FD, and first-cycle FC states in this organic electrolyte. The cell was cycled at a current density of 100 mA g^{-1}.

EXAFS analysis was employed to investigate the local structural evolution of MnO_2 during cycling (Figure 4.10b,d,f), providing atomic-scale insights into the dissolution-redeposition mechanism. The pristine MnO_2 spectrum exhibits characteristic peaks at 1.5 Å (Mn-O), 2.3 Å (Mn-Mn edge-sharing), and 3.1 Å (Mn-Mn corner-sharing), confirming the characteristic tunnel structure of α-MnO_2. Upon discharge, all three peaks exhibit comparable attenuation, indicating similar dissolution extent of the α-MnO_2 in all electrolytes. The subsequent charge cycle exhibits distinct recovery behaviour that varies depending on the electrolyte composition. The Mn–O coordination shows limited recovery in 1 M $Zn(CF_3SO_3)_2$ due to less MnO_2 redeposition, but significantly improves with 0.4 M $Mn(CF_3SO_3)_2$, reflecting enhanced MnO_2 deposition due to the supplemental additive Mn^{2+} present, consistent with XRF results.

Notably, the Mn–Mn corner-sharing interaction at 3.1 Å which is a key structural fingerprint of the α-MnO_2 tunnel framework decreases even when Mn–O coordination is recovered at the top of charge. This indicates that the original α-MnO_2 structure is lost, and

the redeposited MnO_2 adopts a different structure rather than restoring the original tunnel framework.

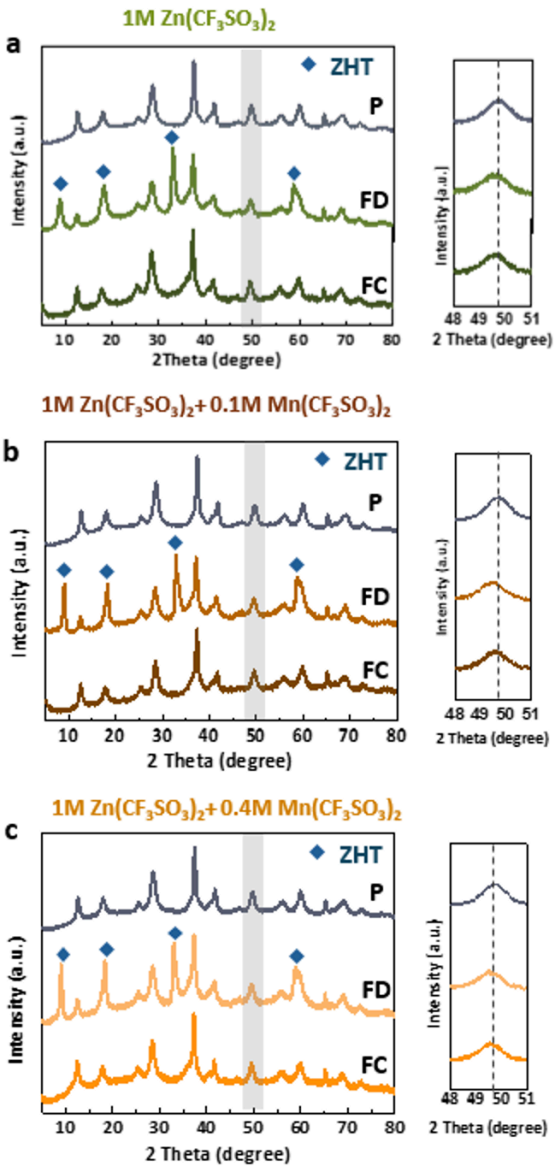

Figure 4.12 (a–c) XRD patterns of α-MnO_2 cathodes at P, first-cycle FD, and first-cycle FC states in the following electrolytes: (a) 1 M $Zn(CF_3SO_3)_2$, (b) 1 M $Zn(CF_3SO_3)_2$ + 0.1 M $Mn(CF_3SO_3)_2$, (c) 1 M $Zn(CF_3SO_3)_2$ + 0.4 M $Mn(CF_3SO_3)_2$.

To further explore these structural changes, ex situ XRD was performed on α-MnO_2 during the first cycle in three electrolytes (1 M $Zn(CF_3SO_3)_2$ without Mn additive, and with 0.1 M and 0.4 M $Mn(CF_3SO_3)_2$ additives). In all cases (Figure 4.12), the discharged samples exhibited diffraction peaks corresponding to ZHT,[20-22] which is due to Mn dissolution during

discharge. This dissolution consumes protons, leading to a local increase in pH and subsequent ZHT precipitation. Interestingly, the charged samples in all three electrolytes displayed diffraction patterns nearly identical to that of the pristine α-MnO_2, with no additional peaks observed, making it difficult to determine the exact phase of the electrodeposited MnO_2. Minor lattice expansion during discharge and partial recovery during charge were observed in all samples, consistent with XANES data and indicating limited Zn^{2+} intercalation and deintercalation (Figure 4.12).

4.3.4 TEM Characterisation

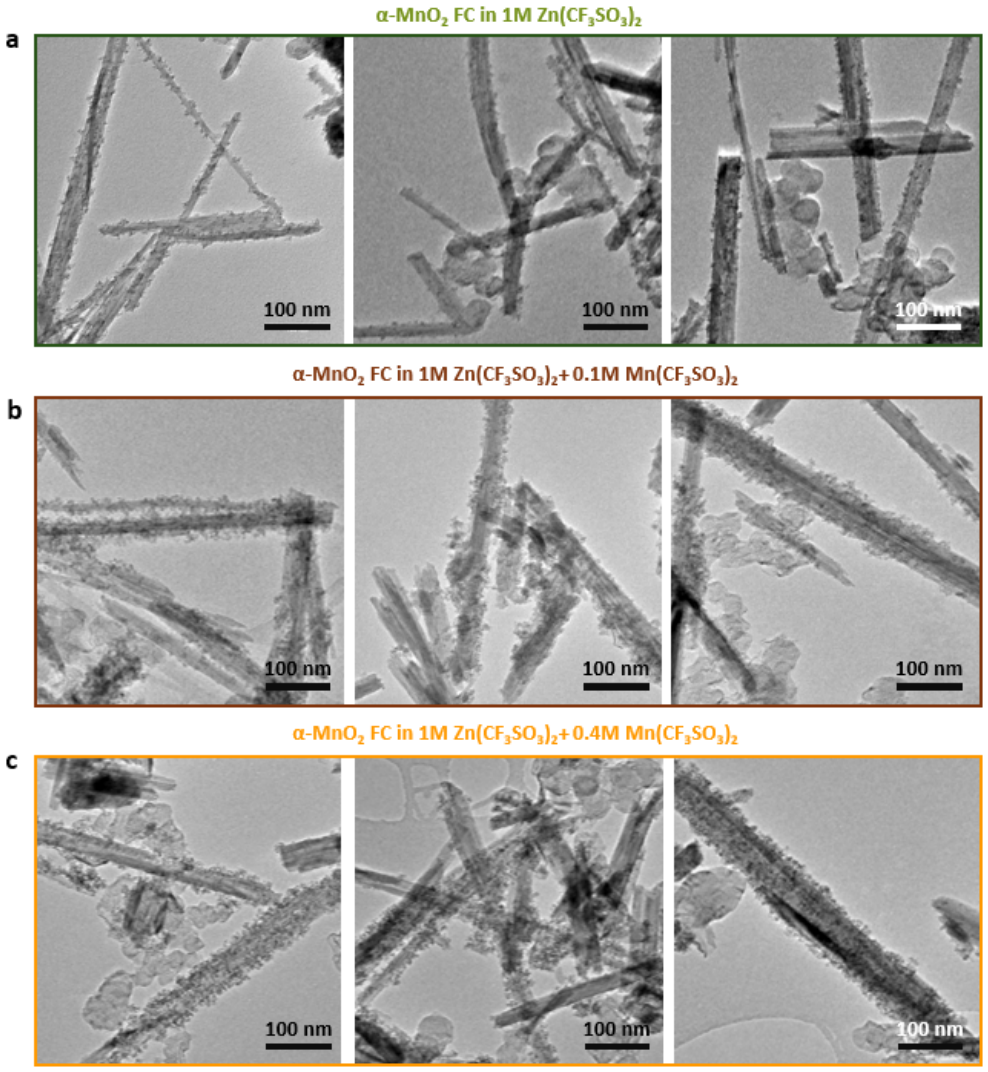

Figure 4.13 HRTEM images of the α-MnO_2 cathode at the FC state in: (a) 1 M $Zn(CF_3SO_3)_2$, (b) 1 M $Zn(CF_3SO_3)_2$ + 0.1 M $Mn(CF_3SO_3)_2$ and (c) 1 M $Zn(CF_3SO_3)_2$ + 0.4 M $Mn(CF_3SO_3)_2$.

To identify structural changes that can elude the ensemble measurement of XRD, HRTEM was performed on the charged α-MnO_2 samples. Compared to the pristine nanorod morphology of α-MnO_2 (Figure 4.1b), newly formed nanoparticulate features were observed decorating the nanorods after charging. The abundance of these nanoparticles increased with higher concentrations of Mn^{2+} additive in the electrolyte, correlating with the enhanced charge capacity and suggesting their identity as electrodeposited MnO_2, as shown in Figure 4.13.

Enlarged HRTEM is shown in Figure 4.14a-c and high magnification HRTEM imaging (Figure 4.14d,e) revealed lattice fringes within these particles, demonstrating that they are crystalline rather than amorphous. Although many studies have described electrodeposited MnO_2 as amorphous based on the absence of corresponding peaks in XRD,[23,24] this result challenge this interpretation. The absence of distinct diffraction features is more accurately attributed to the nanoscale size of the newly formed MnO_2. The strong diffraction from the dominant α-MnO_2 phase likely masks the weaker signals from these nanocrystalline deposits.

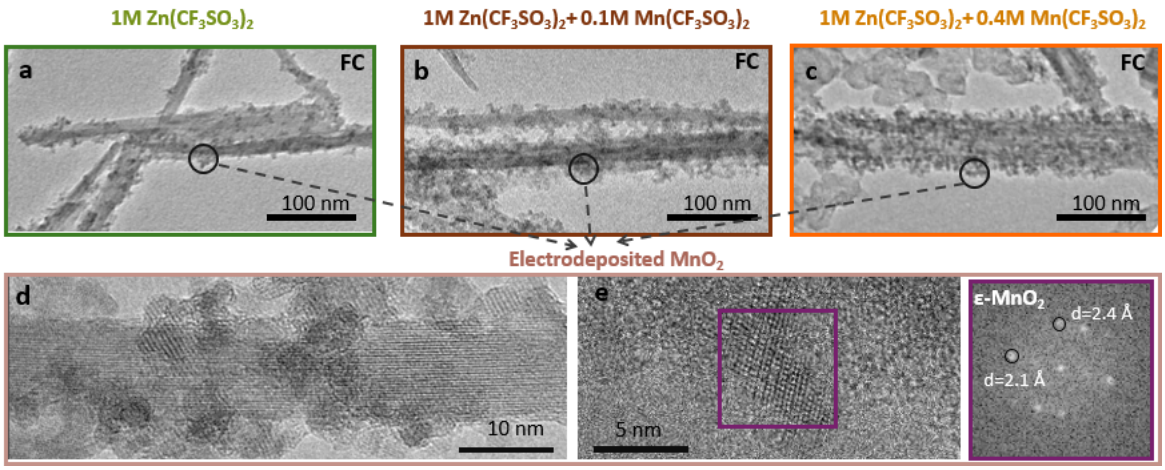

Figure 4.14 (a–c) HRTEM images of the α-MnO_2 cathode at the FC state in: (a) 1 M $Zn(CF_3SO_3)_2$, (b) 1 M $Zn(CF_3SO_3)_2$ + 0.1 M $Mn(CF_3SO_3)_2$, (c) 1 M $Zn(CF_3SO_3)_2$ + 0.4 M $Mn(CF_3SO_3)_2$. (d–e) HRTEM images of electrodeposited MnO_2 which formed in the fully charged state, with a fast Fourier transform of the indicated area in (e).

Further experiments were conducted by directly electrodepositing MnO_2 from a solution containing 1 M $Zn(CF_3SO_3)_2$ and 1 M $Mn(CF_3SO_3)_2$ (Figure 4.15), a widely adopted approach for constructing electrode-free cells in which the active cathode material is formed in situ from the electrolyte.[25-27] The electrodeposited MnO_2 displayed signature diffraction peaks corresponding to the ε-MnO_2 phase.[16,28,29] The diffraction peaks of ε-MnO_2 partially overlap with those of the original α-MnO_2 phase, making it even more challenging to distinguish between the two using XRD alone. Measurement of the lattice features captured by HRTEM (Figure 4.14e) provide further confirmation, revealing reflections at 2.4 Å and 2.1 Å, which can be assigned to the (100) and (101) lattice spacings of ε-MnO_2.

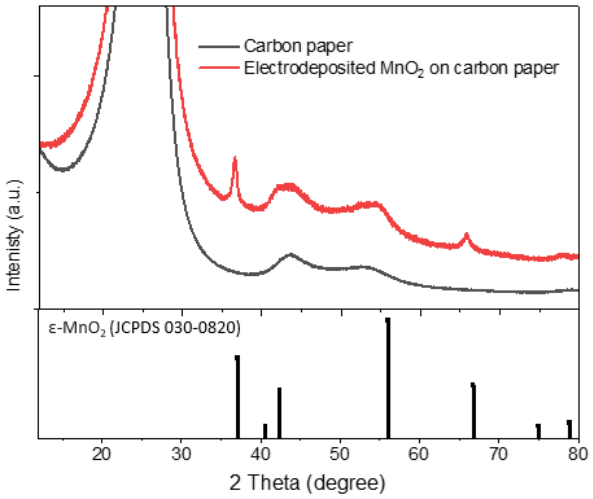

Figure 4.15 XRD pattern of electrodeposited MnO_2 on carbon paper from a solution containing 1 M $Zn(CF_3SO_3)_2$ and 1 M $Mn(CF_3SO_3)_2$, deposited at a current density of 0.5 mA cm^{-2} with a total capacity of 0.2 mAh cm^{-2}. The diffraction peaks confirm the formation of ε-MnO_2 phase.

4.3.5 Capacity Degradation Mechanism

To pinpoint the degradation mechanism over multiple cycles, operando XRF mapping during several cycling was performed in all three electrolytes, focusing here on the evolution of Mn concentration.

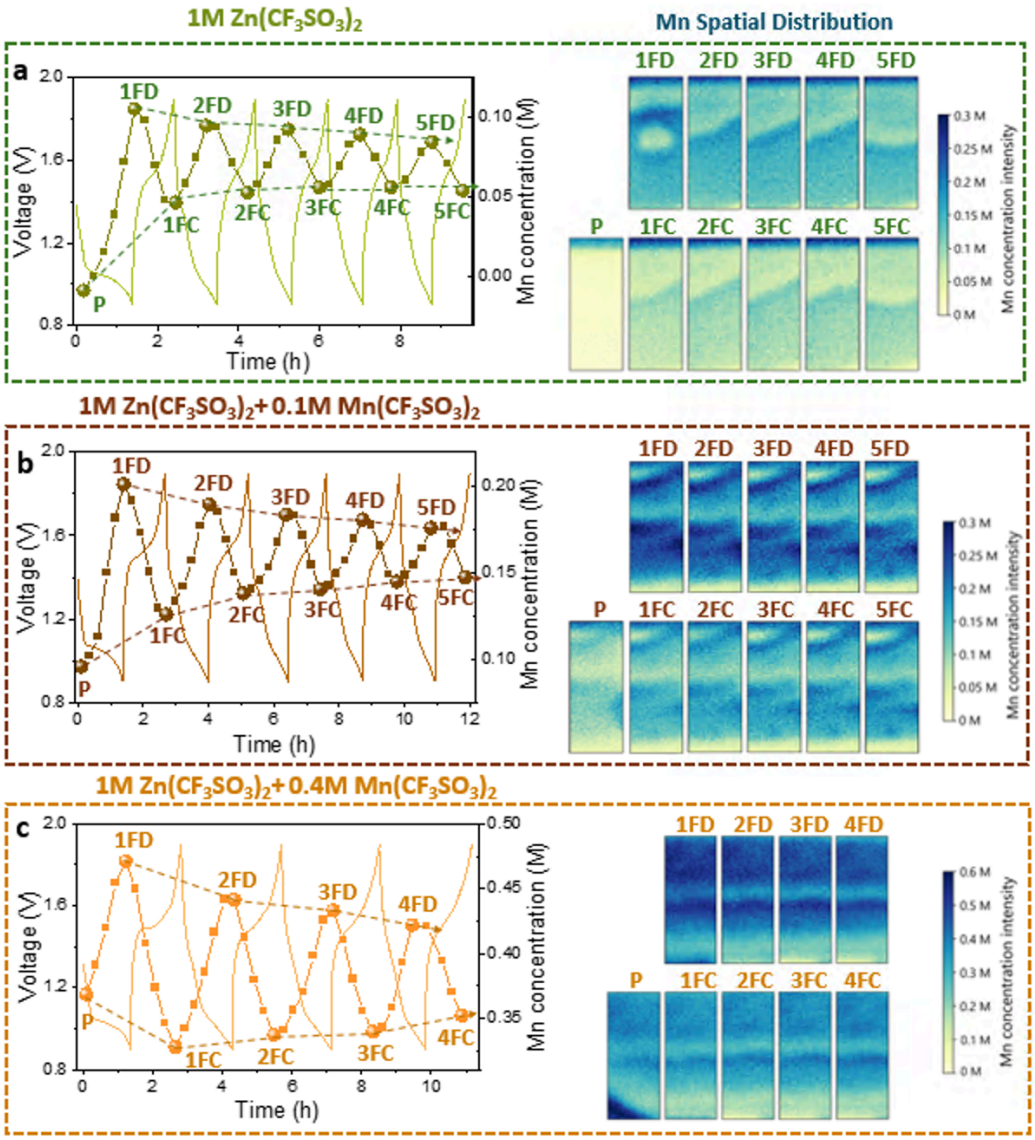

Figure 4.16 (a–c) The initial four cycle load curves of α-MnO_2 in different electrolytes, with corresponding average Mn concentrations across the electrolyte cross-section derived from XRF mapping. Operando XRF maps show Mn K-edge (blue) distributions at key states of charge. Electrolyte compositions: (a) 1 M $Zn(CF_3SO_3)_2$ (b) 1 M $Zn(CF_3SO_3)_2$ + 0.1 M $Mn(CF_3SO_3)_2$ (c) 1 M $Zn(CF_3SO_3)_2$ + 0.4 M $Mn(CF_3SO_3)_2$.

Figure 4.16 presents the Mn concentration evolution over multiple cycles in the three different electrolytes. In the baseline 1 M $Zn(CF_3SO_3)_2$ electrolyte, Mn behaviour during the first cycle (previously shown in Figure 4.6) exhibits a typical pattern: an increase in Mn concentration during discharge, followed by a partial decrease during charge. However, the

Mn level does not return to the pristine state after charging, indicating incomplete redeposition.

Interestingly, when examining the second discharge (2FD), the Mn concentration increase is smaller than in the first discharge (1FD), suggesting that not all redeposited MnO_2 is re-dissolved. This observation leads us to propose a new framework for describing the reversibility of MnO_2 in aqueous ZIBs. Specifically, it is defined as:

Redeposition efficiency: the extent to which dissolved Mn^{2+} is converted back into solid MnO_2 during charge.

Dissolution efficiency: the degree to which redeposited MnO_2 returns to Mn^{2+} in the electrolyte during discharge.

Because the electrochemical capacity arises from both dissolution/redeposition along with a minor contribution from intercalation processes, relying solely on coulombic efficiency (i.e., the discharge-to-charge capacity ratio) is insufficient to fully capture the reversibility of Mn redox reactions. Instead, tracking the Mn content over cycling offers deeper insight.

The charge trend (P → 1FC → 2FC → 3FC → 4FC→ 5FC) reveals a progressive increase in residual Mn after each charge, indicating incomplete redeposition. Similarly, the discharge trend (1FD → 2FD → 3FD → 4FD → 5FD) shows a gradual decrease in Mn content, confirming incomplete dissolution of previously deposited MnO_2.

These two inefficiencies, both the partial redeposition and partial dissolution, lead to the observed capacity fading that occurs both within a single cycle (intra-cycle) and over multiple cycles (inter-cycle). Such behaviour can only be revealed through operando tracking of Mn dynamics in the electrolyte. Applying this analysis to the moderate Mn additive condition (0.1 M Mn^{2+}), while additional Mn enhances the initial charge capacity, the same trends persist.

In the high Mn additive case (0.4 M), the initial charge capacity exceeds the discharge capacity, consuming Mn from the electrolyte and reducing Mn concentration from the pristine state to 1FC. However, subsequent cycles still exhibit increasing residual Mn after each charge (1FC → 2FC → 3FC → 4FC) and decreasing Mn (1FD → 2FD → 3FD → 4FD) release after each discharge. This again confirms that even with an abundant Mn supply, the system suffers from intrinsic inefficiencies in both Mn redeposition and dissolution.

These observations underscore a broader issue: neither the MnO_2 cathode nor the Mn^{2+} additive is fully utilised during electrochemical cycling, primarily due to incomplete Mn dissolution and redeposition. This underutilisation directly limits the achievable energy density of the system. In the baseline Zn electrolyte, the limited reversibility of Mn dissolution and re-electrodeposition restricts the effective use of the MnO_2 cathode. Even when Mn^{2+} additives are introduced, they only partially participate in the redox process, while a substantial portion of the Mn^{2+} additives is not reincorporated into the cathode. As a result, both the solid cathode material and the soluble Mn active species suffer from low utilisation, leading to wasted resources and unnecessary energy expenditure without contributing meaningfully to capacity.

A key implication of our study is that the addition of Mn^{2+} does not fundamentally resolve the limitations associated with the MnO_2 cathode. Instead, our findings suggest that efforts should focus on enhancing the dissolution-redeposition mechanism itself. Unlike conventional conversion- or intercalation-type cathodes, which undergo only solid–solid phase transitions, this process involves a solid–liquid-solid phase transition. Such transitions are inherently heterogeneous, governed by surface reaction kinetics that are highly sensitive to interfacial conditions, including current collector properties and electrode surface area.[30-32] To demonstrate this, MnO_2 was electrodeposited from a solution containing 1 M

$Mn(CF_3SO_3)_2$ and 1 M $Zn(CF_3SO_3)_2$ onto Ti foil and carbon paper current collectors, to evaluate how substrate characteristics influence MnO_2 nucleation and growth voltage (Figure 4.17). The results revealed that carbon paper exhibited both lower nucleation and growth overpotentials compared to Ti foil, likely due to its higher surface area, which provides more favourable sites for nucleation. This underscores the potential of structuring the electrode interface to enhance the dissolution/deposition process.

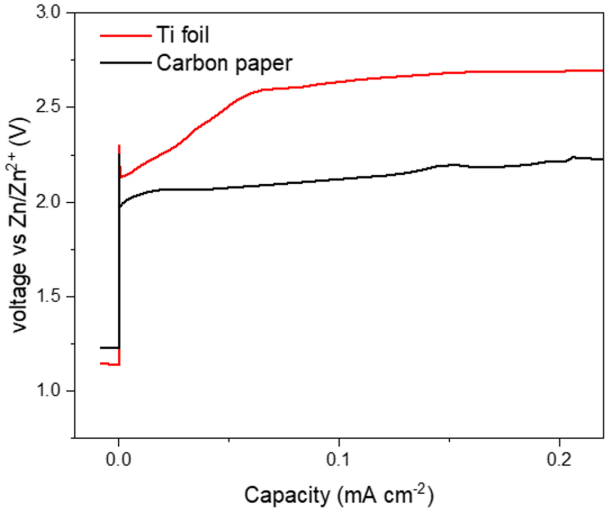

Figure 4.17 Galvanostatic charge curves (0.5 mA cm^{-2}, charged to 0.2 mA h cm^{-2}) for Zn/Ti and Zn/carbon paper cells in an electrolyte containing 1 M $Zn(CF_3SO_3)_2$ and 1 M $Mn(CF_3SO_3)_2$.

Up to this point, our discussion has focused primarily on the behaviour of the α-phase MnO_2. However, due to the polymorphic nature of MnO_2, many other structural variants exist, including β-, γ-, and δ-MnO_2. Previous studies have shown that while different MnO_2 polymorphs exhibit distinct voltage profiles during the initial cycles in aqueous ZIBs, their electrochemical behaviour tends to converge after extended cycling,[33,34] suggesting that the specific polymorph may not strongly influence long-term electrochemical performance.

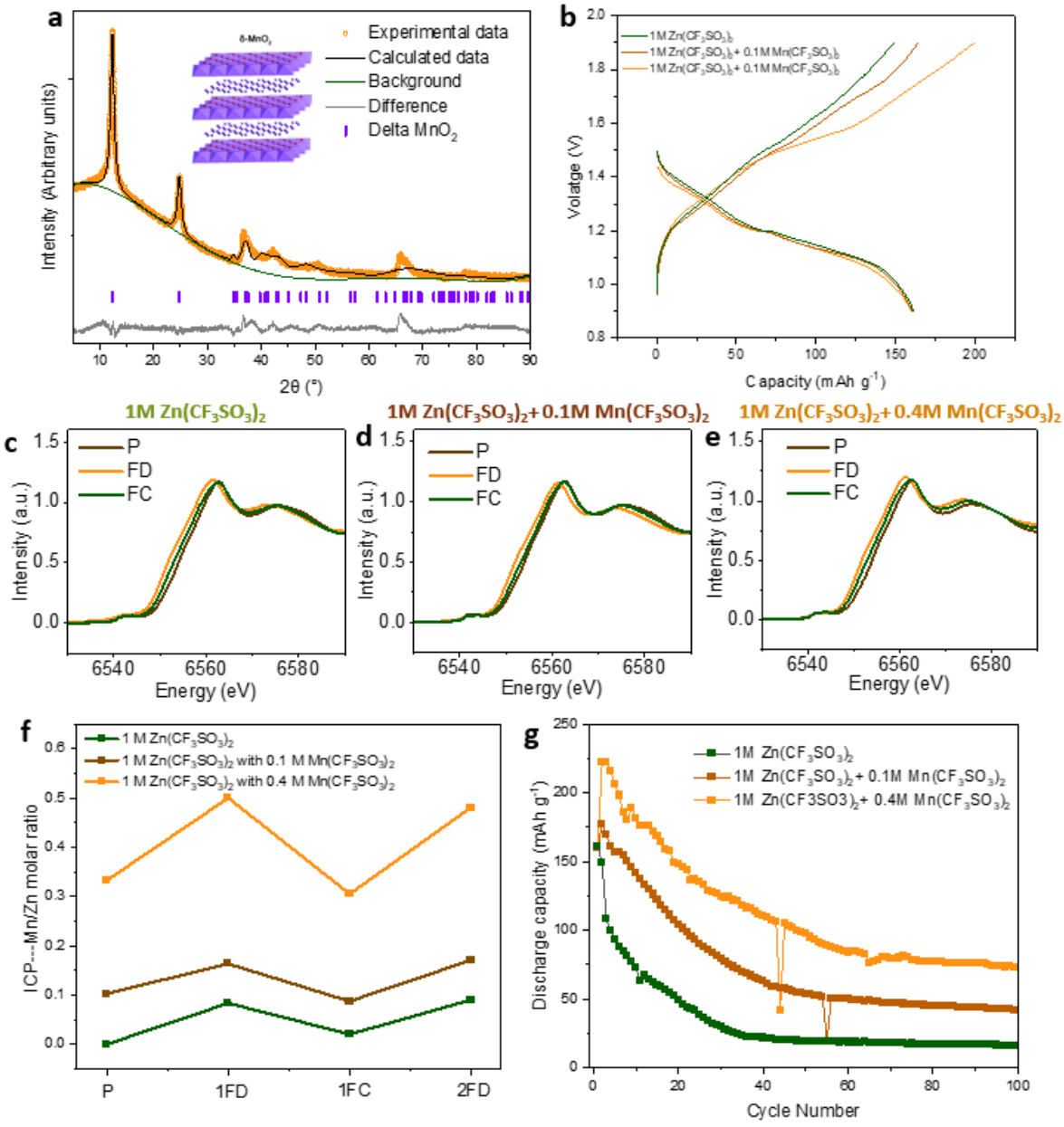

Figure 4.18 (a) Rietveld refinement of the XRD pattern of δ-MnO_2, showing a layered structure with K^+ ions and water molecules and refined using the Cm/m space group. (b) First-cycle voltage profiles of δ-MnO_2 cathodes in the three these electrolytes. Mn K-edge XANES and EXAFS of δ-MnO_2 cathodes at P, first-cycle FD, and first-cycle FC states in different electrolytes: (c) 1 M $Zn(CF_3SO_3)_2$ (cd) 1 M $Zn(CF_3SO_3)_2$ + 0.1 M $Mn(CF_3SO_3)_2$ and (e) 1 M $Zn(CF_3SO_3)_2$ + 0.4 M $Mn(CF_3SO_3)_2$. (f) The relative Mn/Zn ratio in the electrolyte at different states of charge for cells based on ICP-OES results from the coin cell. (g) Cycling performance (discharge capacity) of coin cells with δ-MnO_2 cathodes in three electrolytes: 1 M $Zn(CF_3SO_3)_2$, 1 M $Zn(CF_3SO_3)_2$ + 0.1 M $Mn(CF_3SO_3)_2$, and 1 M $Zn(CF_3SO_3)_2$ + 0.4 M $Mn(CF_3SO_3)_2$. All cells were cycled at a current density of 100 mA g^{-1}.

To explore the applicability of our description to other polymorphs, layered δ-MnO_2 was synthesised, with its structure confirmed by XRD (Figure 4.18a), and evaluated it in three electrolytes: the baseline 1 M $Zn(CF_3SO_3)_2$, and baseline electrolyte with 0.1 M and 0.4 M $Mn(CF_3SO_3)_2$ additives (Figure 4.18b). XANES measurements revealed a more pronounced edge shift compared to α-MnO_2, indicating greater Zn^{2+} intercalation due to the larger inter spacing (Figure 4.18c-e). However, the electrochemical performance exhibited similar first discharge capacities and increased charge capacities with higher Mn additive concentration, which implied that Mn^{2+} additives also play a key role in the redox process (Figure 4.18b). This was further corroborated by the Mn/Zn molar ratio changes observed via ICP-OES analysis which is conducted by Dr. Lijiang Song from university of Warwick (Figure 4.18f). Although ICP-OES cannot quantify the absolute mass fraction of dissolved MnO_2, the trends reflect the contribution of the dissolution/deposition mechanism and the role of Mn^{2+} additive.

4.4 Conclusion

Through operando XRF mapping and ex-situ spectroscopic analyses, the distinct role of Mn from additives and the MnO_2 cathode at different states of charge was decoupled. Our findings demonstrate that Mn^{2+} additives did not suppress Mn cathode dissolution, but rather their role is as an active material reservoir that compensates for cathode capacity loss rather than preventing it. Excess Mn^{2+} additive can artificially inflate apparent capacity, masking the underlying degradation mechanisms and creating a misleading impression of electrochemical reversibility. Critically, even with Mn^{2+} additives, the fundamental issue of capacity fade persists, originating from two intrinsically irreversible processes: incomplete MnO_2 dissolution during discharge and incomplete Mn^{2+} redeposition during charge. To address these limitations, alternative strategies, such as surface functionalisation or the use of porous

scaffolds, may provide strategies to improve both dissolution and nucleation kinetics during deposition.

4.5 Reference

1 Sambandam, B. *et al.* An analysis of the electrochemical mechanism of manganese oxides in aqueous zinc batteries. *Chem.* **8**, 924-946 (2022).

2 Chamoun, M., Brant, W. R., Tai, C.-W., Karlsson, G. & Noréus, D. Rechargeability of aqueous sulfate Zn/MnO_2 batteries enhanced by accessible Mn^{2+} ions. *Energy Storage Mater.* **15**, 351-360 (2018).

3 Soundharrajan, V. *et al.* The dominant role of Mn^{2+} additive on the electrochemical reaction in $ZnMn_2O_4$ cathode for aqueous zinc-ion batteries. *Energy Storage Mater.* **28**, 407-417 (2020).

4 Alfaruqi, M. H. *et al.* Structural transformation and electrochemical study of layered MnO_2 in rechargeable aqueous zinc-ion battery. *Electrochim. Acta* **276**, 1-11 (2018).

5 Cui, S., Zhang, D. & Gan, Y. The effect of Mn^{2+} additives on the capacity of aqueous Zn/δ-MnO_2 batteries: Elucidating the Mn^{2+} concentration dependence of the irreversible transformation of δ-MnO_2. *J. Power Sources* **579**, 233293 (2023).

6 He, Z. F., Lu, Y. T., Wei, T. C. & Hu, C. C. Complementary Operando Electrochemical Quartz Crystal Microbalance and UV/Vis Spectroscopic Studies: Acetate Effects on Zinc-Manganese Batteries. *ChemSusChem.* **16**, e202300259 (2023).

7 Zhao, L., Chénard, E., Çapraz, Ö., Sottos, N. & White, S. Direct detection of manganese ions in organic electrolyte by UV-vis spectroscopy. *J. Electrochem. Soc.* **165**, A345 (2018).

8 Pan, H. *et al.* Reversible aqueous zinc/manganese oxide energy storage from conversion reactions. *Nat. Energy* **1**, 16039 (2016).

9 Zhang, N. *et al.* Rechargeable aqueous zinc-manganese dioxide batteries with high energy and power densities. *Nat. Commun.* **8**, 405 (2017).

10 Yang, J. *et al.* Unravelling the Mechanism of Rechargeable Aqueous Zn-MnO_2 Batteries: Implementation of Charging Process by Electrodeposition of MnO_2. *ChemSusChem.* **13**, 4103-4110 (2020).

11 Guo, X. *et al.* Zn/MnO_2 battery chemistry with dissolution-deposition mechanism. *Mater. Today Energy* **16**, 100396 (2020).

12 Fitz, O. *et al.* Electrolyte Study with in Operando pH Tracking Providing Insight into the Reaction Mechanism of Aqueous Acidic Zn//MnO_2 Batteries. *ChemElectroChem.* **8**, 3553-3566 (2021).

13 Musílek, L., Prokeš, R. & Trojek, T. Overview of methods for determining the depth distribution of elements in X-ray fluorescence analysis. *Radiat. Phys. Chem.* **200**, 110388 (2022).

14 Becknell, N. *et al.* Employing the Dynamics of the Electrochemical Interface in Aqueous Zinc-Ion Battery Cathodes. *Adv. Funct. Mater.* **31**, 2102135 (2021).

15 Zhong, Y., Xu, X., Veder, J. P. & Shao, Z. Self-Recovery Chemistry and Cobalt-Catalyzed Electrochemical Deposition of Cathode for Boosting Performance of Aqueous Zinc-Ion Batteries. *iScience* **23**, 100943 (2020).

16 Aguilar, I. *et al.* Identifying interfacial mechanisms limitations within aqueous Zn-MnO_2 batteries and means to cure them with additives. *Energy Storage Mater.* **53**, 238-253 (2022).
17 Alfaruqi, M. H. *et al.* Electrochemically induced structural transformation in a γ-MnO_2 cathode of a high capacity zinc-ion battery system. *Chem. Mater.* **27**, 3609-3620 (2015).
18 Hanf, L., Henschel, J., Diehl, M., Winter, M. & Nowak, S. Mn^{2+} or Mn^{3+}? Investigating transition metal dissolution of manganese species in lithium ion battery electrolytes by capillary electrophoresis. *Electrophoresis* **41**, 697-704 (2020).
19 Davies, G. Some aspects of the chemistry of manganese (III) in aqueous solution. *Coord. Chem. Rev.* **4**, 199-224 (1969).
20 Rajabi, R. *et al.* Insights into chemical and electrochemical interactions between Zn anode and electrolytes in aqueous Zn− ion batteries. *J. Electrochem. Soc.* **169**, 110536 (2022).
21 Oberholzer, P., Tervoort, E., Bouzid, A., Pasquarello, A. & Kundu, D. Oxide versus nonoxide cathode materials for aqueous Zn batteries: an insight into the charge storage mechanism and consequences thereof. *ACS Appl. Mater. Interfaces* **11**, 674-682 (2018).
22 Wang, L., Huang, K.-W., Chen, J. & Zheng, J. Ultralong cycle stability of aqueous zinc-ion batteries with zinc vanadium oxide cathodes. *Sci. Adv.* **5**, eaax4279 (2019).
23 Siamionau, U., Aniskevich, Y., Ragoisha, G. & Streltsov, E. MnO_2 electrodeposition at the positive electrode of zinc-ion aqueous battery containing Zn^{2+} and Mn^{2+} cations. *J. Solid State Electrochem.* **27**, 1911-1918 (2023).
24 Dong, B., Xue, T., Xu, C.-L. & Li, H.-L. Electrodeposition of mesoporous manganese dioxide films from lyotropic liquid crystalline phases. *Microporous Mesoporous Mater.* **112**, 627-631 (2008).
25 Wang, M. *et al.* Electrode-Less MnO_2-Metal Batteries with Deposition and Stripping Chemistry. *Small* **17**, 2103921 (2021).
26 Li, Y. *et al.* In situ formation of liquid crystal interphase in electrolytes with soft templating effects for aqueous dual-electrode-free batteries. *Nat. Energy* **9**, 1350-1359 (2024).
27 Xie, C. *et al.* A highly reversible neutral zinc/manganese battery for stationary energy storage. *Energy Environ. Sci.* **13**, 135-143 (2020).
28 Guo, D. *et al.* To Make a Painstaking Investigation: Revealing the Electrochemical Reactions in Aqueous Zn– Mn Batteries. *Angew. Chem*. **64**, e202505102 (2025).
29 Rubel, O. *et al.* Electrochemical Stability of $ZnMn_2O_4$: Understanding Zn-Ion Rechargeable Battery Capacity and Degradation. *J. Phys. Chem. C* **126**, 10957-10967 (2022).
30 Ren, Y., Li, H., Rao, Y., Zhou, H. & Guo, S. Aqueous MnO_2/Mn^2+ electrochemistry in batteries: progress, challenges, and perspectives. *Energy Environ. Sci.* **17**, 425-441 (2024).
31 Liang, G. *et al.* A universal principle to design reversible aqueous batteries based on deposition–dissolution mechanism. *Adv. Energy Mater.* **9**, 1901838 (2019).
32 Timmermans, M. Y. *et al.* Electrodeposition of adherent submicron to micron thick manganese dioxide films with optimized current collector interface for 3D Li-ion electrodes. *J. Electrochem. Soc.* **164**, D954 (2017).
33 Liao, Y. *et al.* Unveiling performance evolution mechanisms of MnO_2 polymorphs for durable aqueous zinc-ion batteries. *Energy Storage Mater.* **44**, 508-516 (2022).

34 Siamionau, U. *et al.* Rechargeable zinc-ion batteries with manganese dioxide cathode: How critical is choice of manganese dioxide polymorphs in aqueous solutions? *J. Power Sources* **523**, 231023 (2022).

5

5 Cation-Disordered Rocksalt Cathode for Aqueous Anode-Free ZIBs

5.1 Introduction

Side reactions at the Zn metal anode, such as corrosion, byproduct formation, and hydrogen evolution, occur continuously from the moment of cell assembly, even during resting.[1] These chemical degradations are often underestimated due to the common practice of using excess Zn, with N/P ratios exceeding 150, to offset active material loss.[2,3] While artificial interfacial layers and electrolyte additives have shown some ability to suppress these side reactions, they cannot eliminate them entirely. As long as metallic Zn is present, parasitic reactions with aqueous electrolytes persist.

A radical yet promising solution is the elimination of the Zn metal anode altogether, giving rise to the concept of an anode-free ZIB.[4,5] In this configuration, the anode consists solely of a lightweight current collector onto which Zn is electrochemically plated and stripped during cycling. This approach reduces the N/P ratio to near zero, significantly improving energy density and Zn utilisation. Although progress has been made in optimising current collectors and electrolytes for anode-free systems, the development of cathode materials capable of reversibly supplying Zn^{2+} becomes a critical requirement for realising practical and high-performance anode-free ZIBs.

A prerequisite for an anode-free battery is a cathode that is natively loaded with the active ionic element in its pristine state, such as $LiCoO_2$ for the anode-free lithium-ion battery. In ZIBs, most of the studied cathode materials, including the leading candidates MnO_2 and V_2O_5, do not contain zinc in their pristine state. To realise an anode-free ZIB with these materials would require them to be pre-loaded with zinc before assembly, which is energy-intensive and impractical for commercial scale-up. The pool of Zn-containing cathodes that enable initial charging and offer high energy density is limited to a few materials, such as

$ZnMn_2O_4$,[6,7] $Zn_3V_3O_8$,[8,9] $Zn_{0.56}VOPO_4{\cdot}2H_2O$,[10] $Zn_3V_4(PO_4)_6$,[11] $Zn_3[Fe(CN)_6]_2$,[12,13] $ZnMn_2(PO_4)_2$ [14] and $Zn_2Mo_3O_8$.[15] However, each of these materials has significant limitations.

In this chapter, a novel cathode material, $ZnMnO_2$, was synthesised and demonstrated to be chargeable at first cycle, making it a viable candidate for anode-free ZIBs. $ZnMnO_2$ belongs to the class of cation-disordered rocksalt (DRX) materials, which have shown considerable promise in lithium-ion systems due to their high capacity and minimal volume change upon cycling.[16] Anode-free cells employing $ZnMnO_2$ exhibited stable cycling and good capacity retention over 100 cycles in a mildly acidic aqueous electrolyte, without requiring any modification to the anode current collector or electrolyte composition.

To understand the underlying charge storage mechanism, a suite of advanced characterisation techniques was employed. Additionally, DRX $ZnFeO_2$ utilising the earth-abundant transition metal Fe was synthesised and evaluated, which also demonstrated encouraging performance. The intrinsic Zn content of this family of DRX materials enables them to be charged from the initial state, offering a practical cathode platform for anode-free ZIBs. To the best of our knowledge, this represents the first reported application of cation-disordered rocksalt materials in aqueous ZIBs, opening new avenues for cathode development.

As this work has been published in Energy & Environmental Science, there is some overlap between the content of this chapter and the published manuscript. This chapter is reproduced from Ref. 17 with permission from the rights holder, The Royal Society of Chemistry.

5.2 Experimental Methods

Materials Preparation:

Synthesis of $ZnMnO_2$ and $ZnFeO_2$:

$ZnMnO_2$ was synthesised using a mechanochemical ball milling method. ZnO (99%, Sigma Aldrich) and MnO (99%, Sigma Aldrich) were mixed in a 1:1 molar ratio and sealed in air-tight zirconia jars inside an argon-filled glovebox to prevent Mn oxidation. The mixture was ball-milled for 8 hours at 700 rpm in a Fritsch Pulverisette 7 planetary ball mill. Milling was carried out in 5-minute intervals, separated by 10-minute rests to prevent overheating. $ZnFeO_2$ was synthesised using the same method, with ZnO (99%, Sigma Aldrich) and FeO (99.9%, Sigma Aldrich) in a 1:1 molar ratio.

Synthesis of $ZnMnO_3$:

$ZnMnO_3$ was synthesised using a co-precipitation method. Solution A was prepared by dissolving 3 mmol of $Mn(CH_3COO)_2{\cdot}4H_2O$ (99%, Sigma-Aldrich) and 3 mmol of $Zn(CH_3COO)_2{\cdot}2H_2O$ (97%, Alfa Aesar) in 10 mL of EG (Merck Life Science UK Limited). Solution B was prepared by dissolving 0.54 g of oxalic acid (98%, Sigma-Aldrich) and 1 g of polyvinylpyrrolidone (PVP, Alfa Aesar) in a mixture of 80 mL EG and 10 mL DI water. Solution B was then added dropwise to Solution A under continuous stirring, and the mixture was stirred for 12 hours. The resulting precipitate was collected, washed thoroughly with DI water, and vacuum-dried at 70 °C for 12 hours. The dried product was subsequently annealed at 400 °C for 2 hours in air. The synthesised $ZnMnO_3$ was used as a reference material for XAS analysis.

Electrochemistry:

The free-standing $ZnMnO_2$ cathode film was prepared by mixing $ZnMnO_2$, acetylene black carbon (99.9+%, Thermo Scientific Chemicals) and PTFE (Goodfellow) in a mass ratio of 7:2:1 with a pestle and mortar. The mixture was mechanically rolled into a film with a thickness of ~0.1 mm. The loading mass of $ZnMnO_2$ film per cell is around 5-10 mg. The same procedure

was employed to prepare $ZnFeO_2$ cathode film and TiS_2 (99.9%, Sigma Aldrich) anode films. For the free powder cell, $ZnMnO_2$ was mixed with acetylene black carbon in a mass ratio of 7:2 using a mortar and pestle. The loading mass of $ZnMnO_2$ powder per cell ranging from 10-20 mg. Coin cells (CR2032, anode and cathode casing weight: 1.76 g) were assembled with an anode, cathode (either film or powder) and two layers of glass fiber separator (each weighting 22 mg) soaked in 140 µL electrolyte of 2 M $ZnSO_4$ with 0.2 M $MnSO_4$. The anode configurations used were a Zn foil (0.18 mm thick) for the Zn anode cell, carbon paper for the anode-free cell, and TiS_2 anode for the rocking chair cell. All electrochemical testing was carried out using a Maccor Series 4000 at room temperature.

Characterisation:

The ex-situ characterisation was conducted on $ZnMnO_2$ film or powder samples after charging/discharging to specific states of charge and disassembly from coin cells. The cathode film or powder was thoroughly rinsed several times with DI water to remove any residual electrolyte, followed by vacuum drying at 70 °C.

PXRD was performed using a Rigaku Miniflex diffractometer with Cu Kα1 radiation. The PXRD data were analysed using the Rietveld refinement method with GSAS-II software.

SEM images were obtained using a Carl Zeiss Merlin field emission scanning electron microscope. HRTEM and SAED, was carried out using a JEOL JEM-2100 operating at 200 kV.

STEM with HAADF imaging and EDX were performed using an aberration-corrected JEOL ARM 200F, equipped with an Oxford Instruments windowless EDX detector. STEM was performed by my supervisor Dr. Alex Robertson.

Bulk-sensitive sXAS were obtained in IPFY mode at beamline BL27SU of the Spring-8 synchrotron source. The measurement is conducted by Rui Qi at the university of Oxford.

Hard XAS was conducted at the in-house easyXAFS300+ at the university of Warwick and at beamline BM28 XMaS of the ESRF synchrotron source.

X-ray total scattering data were collected at beamline I15-1 of the Diamond Light Source then converted to X-ray PDF data. The X-ray PDF data were analysed using the refinement method with PDFgui software.

For ICP-OES and ICP-MS on the cathodes, cathode powder was dissolved in concentrated aqua regia and diluted with 2% nitric acid. For ICP-OES analysis of the electrolyte, the separator closest to the anode side was collected, while the separator near the cathode side was discarded due to residual cathode material. The separator was soaked in concentrated nitric acid for 3 days, then diluted with 2% nitric acid prior to ICP-OES analysis. The sample preparation was carried out by me, while the measurements were performed by Dr. Lijiang Song at the university of Warwick.

5.3 Results and Discussion

5.3.1 Materials Characterisation

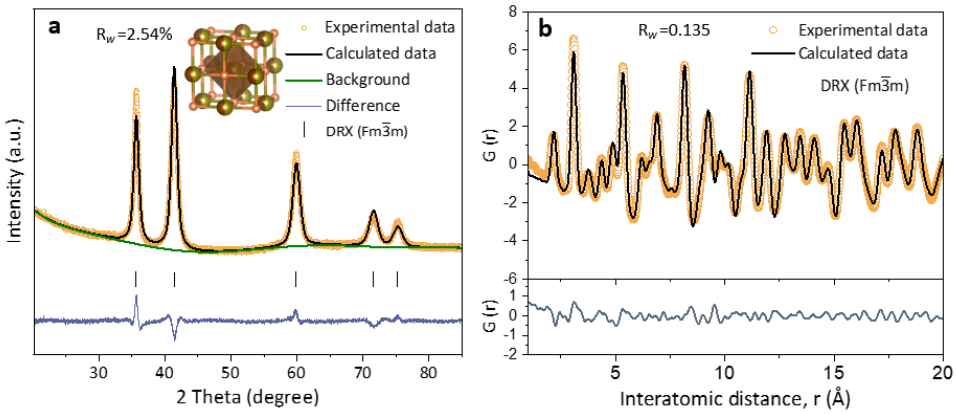

Figure 5.1 (a) Powder XRD pattern of pristine cation-disordered $ZnMnO_2$, refined using the Rietveld method to the Fm$\bar{3}$m space group. (b) PDF analysis of pristine $ZnMnO_2$, derived from total X-ray scattering data collected at room temperature, and refined to the Fm$\bar{3}$m space group.

There has been significant interest in DRX materials as potential cathodes for lithium-ion batteries due to their offering a wide choice of transition metal, high capacity, and small volume change during charging/discharging.[16] In DRX materials, the random distribution of cations across the crystal lattice enables unconventional ion diffusion, making them attractive for ZIBs. Various cations can be doped into Zn-based DRX systems, including Ni, Mg, Co, Fe, and Mn.[18] Among them, Mn was selected in this study due to its range of valence states, redox activity, natural abundance, and as its associated oxides typically exhibit high capacities and high operating voltages in aqueous ZIBs. The extensive research on Mn-based oxides in ZIB provides a solid foundation for further exploration, positioning Mn as a strong candidate for this study.

Table 5.1

The crystal structure data for pristine $ZnMnO_2$ was refined using Rietveld analysis, corresponding to Figure 5.1a. Site occupancies were fixed to the targeted composition of $ZnMnO_2$. The resulting refinement yielded a cell parameter of a = 4.2933(6) Å, with a weighted residual factor R_w = 2.540%.

Atom	Wyckoff position	x	y	z	Occupancy	Uiso
Zn1	4a	0	0	0	0.5	0.0110
Mn1	4a	0	0	0	0.5	0.0061(4)
O1	4b	0.5	0.5	0.5	1	0.0198(2)

Space Group: $Fm\bar{3}m$ a = b = c = 4.2933(6) Å α = β = γ = 90°

The cation-disordered rocksalt material $ZnMnO_2$ was synthesised using ZnO and MnO as precursors. To stabilise ZnO in the rocksalt structure under ambient pressure, offering a compatible rocksalt framework is crucial. MnO is an ideal dopant because of its rocksalt structure and the similar ionic radii of Mn^{2+} (0.82 Å) and Zn^{2+} (0.74 Å). The synthesis presents challenges due to the stability of ZnO's wurtzite structure. Previous studies have shown that

transforming wurtzite ZnO into a rocksalt structure requires high pressure (~7 GPa) and high temperature (700 °C).[18,19]

The mixture of wurtzite ZnO and rocksalt MnO was ball-milled at 750 rpm for 8 hours using a Fritsch high-energy ball mill to form pure DRX $ZnMnO_2$. The high local heat and pressure generated during the ball milling process[20] are essential to induce the phase transformation of wurtzite ZnO into the rocksalt structure. The powder XRD pattern of the resulting DRX $ZnMnO_2$ material (Figure 5.1a and Table 5.1) was analysed using Rietveld refinement. The analysis confirmed that the material conforms to the $Fm\bar{3}m$ cubic rocksalt space group with no impurities and with a lattice parameter of 4.30 Å.

PDF analysis of total X-ray scattering data was conducted for as-synthesised $ZnMnO_2$, as shown in Figure 5.1b. While XRD provides information of the long-range structural ordering of $ZnMnO_2$, PDF analysis allows for examination of the local short-range structure at the atomic scale. The refined PDF data agrees well with the $Fm\bar{3}m$ space group of a disordered rocksalt structure across the entire range from 1 to 20 Å.

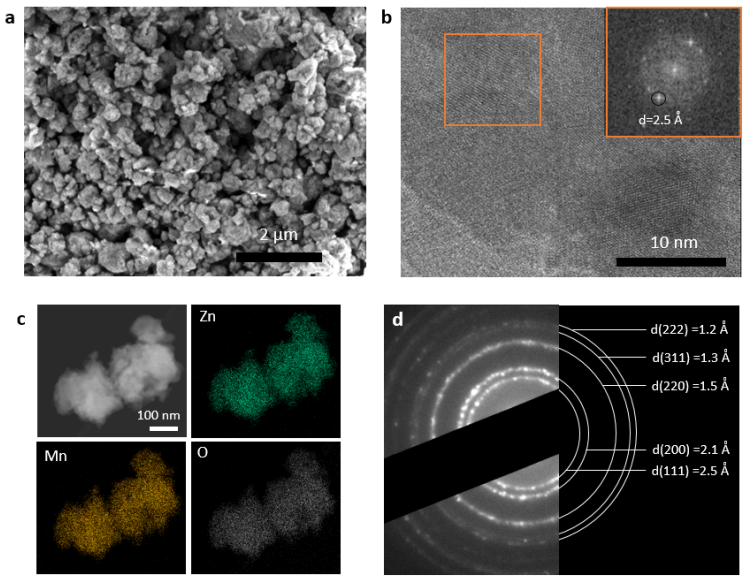

Figure 5.2 (a) SEM image and (b) HRTEM image of pristine $ZnMnO_2$ powder. (c) HAADF-STEM imaging and STEM-EDX mapping illustrating the elemental distribution of Zn, Mn, and O in pristine $ZnMnO_2$. (d) SAED pattern of $ZnMnO_2$ powder.

The agglomerated particle of $ZnMnO_2$ sizes ranged from between 100 to 250 nm, as observed by SEM imaging (Figure 5.2a). HRTEM and its Fourier transform (Figure 5.2b) revealed a lattice spacing of 2.5 Å, corresponding to the (111) plane. The spatial uniformity of the elemental distribution was further confirmed by HAADF-STEM with EDX mapping (Figure 5.2c) which was performed by my supervisor Dr. Alex Robertson. The elements Zn, Mn, and O are evenly distributed throughout the $ZnMnO_2$, with no evidence of segregation into other phases. A SAED pattern from many particles (Figure 5.2d) reveals discrete diffraction rings, consistent with the XRD results and the expected reflections for $ZnMnO_2$.

5.3.2 Cathode Self Dissolution

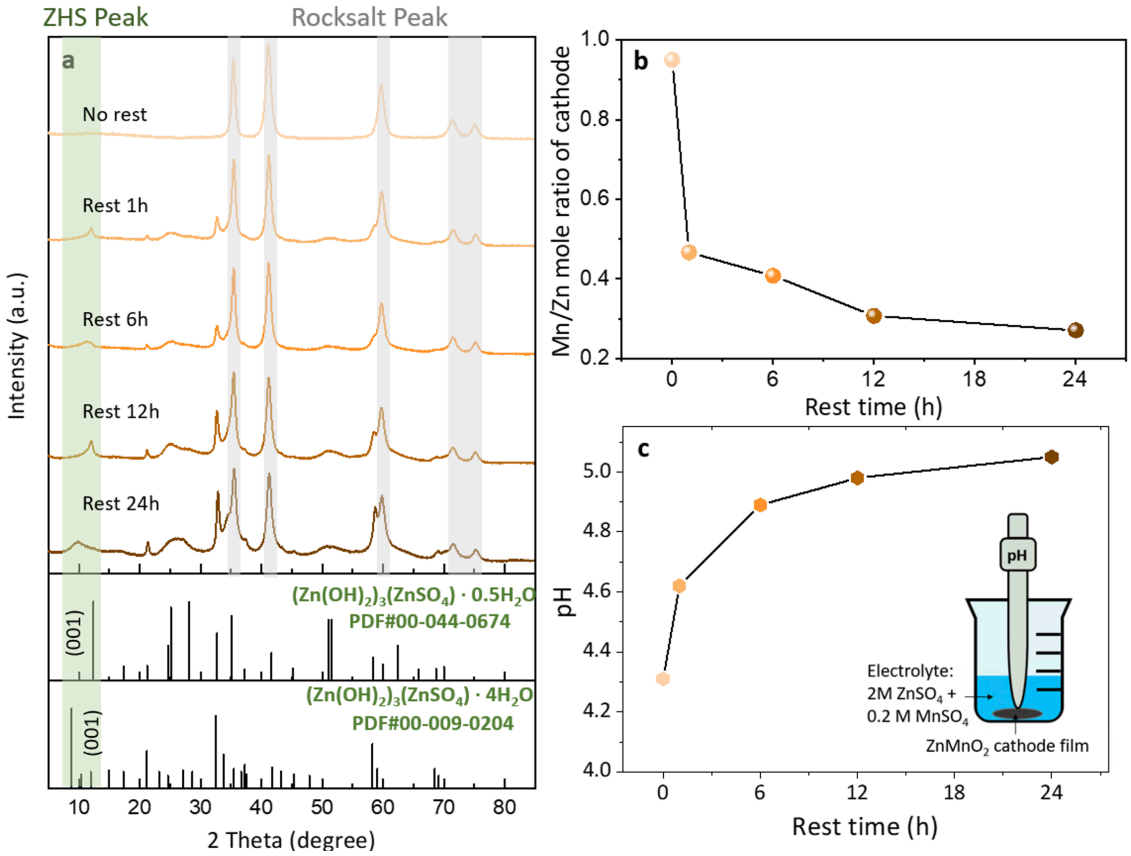

Figure 5.3 (a) Powder XRD patterns of $ZnMnO_2$ after varying resting times in an electrolyte of 2 M $ZnSO_4$ with 0.2 M $MnSO_4$. The peak around 25° can be attributed to Super-P carbon. (b) ICP-OES analysis showing the Mn/Zn ratio of the $ZnMnO_2$ cathode after different resting periods in the same electrolyte. (c) In situ pH measurement near the $ZnMnO_2$ cathode surface while resting in electrolyte of 2 M $ZnSO_4$ with 0.2 M $MnSO_4$ for different times.

Given the inherent instability of Mn(II)-based oxides, which are prone to dissolution in mildly acidic electrolytes,[21] their potential impact on electrochemical performance cannot be overlooked. To investigate this behaviour in DRX $ZnMnO_2$, the material was placed in a coin cell configuration with an electrolyte composed of 2 M $ZnSO_4$ and 0.2 M $MnSO_4$ additive and allowed to rest. Here, "resting" refers to a period during which the material remains in contact with the electrolyte without the application of an external bias. During this resting period, $ZnMnO_2$ was observed to undergo a self-dissolution process.

XRD analysis of the cathode material after various resting times in the aqueous electrolyte reveals that the intensity of peaks corresponding to the corrosion product zinc hydroxide sulphate ($(Zn(OH)_2)_3 \cdot ZnSO_4 \cdot nH_2O$, ZHS) increases over time (Figure 5.3a). After resting for 1 hour, a peak at 12.4° corresponding to the (001) plane of $(Zn(OH)_2)_3 \cdot ZnSO_4 \cdot 0.5H_2O$ (PDF#00-009-0204) is observed. As the resting time extends to 24 hours, an additional peak at 8.8° appears, assigned to the (001) plane of $(Zn(OH)_2)_3 \cdot ZnSO_4 \cdot 4H_2O$ (PDF#00-044-0674). This evolution suggests that with prolonged resting, more water molecules are involved in the formation of hydrated ZHS phases. The self-dissolution process consumes H^+ ions, which increases the local pH and promotes ZHS formation. In situ pH measurements (Figure 5.3c) performed at the cathode surface reveal that the local pH gradually increases with prolonged resting time, eventually stabilising after 6 hours. The proposed chemical reactions in this process are as follows:

$$H_2O \rightarrow H^+ + OH^-$$

$$ZnMnO_2 + 4H^+ \rightarrow Zn^{2+} + Mn^{2+} + 2H_2O$$

$$4Zn^{2+} + SO_4^{2-} + 6OH^- + nH_2O \rightarrow 3Zn(OH)_2 \cdot ZnSO_4 \cdot nH_2O$$

To verify this process, ICP-OES analysis (performed by Dr. Lijiang Song) was conducted on the cathode material after different resting periods (Figure 5.3b). The Mn/Zn molar ratio

of the cathode increases with rest time, corroborating that dissolution of $ZnMnO_2$ occurs during rest accompanied by the formation of ZHS on the cathode.

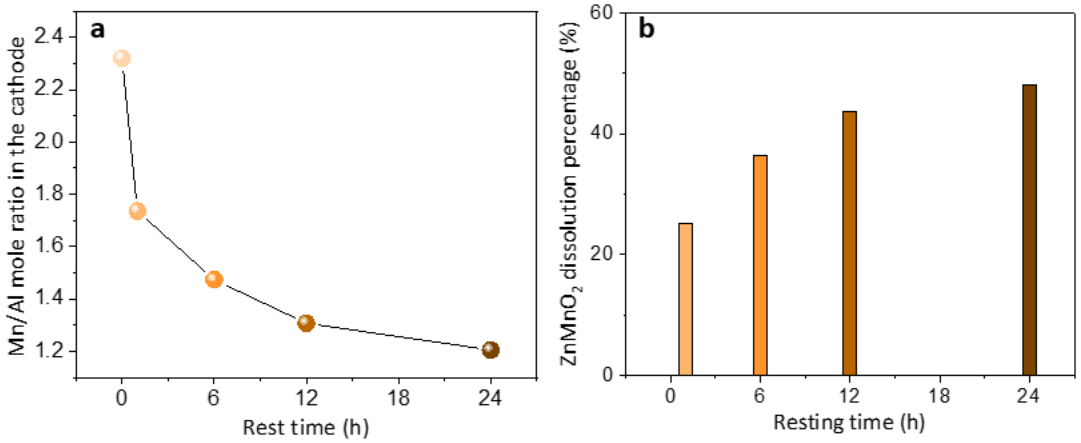

Figure 5.4 (a) ICP-MS analysis showing the Mn/Al molar ratio in the electrode (prepared with $ZnMnO_2$:C:Al_2O_3 at a weight ratio of 7:2:1) after various resting times. (b) Calculated weight percentage of dissolved $ZnMnO_2$ during the resting period.

To quantify the dissolution of $ZnMnO_2$, ICP-MS (performed by Dr. Lijiang Song) was conducted using a reference-material-based internal calibration method. Al_2O_3 was chosen as the reference material due to its excellent chemical stability in mildly acidic aqueous electrolytes. A composite mixture of $ZnMnO_2$ and Al_2O_3 was prepared at a weight ratio of 7:1 and assembled in coin cells with 2 M $ZnSO_4$ + 0.2 M $MnSO_4$ electrolyte. The cells were rested for various durations without applying any electrochemical cycling.

As shown in Figure 5.4a, at the pristine state, the measured Mn/Al molar ratio was 2.32, consistent with the initial composition of the mixture. After 1 hour of rest, the Mn/Al ratio decreased to 1.74, indicating partial dissolution of $ZnMnO_2$ while Al_2O_3 remained stable. Since Al content remains unchanged, the loss of Mn can be used to calculate the degree of $ZnMnO_2$ dissolution, which is determined as: Dissolution (wt%) = (1 – 1.74/2.32) × 100 = 25.2 wt%

This reveals that 25.2 wt% of $ZnMnO_2$ dissolves within just 1 hour. The time-dependent dissolution profile is plotted in Figure 5.4b. It shows a rapid dissolution initially,

reaching 48.1 wt% after 12 hours. Beyond this point, the rate slows, likely due to the gradual rise in local pH near the material surface, which shifts the equilibrium and suppresses further dissolution.

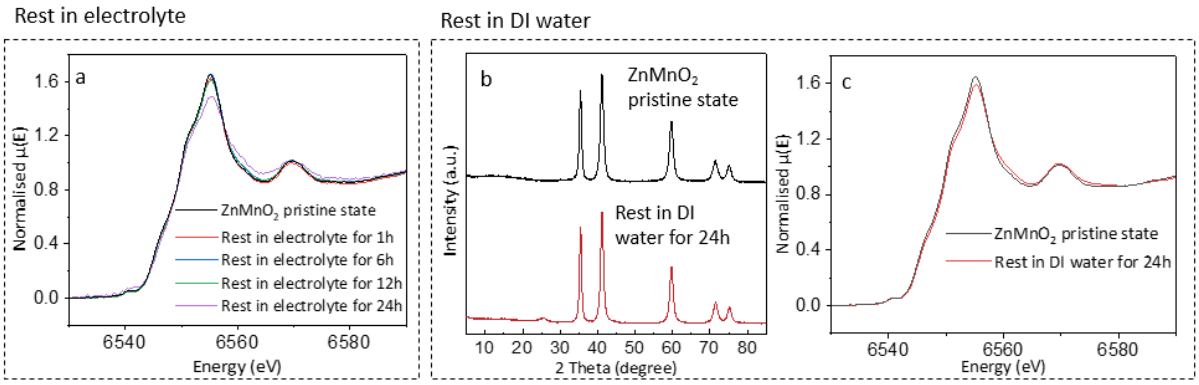

Figure 5.5 (a) Mn K-edge XANES spectra of the $ZnMnO_2$ cathode after resting in the electrolyte for varying time. (b) Powder XRD patterns and (c) Mn K-edge XANES spectra of the $ZnMnO_2$ cathode after resting in DI water for varying time. The peak around 25° can be attributed to Super-P carbon.

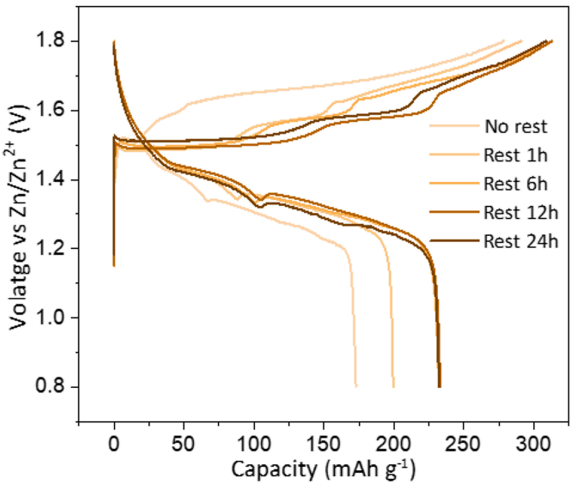

Figure 5.6 The first charge/discharge curves of the $ZnMnO_2$ cathode paired with a Zn metal anode in 2 M $ZnSO_4$ with 0.2 M $MnSO_4$ at a current density of 10 mA g^{-1}, with different resting times prior to operation.

Since part of the cathode material is entirely dissolved while the rest remains the same, this can be viewed as a purely chemical rather than an electrochemical reaction, with the valence state of Mn remaining unchanged. XANES analysis (Figure 5.5a) confirms that the valence state of Mn does not evolve during resting. As a control, the resting behaviour of

$ZnMnO_2$ in DI water was evaluated, showing no formation of ZHS (Figure 5.5b) and no change in Mn valence state (Figure 5.5c). This suggests that $ZnMnO_2$ does not undergo self-dissolution in neutral environments, with self-dissolution requiring the mildly acidic electrolyte.

This significant resting corrosion can be expected to have an influence on the cathode's properties. To investigate the effect of resting time on its electrochemical performance, tests were performed on a full cell comprising a Zn metal anode and a $ZnMnO_2$ cathode in a 2 M $ZnSO_4$ electrolyte with 0.2 M $MnSO_4$ additive (Figure 5.6). The charge voltage profiles revealed differences based on resting time. The "No rest" condition exhibited a higher initial voltage. After a 1-hour resting period, the charging voltage profile displayed lower voltage with two distinct plateaus, a feature that persisted even after 24 hours of resting. The discharge capacity increased progressively with longer resting times, reaching its maximum value after 6 hours of resting.

The observed changes in the charging voltage profile and the increase in discharge capacity with resting time can be attributed to two primary factors:

1. Mn^{2+} ion contribution: The increase in capacity can be attributed to the higher concentration of Mn^{2+} ions in the electrolyte resulting from cathode dissolution. During charging, it is expected that Mn^{2+} in the electrolyte are oxidised and redeposited on the cathode in the form of Mn-based oxide. To confirm the involvement of Mn^{2+}, a comparison experiment was conducted by placing $ZnMnO_2$ in a 2 M $ZnSO_4$ electrolyte without the $MnSO_4$ additive and allowing it to rest for 12 hours (Figure 5.7). The capacity in the electrolyte without the pre-added Mn was lower compared to the same resting time with the $MnSO_4$ additive (Figure 5.7), indicating that the presence of Mn^{2+} ions contribute to capacity. This is consistent with previously reported studies.[22,23] Therefore, as the resting time increases,

more Mn^{2+} ions dissolve into the electrolyte, and participate in the charging process, leading to higher capacity.

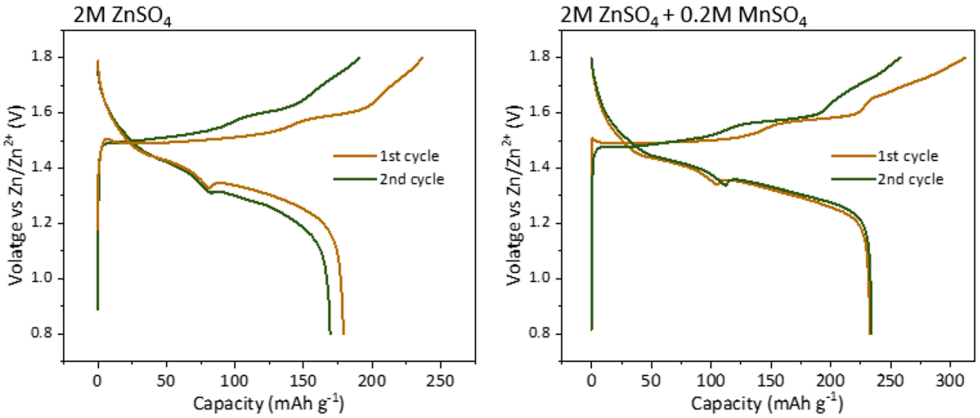

Figure 5.7 First two charge/discharge curve of $ZnMnO_2$ at a current density of 10 mA g^{-1} in the electrolyte 2 M $ZnSO_4$ and 2 M $ZnSO_4$ with 0.2 M $MnSO_4$. The cells were rested for 12 hours before operation.

2. Formation of ZHS: ZHS plays an important role in modulating the voltage profile during charging, as it can act as an OH^- reservoir to suppress pH fluctuations. During charging, the process of oxidation of Mn^{2+} releases H^+ ions, leading to a decrease in pH. In response, ZHS dissolves and releases OH^- ions, effectively buffering pH. In a less acidic environment, the activation energy for Mn^{2+} to redeposit on the cathode as an Mn-based oxide is lower, facilitating more redeposition.[24-27] After resting in the electrolyte for 1 hour, ZHS begins to form on the cathode, lowering the oxidation voltage and promoting oxide redeposition, which leads to an increase in capacity. As the resting time increases, more ZHS is formed, further facilitating Mn oxide redeposition, which continues to improve the capacity until stabilising after 6 h resting.

Since ZHS formation and cathode dissolution occur simultaneously, their individual contributions are difficult to decouple. For consistency, unless otherwise specified, all subsequent electrochemical performance tests and characterisations were conducted after a 12-hour resting period.

5.3.3 Electrochemical Performance

The electrochemical performance $ZnMnO_2$ cathode was further assessed (Figure 5.8). The performance of anode-free cells using a carbon paper anode will be shown in Figure 5.18.

Cyclic voltammetry (CV) was performed over the first five cycles to investigate the electrochemical redox behaviour of $ZnMnO_2$ (Figure 5.8a). In the initial cycle, two anodic peaks appear at 1.55 V and 1.6 V (vs. Zn/Zn^{2+}), corresponding to the stepwise oxidation of Mn species. During subsequent cycles, both anodic peaks broaden, with the 1.55 V peak gradually decreasing in intensity and the 1.6 V peak shifting slightly to higher potential. This evolution suggests that structural change occurs during the initial cycles, which is confirmed by ex-situ XRD presented later in Figure 5.9.

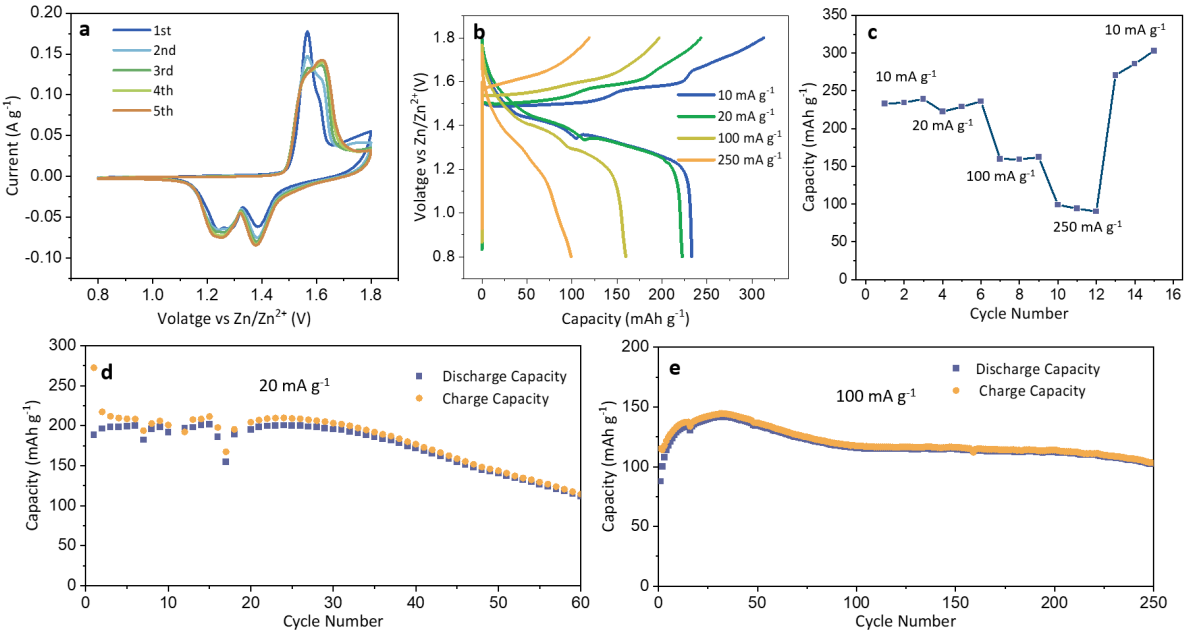

Figure 5.8 Electrochemical and charge-discharge cycling characterisation of DRX $ZnMnO_2$. (a) CV of $ZnMnO_2$ at a scan rate of 0.05 mV s^{-1}. (b) The charge/discharge curves of $ZnMnO_2$ at various current densities within the voltage range of 0.8-1.8 V vs. Zn/Zn^{2+}. (c) Rate performance of discharge capacity of $ZnMnO_2$ at current densities of 10, 20, 100, and 250 mA g^{-1}. Cycling performance of $ZnMnO_2$ at (d) low current density (20 mA g^{-1}) and (e) high current density (100 mA g^{-1}). All cells utilised a $ZnMnO_2$ cathode paired with a Zn metal anode in an electrolyte of 2 M $ZnSO_4$ with 0.2 M $MnSO_4$. All cells were rested for 12 h before operation.

The cathode's rate capability was tested at current densities of 10, 20, 100, and 250 mA g^{-1}. Galvanostatic charge/discharge curves are shown in Figure 5.8b, corresponding to the first, fourth, seventh, and tenth cycles in Figure 5.8c. At a current density of 10 mA g^{-1}, the charging capacity reaches 312.8 mAh g^{-1}. Some capacity is lost during discharging however, with the discharge capacity reaching 233 mAh g^{-1} at 10 mA g^{-1}. At a higher current density of 250 mA g^{-1}, the discharge capacity decreases further, to 99 mAh g^{-1}.

The extended cycling performance of $ZnMnO_2$ was evaluated at a current density of 20 mA g^{-1} and 100 mA g^{-1} (Figure 5.8d-e). At both current densities, the capacity initially increases during the first few cycles, followed by a gradual decay. This "activation process" is related to gradual structural changes to spinel phase, which will be discussed later. Notably, cycling $ZnMnO_2$ at 100 mA g^{-1} demonstrated superior capacity retention over 250 cycles, in contrast to cycling at 20 mA g^{-1}, which showed reduced retention over 60 cycles.

The performance of $ZnMnO_2$ is compared with zinc-containing cathodes that can be charged first in Table 5.2. The discharge capacity of $ZnMnO_2$ (233 mAh g^{-1}) outperforms $ZnMn_2O_4$ (120 mAh g^{-1}),[6] $Zn_{0.56}VOPO_4{\cdot}2H_2O$ (104.2 mAh g^{-1}),[10] and $Zn_3[Fe(CN)_6]_2$ (65.4 mAh g^{-1}).[12] While $Zn_3V_3O_8$ shows a higher discharge capacity of 285 mAh g^{-1},[8] it operates at a lower average discharge voltage (0.7-0.8 V) compared to $ZnMnO_2$ (1.36 V). This combination of high capacity and high discharge voltage gives $ZnMnO_2$ a superior energy density of 318.1 Wh kg^{-1} based on cathode mass, exceeding those of $ZnMn_2O_4$ (202 Wh kg^{-1}),[6] $Zn_{0.56}VOPO_4{\cdot}2H_2O$ (152.6 Wh kg^{-1}),[10] and $Zn_3[Fe(CN)_6]_2$ (100 Wh kg^{-1}).[12] Furthermore, compared to the more widely studied cathodes, the energy density of $ZnMnO_2$ exceeds that of $Zn_{0.25}V_2O_5{\cdot}nH_2O$ (250 Wh kg^{-1})[28] and V_2O_5 (175.2 Wh kg^{-1}),[29] although it is still lower than that of the incumbent Mn-based cathodes, MnO_2 (410.4 Wh kg^{-1})[30] and O_d-MnO_2 (470 Wh kg^{-1}).[31] These results emphasise the advantages of $ZnMnO_2$ in offering a well-balanced combination of high

capacity, high voltage, and competitive energy density, positioning it as a promising cathode material for aqueous ZIB.

Table 5.2 Performance comparison of $ZnMnO_2$ with reported Zn-containing cathodes and other cathodes, all operating in aqueous electrolytes of moderate concentration.

	Cathode material	Electrolyte	Discharge capacity (mAh g^{-1})	Average discharge voltage (V)	Energy density Based on cathode mass (Wh kg^{-1})	Capacity retention and cycling performance	Ref
Zn contained cathode (can be charged first)	**$ZnMnO_2$ (this work)**	2 M $ZnSO_4$ + 0.2 M $MnSO_4$	233 at 10 mA g^{-1}	1.36	318.1	Almost 100% at 100 mA g^{-1} after 250 cycles 60.6% at 20 mA g^{-1} after 60 cycles	-
	$ZnMn_2O_4$	3 M $Zn(CF_3SO_3)_2$	120 at 50 mA g^{-1}	1.35	202	94% at 500 mA g^{-1} after 500 cycles	6
	$Zn_3V_3O_8$	saturated $Zn(CF_3SO_3)_2$	285 at 150 mA g^{-1}	0.7-0.8	-	72.6% at 5 A g^{-1} after 2000 cycles	8
	$Zn_{0.56}VOPO_4{\cdot}2H_2O$	3 M $Zn(CF_3SO_3)_2$	104.2 at 50 mA g^{-1}	1.46	152.6	96% at 1 A g^{-1} after 400 cycles	10
	$Zn_3V_4(PO_4)_6$	3 M $Zn(CF_3SO_3)_2$	105.2 at 22.12 mA g^{-1}	1.5	157.8	Almost 100% at 110.6 mA g^{-1} after 250 cycles	11
	$Zn_3[Fe(CN)_6]_2$	1 M $ZnSO_4$	65.4 at 60 mA g^{-1}	1.7	100	76% at 60 mA g^{-1} after 100 cycles 91% at 300 mA g^{-1} after 100 cycles	12
	$ZnMn_2(PO_4)_2$	1 M $Zn(CF_3SO_3)_2$	67 at 15 mA g^{-1}	1.5	100.5	99.5% at 15 mA g^{-1} after 50 cycles	14
	Zn_2MoO_3	saturated $Zn(CF_3SO_3)_2$	86 at 100 mA g^{-1}	0.4-0.5	-	Almost 100% at 100 mA g^{-1} after 90 cycles	15
Other cathode (need to be discharged first)	V_2O_5	1 m $Zn(CF_3SO_3)_2$	292 at 100 mA g^{-1}	0.6	175.2	36% at 100 mA g^{-1} after 90 cycles	27
	$Zn_{0.25}V_2O_5{\cdot}nH_2O$	1 M $ZnSO_4$	282 at 300 mA g^{-1}	0.8-0.9	250	>80% at 2.4 A g^{-1} after 1000 cycles	28
	$V_2O_5{\cdot}4VO_2{\cdot}2.72\ H_2O$	3 M $Zn(CF_3SO_3)_2$	567 at 100 mA g^{-1}	0.66	375	94.0% at 10 A g^{-1} after 1000 cycles	29
	MnO_2	2 M $ZnSO_4$ + 0.1 M $MnSO_4$	285 at 101.7 mA g^{-1}	1.44	410.4	92% at 1.525 A g^{-1} after 5000 cycles	30
	O_d-MnO_2	1 M $ZnSO_4$ + 0.1 M $MnSO_4$	345 at 200 mA g^{-1}	1.36	470	Almost 100% at 200 mA g^{-1} after 100 cycles 84% at 5 A g^{-1} after 2000 cycles	31

5.3.4 Energy Storage Mechanism

The energy storage mechanism of the DRX $ZnMnO_2$ cathode was investigated by analysing its structural and valence changes. Structural changes were determined using ex-situ powder XRD (Figure 5.9b-c). At the pristine stage, after resting in the electrolyte for 12 hours, the cathode contained the original DRX material plus formed ZHS due to cathode dissolution during resting, as discussed alongside Figure 5.3. As the cell reached a half-charge state, the intensity of the ZHS-related peaks decreased. By the time the cell was fully charged, the ZHS peaks had disappeared entirely, indicating that ZHS dissolved during charging. Since

no electron transfer occurs during the ZHS dissolution process, ZHS itself does not contribute to the overall capacity during charging.

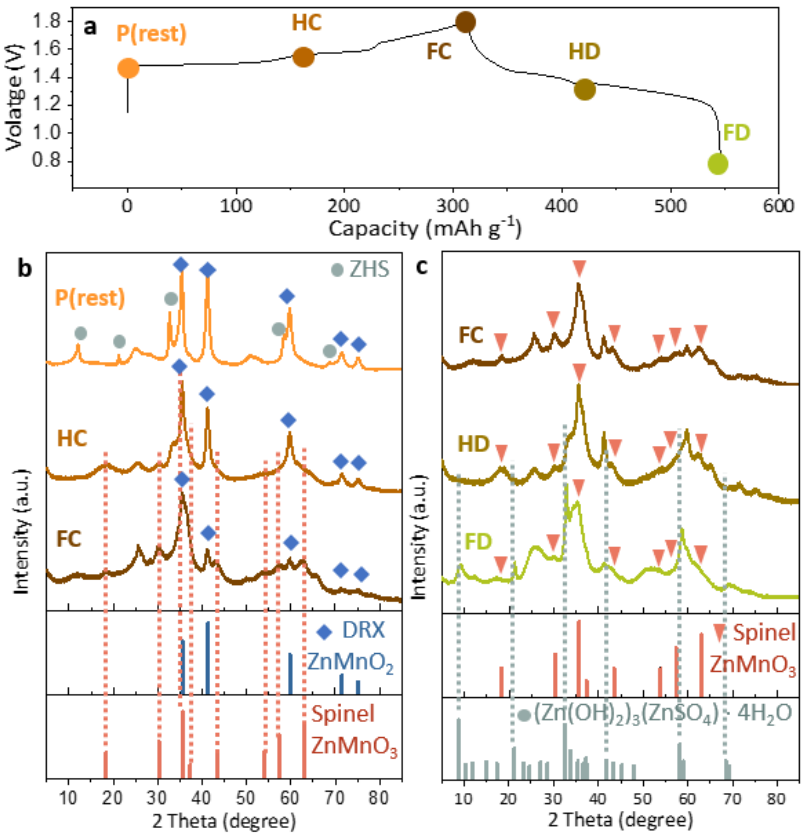

Figure 5.9 (a) Initial charge/discharge curve of $ZnMnO_2$ at a current density of 10 mA g^{-1} in 2 M $ZnSO_4$ with 0.2 M $MnSO_4$ electrolyte. (b) Powder XRD of the cathode at various charge states and (c) at various discharge states, with corresponding states marked in (a). The peak around 25° can be attributed to Super-P carbon. The labels in the figure are: P (rest) for the pristine state after resting in the electrolyte for 12 hours, HC for half charge, FC for full charge, HD for half discharge, and FD for full discharge.

Interestingly, at full charge, the DRX cathode partially transformed into a spinel phase, with 90.8 wt% spinel and 9.2 wt% rocksalt remaining, as determined by XRD refinement (Figure 5.10 and Table 5.3). Based on refinement of the XRD pattern, the composition of the spinel phase is determined to be $Zn_{0.79}Mn_{1.11}O_3$, as shown in Table 5.3. Given its non-stoichiometric nature, this phase is referred to as $Zn_xMn_yO_3$. XRD of the discharged sample (Figure 5.9c) shows the spinel phase remained stable throughout the discharge process and

did not revert to the original DRX structure, indicating that this phase transformation from DRX to spinel is irreversible. The XRD also shows that ZHS reformed due to local pH changes.

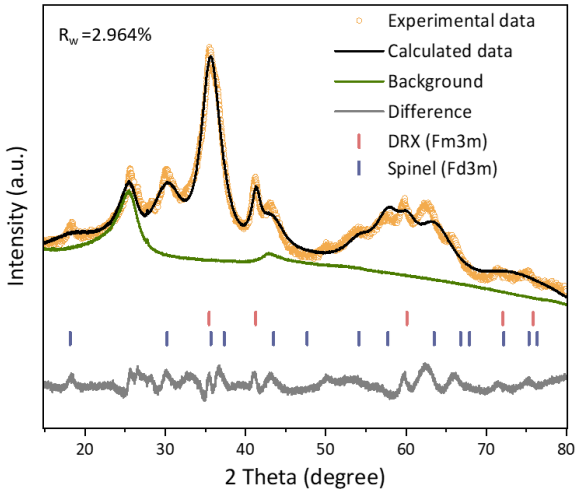

Figure 5.10 Rietveld refinement of the fully charged $ZnMnO_2$ cathode at 1.8 V of first cycle in 2 M $ZnSO_4$ with 0.2 M $MnSO_4$ electrolyte. Detailed structure data is shown in Tables 5.3. The background is from super-P carbon.

Table 5.3

Diffraction data for the $ZnMnO_2$ cathode after the first charge was refined using Rietveld analysis, as shown in Figure 5.10. The refinement yielded a weighted residual factor of R_w = 2.694%. The cathode consists of two phases: disordered rocksalt $ZnMnO_2$ and spinel phase $Zn_xMn_yO_3$.

The crystal structure data for the disordered rocksalt $ZnMnO_2$ phase is as follows:

Atom	Wyckoff position	x	y	z	Occupancy	Uiso
Zn1	4a	0	0	0	0.5	0.0111(2)
Mn1	4a	0	0	0	0.5	0.0081(8)
O1	4b	0.5	0.5	0.5	1	0.0037(8)

Space Group: $Fm\bar{3}m$ a = b = c = 4.3155(9) Å α = β = γ = 90°

Phase weight fraction: 9.2%

The site occupancy of Zn and Mn, as well as the position of O, were refined. The crystal structure data for the spinel $Zn_xMn_yO_3$ phase is as follows:

Atom	Wyckoff position	x	y	z	Occupancy	Uiso
Zn1	8a	-0.125	-0.125	-0.125	0.842(8)	0.0019(3)
Zn2	16d	0.5	0.5	0.5	0.106	0.0422(7)
Mn1	16d	0.5	0.5	0.5	0.741(3)	0.0143(3)
O1	32e	0.2644(7)	0.2644(7)	0.2644(7)	1	0.0042(7)

Space Group: $Fd\bar{3}m$ a = b = c = 8.2178(5) Å α = β = γ = 90°

Phase weight fraction: 90.8%

The composition of $Zn_xMn_yO_3$ after the first charge is $Zn_{0.79}Mn_{1.11}O_3$.

To further confirm the cathode composition at the top of charge, ICP-OES (performed by Dr. Lijiang Song) was conducted on cathode (Figure 5.11) and compared with quantitative phase analysis obtained from XRD Rietveld refinement. The refinement results show that the charged cathode consists of 90.8 wt% of spinel-type $Zn_{0.79}Mn_{1.11}O_3$ and 9.2 wt% of residual DRX $ZnMnO_2$.

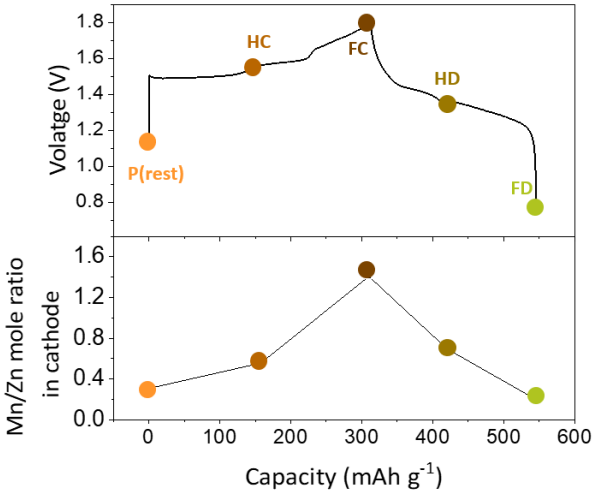

Figure 5.11 ICP-OES results indicating the Mn/Zn ratio in the $ZnMnO_2$ cathode material during the initial charge/discharge cycle at a current density of 10 mA g^{-1}. The cells were rested for 12 h before operation.

Assuming the total mass of the cathode is *m* mg, the mass of each component is 0.908·*m* mg for $Zn_{0.79}Mn_{1.11}O_3$ and 0.092·*m* mg for $ZnMnO_2$. Using the respective molar masses (160.63 g mol^{-1} for $Zn_{0.79}Mn_{1.11}O_3$ and 152.32 g mol^{-1} for $ZnMnO_2$), the molar quantities of each phase are calculated as:

Moles of $Zn_{0.79}Mn_{1.11}O_3$: (0.908·*m*)/160.63

Moles of $ZnMnO_2$: (0.092·*m*)/152.32

From these, the total Zn and Mn content can be determined:

Total Zn = [(0.908·*m*)/160.63]×0.79+[(0.092·*m*)/152.32]

Total Mn = [(0.908·*m*)/160.63]×1.11+[(0.092·*m*)/152.32]

The molar ratio of Mn to Zn is therefore:

Total Mn/ Total Zn ≈1.357

This calculated ratio aligns well with the experimental Mn/Zn molar ratio of 1.407 obtained from ICP-OES (performed by Dr. Lijiang Song, Figure 5.11), indicating strong agreement between structural and compositional data.

To further elucidate the redox mechanism, lattice changes related with Zn deintercalation/intercalation was confirmed by XRD data. Focusing on the (200) plane around 41° and the (311) and (222) planes near 72°-75° for the DRX phase, unit cell changes related to Zn^{2+} movement was monitored (Figure 5.12a). The negligible change in the unit cell during charging and discharging indicates that Zn^{2+} cannot be effectively deintercalated from the DRX structure due to limited zinc-ion diffusion in the close-packed face-centered cubic lattice.[32] In contrast, the in situ-formed spinel phase enables reversible Zn^{2+} intercalation and deintercalation. This is evidenced by spinel phase peaks at the (220) plane around 30° and the (440) plane around 63° during the first discharge (Figure 5.12b), which exhibit subtle peak shifts indicative of unit cell expansion associated with Zn^{2+} intercalation.

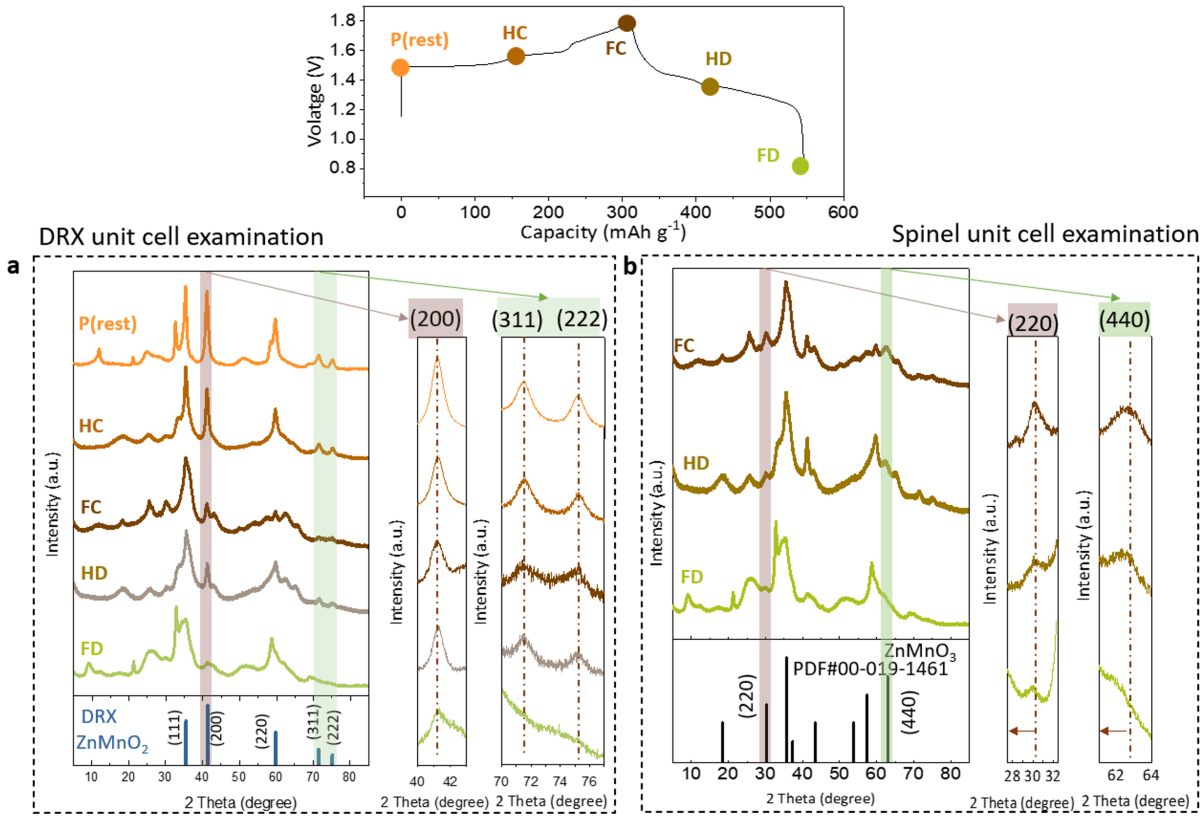

Figure 5.12 (a) XRD pattern focusing on the DRX peak (200) plane around 41° and the (311) and (222) planes near 72°-75°, illustrating negligible lattice change during the first cycle with corresponding states marked in electrochemistry curve. (b) XRD pattern focusing on the spinel peak (220) plane near 30° and (440) plane around 63°, illustrating slight lattice expansion caused by Zn ion intercalation during the first discharge with corresponding states marked in electrochemistry curve.

The irreversible phase transition from DRX to a spinel phase reveals a parallel between Zn- and Li-based DRX materials. In Li-ion batteries, Mn-rich DRX cathodes undergo an in-situ transformation to a spinel-like ordering during cycling, named as the "δ-phase" by the Ceder group.[33,34] This transformation is accelerated by higher Mn content due to the enhanced mobility of Mn,[34] and further studies confirm that the transition is both thermodynamically favourable and kinetically accessible, but only happen in the delithiated DRX state.[35] In contrast, Zn-based DRX $ZnMnO_2$ shows a divergence: Zn^{2+} remains trapped in the DRX structure because it cannot deintercalate, leaving no vacancies for Mn migration. This raises the question as to nature of the driving force behind the transition from DRX $ZnMnO_2$ to

$Zn_xMn_yO_3$ spinel, which needs further research. Notably, a similar phenomenon has been observed in MnS rocksalt cathodes in aqueous ZIBs, where a transition to $ZnMnO_3$ spinel occurs during charging,[36] suggesting that a different mechanism may exist in aqueous ZIB systems.

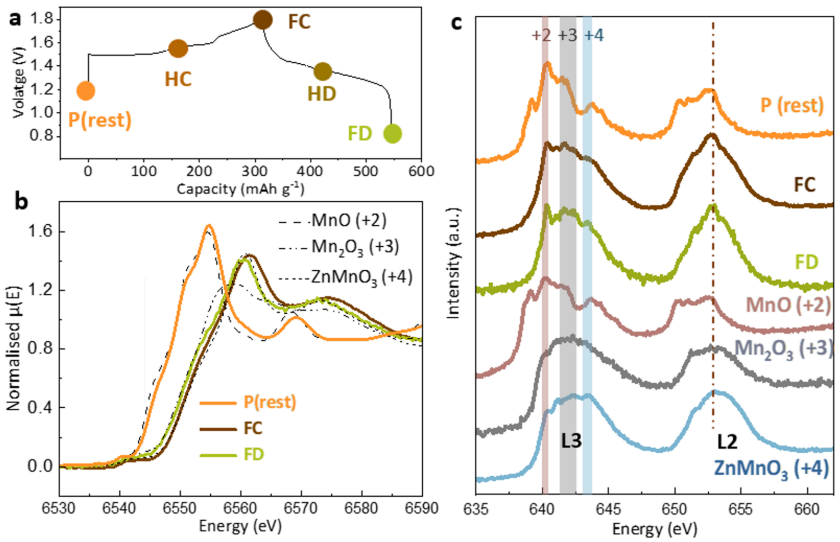

Figure 5.13 (a) Initial charge/discharge curve of $ZnMnO_2$ at a current density of 10 mA g^{-1} in 2 M $ZnSO_4$ with 0.2 M $MnSO_4$ electrolyte. (b) Mn K-edge XANES spectra of the cathode, and (c) Mn L-edge XAS spectra of the cathode collected in IPFY mode at various charge states, with corresponding states marked in (a). All cells were rested for 12 hours before operation.

To understand the redox behaviour of Mn, Mn K-edge XANES measurements were conducted for pristine after 12 h rest (P(rest)), fully charged (FC) and fully discharged (FD) states of charge of the $ZnMnO_2$ cathode (Figure 5.13b). Linear combination fitting (LCF) was used to estimate the valence state of Mn in the electrode. Initially, the Mn valence was 2.04. After the first charge, it increased to 3.72, corresponding to a transfer of 1.68 electrons per metal centre. However, after discharge, the Mn valence only reduced to 3.55 and did not return to its initial state. Complementary soft XAS experiments were conducted to characterise the Mn L-edge using IPFY mode (Figure 5.13c), which effectively mitigates Mn self-absorption artifacts. The crystal field splitting in the L_3 region allows the discrimination of

multiplet features,[37] where the peaks at 640.3 eV, 642 eV, and 643.5 eV are assigned to Mn^{2+}, Mn^{3+} and Mn^{4+}, respectively, in good agreement with previously reported studies.[37,38] The spectra confirmed Mn^{2+} existence in the pristine state and the Mn^{2+}/Mn^{4+} redox couple is involved during charging. Notably, even at the top of charge, Mn^{2+} signals remain. This is consistent with XRD results showing that a small fraction of DRX persists, retaining Mn^{2+}. During discharge, the Mn valence only slightly decreases, which cannot fully account for the delivered capacity. The combined results from XRD, XANES and IPFY measurements suggest that while reversible Zn intercalation/deintercalation in the spinel phase contributes to energy storage, an additional mechanism is responsible for the majority of the capacity.

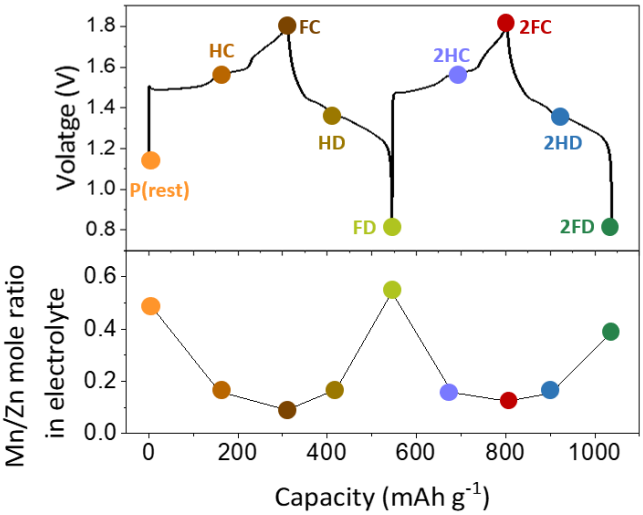

Figure 5.14 First two charge/discharge curve of $ZnMnO_2$ at a current density of 10 mA g^{-1} in 2 M $ZnSO_4$ with 0.2 M $MnSO_4$ electrolyte, along with ICP-OES results showing the Mn/Zn ratio in the electrolyte soaked in separators.

One possible route involves the oxidation of Mn^{2+} to Mn^{4+} during charging and the reduction of Mn^{4+} to Mn^{2+} during discharging, accompanied by its dissolution into the electrolyte. To investigate this, the electrolyte in the separator was analysed using ICP-OES (performed by Dr. Lijiang Song, see Figure 5.14). The initial Mn/Zn molar ratio, prior to cycling but after the cell having rested for 12 hours, was 0.49, compared to 0.1 in the non-resting state, due to the dissolution of $ZnMnO_2$ into the electrolyte. The Mn/Zn ratio during the

charging process decreased as $ZnMnO_2$ reacted with Mn^{2+} and water to form the $Zn_xMn_yO_3$ spinel. However, during discharge, Mn^{2+} dissolved back into the electrolyte, causing the Mn/Zn ratio to return to a value similar to that of the pristine state. This reversible change in the Mn/Zn ratio of electrolyte during charging and discharging indicates that this dissolution and deposition process dominates energy storage. ICP-OES analysis of the electrolyte at second cycle (Figure 5.14) showed a similar reversible pattern, with the Mn/Zn ratio decreasing during charging and increasing during discharging, further confirming that the majority of capacity is derived from this dissolution and (re-)deposition mechanism. The proposed reaction formula for this process is as follows:

First charge:

$$H_2O + (y\text{-}1)\ Mn^{2+} + ZnMnO_2 - (6\text{-}2x\text{-}2y)\ e^- \rightarrow Zn_xMn_yO_3 + 2H^+ + (1\text{-}x)\ Zn^{2+}$$

$$3Zn(OH)_2{\cdot}ZnSO_4{\cdot}nH_2O \rightarrow 4Zn^{2+} + SO_4^{2-} + 6OH^- + nH_2O$$

First discharge and following cycle:

$$Zn_xMn_yO_3 + 6H^+ + (6\text{-}2x\text{-}2y)\ e^- \rightleftharpoons 3H_2O + yMn^{2+} + xZn^{2+}$$

$$4Zn^{2+} + SO_4^{2-} + 6OH^- + nH_2O \rightleftharpoons 3Zn(OH)_2{\cdot}ZnSO_4{\cdot}nH_2O$$

Since the energy storage mechanism has been identified as a reversible Mn dissolution–deposition process and shows clear reversibility by the second cycle (Figure 5.14), structural and valence state analyses were conducted to further elucidate the associated phase and redox behaviour (Figure 5.15). XRD patterns collected during the second charge–discharge cycle (Figure 5.15c) indicate that the cathode retains its spinel structure, confirming that the initial phase transition from DRX to spinel during the first charge is irreversible. Subtle shifts in the spinel XRD peaks—contraction during charging and expansion during discharging—indicate that a limited amount of Zn^{2+} intercalation/deintercalation occurs within the spinel structure. This is further supported by XANES analysis (Figure 5.15b), which

reveals only minor changes in Zn valence state, confirming that Zn^{2+} intercalation contributes modestly to the overall capacity.

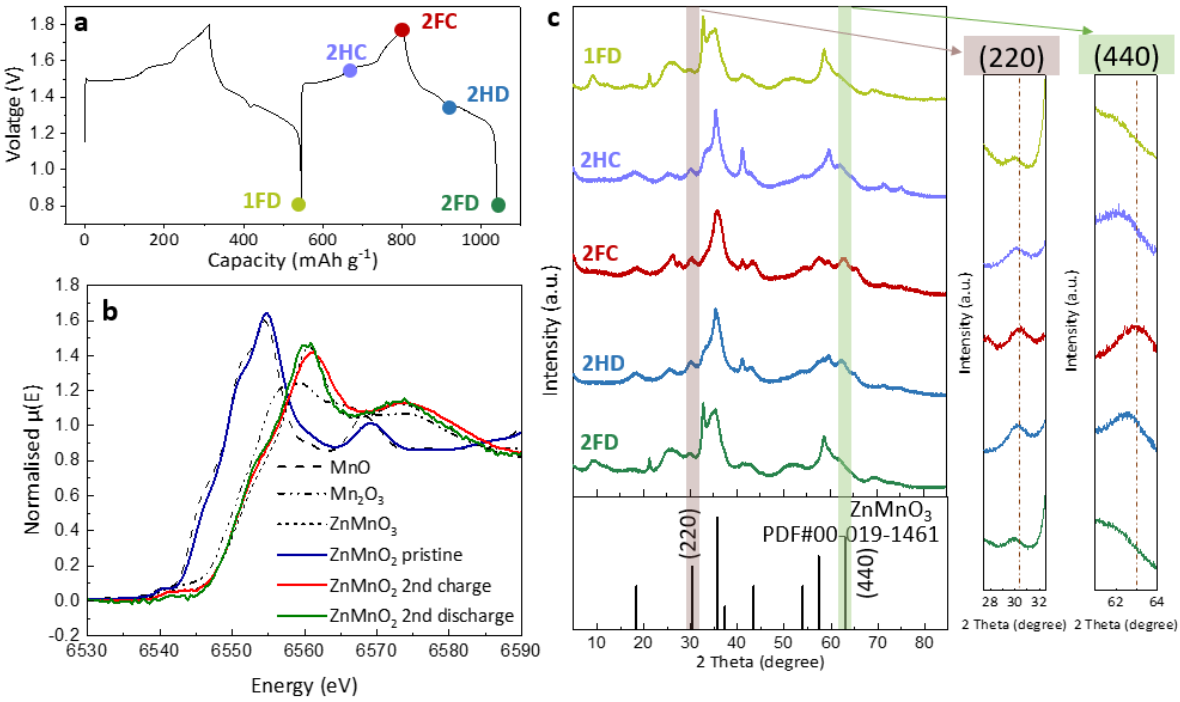

Figure 5.15 (a) First two charge/discharge curves of $ZnMnO_2$ at a current density of 10 mA g^{-1}. (b) Mn K-edge XANES spectra of the cathode during the second cycle. (c) Powder XRD patterns of the cathode at various charge/discharge states in the second cycle, with corresponding states marked in the same colour as in (a). The XRD analysis of the spinel peak (220) plane around 30° and (440) plane around 63° highlights lattice contraction and expansion caused by Zn ion deintercalation and intercalation.

Interestingly, with continued cycling, the residual DRX phase gradually diminishes and eventually transforms entirely into the spinel phase. Rietveld refinement of the cathode after 15 cycles (Figure 5.16 and Table 5.4) at the top of charge reveals diffraction peaks corresponding exclusively to the $Zn_xMn_yO_3$ spinel, with no detectable DRX phase remaining. The refined composition, $Zn_{0.83}Mn_{1.12}O_3$, corresponds to a Mn/Zn ratio of 1.349, which is in excellent agreement with the ICP-OES-derived ratio of 1.318, confirming the consistency between structural and elemental analyses.

This gradual transformation from DRX to spinel during repeated cycling suggests that the spinel phase eventually becomes the dominant structure. The formation of the spinel

phase during cycling likely contributes to the observed capacity increase in the initial cycles, as it enables greater Zn^{2+} intercalation/deintercalation (Figure 5.8d-e). Additionally, this phase transition may account for the gradual peak shifts observed in the CV curves (Figure 5.8a).

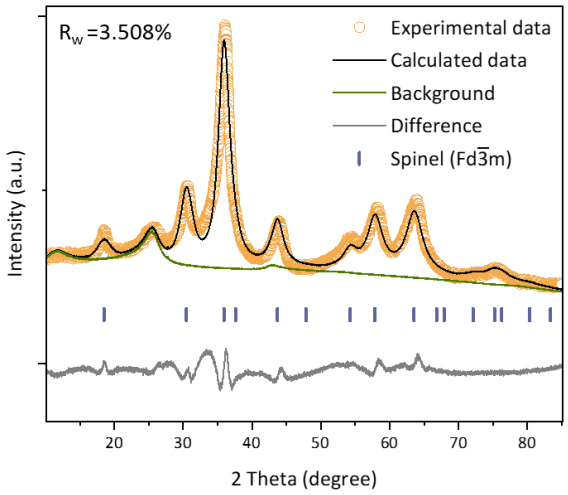

Figure 5.16 Rietveld refinement of the fully charged $ZnMnO_2$ cathode at 1.8 V in an electrolyte of 2 M $ZnSO_4$ with 0.2 M $MnSO_4$ after 15 cycles at a current density of 10 mA g^{-1}. Detailed structure data is shown in Table 5.4. The background is from super-P carbon.

Table 5.4

Diffraction data for the $ZnMnO_2$ cathode after the 15 cycles at full charge was refined using Rietveld analysis, as shown in Figure 5.16. The refinement yielded a weighted residual factor of R_w = 3.508%. The diffraction data only contain spinel phase $Zn_xMn_yO_3$.

The site occupancy of Zn and Mn, as well as the position of O, were refined. The crystal structure data for the spinel $Zn_xMn_yO_3$ phase is as follows:

Atom	Wyckoff position	x	y	z	Occupancy	Uiso
Zn1	8a	-0.125	-0.125	-0.125	0.834(4)	0.0047(4)
Zn2	16d	0.5	0.5	0.5	0.133(9)	0.2492(6)
Mn2	16d	0.5	0.5	0.5	0.744(7)	0.0092(7)
O1	32e	0.2592(2)	0.2592(2)	0.2592(2)	1	0.0009(3)

Space Group: $Fd\bar{3}m$ a = b = c = 8.2628(6) Å α = β = γ = 90°

The refined composition is $Zn_{0.83}Mn_{1.12}O_3$.

The proposed storage mechanism of $ZnMnO_2$ DRX cathode is summarised in Figure 5.17. When the cathode is resting in a mildly acidic electrolyte the $ZnMnO_2$ will partially dissolve and ZHS will be formed as the local pH increases due to proton consumption. During the first charge, the DRX $ZnMnO_2$ undergoes an irreversible phase transition to a $Zn_xMn_yO_3$ spinel structure, while the ZHS dissolves. In subsequent cycles, the spinel phase becomes the dominant cathode material, unlocking the ability to store charge via Zn^{2+} intercalation/deintercalation, but mainly storing energy through the dissolution and deposition of Mn.

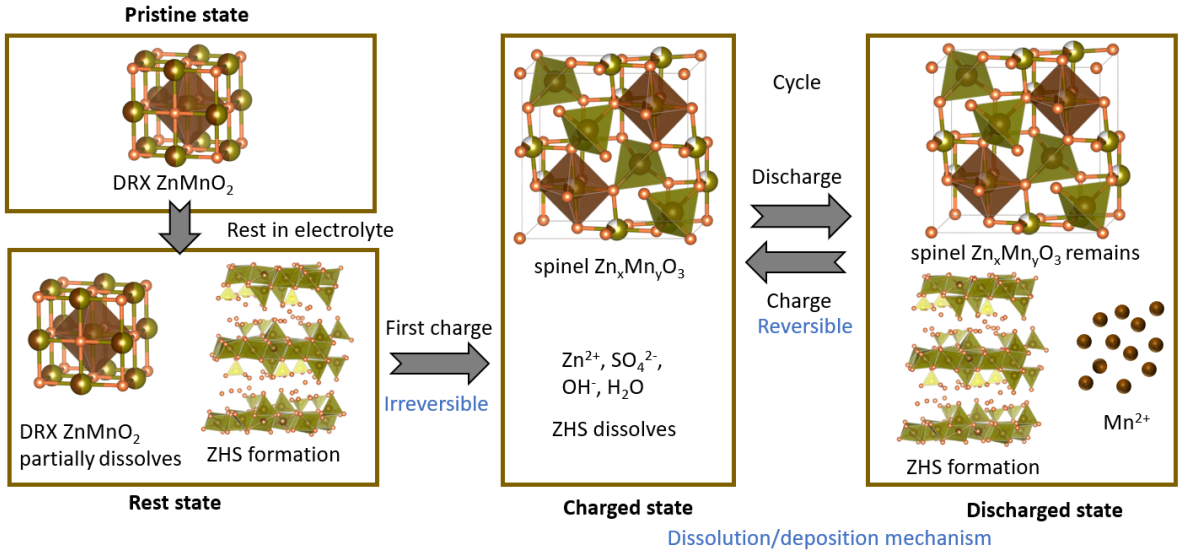

Figure 5.17 Schematic of the energy storage mechanism for the $ZnMnO_2$ DRX cathode in a ZIB.

5.3.5 Anode Free ZIBs

To further explore the potential of Zn-containing cathodes, their performance in Zn metal-free configurations was investigated. In a standard ZIB (Figure 5.18a), the Zn anode reacts with the aqueous electrolyte over time, leading to capacity loss and a deterioration of its shelf life. In this study, the Zn anode thickness reaches up to 180 µm, which corresponds to a high N/P ratio of 50 for a Zn/$ZnMnO_2$ cell, which is a commonly reported value in several studies.[2,3,39,40] By contrast, the anode-free ZIB (Figure 5.18a) reduces the N/P ratio to

effectively zero by eliminating the Zn metal anode. The lack of Zn metal on the initial anode prevents the hydrogen evolution reaction and Zn corrosion when the cell is idle, which improves the cell shelf life.

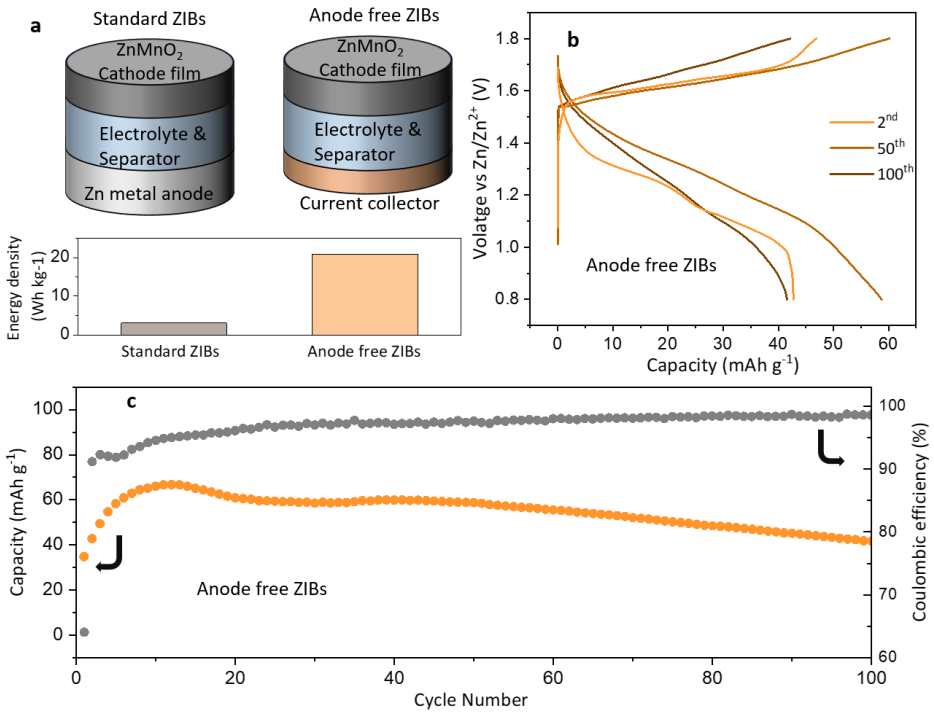

Figure 5.18 (a) Schematic of standard and anode-free ZIB using $ZnMnO_2$ DRX cathode and their energy density based on the total mass of both cathode and anode. (b) The charging/discharging curve of $ZnMnO_2$ based anode-free ZIB with carbon paper as the current collector at 100 mA g^{-1}. (c) Cycling performance of $ZnMnO_2$ based anode-free ZIB at 100 mA g^{-1}, showing the discharge capacity and coulombic efficiency. All cells were rested for 12 h before operation.

In this study, the standard ZIB electrolyte of 2 M $ZnSO_4$ with 0.2 M $MnSO_4$ was used, which is cheap and safe. The only modification of our anode-free cell was the replacement of the Zn metal anode with a carbon paper current collector. The charging/discharging profile of the anode-free ZIB closely resembles that of a standard ZIB (Figure 5.18b), indicating similar redox processes. Across repeated cycling, the anode-free ZIB showed good capacity retention at 100 mA g^{-1} over 100 cycles and a coulombic efficiency exceeding 91.16% after the second cycle (Figure 5.18c). However, compared to the performance of the cell using a Zn foil anode

(Figure 5.8), there is a modest degradation. This is attributed to the limited Zn source in the anode-free setup, meaning any Zn lost due to side reactions or irreversible plating/stripping is unable to be replaced from the deep reservoir of Zn when using a conventional thick metal anode.

Despite the reduction in capacity, eliminating the Zn metal anode significantly enhances the energy density of the full cell. Studies often calculate battery energy density based solely on the mass of the active cathode material, often overlooking the impact of the anode. In this work, the energy density based on the mass of the active material can reach 214.9 Wh kg^{-1} at current densities of 100 mA g^{-1}. However, when the mass of the metallic Zn anode and the entire cathode (including active material, carbon, and binder) is considered, the energy density at 100 mA g^{-1} drops drastically to 3.1 Wh kg^{-1} due to the heavy Zn metal, which weighs 332 mg (16 mm in diameter with thickness of 180 μm).

By contrast, using carbon paper as the anode, which weighs just 10 mg for the same size (16 mm in diameter with the thickness of 100 μm), the energy density based on the anode and the entire cathode reaches 20.9 Wh kg^{-1}—nearly 7 times higher than cell with a Zn metal anode, despite the lower capacity. This underscores the critical role of the Zn anode in determining the cell's energy density and highlights the promising potential of an anode-free battery configuration, as well as the significance of our DRX cathode material in achieving higher energy densities.

Alternative Zn metal-free anodes, such as TiS_2,[41] have also been explored to create rocking chair ZIBs (Figure 5.19), which ideally avoid the issues of irreversible Zn plating and stripping. These configurations demonstrate good cycling performance and retention. However, to further enhance the performance of anode-free cells, additional research is needed to develop more stable current collectors or alternative anode materials.

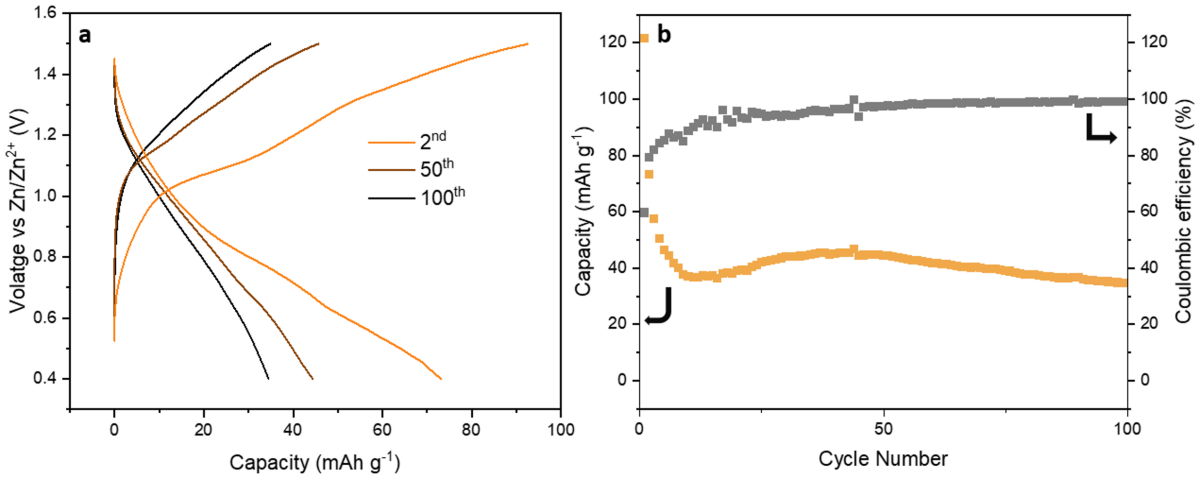

Figure 5.19 (a) Charging/discharging curves of the $ZnMnO_2$-based ZIB using a TiS_2 anode at a current density of 100 mA g^{-1}. (b) Cycling performance of the $ZnMnO_2$-based ZIB with a TiS_2 anode at the same current density.

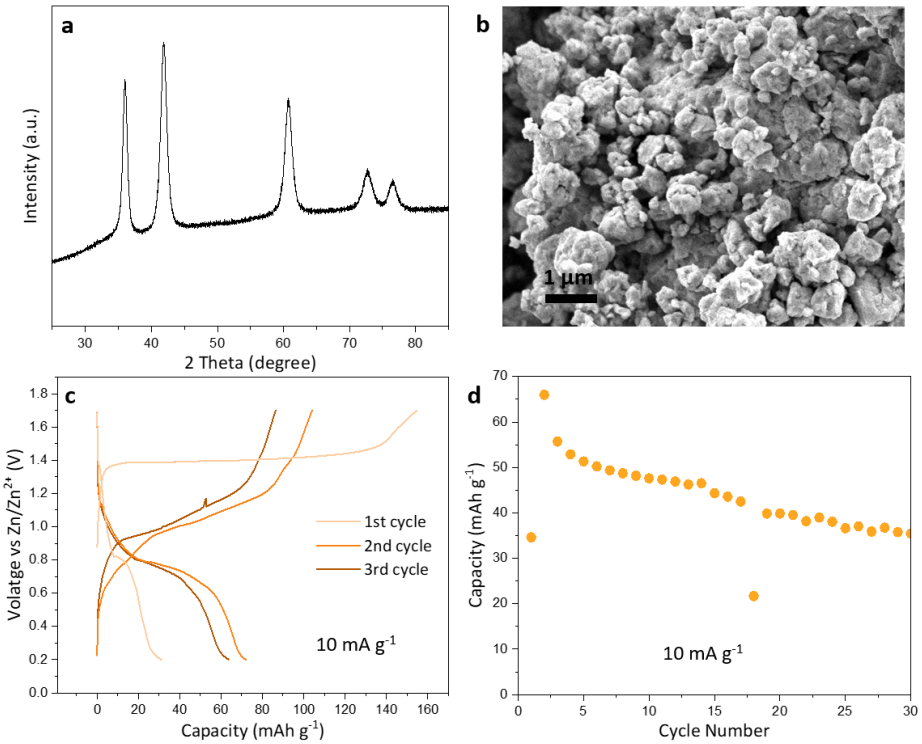

Figure 5.20 (a) XRD and (b) SEM image of pristine $ZnFeO_2$ powder. (c) The load curve over cycles of $ZnFeO_2$ cathode and (d) its cycling performance in coin cell. The cells utilised a $ZnFeO_2$ cathode film paired with a Zn metal anode in an electrolyte of 2 M $ZnSO_4$ with 0.2 M $FeSO_4$. The cells were rested for 12h before operation.

This work presents the first synthesis and application of Zn-containing DRX for aqueous ZIBs, demonstrating its capability for first-charge operation. Furthermore, other

transition metal-based DRX oxides can also be synthesised and utilised. To explore this, $ZnFeO_2$ was prepared as an alternative DRX cathode material and was found to exhibit first-charge capacity as well (Figure 5.20). Given that Fe is an earth-abundant and cost-effective element, this discovery expands the design space for ZIB cathodes, paving the way for a broader range of DRX materials with tuneable properties. These findings establish DRX oxides as a new class of ZIB cathodes, offering new options for developing high-energy-density and anode-free ZIBs.

5.4 Conclusion

The development of a novel $ZnMnO_2$ cathode for the aqueous ZIB addresses the lack of high-capacity, high discharge voltage Zn-containing cathodes suitable for anode-free cells. The $ZnMnO_2$ material, with a cation-disordered rocksalt structure, exhibits a high discharge capacity of 233 mAh g^{-1} and demonstrates stable cycling performance. Notably, the $ZnMnO_2$ cathode is capable of initial charging, making it suitable for anode-free ZIB designs. By replacing the Zn metal anode with carbon paper as the current collector, the energy density of the cell is significantly enhanced—nearly seven times higher than cell with Zn metal anode, despite a lower capacity. The energy storage mechanism of this novel $ZnMnO_2$ cathode is elucidated through various characterisation techniques, revealing that a Zn intercalation/deintercalation contribution arises due to an irreversible shift from a disordered rocksalt structure to spinel, however its capacity is primarily governed by the dissolution and deposition of Mn. This work highlights the potential of anode-free ZIB designs to achieve higher energy densities, positioning them as a promising alternative to traditional ZIBs systems. The study also underscores the potential of DRX oxides based on earth abundant

transition metals, including $ZnMnO_2$ and $ZnFeO_2$, as efficient cathode materials, contributing to the ongoing development of sustainable and high-performance cathodes for aqueous ZIBs.

5.5 Reference

1 Li, Z. & Robertson, A. W. Electrolyte engineering strategies for regulation of the Zn metal anode in aqueous Zn-ion batteries. *Battery Energy* **2**, 20220029 (2023).

2 Zampardi, G. & La Mantia, F. Open challenges and good experimental practices in the research field of aqueous Zn-ion batteries. *Nat. Commun.* **13**, 687 (2022).

3 Zheng, J. *et al.* Reversible epitaxial electrodeposition of metals in battery anodes. *Science* **366**, 645-648 (2019).

4 Bai, Y. *et al.* Advances of Zn Metal-Free "Rocking-Chair"-Type Zinc Ion Batteries: Recent Developments and Future Perspectives. *Small* **20**, e2306111 (2024).

5 Ming, F. *et al.* Co-Solvent Electrolyte Engineering for Stable Anode-Free Zinc Metal Batteries. *J. Am. Chem. Soc.* **144**, 7160-7170 (2022).

6 Zhang, N. *et al.* Cation-Deficient Spinel $ZnMn_2O_4$ Cathode in $Zn(CF_3SO_3)_2$ Electrolyte for Rechargeable Aqueous Zn-Ion Battery. *J. Am. Chem. Soc.* **138**, 12894-12901 (2016).

7 Knight, J. C., Therese, S. & Manthiram, A. Chemical extraction of Zn from $ZnMn_2O_4$-based spinels. *J. Mater. Chem. A* **3**, 21077-21082 (2015).

8 Wu, J. *et al.* Spinel $Zn_3V_3O_8$: A high-capacity zinc supplied cathode for aqueous Zn-ion batteries. *Energy Storage Mater.* **41**, 297-309 (2021).

9 Sun, R. *et al.* Ternary $Zn_3V_3O_8$ superstructure and synergistic modification of separator promote high performance and stable zinc ion battery. *Chem. Eng. J.* **486**, 150377 (2024).

10 Zhao, D. *et al.* Low-strain layered $Zn_{0.56}VOPO_4{\cdot}2H_2O$ as a high-voltage and long-lifespan cathode material for Zn-ion batteries. *Energy Storage Mater.* **66**, 103239 (2024).

11 Zhao, D. *et al.* A stable "rocking-chair" zinc-ion battery boosted by low-strain $Zn_3V_4(PO_4)_6$ cathode. *Nano Energy* **100**, 107520 (2022).

12 Zhang, L., Chen, L., Zhou, X. & Liu, Z. Towards High-Voltage Aqueous Metal-Ion Batteries Beyond 1.5 V: The Zinc/Zinc Hexacyanoferrate System. *Adv. Energy Mater.* **5**, 1400930 (2014).

13 Pan, Z. *et al.* Stabilizing Zinc Hexacyanoferrate Cathode by Low Contents of Cs Cations for Aqueous Zn-Ion Batteries. *ChemSusChem.* **17**, e202400713 (2024).

14 Zhou, L.-F. *et al.* A new phosphate member: $ZnMn_2(PO_4)_2$ as an advanced cathode material for aqueous and nonaqueous zinc ion batteries. *J. Alloys Compd.* **905**, 163939 (2022).

15 Zhang, K. *et al.* Layered structural $Zn_2Mo_3O_8$ as electrode material for aqueous zinc-ion batteries. *Electrochim. Acta* **403**, 139629 (2022).

16 Clément, R. J., Lun, Z. & Ceder, G. Cation-disordered rocksalt transition metal oxides and oxyfluorides for high energy lithium-ion cathodes. *Energy Environ. Sci.* **13**, 345-373 (2020).

17 Li, Z. *et al.* Cation-disordered rocksalt cathode for anode-free zinc-ion batteries. *Energy Environ. Sci.* **18**, 10135-10146 (2025).

18 Baranov, A. N., Sokolov, P. S. & Solozhenko, V. L. ZnO under pressure: from nanoparticles to single crystals. *Crystals* **12**, 744 (2022).

19 Dubinin, S. F. *et al.* Fine structure and magnetism of the cubic oxide compound $Ni_{0.3}Zn_{0.7}O$. *Phys. Solid State* **53**, 1362-1366 (2011).
20 Driscoll, L. L. *et al.* Under pressure: offering fundamental insight into structural changes on ball milling battery materials. *Energy Environ. Sci.* **16**, 5196-5209 (2023).
21 Liu, Y. *et al.* Spontaneously dissolved MnO: A better cathode material for rechargeable aqueous zinc-manganese batteries. *Chem. Eng. J.* **473**, 145490 (2023).
22 Qiu, C. *et al.* The function of Mn^{2+} additive in aqueous electrolyte for Zn/δ-MnO_2 battery. *Electrochim. Acta* **351**, 136445 (2020).
23 Soundharrajan, V. *et al.* The dominant role of Mn^{2+} additive on the electrochemical reaction in $ZnMn_2O_4$ cathode for aqueous zinc-ion batteries. *Energy Storage Mater.* **28**, 407-417 (2020).
24 Ha, K.-H., Moon, H., Joo, E. J., Jo, D. H. & Lee, K. T. Role of zinc hydroxysulfates in the thermodynamics and kinetics of mild-acid Zn-MnO_2 batteries. *Energy Storage Mater.* **65**, 103150 (2024).
25 Fitz, O. *et al.* Electrolyte Study with in Operando pH Tracking Providing Insight into the Reaction Mechanism of Aqueous Acidic Zn//MnO_2 Batteries. *ChemElectroChem.* **8**, 3553-3566 (2021).
26 Chen, H. *et al.* Reunderstanding the Reaction Mechanism of Aqueous Zn-Mn Batteries with Sulfate Electrolytes: Role of the Zinc Sulfate Hydroxide. *Adv. Mater.* **34**, e2109092 (2022).
27 Aguilar, I. *et al.* Identifying interfacial mechanisms limitations within aqueous Zn-MnO_2 batteries and means to cure them with additives. *Energy Storage Mater.* **53**, 238-253 (2022).
28 Hu, P. *et al.* Zn/V_2O_5 Aqueous Hybrid-Ion Battery with High Voltage Platform and Long Cycle Life. *ACS Appl. Mater. Interfaces* **9**, 42717-42722 (2017).
29 Kundu, D., Adams, B. D., Duffort, V., Vajargah, S. H. & Nazar, L. F. A high-capacity and long-life aqueous rechargeable zinc battery using a metal oxide intercalation cathode. *Nat. Energy* **1**, 16119 (2016).
30 Lv, T.-T. *et al.* Crystal water enlarging the interlayer spacing of ultrathin $V_2O_5{\cdot}4VO_2{\cdot}2.72H_2O$ nanobelts for high-performance aqueous zinc-ion battery. *Chem. Eng. J.* **411**, 128533 (2021).
31 Pan, H. *et al.* Reversible aqueous zinc/manganese oxide energy storage from conversion reactions. *Nat. Energy* **1**, 16039 (2016).
32 Xiong, T. *et al.* Defect Engineering of Oxygen-Deficient Manganese Oxide to Achieve High-Performing Aqueous Zinc Ion Battery. *Adv. Energy Mater.* **9**, 1803815 (2019).
33 Ding, J. *et al.* Unlocking the Potential of Disordered Rocksalts for Aqueous Zinc-Ion Batteries. *Adv. Mater.* **31**, e1904369 (2019).
34 Holstun, T. *et al.* Accelerating the Electrochemical Formation of the delta Phase in Manganese-Rich Rocksalt Cathodes. *Adv. Mater*. **37**, e2412871 (2025).
35 Cai, Z. *et al.* In situ formed partially disordered phases as earth-abundant Mn-rich cathode materials. *Nat. Energy* **9**, 27-36 (2023).
36 Li, T. *et al.* Structural Evolution in Disordered Rock Salt Cathodes. *J. Am. Chem. Soc* .**146**, 24296-24309 (2024).
37 Chen, X. *et al.* Charging activation and desulfurization of MnS unlock the active sites and electrochemical reactivity for Zn-ion batteries. *Nano Energy* **75**, 104869 (2020).
38 Dai, K. *et al.* High Reversibility of Lattice Oxygen Redox Quantified by Direct Bulk Probes of Both Anionic and Cationic Redox Reactions. *Joule* **3**, 518-541 (2019).

39 Gilbert, B. *et al.* Multiple scattering calculations of bonding and X-ray absorption spectroscopy of manganese oxides. *J. Phys. Chem. A* **107**, 2839-2847 (2003).
40 Lin, Y. *et al.* Binder-Free Freestanding 3D Zn-Graphene Anode Induced from Commercial Zinc Powders and Graphene Oxide for Zinc Ion Battery with High Utilization Rate. *ACS Appl. Energy Mater.* **5**, 15222-15232 (2022).
41 Zhao, Z. *et al.* Horizontally arranged zinc platelet electrodeposits modulated by fluorinated covalent organic framework film for high-rate and durable aqueous zinc ion batteries. *Nat. commun.* **12**, 6606 (2021).
42 Li, W., Wang, K., Cheng, S. & Jiang, K. An Ultrastable Presodiated Titanium Disulfide Anode for Aqueous “Rocking-Chair” Zinc Ion Battery. *Adv. Energy Mater.* **9**, 1900993 (2019).

6

6 Unlocking Zn-Ion Diffusion in Disordered Rocksalt Cathodes for Nonaqueous ZIBs

6.1 Introduction

Nonaqueous electrolytes for Zn-ion batteries largely mitigate parasitic side reactions and significantly extend the electrochemical stability window, reaching up to ≈3.5 V. This opens the conceptual possibility of higher-voltage ZIBs, provided that suitable cathode materials can be developed.

However, designing suitable intercalation cathodes for nonaqueous ZIBs remains a major challenge. The key obstacle is the strong electrostatic repulsion of divalent Zn^{2+} ions, which severely hinders their diffusion within cathode lattices. Despite extensive efforts, existing materials have shown limited performance, motivating the search for alternative structures.

One promising candidate is the DRX family, which has demonstrated excellent performance in Li- and Na-ion batteries.[1] DRX materials offer high capacity, small volume change, and remarkable compositional flexibility because their disordered structure eliminates the need for strict size matching between ions. Furthermore, the unique Li-hopping mechanism in DRX relies on 0-transition metal (0-TM) channels which is shown in Figure 6.1b, where the absence of transition metals around shared octahedral faces enables Li ions to migrate with low energy barriers.[2] These features make DRX materials attractive candidates for nonaqueous ZIB cathodes.

Yet, applying DRX materials to Zn-ion systems presents additional challenges. The dense rocksalt framework, coupled with the divalent charge of Zn^{2+}, results in significantly slower Zn^{2+} ion diffusion compared to Li^{+} or Na^{+}.

In this chapter, a series of Zn-based DRX compounds, $Zn_xTM_{(2-x)}O_2$ were synthesised, but no electrochemical capacity was measured in these materials. DFT calculations confirmed that Zn^{2+} faces prohibitively high migration barriers even in 0-TM channels due to strong

electrostatic interactions, indicating that the compact DRX framework cannot support Zn^{2+} diffusion.

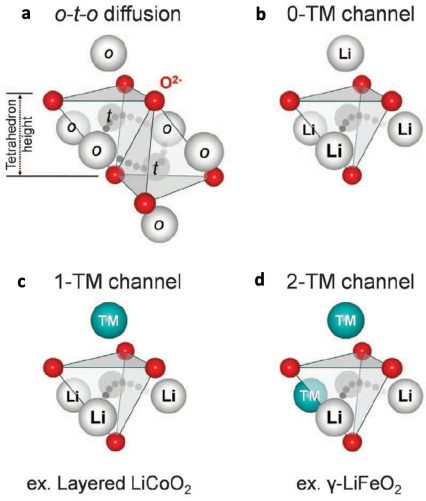

Figure 6.1 Possible environments for an o-t-o Li hop in rocksalt-like Li–TM oxides.[2] (a) o-t-o diffusion: Two tetrahedral pathways connect each pair of neighboring octahedral sites.[2] (b–d) The activated state can share faces with varying numbers of octahedral transition metals: (b) no transition metals (0-TM channel), (c) one transition metal (1-TM channel), or (d) two transition metals (2-TM channel).[2]

To overcome this barrier, cation vacancies were introduced to create percolating diffusion pathways. By delithiating Li-based DRX precursors to introduce intrinsic cation vacancies, reversible Zn^{2+} (de)intercalation in DRX was achieved for the first time. This result confirms the critical role of cation vacancies in unlocking Zn^{2+} diffusion within DRX lattices.

6.2 Experimental Methods

Materials Preparation:

Synthesis of $Zn_xTM_{(2-x)}O_2$:

Compounds in the $Zn_xTM_{(2-x)}O_2$ DRX family including $ZnMnO_2$, $ZnFeO_2$, $ZnCoO_2$, $Zn_{1.2}Co_{0.8}O_2$, $ZnNiO_2$, $Zn_{1.2}Ni_{0.8}O_2$, $Zn_{1.4}Ni_{0.6}O_2$, and $ZnMg_{0.25}Cu_{0.25}Co_{0.25}Ni_{0.25}O_2$, were synthesised via a mechanochemical ball-milling method. ZnO (99%, Sigma-Aldrich) was mixed with transition-metal oxide precursors (MnO, 99%, Sigma-Aldrich; FeO, 99.9%, Sigma-Aldrich;

CoO, 99.5%, Sigma-Aldrich; NiO, 99%, Sigma-Aldrich; MgO, 97%, Sigma-Aldrich; CuO, 99% Sigma-Aldrich) in stoichiometric ratios and sealed in air-tight zirconia jars inside an argon-filled glovebox to prevent TM oxidation. The mixtures were milled for 8 h at 700 rpm using a Fritsch Pulverisette 7 planetary ball mill. For each synthesis, 2 g of precursors were loaded into a 15 mL zirconia jar with 12 g of 5 mm zirconia balls and milled for 8 h at 700 rpm using a Fritsch Pulverisette 7 planetary ball mill. Milling was performed in 5-min intervals with 10-min pauses between cycles to prevent overheating.

Synthesis of DRX $LiMnO_2$:

DRX $LiMnO_2$ was synthesised via a mechanochemical ball-milling method starting from its orthorhombic analogue. Orthorhombic zigzag $LiMnO_2$ was synthesised by mixing Li_2CO_3 (with 5% excess, 99%, Sigma-Aldrich) and Mn_2O_3 (99.9%, Sigma-Aldrich) in a stoichiometric ratio, followed by calcination at 900 °C for 12 h under an Ar atmosphere. DRX $LiMnO_2$ was then obtained by loading 2 g of the orthorhombic $LiMnO_2$ precursor into a 15 mL zirconia jar with 12 g of 5 mm zirconia balls and milling for 8 h at 600 rpm using a Fritsch Pulverisette 7 planetary ball mill. All sample handling was performed in an Ar-filled glovebox to prevent exposure to moisture and air.

Synthesis of DRX $NaMnO_2$:

DRX $NaMnO_2$ was synthesised via a mechanochemical ball-milling method starting from its layered analogue. Monoclinic layered $NaMnO_2$ was synthesised by mixing Na_2CO_3 (99.5%, Sigma-Aldrich) and Mn_2O_3 (99.9%, Sigma-Aldrich) in a stoichiometric ratio, followed by calcination at 700 °C for 24 h under an Ar atmosphere. DRX $NaMnO_2$ was then obtained by loading 2 g of the layered $NaMnO_2$ precursor into a 15 mL zirconia jar with 12 g of 5 mm zirconia balls and milling for 8 h at 600 rpm using a Fritsch Pulverisette 7 planetary ball mill.

All sample handling was performed in an Ar-filled glovebox to prevent exposure to moisture and air.

Synthesis of DRX $Li_4Mn_2O_5$:

DRX $Li_4Mn_2O_5$ was synthesised via a two-step ball-milling process. Orthorhombic $LiMnO_2$ was mixed with Li_2O (97%, Sigma-Aldrich) in a 2:1 molar ratio (~4 g total) and loaded into a 15 mL zirconia jar with 12 g of 5 mm zirconia balls. The mixture was milled for 15 h at 700 rpm using a Fritsch Pulverisette 7 planetary ball mill. Subsequently, 5 wt% acetylene black was added, and the mixture was further milled at 700 rpm for 5 h. All sample handling was performed in an Ar-filled glovebox to prevent exposure to moisture and air.

Synthesis of DRX $Li_{1.2}Mn_{0.4}Ti_{0.2}O_2$:

DRX $Li_{1.2}Ti_{0.4}Mn_{0.4}O_2$ was synthesised by solid-state reaction. Li_2CO_3 (with 10% excess, 99%, Sigma-Aldrich), TiO_2 (99.8%, Sigma-Aldrich), and Mn_2O_3 (99.9%, Sigma-Aldrich) precursors were thoroughly mixed in stoichiometric proportions and calcined at 950 °C for 12 h under an Ar atmosphere. To optimise electrochemical performance, the as-synthesised $Li_{1.2}Ti_{0.4}Mn_{0.4}O_2$ (~2 g) was further pulverised by ball milling. The material was loaded into a 15 mL zirconia jar with 12 g of 5 mm zirconia balls and milled for 8 h at either 300 rpm or 600 rpm using a Fritsch Pulverisette 7 planetary ball mill, producing samples with different degrees of pulverisation.

Synthesis of DRX $LiTiS_2$:

DRX $LiTiS_2$ was synthesised via a mechanochemical ball-milling method starting from its layered analogue. Layered $LiTiS_2$ was synthesised via solid-state reaction using stoichiometric amounts of Li_2S (99.98%, Sigma-Aldrich), Ti (99.5%, Thermo Scientific) and elemental S (99.98%, Sigma-Aldrich). The precursor powders were thoroughly mixed by hand grinding and pelletised in an Ar-filled glove box. The resulting pellets were loaded into graphite

crucibles and placed inside quartz tubes, which were then sealed under vacuum (~10−5 mbar). The sealed tubes were slowly heated to 750 °C over 25 hours, held for 36 hours, and then quenched in air. All sample handling was performed in an Ar-filled glovebox to prevent exposure to moisture and air.

Trial of $Zn_{0.5}MnO_2$ and $Zn_{0.75}FeO_2$:

$Zn_{0.5}MnO_2$ DRX was attempted by ball milling ZnO, MnO, and MnO_2 (99%, Sigma-Aldrich) in a 1:1:1 molar ratio at 700 rpm for 8 h. $Zn_{0.75}FeO_2$ DRX was attempted by ball milling ZnO, FeO, and Fe_2O_3 (96%, Sigma-Aldrich) in a 3:2:1 molar ratio at 700 rpm for 8 h. However, the resulting products were not phase-pure.

Electrochemistry:

Free-standing cathodes, including $Zn_xTM_{(2-x)}O_2$, $LiMnO_2$, $NaMnO_2$, $Li_{1.2}Ti_{0.4}Mn_{0.4}O_2$, and $LiTiS_2$ films, were prepared by mixing the active material, acetylene black, and PTFE in a 7:2:1 mass ratio using a mortar and pestle. For $Li_4Mn_2O_5$, which already contained 5 wt% carbon from synthesis, the mixing ratio was adjusted to 7.37 parts (as-synthesised mixture of $Li_4Mn_2O_5$ and carbon):1.63 parts additional carbon:1 part PTFE, ensuring the final composite maintained the standard 7:2:1 mass ratio of active material, carbon, and PTFE.

For Zn cells, Zn metal foil was used as the anode with 1 M $Zn(TFSI)_2$ in acetonitrile as the electrolyte. For Li cells, Li metal discs served as the anode with 1 M $LiPF_6$ in a 1:1 (v/v) mixture of ethylene carbonate and dimethyl carbonate (EC:DMC, Aldrich) as the electrolyte. For Na cells, Na metal discs (pressed onto Al foil) were used as the anode with 1 M $NaPF_6$ in a 1:1 (v/v) mixture of EC:DMC (E-lyte Innovations) as the electrolyte. Electrode preparation and cell assembly were performed entirely in an Ar-filled glovebox. Electrochemical testing, including galvanostatic cycling, was performed on a Maccor Series 4000 system at room

temperature, while galvanostatic intermittent titration technique (GITT) measurements were carried out using a BioLogic VMP3.

Characterisation:

The ex-situ characterisation was conducted on cathode film or powder samples after charging/discharging to specific states of charge and disassembly from coin cells. The cathode film or powder was thoroughly rinsed several times with acetonitrile or DMC to remove any residual electrolyte, followed by vacuum drying.

PXRD was performed using a Rigaku Miniflex diffractometer with Cu Kα1 radiation. The PXRD data were analysed using the Rietveld refinement method with GSAS-II software.

SEM images were obtained using a Carl Zeiss Merlin field emission scanning electron microscope. TEM, including HRTEM and SAED, was carried out using a JEOL JEM-2100 operating at 200 kV. STEM with HAADF imaging and EDX were performed using an aberration-corrected JEOL ARM 200F, equipped with an Oxford Instruments windowless EDX detector. STEM was performed by my supervisor Dr. Alex Robertson.

XAS was conducted at beamline B18 of the Diamond synchrotron source and the measurements were performed in transmission and fluorescence yield.

Diffusion Coefficient Calculation:

The Li^+ or Zn^{2+} diffusivity can be calculated using the following equation:

$$D_{Li^+/Zn^{2+}} = \frac{4}{\pi}\left(\frac{m_B V_m}{M_B S}\right)^2 \left(\frac{\Delta E_S}{\Delta E_\tau}\right)^2, \qquad (\tau \ll \frac{L^2}{D_{Li^+/Zn^{2+}}})$$

where τ represents the constant current pulse time, m_B, V_m, and M_B are the mass loading, the molar volume, and the molar mass of the inserted electrode material, respectively. S is the area of the electrode–electrolyte interface, ΔE_S is the change of steady-state voltage during a

single-step GITT experiment, and ΔE_τ stands for the total change of cell voltage during a constant current pulse τ of a single-step GITT experiment regardless of the IR-drop.

DFT Calculation:

A collaborator YC Wong at university of Warwick performed DFT calculation. The electronic structure calculation software CASTEP was used to study the DRX materials. Because NEB calculations are computationally expensive, we selected a relatively small supercell of size 2×2×2, containing a total of 64 atoms. The repeating images were separated by at least 8 Å to minimise interference between them. Pre-convergence tests to determine the DFT parameters were performed on pristine DRX structures ranging from supercell size of 1x1x1 to 3x3x3.

A relatively small 3x3x3 k-point sampling was used, as the fully disordered structures are highly anisotropic and asymmetric. Since both $LiMnO_2$ and $ZnMnO_2$ are correlated oxides with localised d electrons, it was necessary to apply a Hubbard U correction of 4.0 eV to obtain accurate density of states and band gaps, ensuring that the materials are not erroneously predicted as metallic. The Hubbard U parameter was determined through convergence tests of the density of states.

A plane-wave cutoff of 800 eV was used, which provided sufficient convergence. NEB calculations utilised between 7 and 11 images, with the number of images adjusted based on the convergence characteristics of individual configurations.

Since ordered $LiMnO_2$ is often regarded as a magnetic material, it is essential to include spin polarisation in our calculations, particularly by assigning initial spin moments to the transition metal ions. Both antiferromagnetic and ferromagnetic configurations were investigated for single-point energy calculations and structure relaxation calculations. The choice of initial spin configuration can influence the system to converge toward a state

resembling the starting configuration. However, for DRX, the situation is less clear due to strong local ordering, and either FM or AFM configurations could be energetically favourable depending on the specific atomic arrangement. To simplify the NEB calculations, only ferromagnetic configurations are considered in this study.

6.3 Result and Discussion

6.3.1 Electrochemical Performance of DRX $Zn_xTM_{(2-x)}O_2$ Cathodes

To investigate the feasibility of Zn-based DRX oxides as cathode, $ZnMnO_2$ was tested in a nonaqueous Zn electrolyte. The material, synthesised via high-energy ball milling, exhibits particle sizes on the nanometer scale as revealed by SEM, with HRTEM confirming crystalline domains of only a few nanometers (Figure 5.2).

Electrochemical testing, however, shows that $ZnMnO_2$ DRX delivers negligible capacity (Figure 6.2a), suggesting that the material is electrochemically inactive toward Zn extraction. This indicates that the $ZnMnO_2$ DRX does not provide accessible diffusion pathways for Zn^{2+}.

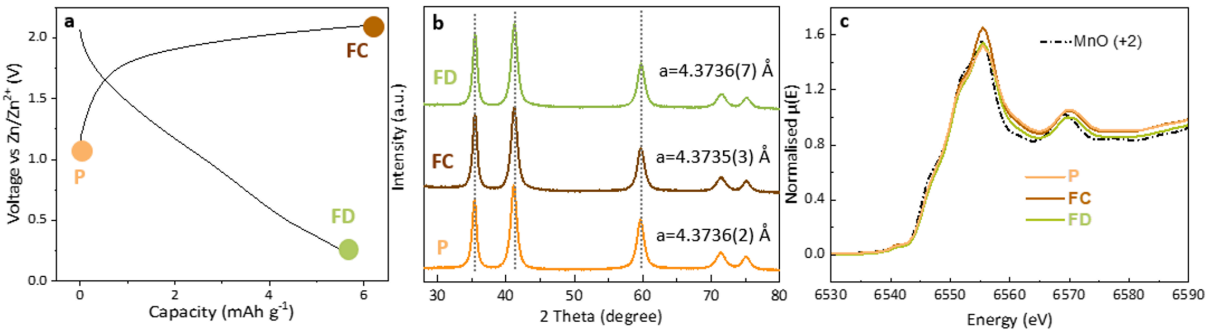

Figure 6.2 (a) Galvanostatic load curve of $ZnMnO_2$ in organic electrolyte at 10 mA g^{-1}. (b) Ex situ XRD patterns of $ZnMnO_2$ powder at different states of charge: P (pristine), FC (fully charged), and FD (fully discharged), with corresponding points indicated in (a). Unit cell parameters were obtained from Rietveld refinement. (c) Ex situ Mn K-edge XANES spectra of $ZnMnO_2$ at P, FC, and FD states, with MnO as a reference.

To substantiate this conclusion, ex situ XRD (Figure 6.2b) was performed on $ZnMnO_2$ in the P, FC, and FD states. The diffraction patterns show no detectable shift in peak positions

or change in unit cell parameters, implying the absence of lattice expansion or contraction normally associated with Zn intercalation/deintercalation. This observation is consistent with chapter 5 studies conducted in aqueous electrolytes, where the diffraction peaks indexed to $ZnMnO_2$ DRX likewise exhibited no shift during charging and discharging, further reinforcing that the inability of Zn diffusion is intrinsic to the DRX host rather than an electrolyte-dependent phenomenon.

Further evidence comes from Mn K-edge XANES analysis (Figure 6.2c), which reveals no change in Mn oxidation state between the different electrochemical states. These results confirm that $ZnMnO_2$ DRX is not electrochemically active and does not accommodate Zn-ion transport.

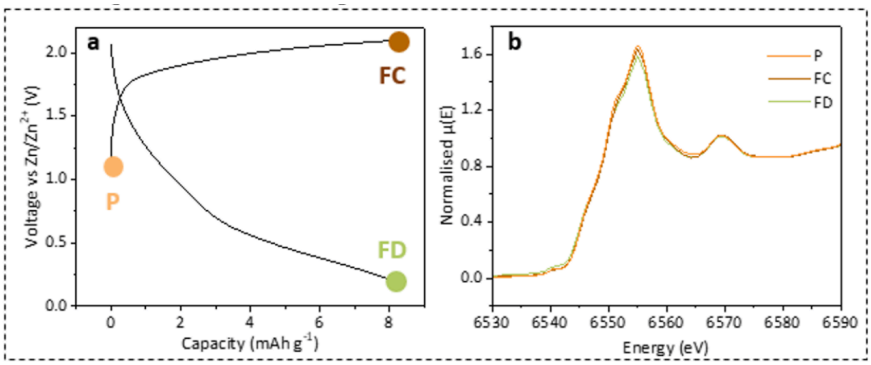

Figure 6.3 (a) Galvanostatic load curve of $ZnMnO_2$ ball-milled with carbon (7:2 ratio) at 300 rpm for 6 h, tested in organic electrolyte at 10 mA g^{-1}. (b) Ex situ Mn K-edge XANES spectra of $ZnMnO_2$ at P, FC, and FD states.

In general, DRX oxides are known to suffer from intrinsically poor electronic conductivity, which can strongly suppress coupled ion–electron transport during (de)intercalation.[3,4] To examine whether this limitation was responsible for the negligible capacity, $ZnMnO_2$ was co-milled with carbon, thereby achieving intimate particle–carbon contact and a uniform conductive coating. Despite the improved electronic conductivity of $ZnMnO_2$ particles, electrochemical testing again revealed negligible capacity (Figure 6.3a), and Mn K-edge XANES (Figure 6.3b) confirmed the invariance of the Mn valence state across

different charge of states. These results indicate that the absence of Zn extraction is not due to electronic limitations.

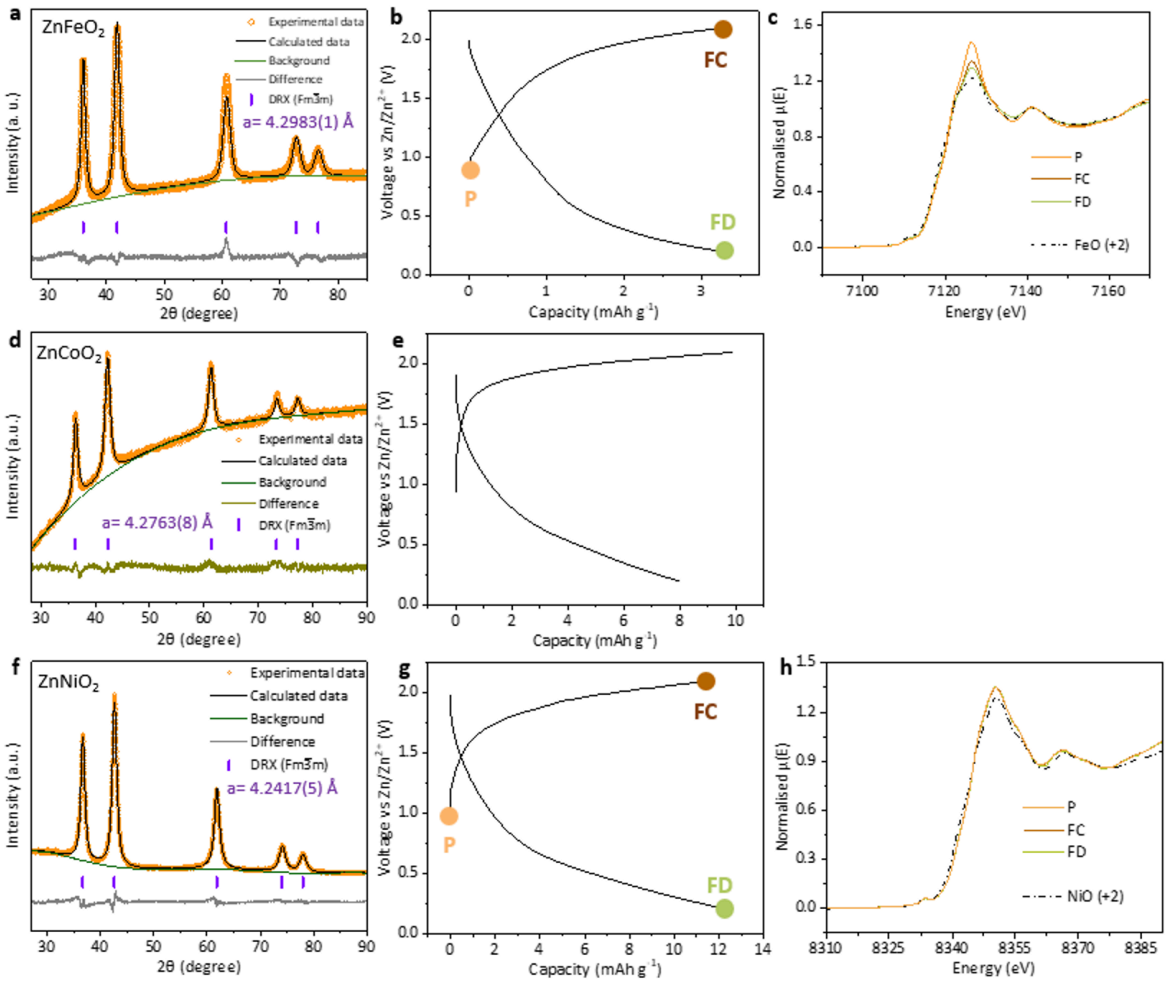

Figure 6.4 (a) Rietveld refinement of XRD data for $ZnFeO_2$ with corresponding unit cell parameters. (b) Galvanostatic load curve of $ZnFeO_2$ in organic electrolyte at 10 mA g^{-1}. (c) Ex situ Fe K-edge XANES spectra of $ZnFeO_2$ at P, FC, and FD states. (d) Rietveld refinement of XRD data for $ZnCoO_2$ with corresponding unit cell parameters. (e) Galvanostatic load curve of $ZnCoO_2$ in organic electrolyte at 10 mA g^{-1}. (f) Rietveld refinement of XRD data for $ZnNiO_2$ with corresponding unit cell parameters. (g) Galvanostatic load curve of $ZnNiO_2$ in organic electrolyte at 10 mA g^{-1}. (h) Ex situ Ni K-edge XANES spectra of $ZnNiO_2$ at P, FC, and FD states.

To determine whether this limitation was specific to Mn or universal among Zn-based DRX oxides, alternative transition metals were investigated. Insights from Li-based DRX systems are instructive here: DRX $LiXO_2$ (X = Ni, Mn, Co, Fe, Ti) has been investigated, and electrochemical performance varies dramatically depending on the transition metal.[5] $LiMnO_2$

delivered the highest reversible capacity, while Ni-, Co-, Fe-, and Ti-based DRXs delivered substantially lower capacities. These differences arise because the transition metal strongly influences electronic structure (e.g., band gap and conductivity), local bonding environments, and the extent of short-range ordering (SRO), which governs the formation of percolating diffusion pathways.[6]

Following this rationale, Zn based DRX with different TM including $ZnNiO_2$, $ZnCoO_2$, and $ZnFeO_2$ were synthesised and tested in nonaqueous electrolyte. However, all exhibited negligible capacity (Figure 6.4), demonstrating that the lack of Zn transport is not unique to Mn-based DRXs. Motivated by reports that high-entropy strategies can suppress SRO and enhance Li transport,[7] a high-entropy Zn-based DRX oxide, $ZnMg_{0.25}Cu_{0.25}Co_{0.25}Ni_{0.25}O_2$ was synthesised and tested. However, this material likewise showed no electrochemical activity (Figure 6.5).

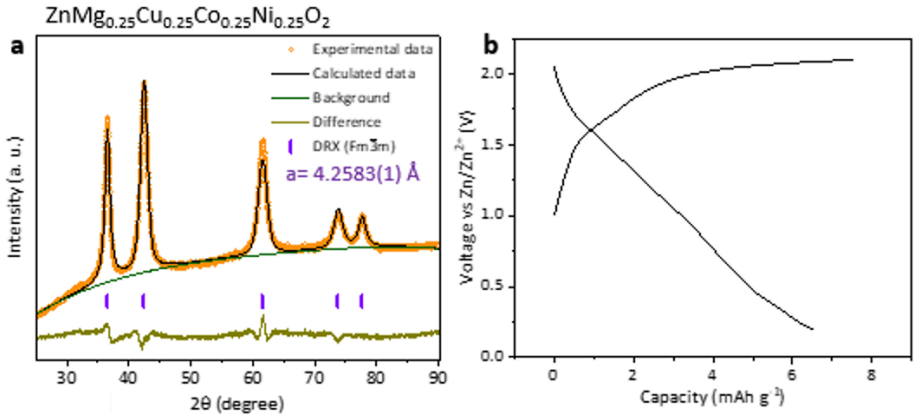

Figure 6.5 (a) Rietveld refinement of XRD data for $ZnMg_{0.25}Cu_{0.25}Co_{0.25}Ni_{0.25}O_2$ with corresponding unit cell parameters. (b) Galvanostatic load curve of $ZnMg_{0.25}Cu_{0.25}Co_{0.25}Ni_{0.25}O_2$ in organic electrolyte at 10 mA g^{-1}.

Previous studies on Li-based DRX oxides have shown that Li-rich compositions can exhibit significantly enhanced Li^+ diffusivity compared to their stoichiometric non Li-rich counterparts. This improvement arises from the increase in 0-TM sites which is tetrahedral sites coordinated solely by Li that serve as low-energy diffusion pathways. A greater

abundance of these sites expands the percolation network for Li transport, leading to enhanced capacity.[8] In stoichiometric DRX, the number of such 0-TM sites is statistically too small to form a continuous percolating network, thereby limiting long-range Li transport. By increasing the Li:TM ratio, more 0-TM sites are introduced, raising the probability of percolation channels and thus enabling faster Li diffusion.[9,10]

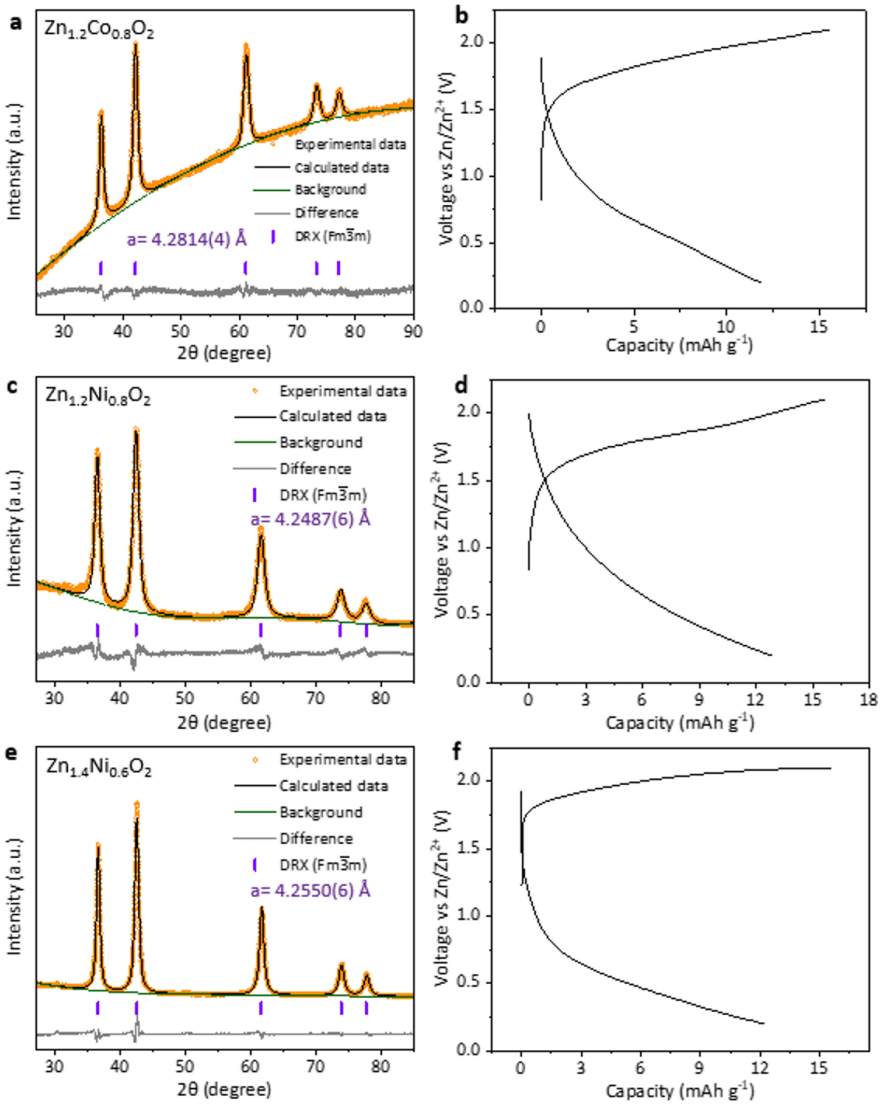

Figure 6.6 (a) Rietveld refinement of XRD data for $Zn_{1.2}Co_{0.8}O_2$ with corresponding unit cell parameters. (b) Galvanostatic load curve of $Zn_{1.2}Co_{0.8}O_2$ in organic electrolyte at 10 mA g^{-1}. (c) Rietveld refinement of XRD data for $Zn_{1.2}Ni_{0.8}O_2$ with corresponding unit cell parameters. (d) Galvanostatic load curve of $Zn_{1.2}Ni_{0.8}O_2$ in organic electrolyte at 10 mA g^{-1}. (e) Rietveld refinement of XRD data for $Zn_{1.4}Ni_{0.6}O_2$ with corresponding unit cell parameters. (f) Galvanostatic load curve of $Zn_{1.4}Ni_{0.6}O_2$.in organic electrolyte at 10 mA g^{-1}.

Motivated by this design principle, Zn-rich DRX oxides were synthesised and evaluated to assess whether increasing Zn content could enhance Zn^{2+} mobility. In Mn- and Fe-based systems, the large size mismatch between Zn^{2+} and Mn^{2+}/Fe^{2+} prevented the formation of pure Zn-rich DRX phases,[11] resulting in ZnO impurities in the final product. To address this challenge, Co- and Ni-based systems were explored, as the smaller ionic radii of Co^{2+} and Ni^{2+} relative to Zn^{2+} allow for the stabilisation of Zn-rich DRX structures.[11] Stable compositions such as $Zn_{1.2}Co_{0.8}O_2$, $Zn_{1.2}Ni_{0.8}O_2$, and $Zn_{1.4}Ni_{0.6}O_2$ were successfully synthesised (Figure 6.6). These Zn-rich phases, in principle, should generate a higher number of 0-TM sites, providing more potential diffusion pathways for Zn^{2+}. However, electrochemical testing revealed negligible reversible capacity in all cases. These results demonstrate that Zn-based DRXs remain electrochemically inactive, regardless of transition metal composition, entropy effects, or Zn excess. This strongly suggests that the fundamental barrier lies in the intrinsic nature of compact DRX lattice, where strong electrostatic interactions severely limit Zn diffusion.

6.3.2 DFT Calculations of Ion Migration Barriers in DRX Structures

In Li based DRX-type oxides, Li^+ migration between adjacent octahedral sites occurs via an intermediate tetrahedral site,[2] known as the octahedral–tetrahedral–octahedral (o–t–o) pathway (Figure 6.1a). The activation barrier for this process is dictated by electrostatic interactions between the migrating ion in the tetrahedral site and the species occupying the two face-sharing octahedra.

This framework highlights a fundamental distinction between Li^+ and Zn^{2+}. While Li^+, with its lower charge density and weaker electrostatic interactions, can readily form percolating o–t–o networks under favourable structural conditions, Zn^{2+} owing to its higher charge and stronger electrostatic repulsion, experiences much stronger electrostatic repulsion, severely limiting its mobility.[12]

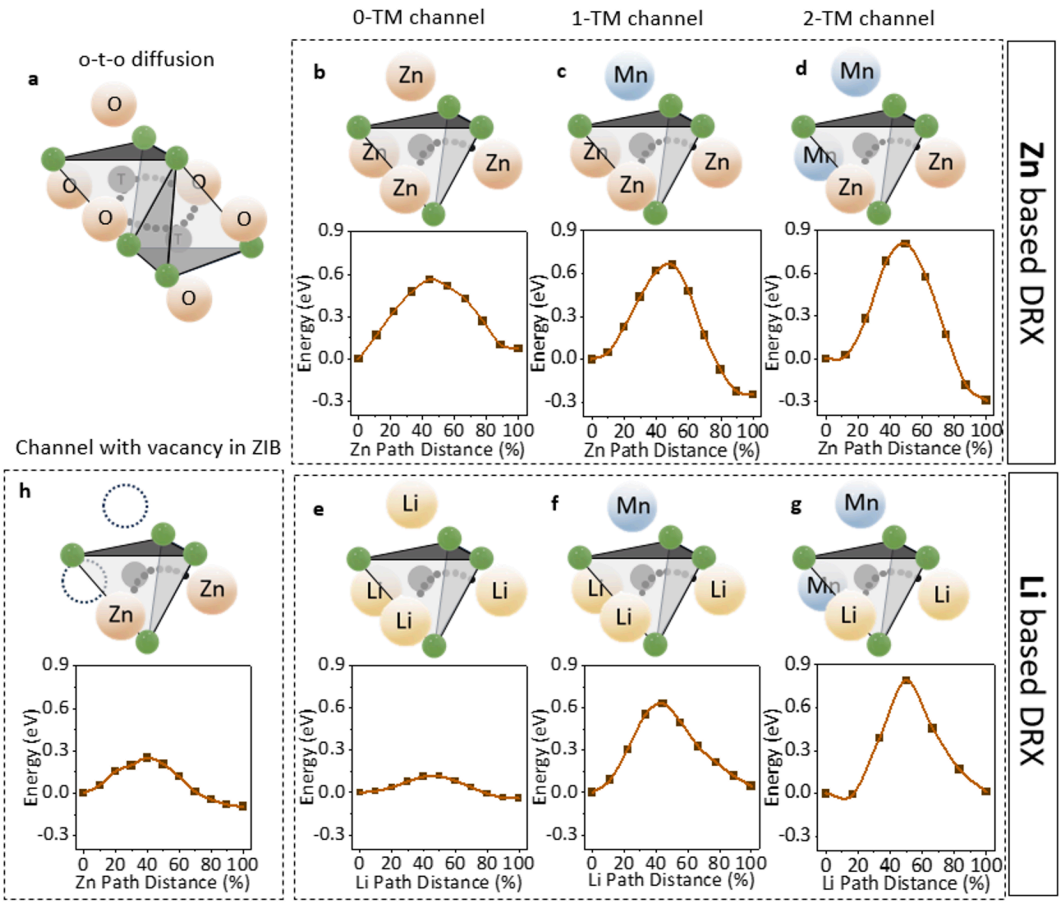

Figure 6.7 (a) Schematic of ion diffusion through an octahedral–tetrahedral–octahedral (o–t–o) channel in a DRX unit cell. (b–d) Calculated migration barriers for 0-TM, 1-TM, and 2-TM channels with Mn^{2+} as the transition metal and Zn^{2+} as the charge carrier in Zn-based DRX. (e–g) Calculated migration barriers for 0-TM, 1-TM, and 2-TM channels with Mn^{3+} as the transition metal and Li^{+} as the charge carrier in Li-based DRX. (h) Migration barrier for the 0-TM channel under vacancy conditions.

To gain mechanistic insight into Zn transport in DRX, Zn^{2+} migration barriers were calculated using DFT for three representative pathways: 0-TM, 1-TM, and 2-TM channels, which correspond to tetrahedral sites sharing faces with zero, one, or two transition-metal cations, respectively. A collaborator YC Wong at university of Warwick performed DFT calculation. Due to the disordered arrangement of cations in DRX, numerous possible ion migration configurations exist. When Zn migrates between two certain adjacent octahedral sites, it can pass through one of two intermediate tetrahedral sites. In this study, a representative case was selected in which the lower tetrahedron shares faces with two TM

cations, while the upper tetrahedron may represent a 0-TM, 1-TM, or 2-TM pathway (Figure 6.8). Under these conditions, strong electrostatic repulsion of TM drives the charge carrier ion to migrate through the upper, less hindered tetrahedral site.

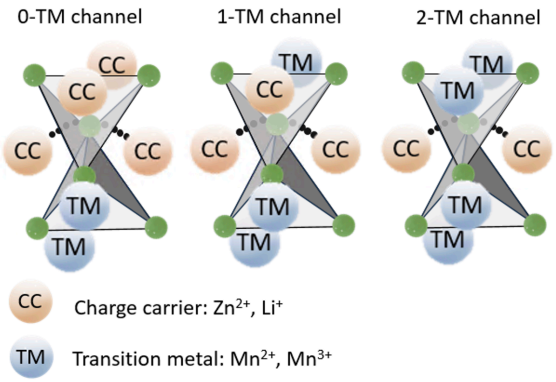

Figure 6.8 Selected representative ion migration pathways for 0-TM, 1-TM, and 2-TM channels.

The calculated migration barriers for the representative pathways shown in Figure 6.7 reveal severe transport limitations for Zn^{2+}. Even in the most favorable 0-TM channel, the barrier remains high at 0.514 eV (Figure 6.7b), increasing further to 0.791 eV in the 2-TM channel (Figure 6.7d). Since both Zn^{2+} and Mn^{2+} are divalent, the increase from the 0-TM pathway (facing four Zn^{2+} ions) to the 2-TM pathway (facing two Zn^{2+} and two Mn^{2+} ions) cannot be attributed to electrostatics alone; it also reflects the strong Mn–O covalency, which stabilises the lattice and further impedes Zn migration. Importantly, the substantial barrier in the 0-TM channel explains why Zn-rich DRX compositions despite increasing the number of 0-TM sites, still fail to deliver measurable electrochemical capacity.

For comparison, Li^{+} migration barriers were calculated in Mn-based DRX. The 0-TM channel for Li^{+} exhibits a much lower barrier of 0.117 eV (Figure 6.7e), consistent with experimental reports of high reversible capacity in Li-rich DRX oxides. This stark contrast demonstrates that divalent nature of Zn^{2+} fundamentally limits its mobility.

While this case provides valuable insight into the fundamental transport behaviour, a more comprehensive analysis across multiple local environments is needed to achieve full statistical accuracy.[13] The migration barriers are sensitive to local site energy differences, leading to asymmetric NEB profiles when the starting and ending configurations differ. As a result, the calculated barrier values represent selected migration pathways and should be interpreted as indicative of the general trend rather than exact quantitative values. Moreover, finite-size effects may influence the results, as relatively small supercells were used; employing larger supercells would improve accuracy but at a substantially higher computational cost. Nonetheless, by comparing identical local configurations between Zn and Li based DRX, this analysis provides a direct and meaningful comparison of their intrinsic ion transport characteristics.

It is well established that SRO in DRX materials can influence the connectivity of migration pathways and, consequently, ion transport.[14-16] However, for Zn^{2+}, the combination of strong electrostatic interactions and high charge density imposes a fundamental constraint. Although SRO may locally alter the arrangement of accessible sites, the high migration barriers prevent Zn^{2+} from forming a percolating diffusion network. This indicates that the limited mobility of Zn^{2+} is intrinsic to its divalent nature and cannot be mitigated by SRO alone, underscoring the need for additional structural modifications such as vacancy introduction.

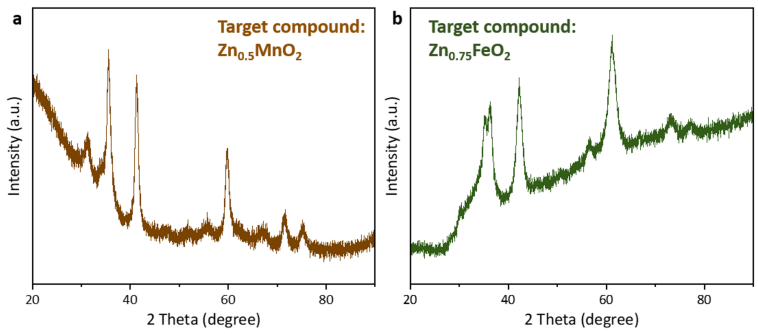

Figure 6.9 XRD patterns of as-synthesised target compounds (a) $Zn_{0.5}MnO_2$ and (b) $Zn_{0.75}FeO_2$ obtained by mechanochemical ball milling.

To address this challenge, the strategy of introducing cation vacancies into the DRX lattice was proposed. DFT calculations revealed that vacancies significantly reduce the Zn^{2+} migration barrier. In the 0-TM channel, replacing two face-sharing Zn^{2+} ions with two vacancies lowered the barrier to 0.25 eV (Figure 6.7h), compared to 0.514 eV for fully occupied channels. This substantial reduction demonstrates that vacancies can create low-energy diffusion pathways, offering a viable strategy to unlock Zn^{2+} mobility and enable the design of electrochemically active DRX cathodes for nonaqueous ZIBs.

Attempts were made to synthesise vacancy-containing Zn-based DRX materials, such as $Zn_{0.5}MnO_2$ and $Zn_{0.75}FeO_2$, to promote Zn diffusion. Introducing Zn vacancies requires adjusting the transition-metal valence states by reducing the amount of rocksalt precursors (e.g., MnO and FeO) while incorporating higher-valence sources such as MnO_2 and Fe_2O_3. However, this compositional adjustment destabilises the DRX framework, leading to the formation of impurity phases (Figure 6.9) due to the reduced ability of the rocksalt component to stabilise the DRX structure.

6.3.3 Delithiated DRX Oxides as Cathodes in Zn-Ion Batteries

A different strategy was adopted to introduce vacancies into the DRX framework. Instead of directly synthesising Zn-based DRX with intrinsic vacancies, a delithiated Li-based DRX was used as a model system. DRX $LiMnO_2$ was chosen for its structural and compositional similarity to $ZnMnO_2$. This material was then electrochemically charged in a Li cell to varying extents, generating controlled concentrations of cation vacancies (Figure 6.10a,b). The delithiated electrodes were subsequently discharged in Zn-ion cells to evaluate their ability to host Zn. As shown in Figure 6.10c, higher vacancy concentrations in the cathode markedly enhanced Zn insertion and discharge capacity, demonstrating that vacancies are essential for enabling Zn diffusion and storage.

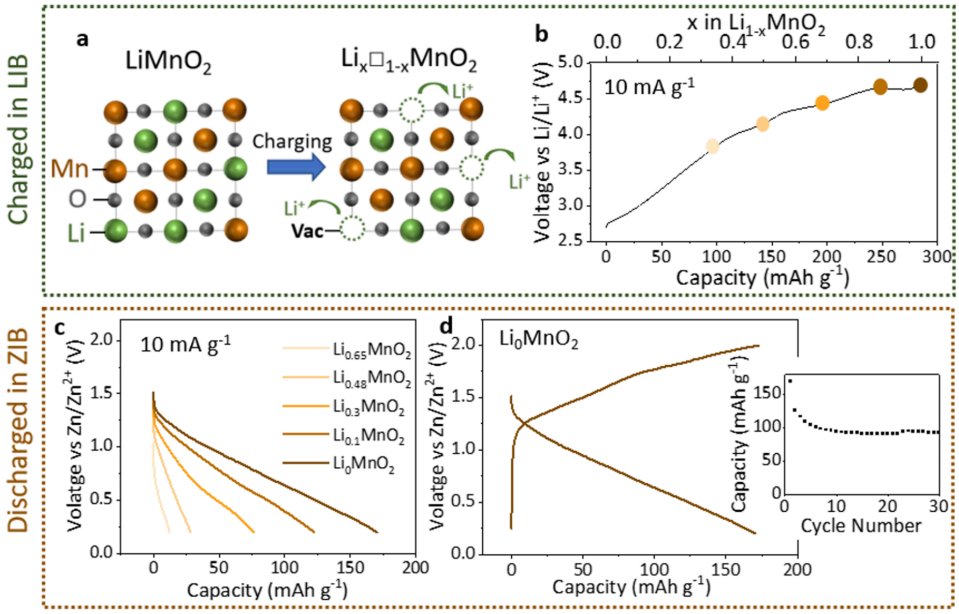

Figure 6.10 (a) Schematic of delithiation of $LiMnO_2$ DRX in a Li-ion battery to generate a vacant DRX structure. (b) Charge curve of $LiMnO_2$ DRX in a Li-ion battery at 10 mA g^{-1}. (c) Discharge capacities of partially delithiated $LiMnO_2$, tested in Zn-ion batteries at 10 mA g^{-1}; the corresponding delithiation states are labeled in panel (b). (d) Charge/discharge profile of fully delithiated Li_0MnO_2 in a Zn-ion battery, with inset showing cycling performance at 10 mA g^{-1}.

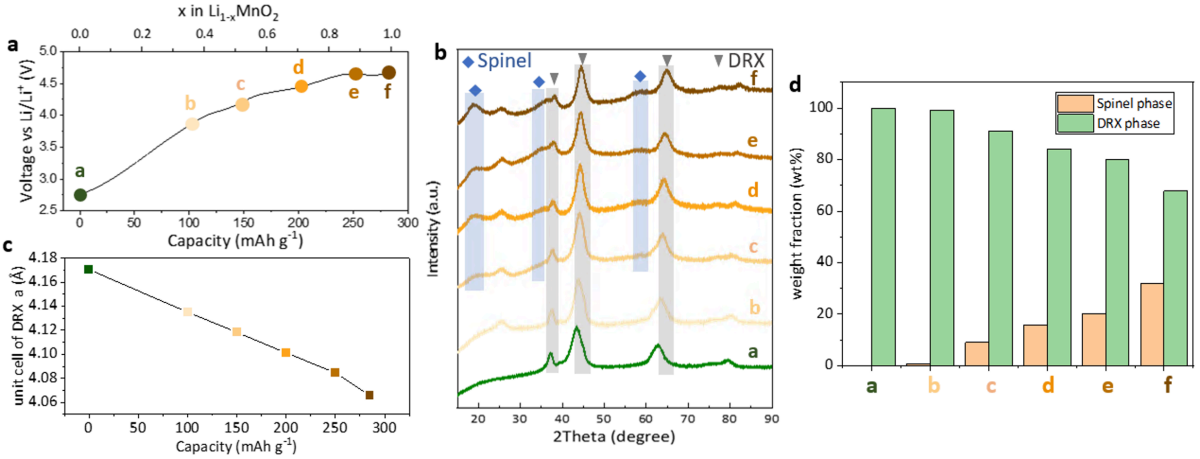

Figure 6.11 (a) Charge curve of $LiMnO_2$ DRX in a Li-ion battery at 10 mA g^{-1}. (b) Ex situ powder XRD of $LiMnO_2$ at different states of charge, corresponding to the points marked in panel (a). (c) Evolution of the unit cell parameters of DRX at different charge states. (d) Weight fractions of spinel and DRX phases at the corresponding states, obtained from Rietveld refinement of the XRD data.

As shown in Figure 6.10d, fully delithiated DRX $LiMnO_2$ discharged in a Zn-ion cell delivered a discharge capacity of ~170 mAh g^{-1}. The following charge process recovered nearly

the same capacity, confirming the reversibility of Zn insertion and extraction. With extended cycling, the capacity gradually declined, yet after 30 cycles the material still retained ~85 mAh g^{-1}.

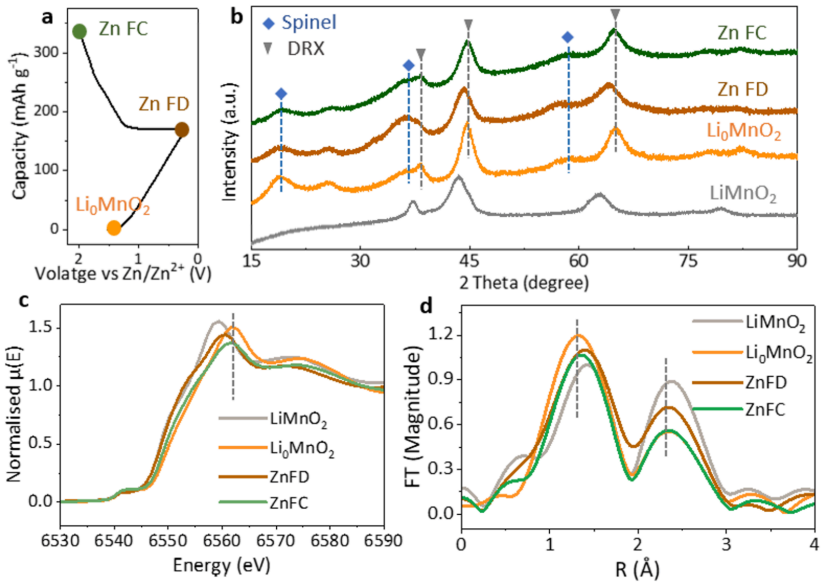

Figure 6.12 (a) First discharge/charge curve of Li_0MnO_2 in a Zn-ion battery at 10 mA g^{-1}. (b) Ex situ powder XRD of pristine $LiMnO_2$, Li_0MnO_2, Zn FD, and Zn FC, corresponding to the points in panel (a). (c) Ex situ Mn K-edge XANES spectra and (d) EXAFS of $LiMnO_2$, Li_0MnO_2, Zn FD, and Zn FC. Zn FD represents the first discharge state in the Zn-ion battery, while Zn FC represents the first charge state in the Zn-ion battery.

However, closer examination revealed that $LiMnO_2$ undergoes substantial structural changes during charging in Li-ion cells. As shown in the ex-situ XRD patterns in Figure 6.11b, the DRX reflections shift to higher angles during charging, consistent with lattice contraction as Li is extracted (Figure 6.11c). Simultaneously, new peaks emerge that can be indexed to a spinel phase. Due to the high mobility of Mn^{3+} ions,[17] the structure progressively and partially transforms into spinel during cycling. Other $LiMnO_2$ polymorphs, such as layered $LiMnO_2$ and orthorhombic $LiMnO_2$ are known to convert to spinel within only a few charge/discharge cycles.[18-20] Although some reports have claimed that the DRX form of $LiMnO_2$ can suppress such structural transformation,[21,22] our results clearly demonstrate that this is not the case. XRD patterns reveal broadened reflections characteristic of a low-crystallinity spinel phase,

and Rietveld refinement shows that the spinel fraction increases progressively with charging, reaching ~40 wt% at the top of charge (Figure 6.11d). This progressive phase transformation provides a plausible explanation for why non-Li-rich DRX $LiMnO_2$ compositions can approach nearly full Li extraction: the concurrent spinel formation facilitates additional electrochemical activity.

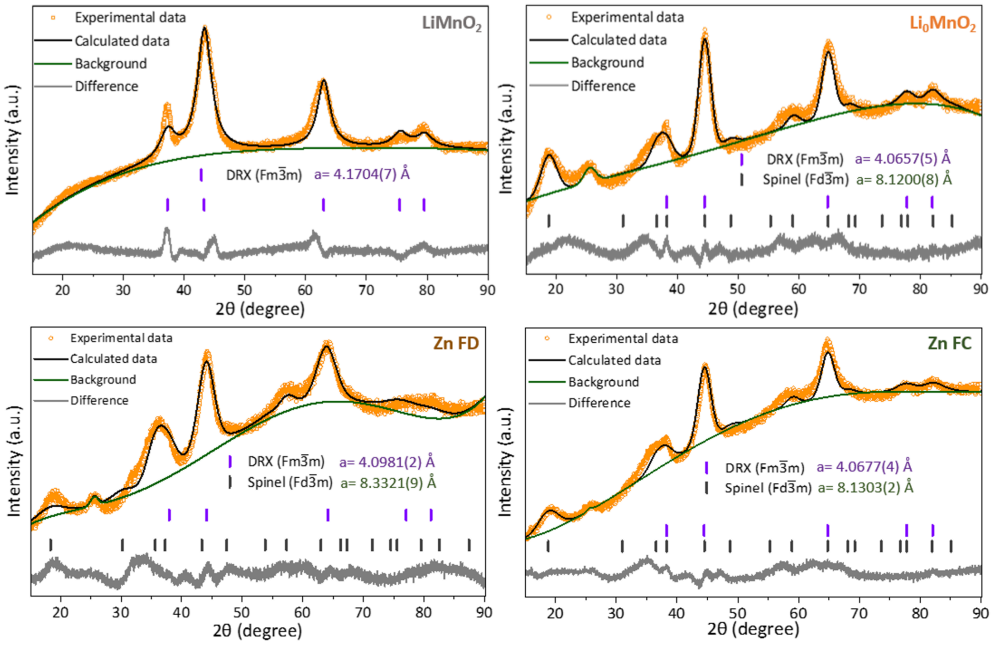

Figure 6.13 Rietveld refinement of XRD patterns for pristine $LiMnO_2$, Li_0MnO_2, Zn FD, and Zn FC.

When the delithiated Li_0MnO_2 was subsequently tested in a Zn-ion cell, ex situ XRD results (Figure 6.12b) showed that both the spinel peak at ~58° and the DRX peak at ~65° shifted to lower angles during Zn discharge. This systematic peak shift corresponds to lattice expansion, which is characteristic of cation insertion, indicating that Zn ions were incorporated into both the spinel and DRX phases. After charging, these reflections returned to their original positions, confirming the reversibility of Zn intercalation and deintercalation in both phases. Detailed refinements of these structural changes are shown in Figure 6.13. Complementary Mn K-edge XANES analysis (Figure 6.12c) revealed that the Mn valence state decreased during Zn insertion, indicating Mn reduction. However, the valence change did not fully return to that

of pristine $LiMnO_2$, consistent with the lower Zn discharge capacity (~170 mAh g^{-1}) compared to the Li charging capacity (~285 mAh g^{-1}). Upon re-charging in the Zn cell, the Mn valence state recovered, demonstrating the reversibility of the redox process. Furthermore, EXAFS analysis (Figure 6.12d) showed that both Mn–O and Mn–Mn bond lengths expanded during Zn intercalation and contracted upon Zn extraction, providing direct structural evidence for the reversible nature of Zn storage in this system.

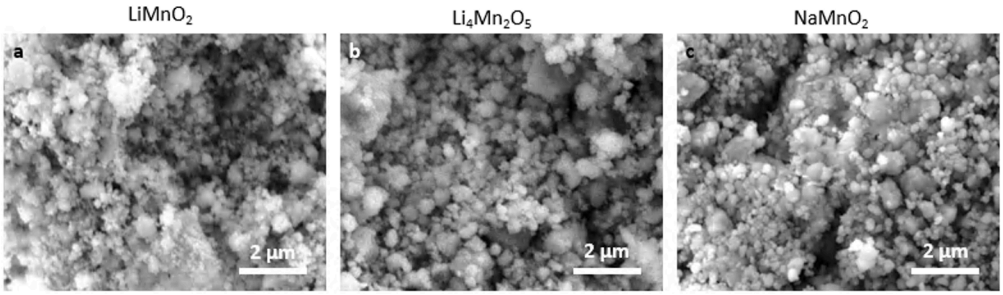

Figure 6.14 SEM images of as-synthesised (a) $LiMnO_2$, (b) $Li_4Mn_2O_5$ and (c) $NaMnO_2$.

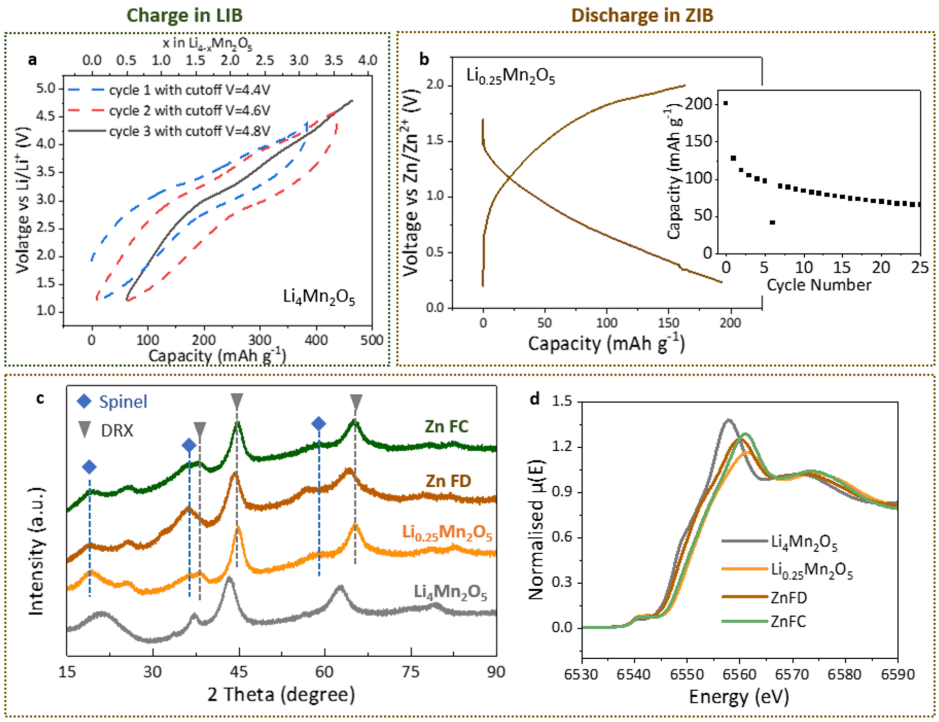

Figure 6.15 (a) Charge curve of $Li_4Mn_2O_5$ DRX in a Li-ion battery at 10 mA g^{-1}. (b) Discharge/charge profile of delithiated $Li_{0.25}Mn_2O_5$ in a Zn-ion battery, with inset showing cycling stability at 10 mA g^{-1}. (c) Ex situ powder XRD of pristine $Li_4Mn_2O_5$, $Li_{0.25}Mn_2O_5$, Zn FD, and Zn FC. (d) Ex situ Mn K-edge XANES spectra of $Li_4Mn_2O_5$, $Li_{0.25}Mn_2O_5$, Zn FD, and Zn FC.

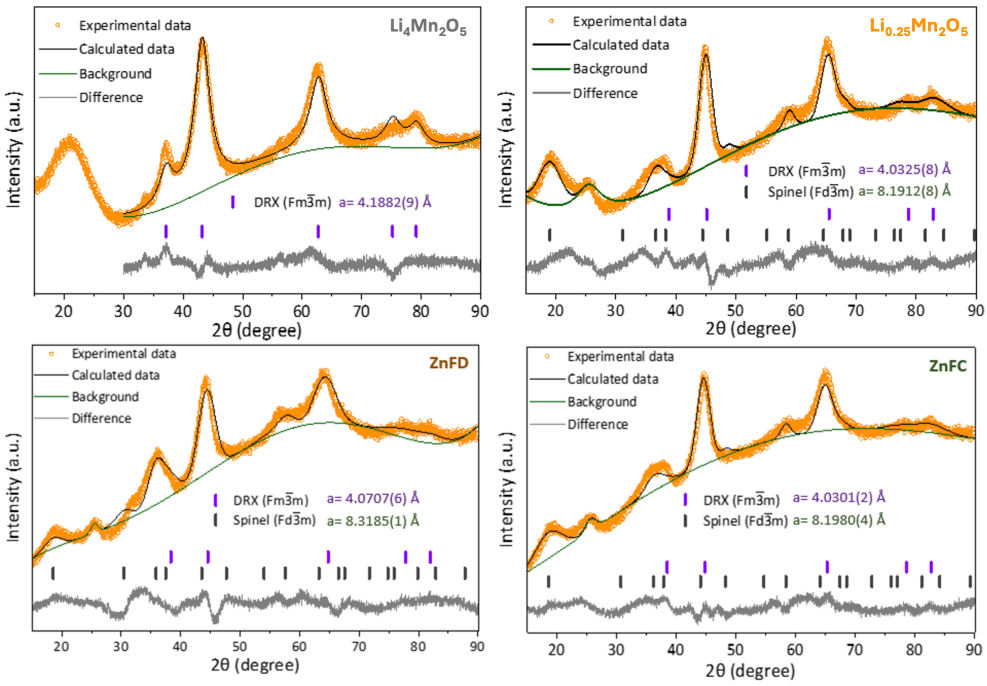

Figure 6.16 Rietveld refinement of XRD patterns for $Li_4Mn_2O_5$, $Li_{0.25}Mn_2O_5$, Zn FD, and Zn FC.

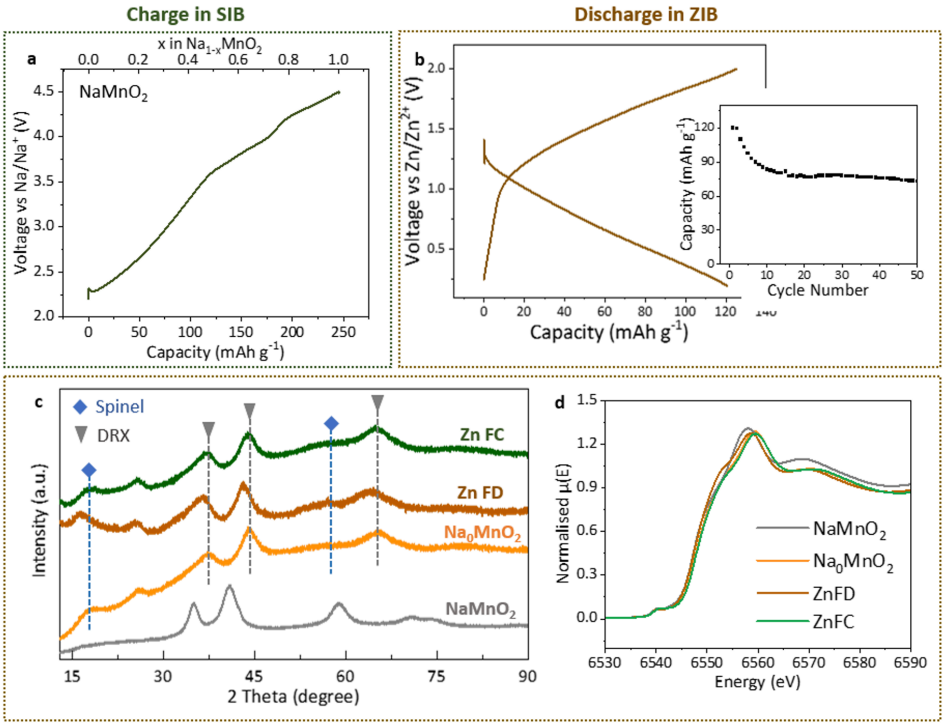

Figure 6.17 (a) Charge curve of $NaMnO_2$ DRX in a Na-ion battery at 10 mA g^{-1}. (b) Discharge/charge profile of delithiated Na_0MnO_2 in a Zn-ion battery, with inset showing cycling stability at 10 mA g^{-1}. (c) Ex situ powder XRD of pristine $NaMnO_2$, Na_0MnO_2, Zn FD, and Zn FC. (d) Ex situ Mn K-edge XANES spectra of $NaMnO_2$, Na_0MnO_2, Zn FD, and Zn FC.

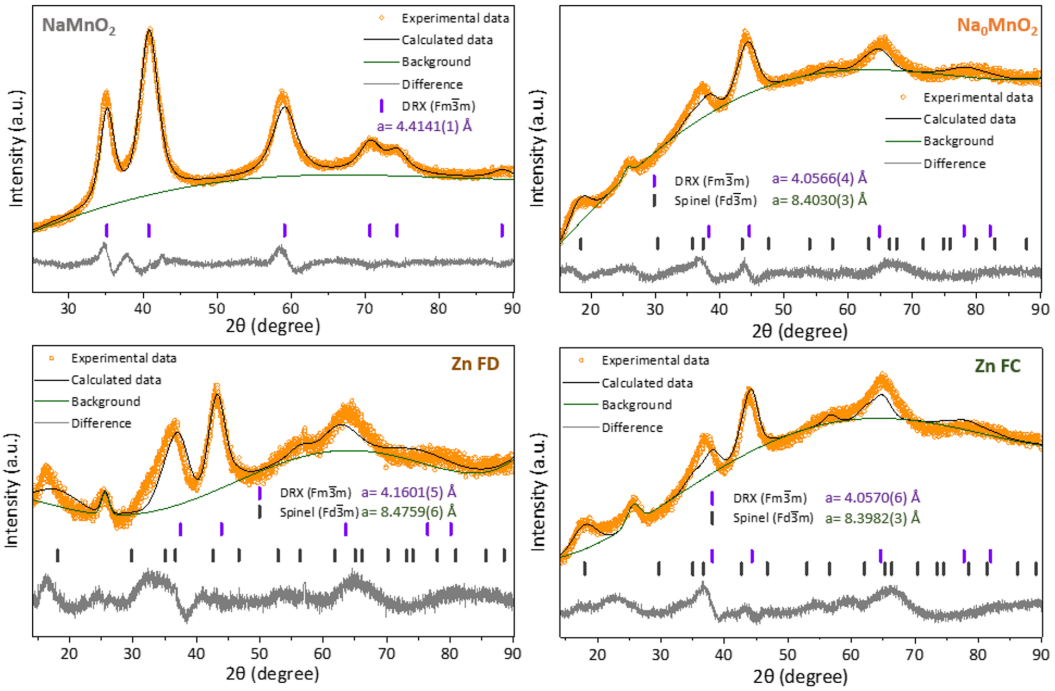

Figure 6.18 Rietveld refinement of XRD patterns for $NaMnO_2$, Na_0MnO_2, Zn FD, and Zn FC.

The challenge, however, is that the mobility of Mn ions, combined with the absence of d^0 metal doping in DRX, drives partial transformation of the DRX phase into spinel during de-lithiation,[23] making complete separation of the two phases difficult. Nevertheless, these results clearly demonstrate that once vacancies are introduced, Zn diffusion in DRX can be unlocked and both DRX and spinel phases can participate in reversible Zn (de)intercalation. To generalise this observation, this study was extended to other Mn-based DRX systems, including Li-rich $Li_4Mn_2O_5$ and Na-based $NaMnO_2$, both synthesised by ball milling with particle sizes ~50-200 nm, comparable to $LiMnO_2$ (Figure 6.14). Similar to $LiMnO_2$, both $Li_4Mn_2O_5$ (Figure 6.15 and 6.16) and $NaMnO_2$ (Figure 6.17 and 6.18) also undergo structural transformation to spinel upon delithiation/desodiation in Li/Na-ion cells due to Mn mobility. When these delithiation/desodiation materials were cycled in Zn-ion cells, both the DRX and the in situ formed spinel phases became electrochemically active (Figure 6.15b and 6.17b). During Zn intercalation and deintercalation, both phases exhibited reversible structural

changes, as confirmed by XRD (Figure 6.15c and 6.17c), along with reversible Mn valence changes, as evidenced by XANES (Figure 6.15d and 6.17d).

To stabilise the DRX framework, it is well established that incorporation of at least one d^0 species is beneficial. d^0 cations preferentially occupy highly distorted octahedral sites, leaving the less distorted sites available for cations with partially filled d orbitals, thereby lowering the overall energy of the disordered structure.[24,25] Guided by this principle, d^0 cation Ti^{4+} was introduced to synthesise $Li_{1.2}Mn_{0.4}Ti_{0.4}O_2$ as a model system. Unlike the other DRX materials discussed in this chapter, which were prepared by high-energy ball milling and naturally adopt particle sizes of ~50-200 nm, this material was initially synthesised via a solid-state route and exhibited large particles (~10 μm), as shown in Figure 6.19a. Since smaller particle sizes are generally required to enhance Li diffusivity in DRX systems,[26,27] the material was subsequently processed by ball milling at 600 rpm for 6 h, reducing the particle size to ~50-200 nm (Figure 6.19c). Then this nanosized material was delithaited to create cation vacancy in Li-ion cell, delivering a charge capacity of ~320 mAh g^{-1} (Figure 6.20a), in good agreement with previous reports.[28]

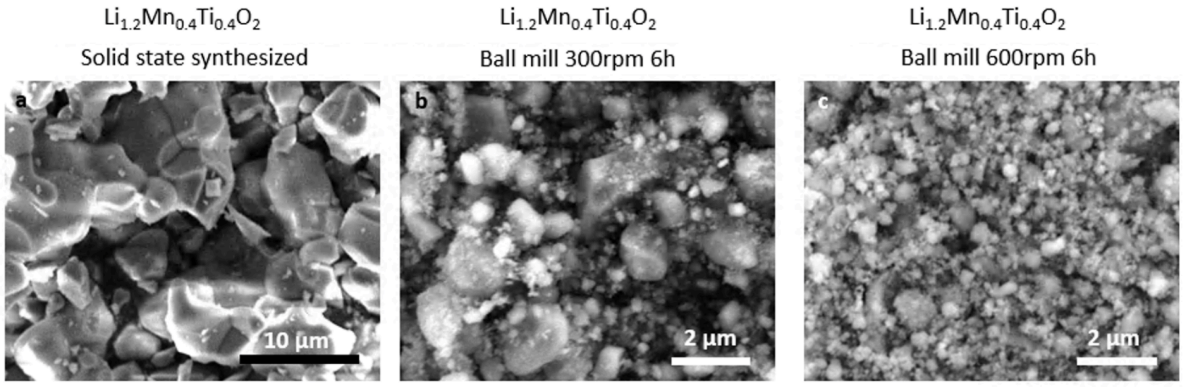

Figure 6.19 SEM images of $Li_{1.2}Mn_{0.4}Ti_{0.4}O_2$: (a) as-synthesised by solid-state method, (b) after ball milling at 300 rpm for 6 h, and (c) after ball milling at 600 rpm for 6 h.

When the delithiated $Li_{1.2}Mn_{0.4}Ti_{0.4}O_2$ cathode was applied to Zn-ion cells, it delivered a high reversible capacity of approximately 170 mAh g^{-1}, with cycling performance as shown

in the inset of Figure 6.20b. The inclusion of Ti proved critical for structural stability: even in the fully delithiated state ($Li_{0.23}Mn_{0.4}Ti_{0.4}O_2$), the material maintained a single-phase DRX structure without the formation of secondary phases. During Zn intercalation, XRD patterns in Figure 6.20c and Figure 6.21 revealed unit-cell expansion upon Zn insertion, followed by contraction upon Zn extraction, with peaks fully returning to their original positions, confirming the DRX structural reversibility of Zn (de)intercalation.

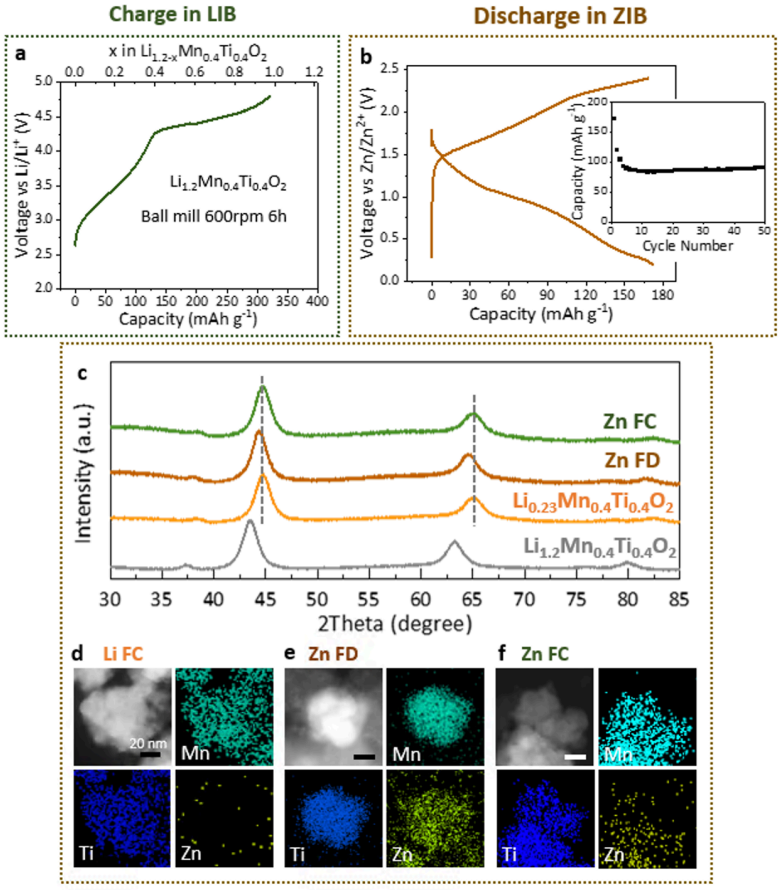

Figure 6.20 (a) Charge curve of $Li_{1.2}Mn_{0.4}Ti_{0.4}O_2$ DRX (ball-milled at 600 rpm for 6 h) in a Li-ion battery at 10 mA g^{-1}. (b) Discharge/charge profile of delithiated $Li_{1.2}Mn_{0.4}Ti_{0.4}O_2$ in a Zn-ion battery, with inset showing cycling stability at 10 mA g^{-1}. (c) Ex situ powder XRD of pristine $Li_{1.2}Mn_{0.4}Ti_{0.4}O_2$, $Li_{0.23}Mn_{0.4}Ti_{0.4}O_2$, Zn FD, and Zn FC. (d-f) STEM-EDX mapping of Mn, Ti, and Zn in LiFC ($Li_{0.23}Mn_{0.4}Ti_{0.4}O_2$), Zn FD, and Zn FC.

Furthermore, STEM-EDX mapping (performed by my supervisor Dr. Alex Robertson) in Figure 6.20d provided direct nanoscale evidence of Zn insertion, showing Zn signals appearing during discharge and disappearing upon charge. This confirms that Zn insertion and extraction

are highly reversible and uniform at the particle level. These findings demonstrate that introducing vacancies into a stabilised single-phase DRX framework enables accessible Zn diffusion, in strong agreement with the DFT calculation result.

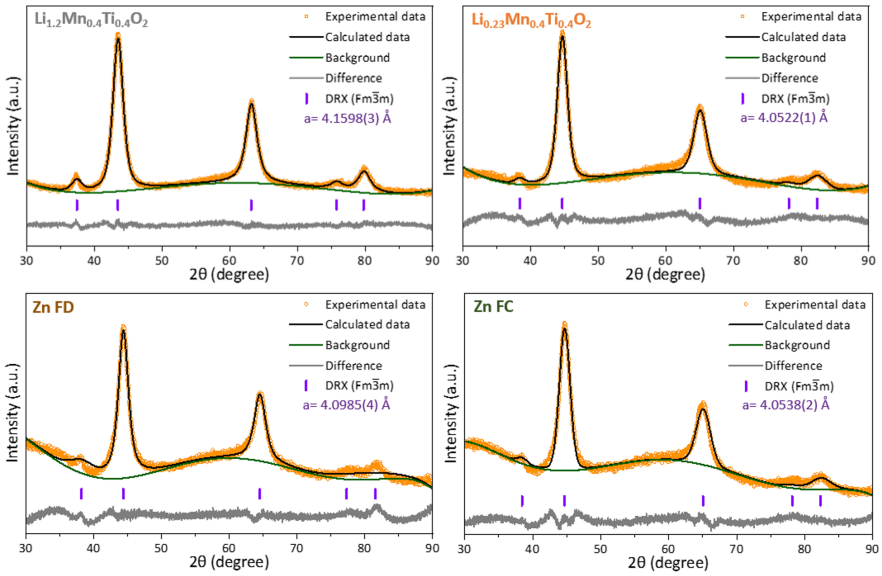

Figure 6.21 Rietveld refinement of XRD patterns for $Li_{1.2}Mn_{0.4}Ti_{0.4}O_2$, $Li_{0.23}Mn_{0.4}Ti_{0.4}O_2$, Zn FD, and Zn FC.

Interestingly, particle size was found to have influence on Zn diffusion. For comparison, the as-synthesised material was ball milled under milder conditions (300 rpm, 6 h), producing submicron particles (~200–1000 nm) as shown in Figure 6.19b. When delithiated in Li-ion cells, this material delivered nearly the full charge capacity of ~315 mAh g^{-1} (Figure 6.22a), comparable to the ~320 mAh g^{-1} achieved with the finer nanosized material prepared at 600 rpm for 6 h (Figure 6.20a). This indicates that Li diffusion can occur effectively within submicron particles, providing sufficient transport pathways for near-full electrochemical utilisation.

In contrast, when cycled in Zn-ion cells, the same submicron material (ball milled 300 rpm, 6 h) delivered only ~80 mAh g^{-1} (Figure 6.22b), far below the 170 mAh g^{-1} obtained with the finer particles produced under harsher milling conditions (600 rpm, 6 h) (Figure 6.20b).

This demonstrates that Zn requires much shorter diffusion lengths, only achievable in nanoscale particles, to overcome its intrinsically sluggish mobility.

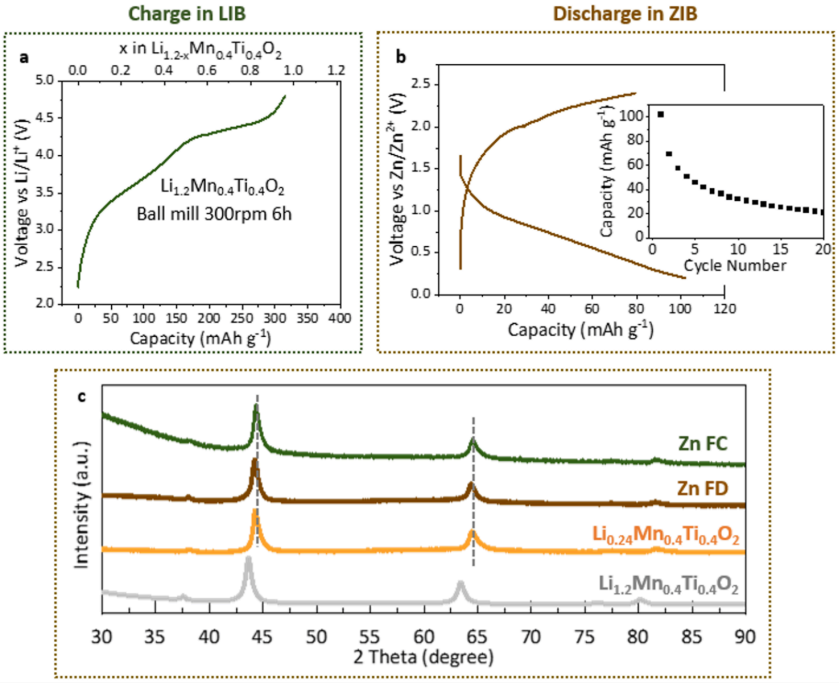

Figure 6.22 (a) Charge curve of $Li_{1.2}Mn_{0.4}Ti_{0.4}O_2$ DRX (ball-milled at 300 rpm for 6 h) in a Li-ion battery at 10 mA g^{-1}. (b) Discharge/charge profile of delithiated $Li_{0.24}Mn_{0.4}Ti_{0.4}O_2$ in a Zn-ion battery, with inset showing cycling stability at 10 mA g^{-1}. (c) Ex situ powder XRD of pristine $Li_{1.2}Mn_{0.4}Ti_{0.4}O_2$, $Li_{0.24}Mn_{0.4}Ti_{0.4}O_2$, Zn FD, and Zn FC.

This stark contrast highlights the fundamental difference between Li^+ and Zn^{2+} transport: Li^+, with its lower charge density and weaker electrostatic interactions, can migrate efficiently even in relative larger particles, whereas Zn^{2+} diffusion is severely constrained, demanding fine particle sizes to achieve high electrochemical performance.

To compare the ion transport kinetics of Li^+ and Zn^{2+} in DRX materials, GITT measurements were carried out on delithiated $Li_{1.2}Mn_{0.4}Ti_{0.4}O_2$ which was prepared under harsher ball-milling conditions (600 rpm, 6 h). After electrochemical delithiation, the resulting $Li_{0.23}Mn_{0.4}Ti_{0.4}O_2$ phase was used as a starting point for subsequent ion insertion/ectraction experiments with either Li^+ or Zn^{2+}. This material exhibits both Mn and oxygen redox activity. Since Zn insertion delivers a reversible capacity of ~170 mAh g^{-1}, the same cutoff capacity was

applied for Li insertion to ensure that identical redox species were involved in both cases. This controlled approach allowed a fair comparison of the kinetic behaviour of Li^+ and Zn^{2+}, eliminating differences that could arise from probing different redox processes.

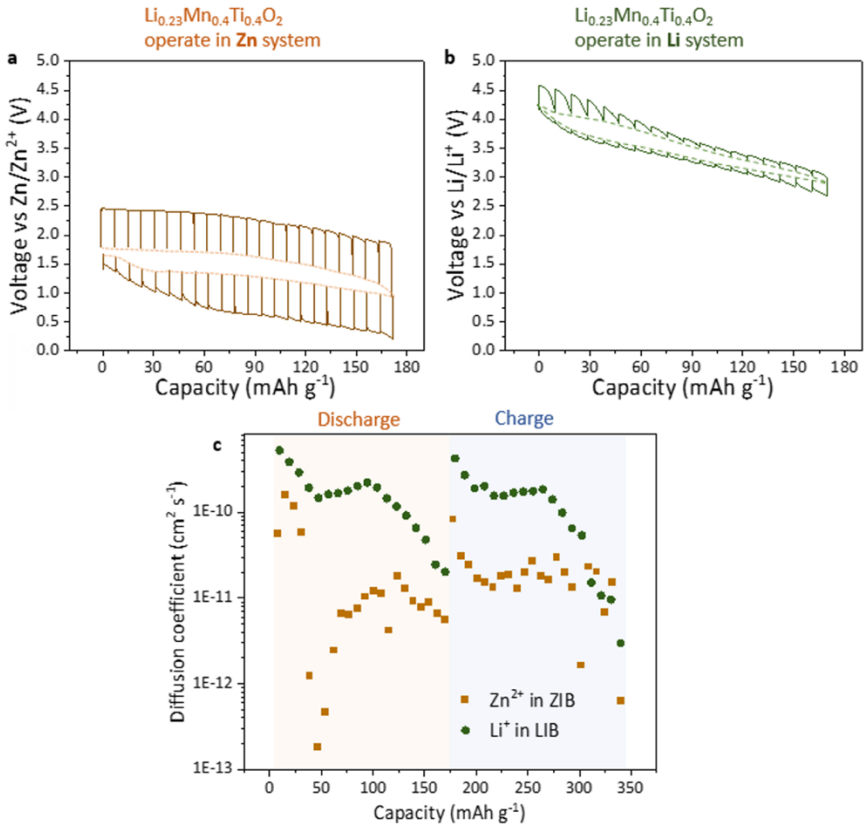

Figure 6.23 GITT profiles of delithiated $Li_{0.23}Mn_{0.4}Ti_{0.4}O_2$ DRX (ball-milled at 600 rpm for 6 h) measured at 10 mA g^{-1} with 1 h current pulses followed by 4 h relaxation to reach equilibrium, tested in (a) a Zn-ion battery and (b) a Li-ion battery. (c) Calculated Zn and Li diffusion coefficients in delithiated $Li_{1.2}Mn_{0.4}Ti_{0.4}O_2$ DRX during discharge and charge.

Under these controlled conditions, the GITT measurements revealed a clear kinetic contrast between Li^+ and Zn^{2+} insertion. As shown in Figure 6.23b, Li^+ insertion/extraction curve showed a small polarisation of only ~0.3 V. In stark contrast, Zn^{2+} insertion/extraction curve exhibited a much larger voltage hysteresis of ~1.6 V (Figure 6.23a), despite being tested at the same low current density (10 mA g^{-1}). By tracking the quasi-equilibrium potential after each current pulse (dashed lines in Figure 6.23a), it was observed that in the Zn-ion cell, the quasi-equilibrium discharge and charge curves closed most of the hysteresis gap. This

indicates that the large voltage hysteresis primarily due to slow Zn^{2+} insertion and extraction kinetics. In contrast, for Li^{+} (Figure 6.23b), the quasi-equilibrium potential only slightly narrowed the gap between the charge and discharge curves, indicating much faster Li^{+} ion transport and lower kinetic barriers. The diffusion coefficients calculated from GITT (Figure 6.23c) further quantify this disparity. Zn^{2+} exhibited diffusivities in the range of ~10^{-13} to 10^{-10} cm^2 s^{-1}, nearly two orders of magnitude lower than those of Li^{+}, which ranged from ~10^{-11} to 10^{-9} cm^2 s^{-1}. This provides direct, quantitative evidence that Zn^{2+} transport is intrinsically sluggish compared to Li^{+} at the cathode level, fully consistent with the high migration barriers obtained by DFT calculations.

6.3.4 Delithiated DRX Sulphides as Cathodes in Zn-Ion Batteries

To accelerate Zn diffusion in DRX frameworks, it is useful to revisit the established diffusion mechanism for Li^{+} in oxides. The migration barrier is primarily determined by electrostatic interactions between the migrating ion in the tetrahedral site and the cations occupying the two face-sharing octahedra. This barrier is strongly influenced by the local structural environment, particularly the tetrahedral height, which dictates the space available for ion relaxation during migration. Increasing the tetrahedral volume is therefore expected to reduce electrostatic repulsion and lower the migration barrier,[29] potentially enabling more facile Zn^{2+} transport, as shown in Figure 6.24a. Guided by this principle, sulfide-based DRX materials were investigated, focusing on $LiTiS_2$, where the larger S^{2-} anions expand the tetrahedral dimensions relative to oxides,[30] offering a promising route to improve Zn mobility.

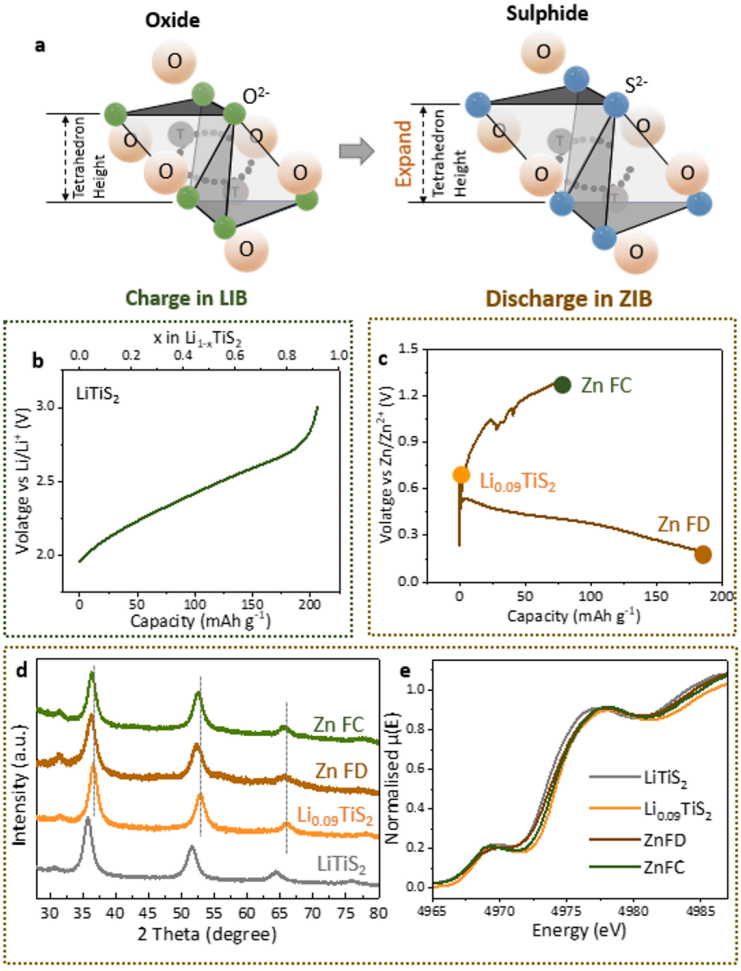

Figure 6.24 (a) Schematic of sulphide DRX, highlighting its larger tetrahedral height compared to oxide DRX. (b) Charge curve of $LiTiS_2$ DRX in a Li-ion battery at 10 mA g^{-1}. (c) Discharge/charge profile of delithiated $LiTiS_2$ in a Zn-ion battery at 10 mA g^{-1}. (d) Ex situ powder XRD of pristine $LiTiS_2$, $Li_{0.09}TiS_2$, Zn FD, and Zn FC. (e) Ex situ Ti K-edge XANES spectra of $LiTiS_2$, $Li_{0.09}TiS_2$, Zn FD, and Zn FC.

Based on Rietveld refinement of XRD data (Figure 6.24d and 6.25), the delithiated $LiTiS_2$ structure exhibits a unit cell parameter of 4.9075 Å, substantially larger than that of the delithiated DRX oxide $Li_{1.2}Mn_{0.4}Ti_{0.4}O_2$, which has a unit cell size of 4.0522 Å (Figure 6.21). This confirms that sulfide DRX frameworks provide larger tetrahedral sites compared to oxides.

Electrochemical testing showed that delithiated $LiTiS_2$ delivered a high initial discharge capacity in Zn-ion cells. However, its reversibility was poor, as indicated by a much lower charge capacity (Figure 6.24c). GITT analysis (Figure 6.26c,d) further revealed that Zn^{2+} diffusion coefficients during insertion were significantly higher in the sulfide than in the oxide,

confirming that the expanded tetrahedral environment of the sulfide indeed facilitates Zn^{2+} mobility. Despite this improvement, Zn extraction remained sluggish, with a much lower diffusion coefficient during charge, highlighting a critical kinetic asymmetry that limits reversibility.

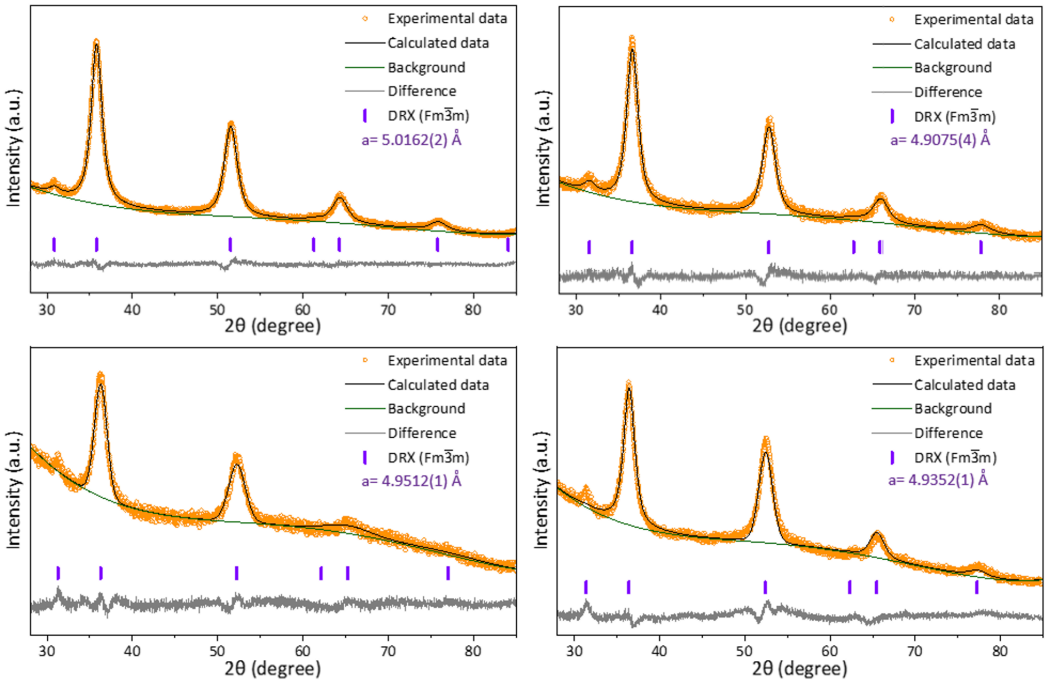

Figure 6.25 Rietveld refinement of XRD patterns for $LiTiS_2$, $Li_{0.09}TiS_2$, Zn FD, and Zn FC.

While the poor reversibility limits practical application, these findings provide proof-of-concept that expanding the tetrahedral size through anion substitution can reduce the Zn migration barrier and facilitate Zn diffusion in DRX materials. This approach could be extended to other larger anions, such as Cl^-,[29] to enhance Zn mobility. More broadly, it highlights lattice-engineering strategies, such as anion substitution or mixed-anion frameworks, as a promising pathway to enable faster Zn diffusion and improved performance in DRX cathodes for non-aqueous ZIBs.

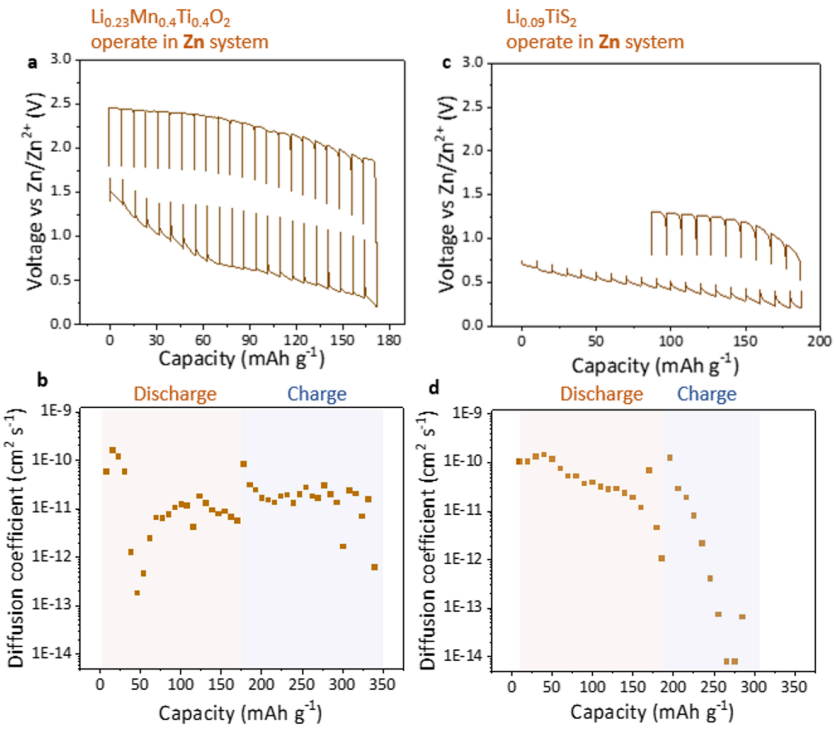

Figure 6.26 (a) GITT profile of delithiated $Li_{1.2}Mn_{0.4}Ti_{0.4}O_2$ DRX (ball-milled at 600 rpm for 6 h) measured at 10 mA g^{-1} with 1 h current pulses followed by 4 h relaxation, tested in a Zn-ion battery. (b) Zn diffusion coefficients of delithiated $Li_{1.2}Mn_{0.4}Ti_{0.4}O_2$ DRX during discharge and charge. (c) GITT profile of delithiated $LiTiS_2$ DRX measured under the same conditions in a Zn-ion battery. (d) Zn diffusion coefficients of delithiated $LiTiS_2$ DRX during discharge and charge.

6.4 Conclusion

To achieve high-voltage ZIBs while minimising side reactions at both the cathode and anode, nonaqueous electrolytes were explored. To identify suitable and compatible cathode materials for nonaqueous ZIBs, DRX structures were investigated due to their demonstrated advantages in Li- and Na-based systems, including small volume change and high capacity. A wide range of Zn-based DRX compositions were synthesised and evaluated, varying transition metal species, Zn content, and configurational entropy. However, none of these materials exhibited measurable capacity. This lack of activity was traced to the intrinsic DRX framework, where Zn^{2+} faces strong electrostatic repulsion that severely limits its diffusion.

DFT calculations confirmed this limitation, showing that even the most favourable 0-TM channels present prohibitively high migration barriers for Zn^{2+} transport. Introducing cation vacancies can significantly reduce these barriers. Experimentally, this strategy was validated using delithiated Li-based DRX ($Li_{1.2}Mn_{0.4}Ti_{0.4}O_2$), which delivered a reversible capacity of 170 mAh g^{-1} in a Zn-ion cell. GITT measurements further quantified Zn^{2+} diffusivity, revealing values nearly two orders of magnitude lower than those for Li^+, highlighting the sluggishness of Zn transport.

To further enhance Zn diffusion, anion engineering was explored. Larger anions, such as sulfur, expand the unit cell and reduce electrostatic constraints, thereby lowering migration barriers. This work provides critical insights into defect engineering strategies to unlock Zn mobility in DRX frameworks, offering design principles relevant not only for ZIBs but also for other multivalent ion storage systems.

6.5 Reference

1 Chen, D., Ahn, J. & Chen, G. An overview of cation-disordered lithium-excess rocksalt cathodes. *ACS Energy Lett.* **6**, 1358-1376 (2021).

2 Lee, J. *et al.* Unlocking the potential of cation-disordered oxides for rechargeable lithium batteries. *Science* **343**, 519-522 (2014).

3 Xu, J. *et al.* Enhancing the electrode gravimetric capacity of $Li_{1.2}Mn_{0.4}Ti_{0.4}O_2$ cathode using interfacial carbon deposition and carbon nanotube-mediated electrical percolation. *ACS Appl. Mater. Interfaces* **15**, 31711-31719 (2023).

4 Zhou, K. *et al.* Elucidating and mitigating the degradation of cationic–anionic redox processes in $Li_{1.2}Mn_{0.4}Ti_{0.4}O2$ cation-disordered cathode materials. *ACS Appl. Mater. Interfaces* **11**, 45674-45682 (2019).

5 Obrovac, M., Mao, O. & Dahn, J. Structure and electrochemistry of $LiMO_2$ (M= Ti, Mn, Fe, Co, Ni) prepared by mechanochemical synthesis. *Solid State Ionics* **112**, 9-19 (1998).

6 Niu, Y. *et al.* Regulation of Oxygen Redox in Disordered Rock-Salt $LiXO_2$ Li-Ion Cathodes by Cation Effects: A First-Principles Study. *J. Phys. Chem. Lett.* **16**, 8105-8113 (2025).

7 Lun, Z. *et al.* Cation-disordered rocksalt-type high-entropy cathodes for Li-ion batteries. *Nat. Mater.* **20**, 214-221 (2021).

8 Ji, H. *et al.* Hidden structural and chemical order controls lithium transport in cation-disordered oxides for rechargeable batteries. *Nat. Commun.* **10**, 592 (2019).

9 Urban, A., Lee, J. & Ceder, G. The configurational space of rocksalt-type oxides for high-capacity lithium battery electrodes. *Adv. Energy Mater.* **4**, 1400478 (2014).

10 Wang, Y. *et al.* Unraveling the nature and role of layered cation ordering in cation-disordered rock-salt cathodes. *J. Am. Chem. Soc.* **144**, 19838-19848 (2022).
11 Baranov, A. N., Sokolov, P. S. & Solozhenko, V. L. ZnO under pressure: from nanoparticles to single crystals. *Crystals* **12**, 744 (2022).
12 Rong, Z. *et al.* Materials design rules for multivalent ion mobility in intercalation structures. *Chem. Mater.* **27**, 6016-6021 (2015).
13 Kang, B. *et al.* Elucidating lithium-ion diffusion kinetics in cation-disordered rocksalt cathodes. *Energy Environ. Sci.* **18**, 2330-2341 (2025).
14 Li, L. *et al.* Atomic-scale probing of short-range order and its impact on electrochemical properties in cation-disordered oxide cathodes. *Nat. Commun.* **14**, 7448 (2023).
15 Szymanski, N. J. *et al.* Modeling short-range order in disordered rocksalt cathodes by pair distribution function analysis. *Chem. Mater.* **35**, 4922-4934 (2023).
16 Sun, Y. *et al.* Expandable Li percolation network: the effects of site distortion in cation-disordered rock-salt cathode material. *J. Am. Chem. Soc.* **145**, 11717-11726 (2023).
17 Cai, Z. *et al.* In situ formed partially disordered phases as earth-abundant Mn-rich cathode materials. *Nat. Energy* **9**, 27-36 (2024).
18 Jang, Y. I., Huang, B., Wang, H., Sadoway, D. R. & Chiang, Y. M. Electrochemical cycling-induced spinel formation in high-charge-capacity orthorhombic $LiMnO_2$. *J. Electrochem. Soc.* **146**, 3217 (1999).
19 Chiang, Y.-M., Wang, H. & Jang, Y.-I. Electrochemically induced cation disorder and phase transformations in lithium intercalation oxides. *Chem. Mater.* **13**, 53-63 (2000).
20 Miyaoka, Y. *et al.* A Practical and Sustainable Ni/Co-Free High-Energy Electrode Material: Nanostructured $LiMnO_2$. *ACS Cent. Sci.* **10**, 1718-1732 (2024).
21 Mahara, Y. *et al.* Appearance of the 4 V signal without transformation to spinel-related oxides from loose-crystalline rock-salt $LiMnO_2$. *J. Power Sources* **497**, 229788 (2021).
22 Sato, T., Sato, K., Zhao, W., Kajiya, Y. & Yabuuchi, N. Metastable and nanosize cation-disordered rocksalt-type oxides: revisit of stoichiometric $LiMnO_2$ and $NaMnO_2$. *J. Mater. Chem. A* **6**, 13943-13951 (2018).
23 Wu, V. *et al.* High energy density and micrometer-sized d^0-free disordered rocksalt cathodes. *Energy Environ. Sci.* (2025) DOI: 10.1039/d5ee01564b.
24 Song, H. *et al.* Regulating d^0 transition metals and facilitating high-performance Li-excess cation-disordered rock salt cathode materials. *J. Mater. Chem. A* **12**, 15154-15162 (2024).
25 Outka, A. *et al.* Electron localization in cation-disordered rock salt electrodes. *ACS Energy Lett.* **9**, 1863-1870 (2024).
26 Zhang, Y. *et al.* Investigating particle size-dependent redox kinetics and charge distribution in disordered rocksalt cathodes. *Adv. Funct. Mater.* **32**, 2110502 (2022).
27 Zhang, Y., Ugata, Y., Campéon, B. L. & Yabuuchi, N. Unlocking Electrode Performance of Disordered Rocksalt Oxides Through Structural Defect Engineering and Surface Stabilization with Concentrated Electrolyte. *Adv. Energy Mater.* **14**, 2304074 (2024).
28 Yabuuchi, N. *et al.* Origin of stabilization and destabilization in solid-state redox reaction of oxide ions for lithium-ion batteries. *Nat. Commun.* **7**, 13814 (2016).
29 Tang, W. *et al.* Regulating the anion redox and suppressing the structural distortion of cation-disordered rock-salt cathode materials to improve cycling durability through chlorine substitution. *ACS Appl. Mater. Interfaces* **15**, 17938-17946 (2023).

30 Shinoda, M., Rajendra, H. B. & Yabuuchi, N. Rocksalt and layered metal sulfides for Li storage applications: $LiMe_{0.5}Ti_{0.5}S_2$ (me=Fe^{2+}, Mn^{2+}, and Mg^{2+}). *ACS Appl. Energy Mater.* **5**, 2642-2646 (2022).

7

7 Conclusion and Future Work

7.1 Conclusion

Over the past decade, ZIBs have attracted considerable attention. Due to the favourable redox potential of Zn, Zn anode is compatibility with aqueous electrolytes. Aqueous electrolyte attributes offer compelling advantages in safety, cost, and environmental sustainability. However, persistent interfacial instabilities, such as parasitic reactions and dendritic growth at the Zn anode, along with Mn dissolution and structural degradation at Mn-based cathodes, continue to limit cycle life and practical deployment. While many studies have examined these issues in isolation, few have adopted a holistic, cell-level approach. This thesis addresses this gap by developing a mechanistic understanding of interfacial degradation and proposing integrated strategies to enhance overall ZIB performance.

The first part of this thesis focuses on the zinc anode–electrolyte interface. Planar zinc deposition is identified as critical for suppressing side reactions and achieving stable cycling. While high current densities (>20 mA cm^{-2}) naturally promote planar growth, they are incompatible with typical cathode operation. To overcome this, an approach employing uniaxial mechanical pressure was introduced, enabling planar Zn growth at cathode-compatible current densities. Zn anodes plated under applied pressure exhibit pliable microstructures and uniform deposition, which enhance interfacial conformity and resist detachment during stripping, thereby minimising the formation of dead zinc. Moreover, the preferred crystallographic orientation induced by pressure-assisted plating provides improved resistance to corrosion. Together, these effects significantly enhance full-cell cycling performance under cathode-compatible operating conditions.

The second part focuses on the cathode–electrolyte interface, with an emphasis on the widely studied MnO_2 cathode. Using operando XRF mapping and ex-situ spectroscopic analyses, the primary charge storage mechanism was shown to proceed via reversible Mn

dissolution and redeposition. The role of Mn^{2+} additives was clarified: rather than preventing Mn dissolution, they act as a reservoir of active material, boosting capacity. However, two intrinsically irreversible processes: incomplete MnO_2 dissolution during discharge and incomplete Mn^{2+} redeposition during charge remain the fundamental cause of capacity fade, regardless of Mn^{2+} electrolyte addition. These findings underscore the need to improve dissolution and deposition efficiency to achieve long-term stability, highlighting the critical role of the cathode–electrolyte interphase in governing MnO_2 cathode performance.

Recognising that many challenges of Zn metal arise from the aqueous environment, the third part of this thesis explores anode-free ZIB architectures. In this design, no metallic Zn is present initially, reducing side reactions typically associated with zinc metal during resting. A novel Zn-containing DRX cathode, $ZnMnO_2$, was developed to release Zn^{2+} during the initial charge, providing the zinc source for subsequent cycling. $ZnMnO_2$ delivers a high discharge capacity of 233 mAh g^{-1} and demonstrates stable cycling. When paired with a Zn-free current collector, the energy density is significantly increased—nearly sevenfold compared to conventional zinc metal anodes—despite a lower overall capacity. The dominant capacity mechanism remains Mn dissolution and redeposition. This work establishes $ZnMnO_2$ as a promising cathode material for anode-free ZIBs and highlights the broader potential of DRX oxides based on earth-abundant elements, such as $ZnFeO_2$, for sustainable high-performance energy storage.

The final part of this thesis explores non-aqueous ZIBs, which, while less safe than aqueous systems, offer a wider electrochemical stability window, enabling higher voltages and greater energy density. DRX frameworks were investigated as potential cathodes due to their proven success in Li- and Na-ion systems, but Zn-based DRX showed poor activity due to high Zn^{2+} migration barriers, confirmed by DFT calculations. To overcome this, cation vacancies

were introduced, significantly reducing migration barriers and validated experimentally using delithiated Li-based DRX, which delivered a reversible capacity of 170 mAh g^{-1}. GITT measurements revealed Zn^{2+} diffusion is two orders of magnitude slower than Li^{+}, highlighting the challenge of multivalent ion transport. Anion engineering with larger anions further enhanced diffusion, providing design principles for next-generation multivalent batteries.

Collectively, this thesis presents a comprehensive strategy to address the interconnected challenges of Zn anodes, Mn-based cathodes, and electrolytes in both aqueous and non-aqueous ZIBs. By linking fundamental mechanisms with practical cell-level solutions, it tackles key degradation pathways and demonstrates integrated approaches to enhance performance, ultimately advancing the potential of ZIBs for sustainable energy storage.

7.2 Future work

7.2.1 Fundamental Understanding

Mn-based oxides remain the most widely studied cathodes for aqueous ZIBs. In aqueous electrolytes, these materials typically operate through a Mn dissolution–deposition mechanism that appears largely independent of the parent oxide's initial composition or crystal structure. To improve long-term cycling stability and enhance cathode utilisation, it is crucial to develop a fundamental understanding of the factors that govern this process and to identify strategies to control it. Because Mn dissolution and deposition are cathode-electrolyte interfacial processes, the electrolyte plays a central role in determining Mn-based oxide cathode performance, with both pH and electrolyte composition exerting significant influence.

pH is one of the most critical factors governing the dissolution–deposition behaviour. Previous studies have shown that lowering the electrolyte pH decreases the MnO_2 dissolution potential to below 1 V vs. Zn^{2+}/Zn while simultaneously providing protons that facilitate Mn dissolution. This combined effect accelerates Mn dissolution, initially increasing the discharge capacity by generating a more readily accessible pool of electroactive Mn species. While this may appear advantageous, low pH also raises the Mn^{2+} deposition potential toward ~2 V vs. Zn^{2+}/Zn. Such a high deposition potential can exceed the electrochemical stability window of aqueous electrolytes, triggering parasitic side reactions, such as water splitting. In addition, acidic conditions accelerate corrosion of the Zn anode and promote other undesirable interfacial reactions that compromise overall cell stability. Transitioning to near-neutral pH electrolytes can mitigate these parasitic reactions at the anode, yet this shift introduces new challenges. At higher pH, the thermodynamic driving force for MnO_2 dissolution decreases, which may limit cathode utilisation and lead to incomplete redox activity. Consequently, neither highly acidic nor neutral electrolytes alone offer a perfect solution. The relationship between pH, cathode dissolution–deposition dynamics, and Zn anode stability remains complex and poorly understood. Future studies should systematically investigate how electrolyte pH influences both half-cell and full-cell performance, including the interplay between Mn-based cathodes and Zn anodes.

Beyond pH, the chemistry of the electrolyte anions also plays a pivotal role. For example, MnO_2 exhibits strikingly different electrochemical behaviours in 1 M $ZnSO_4$, 1 M $Zn(CF_3SO_3)_2$, and 1 M $Zn(CH_3COO)_2$ electrolytes. While part of this variation arises from differences in pH, other factors are also at play, including changes in solvation structure and ion coordination. The identity and concentration of anions directly influence Zn^{2+} and Mn^{2+} coordination environments, affecting Gibbs free energies for desolvation and potentially

altering surface interactions and solvent co-intercalation behaviour. Carefully designed experiments are needed to disentangle these effects and determine how specific anions govern Mn dissolution, redeposition, and cathode performance. A comprehensive understanding of this relationship will be essential for defining an optimal pH window and electrolyte composition that maximises Mn utilisation, minimises parasitic reactions, and ensures long-term cycling stability and efficiency in practical ZIBs.

Even beyond the influence of the electrolyte, the dissolution–deposition process itself remains poorly understood. While it is clear that Mn-based oxides dissolve to produce Mn^{2+} in the electrolyte, the nature of the redeposited phase during charging is less well defined. For instance, this thesis shows that in DRX $ZnMnO_2$ systems, the phase formed upon charging is spinel-type $ZnMnO_3$, whereas in α-MnO_2 systems, the redeposited phase is ε-MnO_2. This suggests that the initial cathode structure may act as a template, guiding the nucleation and growth of the redeposited material. Such structural templating could play a crucial role in determining the reversibility and efficiency of the dissolution–deposition pathway. Electrolyte additives have been also reported to influence this deposition process, modifying nucleation pathways and altering the structure of the redeposited phase, but the underlying mechanisms are still not fully understood. Achieving controlled deposition will not only improve Mn utilisation but also enhance long-term cycling stability, ultimately enabling Mn-based cathodes to reach their full potential in practical aqueous ZIBs.

7.2.2 Potential Application Scenarios

Aqueous ZIBs offer several intrinsic advantages, including low cost, high safety due to the non-flammable nature of aqueous electrolytes, and compatibility with environmentally benign materials. However, these benefits are coupled with inherent challenges that also arise from the aqueous electrolyte itself. The most critical issue is the unavoidable side reactions

between metallic Zn and electrolyte, which lead to continuous hydrogen evolution. This reaction poses a serious safety risk: in a sealed system, the accumulation of hydrogen gas can create internal pressure, eventually causing cell rupture or even explosion. While an aqueous electrolyte will not ignite like organic electrolytes used in Li-ion batteries, the mechanical failure of a cell due to gas buildup still represents a major hazard for practical deployment. Moreover, this side reaction is chemical rather than purely electrochemical, meaning it can occur even when the battery is idle. As a result, catastrophic failure could happen before the battery is even put into operation, raising substantial concerns for safe handling and storage.

In this thesis, anode-free ZIB configurations were explored as a strategy to mitigate these issues by avoiding the direct use of metallic Zn at the beginning of cycling. However, during charging, Zn is inevitably electrodeposited onto the current collector. Once metallic Zn is present, parasitic reactions with water resume, leading again to hydrogen evolution and gas accumulation. This represents a fundamental limitation to the safety of aqueous ZIBs and underscores why these systems face persistent challenges in sealed-cell designs. Thus, addressing this issue is essential for any future commercialisation of ZIBs.

One potential route forward is the development of ZIBs using nonaqueous or solid-state electrolytes. By eliminating water from the system, the thermodynamic pathway for hydrogen evolution can be completely avoided, thereby removing the root cause of gas generation. However, this approach comes with its own challenges. Because the operating voltage of ZIBs is inherently lower than that of LIBs, the performance metrics of reported nonaqueous Zn systems have so far struggled to match those of their lithium counterparts. For ZIBs to compete, their primary selling point must remain their superior safety profile. This means that the selected nonaqueous electrolyte must itself be non-flammable, stable, and inexpensive, in order to leverage Zn's intrinsic safety and economic advantages. Recent studies

have explored the use of low-cost electrolytes such as $ZnCl_2$ dissolved in ethyl acetate (EA), which show promise as safer alternatives to traditional organic solvents. However, Cl^- anions are incompatible with many high-voltage cathodes due to their limited oxidative stability, limiting their practical utility. Solid-state electrolytes are another promising pathway, but even in Li-ion systems which are far more mature, solid-state batteries face significant challenges, including interfacial contact, poor ionic conductivity, and mechanical instability. Translating these technologies to Zn-based systems will likely encounter similar hurdles.

Another promising application scenario is in redox flow batteries. Unlike sealed portable devices, redox flow batteries are typically installed in large-scale stationary settings, such as grid energy storage systems. This allows them to safely use aqueous electrolytes while managing hydrogen evolution more effectively. Because redox flow batteries are not completely sealed, hydrogen gas generated by parasitic reactions can be vented or captured, reducing the risk of catastrophic failure. Furthermore, the evolved hydrogen could even be harvested as a secondary energy carrier, improving overall system efficiency and sustainability.

In summary, while the intrinsic reactivity of Zn with mild acidic aqueous electrolyte poses a major barrier to the use of aqueous ZIBs in portable or sealed applications, alternative strategies can be envisioned to overcome this challenge. Transitioning to nonaqueous or solid-state electrolytes could eliminate parasitic hydrogen evolution altogether, provided the safety and cost benefits of Zn are preserved. Alternatively, deploying aqueous ZIBs in open or semi-open systems such as redox flow batteries offers a practical pathway by managing hydrogen generation rather than preventing it. Future research should therefore focus on matching the electrolyte strategy to the intended application, ensuring that ZIBs can be developed in ways that fully leverage their advantages while addressing their fundamental safety limitations.